DISSERTATION

FORMATION AND EVOLUTION OF SECONDARY ORGANIC AEROSOL IN LABORATORY EXPERIMENTS: PRECURSORS, PROCESSES, AND PROPERTIES

Submitted by

Yicong He

Department of Mechanical Engineering

In partial fulfillment of the requirements

For the Degree of Doctor of Philosophy

Colorado State University

Fort Collins, Colorado

Spring 2022

Doctoral Committee:

Advisor: Shatanu H. Jathar

Jeffrey R. Pierce
Tami C. Bond
John Volckens

ABSTRACT

FORMATION AND EVOLUTION OF SECONDARY ORGANIC AEROSOL IN LABORATORY EXPERIMENTS: PRECURSORS, PROCESSES, AND PROPERTIES

Secondary organic aerosol (SOA) is an important fraction of atmospheric $PM_{2.5}$ which is defined as fine-mode aerosols with diameters less than 2.5 μm. SOA is ubiquitous in the atmosphere and can have considerable impacts on the climate, air quality and human health. We are limited in our ability to predict the spatial and temporal distribution of SOA and assess its environmental impacts, because current three-dimensional chemical transport models (CTM) still have large biases and relatively weak correlations with observations of SOA. One reason for the model-observation discrepancy could be that we still lack a full understanding of the precursors, chemical/physical processes, and properties of SOA that govern its formation and evolution. Therefore, there is a need to further study the precursors, processes, and properties of SOA in laboratory experiments, and to develop more accurate SOA parameterizations that can be used to update the current CTMs.

In Chapter 2, I studied SOA formation from several novel precursors which were vapors from biofuels that were under development at the National Renewable Energy Laboratory (NREL) to be used as future blendstocks to gasoline, and I developed SOA parameterizations for these biofuel precursors that corrected for the influence of vapor wall loss, using a kinetic SOA model called SOM-TOMAS (Statistical Oxidation Model coupled with TwO-Moment Aerosol Sectional Model). Although vapor wall loss has been shown to significantly impact SOA formation in environmental chamber experiments, it has rarely been corrected for in the development of SOA

parameters used in atmospheric models. Our parameterizations predicted that under atmospherically relevant conditions, some of the biofuels may produce similar or even more SOA than gasoline, possibly offsetting the environmental benefits they offered. In addition, the parameterizations predicted that correcting for vapor wall loss in chambers always resulted in similar or increased atmospheric SOA mass yields compared to chamber yields, highlighting the potential for vapor wall loss correction to increase SOA predictions from CTMs and to bridge the gap with observations.

In Chapter 3, I demonstrated a novel technique to constrain the SOA particle bulk diffusivity (D_b) in chamber experiments, using a kinetic model (i.e., SOM-TOMAS) and measurements of the particle size distribution. D_b is a property that controls the gas/particle partitioning timescale of SOA, where a higher D_b (i.e., liquid aerosol) means faster partitioning and a lower D_b (i.e., semi-solid aerosol) means slower partitioning. Here, I showed that the measured particle size distribution in SOA formation experiments contained sufficient information to constrain D_b without direct measurement of the particle phase state or viscosity.

In Chapter 4, I investigated the differences in the SOA mass yields measured in environmental chambers and oxidation flow reactors. Both chambers and flow reactors can simulate the photooxidation of Volatile Organic Compounds (VOCs), but flow reactors can achieve higher aging time (>2 weeks) than chambers (<1 day) by using very high oxidant concentrations. Their photooxidation chemistry pathways have been thought to be similar, but they produce different SOA mass yields at similar photochemical ages, which remains an unsolved problem. Here, I integrally simulated vapor and particle wall loss, semi-solid phase state, heterogeneous oxidation, particle-phase oligomerization, and new particle formation in chambers and flow reactors with experimentally constrained parameters for these processes. I showed that

the SOA mass yield difference could be explained by the different contribution of these processes to SOA formation and evolution in chambers and flow reactors. Furthermore, with a single set of SOA parameterizations for photooxidation, the model was able to simultaneously predict the SOA mass concentration, bulk chemical composition (O:C ratio), and size distribution in chambers and flow reactors. The results highlight that flow reactor data can be modeled consistently with chamber data, and they should be used in synergy with chamber data to develop SOA parameterizations applicable to long photochemical aging times.

In Chapter 5, in collaboration with Dr. Kelsey Bilsback, we investigated a widely employed assumption for particle wall loss correction in chamber experiments, regarding the interaction between wall-deposited particles and suspended vapors. Furthermore, as a continuation of the work from Chapter 2, we developed SOA parameterizations that corrected for both vapor and particle wall loss, and integrated these updated parameterizations into a CTM to assess the impacts on atmospheric SOA predictions. Specifically, we first showed that the interaction between vapors and wall-deposited particles was negligible through kinetic modeling, and accurate particle wall loss correction should assume no interaction between the two. We then found that the wall-loss-corrected SOA parameterizations greatly enhanced SOA formation in the CTM, reducing the gap with the observations. We argue that vapor and particle wall loss should be routinely accounted for in developing SOA parameterization.

ACKNOWLEDGEMENTS

It was almost 10 years ago when I first learned the word “smog” back in China, when it suddenly started to appear in the news, on the internet, and everywhere; I would look at the grey (sometimes yellowish) opaque soggy “thing” hovering above city sky and wonder if someone would invent an “atmospheric vacuum” device to clean it out. That was just wild imagination.

Yet years later now, I’m about to finish a Ph.D. program in this exact same field that kindled my interest in the environmental sciences, and ready to move on as a researcher to tackle the challenges. I cannot overstate how lucky I feel I am, and how thankful I am to those who propelled me, for me to be able to have come this far.

First and foremost, I would like to thank my advisor, Shantanu Jathar, for giving me the opportunity to even get started. I would probably have gone a different way if you overlooked my resume. Moreover, I would like to thank you for being an incredible mentor: you placed me on variously flavored projects from which I gained invaluable experiences in laboratory experiments and computer modeling; you were always quick in response when I needed guidance on my research and writing; you encouraged me (and everyone in the group) to always learn new tools and keep abreast with the latest in the field; and you sponsored my attendance at many conferences where I could share my research and build connections. Last but not least, you invited us over to your house (balcony, to be precise) and the Falooda ice cream was speechlessly good!

Secondly, I would like to thank the committee members, Jeff Pierce, Tami Bond, and John Volckens for being supportive to my research, providing feedbacks on my dissertation proposal and final documents, and making time to administer my qualification, preliminary and final exams.

Special shoutout to Jeff for pointing out ideas to try with the model that turned out to be critical in the works.

Also, I would like to thank everyone in our group, Ali, Wayne, Kelsey, Sreejith, Abe, and Dylan for being incredible co-workers. Specially to Ali, Wayne, and Kelsey: you have always been collaborative and resourceful, and my work would have moved forward slowly if not for your help. Moreover, I would like to thank all the collaborators from other groups, universities, and national laboratories.

Finally, I would like to thank my father, He Haodong, and mother, Fu Xuelian, for teaching me to be motived, dedicated, and patient. I thank my parents for making it possible for me to study abroad in the U.S. and will carry on their hardworking spirit in navigating through my career.

I acknowledge that my work has been sponsored by the U.S. Department of Energy (DOE) Office of Science, the U.S. Environmental Protection Agency (EPA), and the National Oceanic and Atmospheric Administration (NOAA). I also thank the Mechanical Engineering and Atmospheric Science departments at Colorado State University for their support.

TABLE OF CONTENTS

LIST OF TABLES

LIST OF FIGURES

CHAPTER 1: Introduction

Atmospheric $PM_{2.5}$, defined as fine-mode aerosols with diameters less than 2.5 μm, are ubiquitous and can have considerable impacts on the climate, air quality and human health (Jimenez et al., 2009). They can: (1) significantly perturb the climate system through direct radiative scattering and cloud formation (Pachauri et al., 2014; Shrivastava et al., 2017; Pai et al., 2020); (2) contribute to severe air pollution increasingly experienced in fast-developing countries around the world (Zhang et al., 2015a); and (3) be a leading cause of global disease burden, estimated to have caused 4.2 million deaths annually (Cohen et al., 2017). Organic aerosol (OA) is the most important constituent of atmospheric $PM_{2.5}$, accounting for 20-90% of $PM_{2.5}$ mass (Jimenez et al., 2009). A large fraction of OA is formed through the oxidation of volatile organic compounds (VOC) as secondary organic aerosol (SOA), as opposed to through direct emission as primary organic aerosol (POA) (de Gouw et al., 2005; Volkamer et al., 2006; Zhang et al., 2007).

Chemical transport models (CTM) are three-dimensional models that can simulate the emission, atmospheric transport, chemical reactions, and deposition of atmospheric constituents, including aerosols. Current CTMs struggle to reproduce the observed OA mass loading and its spatial/temporal distribution in the atmosphere, which inhibits our ability to understand the environmental impacts of atmospheric $PM_{2.5}$, identify the sources contributing to its formation, and predicting the climatic/air quality response to combined technology, policy, and social interventions (Tsigaridis et al., 2014; Murphy et al., 2017; Pai et al., 2020).

The reasons for the model-observation difference is an active field of research and can be many fold, including uncertainties associated with transport and deposition of OA in CTMs, the SOA precursor emission inventories, and the chemical/physical processes governing SOA formation and evolution, for example (Pai et al., 2020). Herein, I focus on the uncertainties in SOA

precursors and the various chemical/physical processes that can affect its formation and evolution in the atmosphere. As for the SOA precursors, a large number of them may be missing in emission inventories of CTMs (Robinson et al., 2007); many of these may be semi- or intermediate-volatile species that have not been previously identified. For instance, McDonald et al. (2018) have identified daily-use volatile chemical compounds (e.g., pesticides, ink, personal care products, etc.) to be important contributors to SOA formation. Also, the development and use of novel fossil fuel substitutes (e.g., biofuels at National Renewable Energy Laboratory (McCormick et al., 2017)) may also add to the list of atmospheric SOA precursors in the future. Continued research to measure the SOA forming potential of these precursors and include them in emission inventories is necessary to bridge the model-observation gap.

As for the chemical/physical processes that govern the formation and evolution of SOA, many of them have only been represented or accounted for in atmospheric simulations in CTMs in very simplified ways, if not accounted for. Prominently, we have relied on environmental chamber studies to measure SOA forming potentials of different precursors and to develop SOA parameterizations by fitting the parameters to measured data (e.g., SOA mass, O:C, size distributions); however, the chamber artifacts of particle and vapor wall loss have rarely been properly accounted for in previous studies. Particularly for vapor wall loss, it has not been corrected for in most SOA parameterizations, although its influence has been shown to be substantial (Zhang et al., 2014; Krechmer et al., 2016). Moreover, studies using oxidation flow reactors (Lambe et al., 2015; Palm et al., 2016; Ortega et al., 2016; Palm et al., 2018) have shown that heterogeneous oxidation of SOA particles may be an important driver of SOA evolution at longer photochemical ages, but this process is rarely considered in the interpretation of laboratory data or atmospheric predictions of SOA. In addition, SOA phase state has almost always been

assumed to be liquid, indicating nearly instant gas/particle partitioning, although studies have shown that SOA may be semi-solid, thus greatly slowing down gas/particle partitioning, under dry or cold conditions in both laboratory experiments and the real atmosphere (Vaden et al., 2011; Pajunoja et al., 2014; Reid et al., 2018; Shiraiwa et al., 2017). Particle-phase oligomers have been observed to account for a substantial fraction of chamber SOA (Zaveri et al., 2020; Bakker-Arkema et al., 2020). The formation of oligomers can shift gas/particle partitioning of semi-volatile vapors (Zaveri et al., 2014; Zaveri et al., 2020), and is believed to be responsible for the observed semi-solid phase of SOA (Shiraiwa et al., 2017; DeRieux et al., 2018). However, oligomerization has not been accounted for in most previous chamber studies. New particle formation, or nucleation, can be significant in unseeded chamber experiments and in seeded/unseeded flow reactor experiments; however, its influence on the available condensation sink, in competition with other processes (e.g., gas-phase aging), and on particle size distributions have rarely been accounted for, except in one previous study (Hodshire et al., 2018).

To integrally simulate the SOA-relevant processes, I updated the SOM-TOMAS kinetic SOA model to include: (1) particle and vapor wall loss; (2) heterogeneous oxidation; (3) semi-solid phase state and its influence on gas/particle partitioning; (4) particle-phase oligomerization; and (5) new particle formation. SOM-TOMAS is a combination of the Statistical Oxidation Model (Cappa and Wilson, 2012), which simulates the multi-generational aging of VOCs in a statistical framework, and the TwO-Moment Aerosol Sectional Model (Adams and Seinfeld, 2002), which simulates the dynamics of the particle size distribution driven by condensation, evaporation, and coagulation. I leveraged SOA data from environmental chambers and oxidation flow reactors, including SOA mass concentration, chemical composition (O:C ratio) and particle size distribution,

to constrain and correct for these processes. Lastly, I demonstrated how the updated SOA parameterizations can be translated and incorporated into CTMs in a computationally efficient way.

In Chapter 2, I compared the air pollution impacts of four newly developed biofuels with respect to that of gasoline, on basis of the vapor-wall-loss-corrected atmospheric SOA mass yields for their unburned vapors. In Chapter 3, I showed that kinetic SOA modeling could constrain the bulk diffusivity (D_b), or equivalently the phase state, of SOA in chamber experiments, when model predictions were matched to measurements of the particle size distribution. In Chapter 4, I showed that SOA formation in environmental chambers and oxidation flow reactors could be consistently modeled if I accounted for the various processes in both types of reactors. In Chapter 5, I showed that vapor interaction with wall-deposited particles was negligible; also, we translated wall-loss-corrected atmospheric SOA mass yields predicted by SOM-TOMAS with volatility basis set (VBS; Donahue et al. (2006)) fitting, and the updated VBS parameters were able to improve the performance of a global CTM in simulating atmospheric OA.

CHAPTER 2: Secondary Organic Aerosol Formation from Evaporated Biofuels: Comparison to Gasoline and Correction for Vapor Wall Losses[1]

2.1 Introduction

Volatile organic compounds (VOCs), emitted by anthropogenic and biogenic sources, undergo oxidation in the atmosphere to form secondary organic aerosol (SOA). SOA is an important fraction of fine particulate matter and consequently has adverse impacts on climate, air quality, and human health (Jimenez et al., 2009). Despite the large SOA contribution to fine particle pollution, there are large uncertainties surrounding the precursors, pathways, and properties of SOA (Fuzzi et al., 2015). For instance, SOA mass concentrations are underestimated by chemical transport models in polluted urban environments (Hayes et al., 2015) and uncertainties in global burdens of SOA span nearly an order of magnitude (Shrivastava et al., 2017). There is a continued need for more laboratory and field measurements to improve our understanding of SOA and for better models of SOA formation, transport, and fate in the atmosphere.

For reasons ranging from energy independence to environmental sustainability, there is ongoing interest in the production of biofuels from sustainable feedstocks to meet current and future energy demands (Morrison et al., 2015). Ethanol, a biofuel sourced mainly from corn and sugarcane, is currently blended with gasoline (average of 10% by volume) for use in the transportation sector in the United States. With an eye towards the future, the United States Department of Energy recently invested in a large, multi-agency initiative titled Co-Optimization of Fuels and Engines (or Co-Optima) that aims to optimize biofuels and engines for improvements in engine performance while reducing tailpipe emissions (Farrell et al., 2019). As part of the study

[1] This chapter is published as: He, Y., King, B., Pothier, M., Lewane, L., Akherati, A., Mattila, J., Farmer, D. K., McCormick, R. L., Thornton, M., Pierce, J. R., Volckens, J., and Jathar, S. H.: Secondary organic aerosol formation from evaporated biofuels: comparison to gasoline and correction for vapor wall losses, Environ. Sci. Process. Impacts, 22, 1461–1474, 2020.

focused on fuel selection, McCormick et al. (2017) developed a method to screen biofuel molecules and mixtures that could be blended with gasoline and have properties enabling more efficient engine designs and operating strategies. The selection criteria included limits on physical (e.g., boiling point), chemical (e.g., biodegradability), combustion (e.g., research octane number), and health-relevant (e.g., carcinogenicity) properties. However, they did not consider impacts from oxidation of these biofuel molecules and mixtures in the atmosphere and their ability to form SOA. Biofuel molecules, similar to those found in any liquid fuel, are emitted to the atmosphere, either through evaporative processes or as unburned species in the tailpipe. May et al. (2014) found that a third to a half of the non-methane organic compounds emissions from light-duty gasoline vehicles consisted of unburned fuel. The potential of a biofuel, or any other precursor, to form SOA depends on its molecular structure and volatility (Jathar et al., 2014). If the SOA mass yield for a biofuel is larger than that for gasoline, SOA formation can negatively offset some of the environmental benefits that come from being optimized to reduce primary particle emissions in the tailpipe.

Researchers have typically relied on laboratory-based environmental chamber data to develop parameterizations to represent SOA formation in air quality models. To date, most SOA model parameterizations have not been corrected for losses of vapors to the walls of the Teflon® chamber, which can bias SOA production in chamber experiments (Zhang et al., 2014; Krechmer et al., 2016; Huang et al., 2018). Furthermore, chamber experiments have historically used high initial VOC and oxidant concentrations to ensure abundant SOA production (>20 μg m^{-3}) at levels above instrument detection limits (>1 μg m^{-3}). These concentrations are significantly elevated compared to those found in the atmosphere, including most urban areas (van Donkelaar et al., 2010). Direct SOA parameterizations derived under these highly polluted conditions may

overestimate SOA production in lower-concentration conditions, and may not reflect the magnitude and properties of SOA formed in the atmosphere (Shilling et al., 2008; Chen et al., 2019a). Experiments are often challenging to perform under atmospherically relevant conditions (the experiments in this work were also performed at elevated VOC levels). Thus, detailed models, such as those used in this work, that can simulate experimental artifacts (e.g., vapor wall losses) and the subsequent cascade of oxidation reactions (e.g., functionalization and fragmentation reactions), can help to translate chamber data (where VOC and SOA concentrations are elevated) to the more atmospherically-relevant conditions simulated in air quality models (where VOC and SOA concentrations are much lower).

In this work, we performed chamber experiments to study the SOA formation from four biofuels and one mixture of gasoline fuel with 10% ethanol by volume under high-NO_x conditions representative of those found in urban environments. The SOA formation was modeled using a state-of-the-science model that accounted for the influence of vapor wall losses and allowed us to determine atmospherically relevant SOA mass yields.

2.2 Methods

2.2.1 SOA Measurements

Environmental Chamber. The SOA experiments were performed with the Colorado State University (CSU) environmental chamber. The CSU chamber consists of a temperature and relative-humidity controlled 10 m^3 Teflon®-FEP (Fluorinated Ethylene Propylene) bag inside a steel-plywood enclosure. Based on chemical actinometry experiments, 80 UV-A black lights mounted inside the enclosure produced a maximum NO_2 photolysis rate of ~0.25 min^{-1} (Figure A1). The UV-A bulbs produced light with wavelengths between 315 and 400 nm with a peak

intensity at 350 nm. The temperature inside the chamber was managed to below 28 ℃ using a 3.5 kW air conditioner.

Chamber Operation. Prior to beginning the experiment, the chamber was flushed with HEPA and activated-charcoal filtered air for at least 12 hours with the UV lights turned on. These measures were found to be sufficient in keeping the background contribution, especially from oxidation of desorbed vapors from the walls, to SOA formation to a minimum (<0.5 μg m^{-3}). Ammonium sulfate particles were nebulized using an aerosol generation system (AGS, Brechtel Inc., CA) and injected into the chamber to provide the seed for SOA condensation. The initial seed surface area concentration in our experiments was 1100±400 μm^2 cm^{-3}. Nitrous acid (HONO) was synthesized and added to the chamber following the methods of Ng et al. (2007) but with one minor modification. Clean air was bubbled through a fresh mixture of 50 mL of 10% H_2SO_4 and 25 mL of 1% $NaNO_2$ solution and vented for ~30 minutes, following which the bubbled air was added to the chamber for ~30 minutes. The rationale for venting is described in the appendix (A1 HONO synthesis). HONO photolyzes under UV-A lights to yield a burst of hydroxyl radicals (OH) in the first hour of the experiment (>10^7 molecules cm^{-3}) with a much lower concentration over the next few hours (~10^6 molecules cm^{-3}). The chamber experiments were performed with unburned fuel based on the observations of Jathar et al. (2013) that the unburned fuel system could serve as an appropriate, but a more convenient model, to study the SOA formation from tailpipe exhaust. Each fuel was studied in isolation and not as a blend with gasoline to determine each fuel's distinct potential to form SOA. The fuel was injected into the chamber by passing hot air (~5 L min^{-1} at ~200 ℃) over the tip of a microliter syringe that was gradually depressed over the course of several minutes. After the fuel was injected, the contents of the chamber were allowed to mix for at least 45 minutes prior to the lights being turned on. The mixing time was determined

based on observations of the time required for injected species (NO, NO_2, toluene) to reach stable concentrations in the chamber. In each experiment, the contents of the chamber were irradiated by the lights for a maximum of six hours.

Gas and Particle Measurements. Gas analyzers (42C and 49C, ThermoFisher Scientific, MA) measured concentrations of ozone (O_3), NO, and NO_2^*. The NO_x instrument uses a molybdenum converter to convert NO_2 and other reactive nitrogen species including HONO and peroxyacyl nitrates to NO prior to measurement (Dunlea et al., 2007), which is typically referred to as NO_2^* (Dickerson et al., 2019). A scanning mobility particle sizer (SMPS, GRIMM Aerosol Technik, Austria) measured the aerosol size distribution between 32 and 717 nm. An aerosol chemical speciation monitor (ACSM, Aerodyne Research, MA) detected aerosol mass concentrations and the bulk chemical composition (Ng et al., 2011; Fröhlich et al., 2013). There were no direct VOC measurements during the chamber experiments. Instead, we assumed a 100% injection efficiency to determine the initial VOC concentrations and used estimates of OH concentrations to determine the decay of the VOC species with time. The OH concentrations during the experiments were determined from simulations performed with the SAPRC gas-phase chemical mechanism (Carter, 2000; Knote et al., 2018); OH concentrations are typically estimated in chamber experiments using the measured decay of VOCs (Yee et al., 2013; Tkacik et al., 2012; Li et al., 2018). Details of the OH concentration estimates can be found in the appendix (A2 SAPRC modeling). Briefly, a SAPRC simulation was performed by specifying the experiment-specific initial concentrations of NO, O_3, and VOC(s) and chamber-specific photolysis rates for all species in SAPRC. The initial HONO concentration was adjusted until the SAPRC model predictions matched the observed concentrations of NO and O_3. This method to estimate the OH concentrations was first validated against four chamber experiments performed with toluene where

the toluene decay was measured with a gas chromatograph photoionization detector (GC-PID, SRI Instruments, CA). The SAPRC simulations were then used to determine OH concentrations for the fuel experiments. The implications of our inability to measure the VOCs in these experiments are presented in the 'Discussion' section.

Fuels and Experimental Matrix. A total of twelve experiments were performed on five different fuels at different initial concentrations. Details of the experiments are presented in Table 2.1. Four of the fuel molecules and mixtures, namely diisobutylene, cyclopentanone, an alkylfuran mixture, and an ethanol-to-hydrocarbon (ETH) mixture (referred to as Vertifuel in previous literature by Lunderman et al. (2018)), can be synthesized from sustainable feedstocks and were chosen from a list of eight identified by McCormick et al. (2017) that were compatible with spark-ignition engines. These biofuels were deliberately picked since their molecular structures and composition indicated that they have some potential to form SOA. The rest were small alcohols (e.g., ethanol, propanol, butanol) and are expected to form little to no SOA. Diisobutylene is a mixture of 75% 2,4,4-trimethyl-1-pentene and 25% 2,4,4-trimethyl-2-pentene by mass. The alkylfuran mixture was 40% 2-methylfuran and 60% 2,5-dimethylfuran by mass. ETH is synthesized from ethanol (Narula et al., 2015), and resembles a petrofuel. Specifically, ETH is a complex mixture of alkanes (14.5%), aromatics (70%), alkenes (12%), oxygenates including ethanol (1%), and a small number of unknown compounds (2.5%); numbers in parentheses are mass percentages. To contrast the SOA formation from these select biofuels, we performed experiments with an E10 gasoline (gasoline blended with 10% ethanol by volume) prepared by blending ethanol into a commercial reformulated blendstock for oxygenate blending (RBOB) obtained from a petroleum refiner. A detailed speciation for all the fuels along with additional information (e.g., carbon number, k_{OH}) is included in a separate Excel spreadsheet (Section A4†).

All five fuels (four biofuels and E10 gasoline) were sourced in small sterile vials from the National Renewable Energy Laboratory (NREL) and refrigerated at 4 °C prior to use. In addition to the fuel experiments, we performed two blank chamber experiments where all steps described earlier were undertaken, except no fuel was added to the chamber. These blank experiments produced very little SOA (<0.25 μg m^{-3}) and this small SOA contribution was subtracted from the SOA formed during the fuel experiments.

Table 2.1: Gas and aerosol results for all experiments performed in this work. In order, we tabulate the fuel name, reaction rate constant with OH (k_{OH}), average carbon number (*C#*), initial concentrations of VOC, NO, NO_2^*, and seed, total VOC reacted, final SOA mass concentration and O:C, and final SOA mass yield. ^Gathered and/or calculated from EPISuite (http://www. chemspider.com/). *All reactive N except NO. @End-of-experiment values. #SOA estimates based on SMPS data only. &Not-corrected for vapor wall losses. NM=not measured. BDL=Below detection limit.

Date (2018)	*Fuel Mol./Mixture*	*$k_{OH} \times 10^{12}$ (cm^{-3} s)^*	*C #*	*$[VOC]_0$ (ppbv)*	*$[NO]_0$ (ppbv)*	*$[NO_2]_0$ (ppbv)**	*[Seed]$_0$ (μm^2 cm^{-3})*	*[ΔVOC] (ppbv)@*	*SOA (μg m^{-3})@*	*SOA O:C@*	*SOA Mass Yield (%)@&*
Mar 1#	Cyclopentanone	6.8	5.0	661	NM	NM	1780	134	BDL	NM	BDL
Apr 3	Cyclopentanone	6.8	5.0	1323	23	201	794	165	1±1	1.31	0.2 ± 0.2
Mar 6	Diisobutylene	58.8	8.0	374	41	155	975	302	2±1	NM	0.1 ± 0.1
Mar 20	Diisobutylene	58.8	8.0	748	58	221	1158	524	2±2	0.76	0.1 ± 0.1
Mar 3	Alkylfuran Mix	101.3	5.6	583	39	138	1065	409	23±4	0.85	1.8 ± 0.3
Mar 11#	Alkylfuran Mix	101.3	5.6	874	57	143	1261	494	27±1	NM	1.7 ± 0.1
Mar 15#	Alkylfuran Mix	101.3	5.6	874	54	133	1088	381	14±1	NM	1.2 ± 0.1
Feb 27	ETH	20.1	8.2	335	68	246	415	176	110±16	0.51	16.4 ± 2.4
Mar 8	ETH	20.1	8.2	223	43	157	1501	118	47±6	0.60	10.4 ± 1.2
Apr 5	ETH	20.1	8.2	447	37	186	1482	145	43±7	0.59	7.8 ± 1.2
Mar 27	Gasoline	12.7	7.3	867	NA	NA	1075	261	18±3	0.69	2.0 ± 0.3
Mar 29	Gasoline	12.7	7.3	650	49	176	931	196	13±2	0.73	1.9 ± 0.3

Experimental Data Analysis. The particle-wall-loss corrected SOA mass concentrations were determined for each experiment following Hildebrandt et al. (2009). The lower bound, particle-wall-loss corrected SOA estimate ($SOA_{w=0}$) was calculated using the following equations by assuming that the SOA vapors only condensed on the suspended particles:

$$AS_{sus}(t) = \rho_{AS} \cdot V_{sus}^{AS}(0) \cdot e^{-\int_0^t k_{par}(t)dt} \quad (2.1)$$

$$SOA_{sus}(t) = \rho_{SOA}(V(t) - AS_{sus}(t)/\rho_{AS}) \quad (2.2)$$

$$SOA_{w=0}(t) = SOA_{sus}(t) + \int_0^t k_{par}(t) \cdot SOA_{sus}(t) \cdot dt \quad (2.3)$$

Eqn (2.1) and (2.2) calculate the suspended ammonium sulfate (AS_{sus}) and SOA (SOA_{sus}) mass concentrations and eqn (2.3) calculates the lower-bound, particle-wall-loss corrected estimate for the SOA mass concentration. In those equations, ρ_{AS} is the density of ammonium sulfate in g cm^{-3} (1.78 g cm^{-3}), $V_{sus}^{AS}(0)$ is the volume concentration of the suspended ammonium sulfate at lights on in μm^3 cm^{-3}, $k_{par}(t)$ is the time-dependent particle wall-loss rate in s^{-1}, ρ_{SOA} is the SOA density in g cm^{-3} (assumed to be 1.4 g cm^{-3}), and $V(t)$ is the volume concentration of the suspended aerosol at time t in μm^3 cm^{-3}. $k_{par}(t)$, was determined by fitting the change in the ammonium sulfate mass concentration measured by the ACSM. The upper bound, particle-wall-loss corrected SOA estimate ($SOA_{w=1}$) was calculated using the following equation by assuming that the SOA vapors condensed on both the suspended particles and the particles deposited on the walls:

$$SOA_{w=1}(t) = (SOA_{sus}(t)/AS_{sus}(t)) \cdot V_{sus}^{AS}(0) \cdot \rho_{AS} \qquad (2.4)$$

where $SOA_{sus}(t)/AS_{sus}(t)$ is the ratio of suspended SOA and ammonium sulfate concentrations directly measured by the ACSM at time t.

We used the relationship developed by Canagaratna et al. (2015), O:C = 0.079 + 4.31 × f_{44}, to determine the SOA atomic O:C ratio from the mass fraction measured by the ACSM at a mass-to-charge ratio of 44. The end-of-experiment SOA mass yields were calculated as a ratio of the SOA formed and fuel reacted (i.e., ΔVOC). The amount of fuel reacted was determined using the following equation:

$$\Delta VOC = \sum_i VOC_{i,0}\left(1 - e^{-k_{OH,i}OH_{exp}}\right) \qquad (2.5)$$

where $VOC_{i,0}$ is the initial concentration of species i at lights on in μg m^{-3}, $k_{OH,i}$ is the reaction rate constant of species i with OH in cm^3 molecules^{-1} s^{-1}, and OH_{exp} is the end-of-experiment OH exposure in molecules-s cm^{-3}. The $k_{OH,i}$ values were either determined from the primary literature

(e.g., Atkinson and Arey (2003)) or from the Estimation Program Interface Suite (EPISuite (EPA, 2012)) and values for all VOCs have been tabulated in the appendix (Section A4†). The initial concentration for species *i* was calculated from the normalized speciation for each fuel and the total volume of fuel injected into the chamber. These calculations assumed a 100% injection efficiency for the fuel into the chamber and no loss of fuel to the Teflon® walls prior to turning the lights on or photolysis from the UV-A lights. All VOC species in this work were sufficiently volatile ($C^*>10^6$ μg m^{-3}; C^* is the effective saturation concentration (Donahue et al., 2006)) that they are unlikely to be lost to the walls of the chamber (Grosjean, 1985); C^*s for all VOC species are listed in the appendix (Section A4†). More recent work has suggested that oxygenated VOCs with C^*s smaller than 10^6 μg m^{-3} (Krechmer et al. (2016) and Matsunaga and Ziemann (2010)) may partition into the chamber walls and hence these losses were accounted for in modeling the SOA formation (see 'Vapor Wall Losses' in next section).

2.2.2 SOA Modeling

SOM-TOMAS Model. We used the recently developed Statistical Oxidation Model-TwO Moment Aerosol Sectional (SOM-TOMAS) model to simulate the SOA formation in our chamber experiments. The SOM simulates the gas-phase chemistry and calculates the thermodynamic properties of the oxidation products from SOA precursors (Cappa and Wilson, 2012). The TOMAS model uses a sectional approach to track the number and mass moments of the aerosol size distribution and simulates nucleation, coagulation, and gas/particle partitioning (Adams and Seinfeld, 2002). A brief description of the SOM and TOMAS models is provided below.

The SOM uses a carbon-oxygen grid to track the gas- and particle-phase organic species arising from VOC oxidation. Each cell in the carbon-oxygen grid represents a model organic species, which reflects the average properties (e.g. vapor pressure, reactivity) of all actual species

with the same number of carbon (N_C) and oxygen (N_O) atoms that are produced from a given precursor. All gas-phase SOM species are assumed to be reactive towards OH. These reactions lead to either functionalization or fragmentation, resulting in movement through the carbon-oxygen grid. All SOM species properties (e.g., k_{OH}, C^*) are described in terms of N_C and N_O. Six adjustable parameters determine the chemistry and thermodynamics in each SOM grid: (i-iv) p_1-p_4, the yields of four functionalized products that add one, two, three, and four oxygen atoms to the carbon backbone respectively, (v) m_{frag}, the parameter that characterizes the fragmentation probability, P_{frag}, and (vi) ΔLVP, the decrease in vapor pressure (or volatility) of the model species per addition of an oxygen atom. The probability of fragmentation (P_{frag}) is designed to be a function of the O:C ratio of the model species and is parameterized as $P_{frag} = (O:C)^{m_{frag}}$. The volatility is represented using the effective saturation concentration (C^*) and is parameterized as follows: $C^* = 10^{(-0.0337 \cdot MW_{HC} + 11.56 - N_O \cdot \Delta LVP)}$, where MW_{HC} is the molecular weight of the hydrocarbon excluding the oxygen atoms. SOM is coupled to the TOMAS model (Adams and Seinfeld, 2002; Pierce et al., 2011), which tracks two moments (aerosol number and mass) across 36 size sections. For the mass moment, the particle phase of the SOM model species is tracked in each TOMAS size section. Particles within each size section are assumed to be internally mixed in composition. In this study, TOMAS simulates the kinetic condensation and evaporation of all SOM species for each TOMAS size section, and it also simulates coagulation of particles between and within size sections.

Model Application. For the fuels studies in this work, the SOM-TOMAS model was used to: (i) account for the influence of vapor losses to the walls of the Teflon® chamber and (ii) determine atmospherically relevant SOA mass yields. In the absence of any previous chamber data, SOM parameters were developed for the alkylfuran mixture, diisobutylene, and cyclopentanone,

using the chamber data collected in this work. The SOM parameters were fit to reproduce the measured temporal evolution of the SOA mass concentrations. As the ETH and gasoline fuel compositions were known - and were primarily composed of previously studied SOA precursors (e.g.,alkanes, aromatics) - historical SOM parameters were used to predict the SOA formation in these fuel experiments. Seven SOM grids, one for each SOA precursor class, were used to account for the diversity of organic compounds present in those fuels: linear alkanes (*n*-dodecane), branched alkanes (methylundecane), cyclic alkanes (hexylcyclohexane), benzene, toluene, lumped aromatics (*m*-xylene for ETH and *o*-xylene for gasoline), and polycyclic aromatic hydrocarbons (naphthalene). The SOM parameters for each grid are based on the species mentioned in the parentheses and these parameters are listed in Table A1. This approach to use a single surrogate to represent the SOA formation from a class of VOC compounds is largely consistent with the approach used in other SOA models such as the volatility basis set (VBS) (Murphy et al., 2017; Shrivastava et al., 2016; Pai et al., 2020). One of the differences between the SOM and VBS approaches is that in the SOM the parameters for the surrogate inform the statistical trajectory of the VOC oxidation in a carbon-oxygen grid and hence the surrogate and VOC (unless they are the same) are likely to have different SOA mass yields. In a VBS approach, all VOCs assigned to the same surrogate, by design, share the same SOA mass yield. A similar SOM grid-model setup was previously used and found to work quite well to model SOA formation in box (Eluri et al., 2018) and three-dimensional models (Jathar et al., 2016; Cappa et al., 2016; Akherati et al., 2019).

Vapor Wall Losses. Loss of vapors to the walls of the Teflon® chamber is currently handled in the SOM-TOMAS model following Zhang et al. (2014) and Krechmer et al. (2016). Briefly, the first-order uptake to the walls is modeled using the rate coefficient $k_{vap,on}$ and the rate of release of vapors from the walls, $k_{vap,off}$, is modeled using absorptive partitioning theory with

the Teflon® wall serving as an absorbing mass with an effective mass concentration of C_{wall}. $k_{vap,on}$ and $k_{vap,off}$ for a model vapor species are calculated as follows:

$$k_{vap,on} = (2/\pi) \cdot (A/V) \cdot \sqrt{k_e D_v} \quad (2.6)$$

$$k_{vap,off} = (C^*/C_{wall}) \cdot k_{vap,on} \quad (2.7)$$

where A/V is the surface area to volume ratio for the Teflon® chamber in m^{-1}, k_e is the coefficient of eddy diffusion in s^{-1}, and D_v is the gas-phase diffusion coefficient of the vapor molecule in m^2 s^{-1}. Based on the observations of Krechmer et al. (2016), C_{wall} was varied with the C^* of the model species, with higher values used for more volatile species and vice versa: $C_{wall}=10^4$ μg m^{-3} for $C^*>10^4$ μg m^{-3}, $C_{wall}=16 \times (C^*)^{0.6}$ μg m^{-3} for $C^*<10^4$ μg m^{-3}, and $C_{wall}=16$ μg m^{-3} for $C^*<1$ μg m^{-3}. k_e for our CSU chamber was calculated following the methods described in Bian et al. (2015), although a single k_e value was calculated by combining the data from a subset of experiments instead of determining experiment-specific values. Details of the k_e calculation can be found in the appendix (A3 Coefficient of Eddy Diffusion). We calculated a study-wide k_e of 0.13±0.02 s^{-1}, which for a gas-phase diffusion coefficient of 4×10^{-6} m^2 s^{-1}, produced a $k_{vap,on}$ of 1.28×10^{-3} s^{-1}, according to eqn (2.6). The time scale for gas-wall partitioning, or the inverse of $k_{vap,on}$, was about 13 minutes and agreed well with the 7 to 13 minute gas-wall partitioning time scale calculated by Krechmer et al. (2016) for a slightly smaller Teflon® chamber (8 m^3). We should note that the SOM parameters in Table A1 had to be refit to the original data since the earlier set of SOM parameters did not integrate the observations of Krechmer et al. (2016).

2.3 Results

2.3.1 Results from a Sample Experiment

Results from an example chamber experiment performed on the alkylfuran mixture are shown in Figure 2.1. In Figure 2.1(a), we show the evolution of the particle volume concentration

as measured by the SMPS. Before the lights were turned on, the volume concentration increased with the injection of ammonium sulfate seed and decreased with steady loss of ammonium sulfate seed particles to the wall. After the lights were turned on, the volume concentration increased initially with condensation of SOA but decreased later on as SOA production stopped and ammonium sulfate+SOA particles and vapors were lost to the walls. Based on the loss of the ammonium sulfate seed particles to the walls, we estimated the suspended volume concentrations of the ammonium sulfate seed particles (dashed blue) and SOA (dashed orange) after the lights were turned on. In Figure 2.1(c), we show the lower (w=0) and upper (w=1) bound SOA mass concentrations that were corrected for losses of particles to the walls. The upper bound estimate relied on the organic:ammonium sulfate ratio measured by the ACSM (shown in Figure 2.1(b)). Vapor wall losses were modeled with the SOM-TOMAS model and those corrections are described later. The central SOA estimate, used henceforth, was calculated as an average of the lower and upper bound estimates. We estimated the uncertainty range by assuming that the lower and upper bounds were separated by four standard deviations; the ± ranges given for the SOA mass concentrations in Table 2.1 are one-quarter of this range and hence equivalent to the error. Unlike some previous chamber experiments (Song et al., 2007; Shakya and Griffin, 2010), there was very little delay or 'induction time' between when the lights were turned on and when a sizable condensable SOA mass was detected by the particle instruments. This might have been on account of using a higher initial seed surface area for vapor condensation and/or a high OH concentration at the beginning of the experiment. SOA production was found to reduce particle losses in the ACSM (Middlebrook et al., 2012), presumably because the SOA coating on the ammonium sulfate particles tended to reduce bounce in the vaporizer (Figure A7).

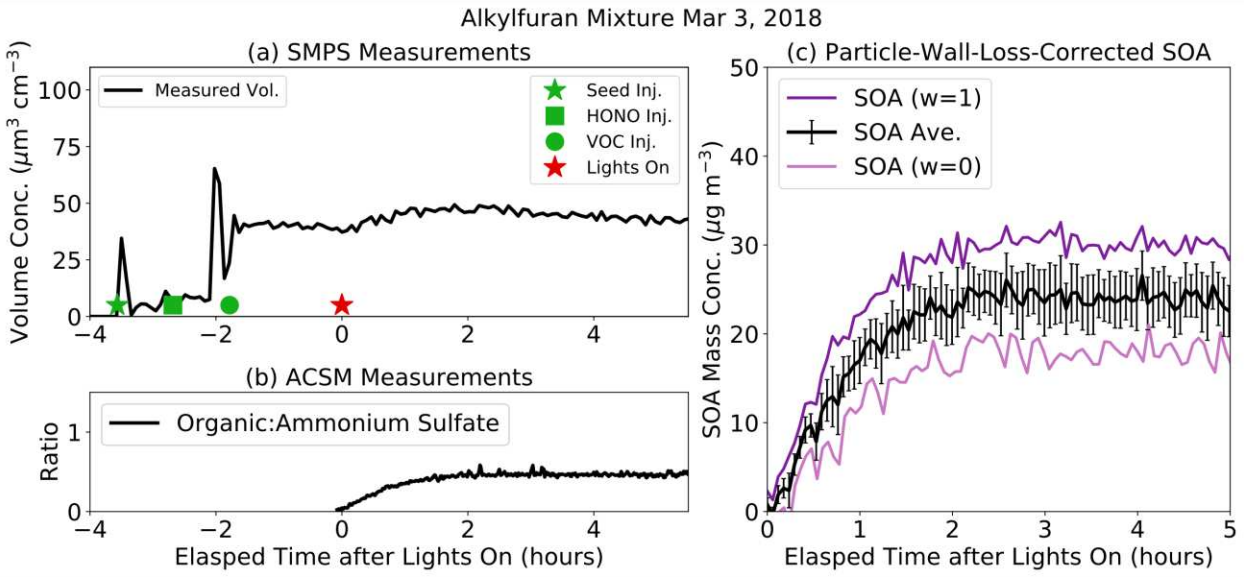

Figure 2.1: Aerosol results from the alkylfuran mixture experiment performed on Mar 3, 2018 that show the time evolution of the (a) total volume measured by the SMPS, (b) organic:ammonium sulfate ratio measured by the ACSM, and (c) particle-wall-loss corrected SOA mass concentration estimates. The volume concentration increase at two different times before the lights on can be attributed to two separate aerosol injections. The second aerosol injection was done to ensure sufficient seed concentrations for SOA condensation.

2.3.2 SOA from Photooxidation of Evaporated Biofuels

Results from all the experiments performed in this work are summarized in Table 2.1. The end-of-experiment values in Table 2.1 were calculated three hours after the lights were turned on as there was very little change in the SOA mass and composition beyond three hours. This agrees well with the little to no change in estimated and modeled OH exposure, three hours after turning the lights on (Figure A4(b)). Despite large additions of the biofuel to the chamber (>370 ppbv or >1400 μg m^{-3}), cyclopentanone and diisobutylene were found to produce very little SOA (<4.0 μg m^{-3}). Their SOA mass yields were correspondingly quite low and did not exceed 0.2% for either biofuel. Lim and Ziemann (2009) measured an SOA mass yield of 4% for cyclohexane, a cyclic compound one larger in carbon number than cyclopentanone. A lower carbon number and increased susceptibility to fragmentation from the presence of a carbonyl group seems to have dramatically lowered the SOA mass yield for cyclopentanone in our work (Chacon-Madrid et al.,

2013). The average SOA mass yield for diisobutylene (0.1%) in our experiments was slightly lower than that observed in previous experiments performed with 1-octene (an isomer of diisobutylene) (Forstner et al., 1997). The lower SOA mass yield likely indicates the role of carbon branching of the precursor on SOA formation (Tkacik et al., 2012).

We observed much higher SOA mass yields for the alkylfuran mixture (average of 1.6%) when compared to those from cyclopentanone and diisobutylene. The SOA mass yields for the alkylfuran mixture (that contained species with carbon numbers of 5 and 6) were considerably larger than those for alkanes with similar carbon numbers, which have been shown to produce little to no SOA (Lim and Ziemann, 2009). Furans are heterocyclic compounds that contain a five-membered aromatic ring, yet their SOA mass yields were substantially lower than those for typical aromatic hydrocarbons measured under high-NOx conditions; historical chamber yields for benzene, toluene, and xylenes have varied between 3 and 60% (Zhang et al., 2014; Ng et al., 2007; Chan et al., 2009; Li et al., 2016). The oxidation pathways and products from furan chemistry are hence expected to be different than those from aromatic hydrocarbons (Strollo and Ziemann, 2013), noting that furan derivatives have been observed during the photooxidation of aromatic compounds (Li et al., 2016; Bloss et al., 2005; Al-Naiema et al., 2017).

A handful of studies have performed chamber experiments with furanic compounds and reported on SOA mass yields. Two previous chamber studies have reported on SOA formation from 3-methylfuran, which is similar to the molecules present in our alkylfuran mixture (mixture of 2-methylfuran and dimethylfuran). Joo et al. (2019) measured an SOA mass yield of ~2% for 3-methylfuran although the oxidation was performed with the nitrate radical and particulate organic nitrates (PONs) accounted for nearly 40% of the SOA formed. Strollo and Ziemann (2013) measured a much larger SOA mass yield from OH oxidation of 3-methylfuran (9-15%), but the

substantially large SOA mass concentrations produced in those experiments (>2000 μg m^{-3}) makes it difficult to compare the mass yields directly to our study.

The ETH produced the highest SOA mass yields (7.8-16.4%) amongst the four Co-Optima fuels. The high SOA mass yields, as we show later, can be attributed to the relatively large fraction of aromatic compounds (60%) in this fuel. The range in SOA mass yields reported in Table 2.1 for a given fuel molecule/mixture (≤factor of 2) was generally similar to the range observed in earlier studies where SOA mass yields from the same precursor were compared between experiments from the same chamber (Yee et al., 2013; Hildebrandt et al., 2009; Loza et al., 2014).

The SOA O:C ratios are presented in Table 2.1. Unlike the SOA mass concentrations, the SOA O:C ratios varied little over the course of the experiment, suggesting, to first order, that the composition of the oxidation products in the particle phase did not change with time. Oxidation of cyclopentanone produced SOA with the highest O:C ratio (1.31) while oxidation of ETH produced SOA with the lowest O:C ratio (average of 0.56). The SOA O:C ratios are later shown to be useful in evaluating the model used in this work.

2.3.3 Comparisons to Gasoline SOA

The SOA mass yields for gasoline in our experiments (average of 2.0%) compared reasonably well with chamber data from Jathar et al. (2013) and Chen et al. (2019b), who measured an SOA mass yield between 1 and 4%, and modeled data from Gentner et al. (2012), who predicted an SOA mass yield of 2.3% (Jathar et al. (2013) and Gentner et al. (2012) studied summertime California gasoline while Chen et al. (2019b) studied gasoline from China). Differences in the SOA mass yields between the studies could be attributed to small differences in the aromatic fraction and composition of the fuel studied. Overall, when compared to gasoline, two of the Co-Optima fuels - cyclopentanone and diisobutylene - had very low SOA mass yields (≤0.2%). The

alkylfuran mixture had a slightly lower SOA mass yield compared to gasoline (average of 1.6% versus average of 2.0%). ETH had an average SOA mass yield of 11.5% that was six times higher than that for gasoline. Purely from an SOA perspective and assuming equivalent emissions of these species into the atmosphere, cyclopentanone and diisobutylene appear to be ideal candidates to be blended with gasoline. It is unclear if the alkylfuran mixture has any benefits over gasoline while ETH is likely to be a poor substitute. These conclusions are based on the assumption that the composition of the SOA precursors in the tailpipe is similar to the composition of the unburned fuel (May et al., 2014; Jathar et al., 2013). Future work may need to examine the SOA formation from tailpipe exhaust.

2.3.4 Modeling the SOA Formation and Composition

We used the SOM-TOMAS model to fit or predict the SOA formation and composition in our chamber experiments while correcting for the influence of vapor wall losses. In the absence of any historical data, SOM parameters were developed based on representative chamber experiments performed on the alkylfuran mixture, diisobutylene, and cyclopentanone. Results from that exercise, where the model was fit to reproduce the evolution of the SOA mass concentrations, are shown in Figure 2.2 (gasoline and ETH results are in Figure 2.3). The SOM parameters are presented in Table 2.2. The SOM parameters were able to reproduce the measured SOA mass concentrations and O:C ratio (within 30%) for all experiments. We should note that the SOA O:C ratio was not used as a constraint during the fitting and the O:C agreement points to the ability of the SOM to capture the general features of the oxidation chemistry. We should note that the model performance for SOA mass concentrations and O:C was much better for the alkylfuran experiment compared to the diisobutylene and cyclopentanone experiments. This could be partly attributed to

the observed variability and low SOA mass concentrations in the diisobutylene and cyclopentanone experiments.

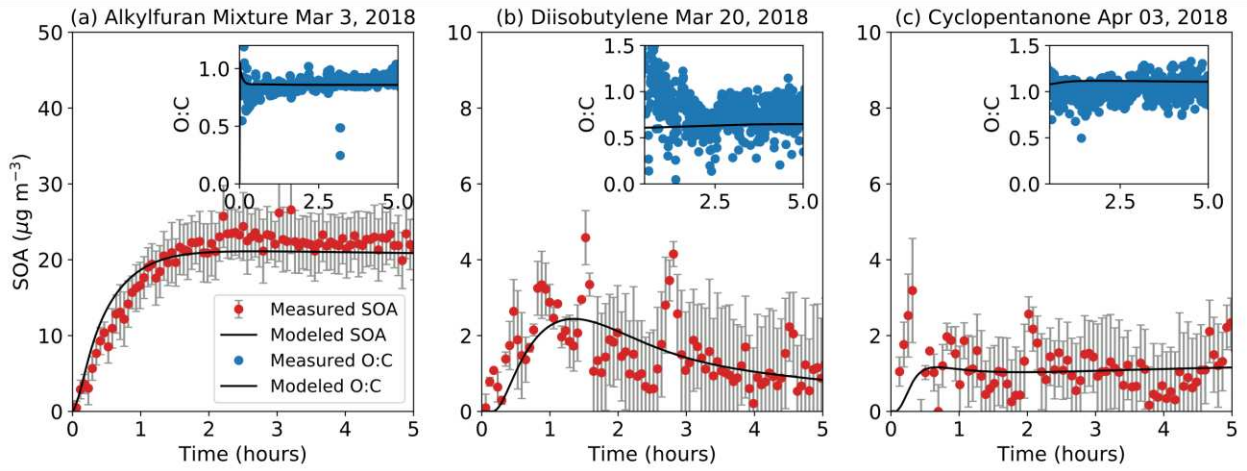

Figure 2.2: SOM-TOMAS model predictions based on parameter fits (solid black lines) compared to measurements (symbols) of SOA mass concentrations and SOA O:C for the (a) alkylfuran mixture, (b) diisobutylene, and (c) cyclopentanone. Model predictions for O:C are shown only after the first half hour as they were found to be unreliable at earlier times when the SOA mass concentrations were lower than 0.5 μg m^{-3}.

Table 2.2: SOM-TOMAS parameters determined by fitting to the experimental data presented in Figure 2.2

Fuel	m_{frag}	ΔLVP	p_{f1}	p_{f2}	p_{f3}	p_{f4}
Alkylfuran Mix.	0.449	1.459	0.000	0.001	0.998	0.000
Diisobutylene	0.277	1.509	0.946	0.042	0.000	0.013
Cyclopentanone	0.434	1.613	0.369	0.256	0.329	0.047

The SOM-TOMAS model results for gasoline and ETH are shown in Figure 2.3. Model predictions of the precursor contribution to the end-of-experiment SOA for both experiments are also shown in Figure 2.3. A slightly different model configuration was used for the two experiments to optimize the model-measurement comparison. For the gasoline experiment, a model configuration that treated all C_8 and higher single-ring aromatic compounds as low-yield aromatics (based on fits to *o*-xylene experiments) seemed to work best in reproducing the SOA mass concentration and O:C ratio. This configuration, however, did not work with the ETH experiment, and all C_8 and higher single-ring aromatic compounds had to be treated as high-yield

aromatics (based on fits to *m*-xylene experiments) to reproduce the measured SOA mass concentration and O:C ratio. The treatment of PAHs was kept the same for both fuels. The use of a xylene to model the SOA formation from C_8 and larger single-ring aromatic compounds is consistent with its treatment in atmospheric models (Murphy et al., 2017; Pai et al., 2020; Athanasopoulou et al., 2013). That the single-ring aromatic compounds had to be treated in slightly different ways suggests that the aromatic composition between the two fuels was sufficiently different that they exhibited different potentials to form SOA. A closer examination of the aromatic composition indicated that the gasoline fuel had, on average, a slightly smaller aromatic carbon number (8.4 versus 8.7) and less alkyl substituents (0.61 versus 1.14 alkyl substituents per mole of fuel) than ETH. Aromatic carbon number and alkyl substituents on an aromatic ring have been found to influence SOA production (Li et al., 2016; Odum et al., 1997). Our results imply that chemical mechanisms to model SOA formation need to consider the diversity in SOA potential for C_8 and larger aromatic emissions, in addition to distinguishing between benzene, toluene, and larger aromatics. Regardless of the differences in the model configurations used for ETH and gasoline, non-benzene aromatic compounds contributed to more than 90% of the predicted SOA.

When the model was applied to experiments other than those shown in Figure 2.2 and 2.3, the SOM-TOMAS model was able to reproduce the end-of-experiment SOA mass concentrations and O:C ratios for all fuels (Figure A8). This suggested that the fits developed for diisobutylene and the alkylfuran mixture and the treatment of C_8 and larger single-ring aromatic compounds for gasoline and ETH worked well in reproducing the SOA formation in other experiments performed on the same fuel. We also performed simulations with the SOM-TOMAS model to assess the influence of the uncertainty in k_e. Those results, shown in Figures A9 and A10, suggest that the

predictions in the SOA mass concentrations and O:C ratios were relatively insensitive to the uncertainty linked to the vapor wall loss rate.

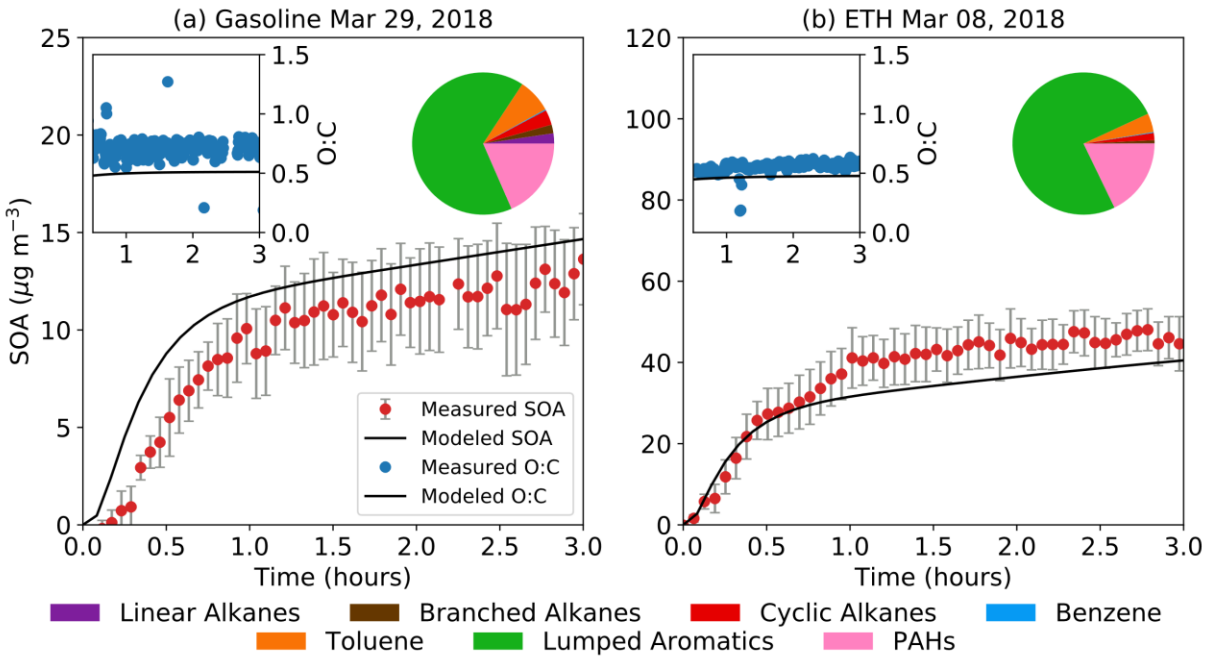

Figure 2.3: SOM-TOMAS model predictions (solid black lines) compared to measurements (symbols) of SOA mass concentrations and O:C for a representative (a) gasoline and (b) ETH experiment. The precursor contribution to SOA at the end of the experiment is shown as a pie chart in the top right corner of the panel. Note that the lumped aromatics were simulated with SOM parameters for *o*-xylene for gasoline and for *m*-xylene for ETH.

2.3.5 Atmospherically Relevant SOA Mass Yields

The SOM-TOMAS model was used to simulate the atmospheric SOA mass yield by emitting a trace amount of precursor (~1 pptv) into an ambient environment that had a constant organic aerosol mass concentration of 10 μg m^{-3} and an OH concentration of 1.5×10^{6} molecules cm^{-3}. Only a trace amount of precursor was added so that the SOA produced did not affect the organic aerosol mass concentration and the SOA mass yields between the different precursors could be compared at the same organic aerosol loading. A constant organic aerosol loading and OH concentration was used for simplicity while noting that both of these quantities change in the ambient environment with time. Vapor wall losses were turned off for these simulations. Results

from those simulations, presented as an SOA mass yield with photochemical age, are shown in Figure 2.4(a). These SOA mass yields are expected to be more atmospherically relevant than the chamber yields because vapors are not lost in the atmosphere as in a chamber and the calculations were performed at organic aerosol mass concentrations reflective of those found in typical urban environments. The atmospheric simulations predicted a similar ranking for the potential of the fuels to form SOA as the experimental data shown in Table 2.1, i.e., ETH had the highest SOA mass yield followed by the alkylfuran mixture and gasoline, and then by cyclopentanone and diisobutylene. However, at the same photochemical age as at the end of the experiment, the absolute SOA mass yields from the atmospheric simulations, shown in Figure 2.4(b), were always equal to or higher than those measured in the chamber and reported in Table 2.1.

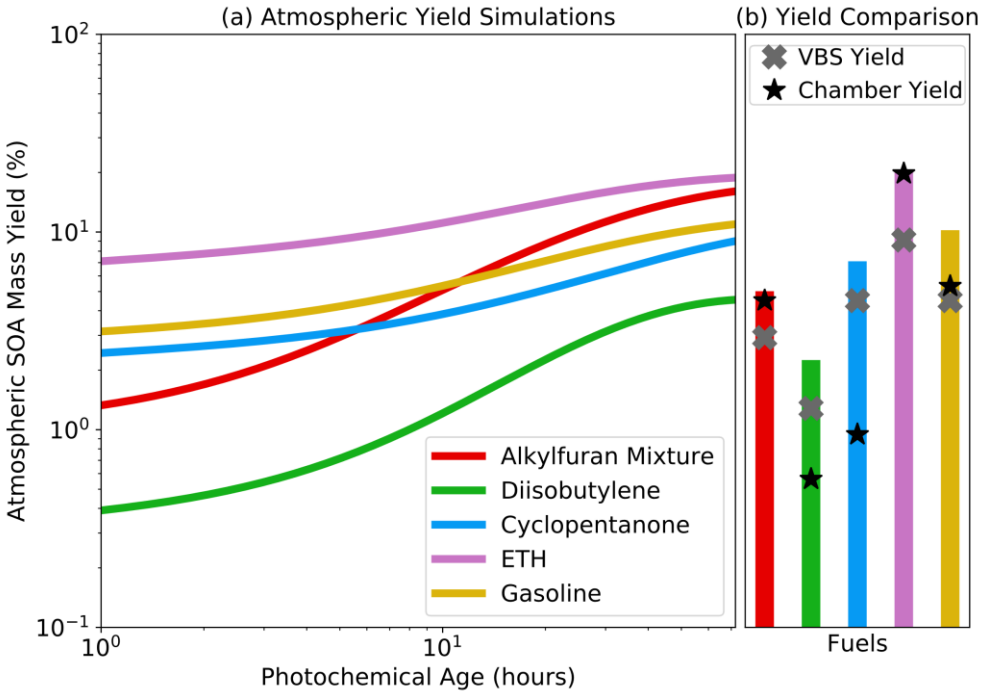

Figure 2.4: (a) SOA mass yields calculated from atmospheric simulations performed with the SOM-TOMAS model as a function of photochemical age for the five different fuels studied in this work. (b) Comparison of SOA mass yields from the SOM-TOMAS model predictions, chamber, and VBS fits. The SOM-TOMAS model predictions are those from panel (a) but corresponding to the photochemical age at the end of the chamber experiment. The SOA mass yields from the chamber are those measured at the end of the experiment. The SOA mass yields for the VBS are from fits to the chamber data but at an OA mass concentration of 10 μg m^{-3}.

The difference in the SOA mass yields between the atmospheric simulations and the chamber experiments was a result of two competing effects. The SOA mass yields in the atmospheric simulations were expected to be higher than that in the experiments because the condensable and precursor vapors that were lost to the Teflon® walls in the chamber experiment were now allowed to contribute to SOA formation. On the other hand, the SOA mass yields in the experiments were expected to be higher than that in the atmospheric simulations because the SOA mass concentrations experiments except for cyclopentanone and diisobutylene were larger than 10 $\mu g\ m^{-3}$, which allowed a larger fraction of the organic mass to partition into the particle phase. That the SOA mass yields in the atmospheric simulations at equivalent photochemical ages were higher than those reported in Table 2.1 suggested that the vapor-wall-loss effects more than offset the partitioning effects. This implies that the end-of-experiment SOA mass yields, despite being calculated at OA mass concentrations higher than those encountered in urban environments, are still likely to be lower than those that have been corrected for vapor wall losses and estimated at atmospherically relevant conditions. Although the SOA mass yields were higher in the atmospheric simulations than in the chamber experiments, the relative change in the SOA mass yields between the two seemed to vary with the fuel. These were very likely a result of the complex interplay of gas-phase chemistry and partitioning of the condensable vapors to the suspended particles and the walls of the Teflon® chamber.

In Figure 2.4(b), we also compared predictions from the SOM-TOMAS model to predictions from a volatility basis set (VBS) model that was fitted directly to the chamber data; VBS fits to the chamber data are shown in Figure A11. The VBS SOA mass yields, at an organic aerosol mass concentration of 10 $\mu g\ m^{-3}$, did not vary with photochemical age and were lower than those predicted by the SOM-TOMAS model. The VBS SOA mass yields were lower because they

did not account for the influence of vapor wall losses and, by assuming a constant volatility distribution, tended to underestimate the mass yields of the lower volatility species.

2.4 Discussion

The chamber experiments and numerical modeling performed in this work suggested that two of the Co-Optima fuels, namely cyclopentanone and diisobutylene, had a significantly lower potential to form SOA when compared to gasoline. A third fuel, the alkylfuran mixture, had the same SOA forming potential as gasoline. In contrast, ETH, on account of a large aromatic fraction, had a much higher potential to form SOA compared to gasoline. The Co-Optima initiative, so far, has ignored the atmospheric production of SOA from oxidation of compounds emitted from biofuel use. Our work shows that not only is the SOA potential significantly different between these biofuels but that some of them might be worse than gasoline (i.e., ETH or fuels with a high fraction of aromatic compounds). While biofuels might be environmentally more sustainable and optimized for combustion in spark-ignited engines, ignoring their impact on SOA formation may offset some of the projected environmental gains. An additional consideration that was not considered in this work is the potential of biofuel emissions to produce ozone (O_3) in the atmosphere. Ozone is an atmospheric oxidant, a criteria pollutant, and a greenhouse gas that is produced during VOC oxidation in the presence of NO_x (Monks et al., 2015). Aromatic compounds are important contributors to O_3 production in urban environments (Lewis et al., 2000) and it is likely that ETH would contribute not only to SOA production but also O_3 production.

We did not directly measure the VOC concentrations in this study because we did not have access to a complete suite of appropriate instrumentation. This prevented us from estimating the OH concentrations and exposure during the chamber experiments. These are important limitations of this study. By assuming a 100% injection efficiency and no losses of VOCs to the chamber

walls, the SOA mass yields reported in this work represent a lower bound estimate. We attempted to reduce the uncertainty in the OH estimates by explicitly modeling the gas-phase chemistry and radical concentrations in each individual experiment using a chemical mechanism (i.e., SAPRC). While this modeling technique was evaluated for toluene photooxidation, the technique will need to be evaluated in the future for the other VOCs studied in this work. Another limitation of this work is that we did not measure or model the formation of oligomers in the condensed phase that likely play an important role in controlling the mass yields and properties of atmospheric SOA. Oligomers have been previously observed in the SOA formed from aromatic (Sato et al., 2012) and heterocyclic compounds (Joo et al., 2019) and subsequent work should attempt to understand the oligomeric composition of biofuel SOA.

In addition to being considered as a potential biofuel, furans and substituted furans account for a modest fraction of the gas-phase organic emissions from residential wood combustion (Bruns et al., 2016) and wildfires (Hatch et al., 2015; Stockwell et al., 2015; Koss et al., 2018). The furan mixture studied herein had a measured SOA mass yield of ~1.6% and an atmospherically relevant SOA mass yield of 10% after a day of photochemical aging. Although not as large as those for most aromatic compounds, the SOA mass yields were sufficiently large that furanic compounds could contribute modestly to biomass burning SOA (Joo et al., 2019). Furanic compounds, despite being much more reactive, are modeled as aromatic species in gas-phase chemical mechanisms used in atmospheric models (Carter, 2010). These models are thus likely to simultaneously underestimate the reactivity, but overestimate the SOA formation from furanic compounds. Both of these factors will tend to distort the magnitude and spatial distribution of the SOA from this class of compounds. Furanic compounds must be studied in much more detail to understand their potential to form SOA.

The atmospheric simulations performed in this work suggested that SOA mass yield data gathered in chamber experiments need to be interpreted using models, such as those used here, to account for the influence of vapor wall losses and to calculate atmospherically relevant SOA mass yields. We find that ignoring the influence of vapor wall losses, especially in smaller chambers where gas/wall partitioning timescales are on the order of minutes, as well as direct application of VBS-type parameterizations based on chamber data, may underestimate SOA production in air quality models (Zhang et al., 2014). This finding, however, needs to be evaluated in the future by performing laboratory experiments at lower organic aerosol mass concentrations (<10 $\mu g\ m^{-3}$) and where chamber wall losses can be minimized.

CHAPTER 3: Particle Size Distribution Dynamics Can Help Constrain the Phase State of Secondary Organic Aerosol[2]

3.1 Introduction

Secondary organic aerosol (SOA) accounts for a substantial fraction of the submicron atmospheric aerosol burden and, consequently, has impacts on climate, air quality, and human health (Jimenez et al., 2009; Fuzzi et al., 2015). The particle phase state is an important property that likely affects the abundance and properties of atmospheric SOA since it has been shown to exert control on the equilibration timescale (Shiraiwa and Seinfeld, 2012), multiphase chemistry (Shiraiwa et al., 2011; Mu et al., 2018), long-range transport of organic pollutants (Shrivastava et al., 2017; Zhou et al., 2019; Mu et al., 2018), and formation of ice clouds (Murray et al., 2010; Wang et al., 2012; Berkemeier et al., 2014; Mu et al., 2018). However, there are large uncertainties in quantifying the evolving phase state of SOA and this has made it challenging to accurately represent the SOA phase state and its impacts in atmospheric models.

Anthropogenic and biogenic SOA formed from the oxidation of volatile organic compounds (VOCs) can be semisolid or viscous under a wide range of atmospheric conditions (0<RH<90% and T<298 K) (Reid et al., 2018). As a model system, the SOA formed from the oxidation of α-pinene has been extensively probed to study its phase state (Renbaum-Wolff et al., 2013; Kidd et al., 2014; Pajunoja et al., 2014; Zhang et al., 2015b; Bateman et al., 2015; Grayson et al., 2016; Zaveri et al., 2018, 2020). The particle phase state is often quantified using the dynamic viscosity (ν; Pa·s) or the bulk diffusion coefficient (D_b; cm^2 s^{-1}); they are related to each other via the Stokes-Einstein equation ($D_b = \frac{kT}{6\pi a \nu}$, where k is the Boltzmann constant, T is the

[2] This chapter is published as: He, Y., Akherati, A., Nah, T., Ng, N. L., Garofalo, L. A., Farmer, D. K., Shiraiwa, M., Zaveri, R. A., Cappa, C. D., Pierce, J. R., and Jathar, S. H.: Particle Size Distribution Dynamics Can Help Constrain the Phase State of Secondary Organic Aerosol, Environ. Sci. Technol., https://doi.org/10.1021/acs.est.0c05796, 2021.

temperature, and a is the effective molecular diameter). The consensus seems to be that α-pinene-derived SOA is unlikely to behave like a liquid when formed and sampled under relatively dry conditions (RH<30%) but the estimated phase state range for this SOA spans over 6 orders of magnitude; ν=10^{6}-10^{12} Pa·s or D_b =10^{-15}-10^{-21} cm^2 s^{-1} (Renbaum-Wolff et al., 2013; Pajunoja et al., 2014; Zhang et al., 2015b; Grayson et al., 2016; Zaveri et al., 2020; Abramson et al., 2013; Zhou et al., 2013). Some of the uncertainty in the estimated particle phase state can be attributed to differences in the techniques used to probe the SOA. For instance, some have collected the SOA onto a media (e.g., filters, microscopy grids) and examined the flow properties of raw or reconstituted particles to estimate the viscosity (Pajunoja et al., 2014; Grayson et al., 2016). Others have inferred viscosity of suspended particles by studying the bounce fraction on impaction plates (Kidd et al., 2014; Bateman et al., 2015) and the time for particles to coalesce (Pajunoja et al., 2014; Zhang et al., 2015b). Finally, a handful of studies have estimated D_b, instead of viscosity, by investigating the growth/evaporation kinetics of particles (Zaveri et al., 2018, 2020; Vaden et al., 2011; Yli-Juuti et al., 2017). Additional uncertainties in previous estimates are also likely related to differences in the SOA composition that result from different formation conditions (e.g., chamber versus flow tube, fresh versus aged) and mass concentrations (Grayson et al., 2016). Regardless, current estimates for ν and D_b for α-pinene-derived SOA under dry conditions translate to a mixing and equilibration timescale that spans from a few minutes to several years. There appears to be a need for novel techniques and approaches that can aid in reducing the large uncertainty in the phase state of SOA.

The phase state of SOA can influence the evolution of the particle size distribution. For SOA mass condensing into a liquid-like aerosol, vapors should partition into the entire particle volume regardless of the particle size. For condensation into a semisolid aerosol, vapors should

mostly partition into the entire volume for the smaller particles but closer to the edge for the larger particles as the timescales for mixing are proportional to the square of the particle size ($\tau_{diff} = \frac{R_p^2}{\pi^2 D_b}$, where R_p is the particle radius). Hence, for the same amount of condensing SOA mass, a semisolid aerosol should promote faster diameter growth of nucleation (1-10 nm) and Aitken (10-100 nm) mode particles relative to accumulation (100-1000 nm) mode particles compared to a liquid-like aerosol and produce a narrowing of the particle size distribution with SOA formation (Zaveri et al., 2014). This effect has been observed in a handful of studies. For example, in SOA formed from *n*-dodecane in a laboratory experiment, Shiraiwa et al. (2012) found that, in addition to modeling the multiphase chemistry, they had to assume a semisolid SOA (D_b of 10^{-12} cm^2 s^{-1}) to explain the observed narrowing in the particle size distribution with time. Similarly, Zaveri and co-workers (Zaveri et al., 2018, 2020) found that α-pinene-derived SOA was likely to be semisolid because only a D_b between 10^{-15} and 10^{-14} cm^2 s^{-1} in their aerosol model could reproduce observations of the rapid growth of Aitken mode particles with isoprene-derived SOA. We should note that the volatility of the condensing species (C^*, effective saturation concentration) (Donahue et al., 2006) can have a similar, but less pronounced, effect on the particle size distribution (Riipinen et al., 2011; Pierce et al., 2011; Tröstl et al., 2016). In instances where the phase state affects the evolution of the particle size distribution, these data, which are routinely measured in laboratory experiments, could be leveraged to constrain the phase state of SOA in both idealized (e.g., single VOC) and realistic (e.g., VOC mixtures, combustion emissions) model systems.

In this work, we include a treatment of the particle phase state in a detailed chemistry, thermodynamics, and micro-physics model for SOA (i.e., Statistical Oxidation Model coupled to the TwO Moment Aerosol Sectional (SOM-TOMAS)) and apply this model to study the phase state of SOA formed from α-pinene ozonolysis. We show that routine environmental chamber data

can be used to constrain the bulk diffusion coefficient (D_b) of SOA, requiring only measurements of the time-evolving SOA mass concentration and particle size distribution. Our work demonstrates that the particle phase state of SOA can be inferred from historical laboratory data and complement future laboratory studies and field observations of the particle phase state.

3.2 Materials and Methods

3.2.1. Environmental Chamber Data

We modeled the SOA formation from a set of α-pinene ozonolysis experiments that are described in detail in Nah et al. (Nah et al., 2016). These experiments were chosen for several reasons. First, these experiments were characterized for vapor loss and size-dependent losses of particles to the chamber walls, inputs necessary to predict the time-varying suspended particle data. Second, they included both seeded and unseeded experiments; the unseeded experiment proved particularly useful because the modeled evolution of the particle size distribution varied substantially with the use of different D_b values and this effect was used to constrain the D_b (explained later). Third, the phase state of α-pinene-derived SOA has been extensively studied in the past and thus the results from this work could be compared with historical data (Renbaum-Wolff et al., 2013; Pajunoja et al., 2014; Zhang et al., 2015b; Grayson et al., 2016; Zaveri et al., 2018, 2020; Abramson et al., 2013; DeRieux et al., 2018).

The experiments of Nah et al. (Nah et al., 2016) were performed in the 13 m^3 Georgia Tech Environmental Chamber (GTEC) facility, with full details provided in previous work (Boyd et al., 2015). In all experiments, 50 ppbv of α-pinene was added to a clean chamber along with 22 ppm of cyclohexane, which served as an OH scavenger and ensured that the α-pinene reacted only with O_3. Experimental conditions featured low NO_x concentrations (<1 ppbv), a temperature of 25 °C, and relative humidity of <5%. Experiments were performed either with 100 or 500 ppbv of O_3,

which reacted immediately with α-pinene under dark conditions. For each O_3 level, one experiment was performed with no seed particles which resulted in homogeneous nucleation and growth of the freshly formed particles. Two other experiments were performed with low (~1000 μm^2 cm^{-3}) and high (~3000 μm^2 cm^{-3}) initial dry ammonium sulfate seed concentrations, where SOA condensed onto the seeds. The instrumentation used to measure the gas- and particle-phase species is summarized in Table B1.

3.2.2. SOM-TOMAS Model and Updates for Highly Oxygenated Organic Molecules (HOM) Formation

We used the Statistical Oxidation Model coupled to the TwO Moment Aerosol Sectional model (SOM-TOMAS) to simulate the SOA formation from α-pinene ozonolysis in environmental chamber experiments. Detailed descriptions of the SOM (Cappa and Wilson, 2012; Jathar et al., 2015) and TOMAS (Adams and Seinfeld, 2002; Pierce et al., 2007) models can be found in previous publications. More recently, the SOM-TOMAS model was used to model SOA formation in chamber experiments performed on unburned biofuels (He et al., 2020) and emissions from biomass burning (Akherati et al., 2020).

The SOM tracks the chemical evolution of the VOC and its oxidation products using a two-dimensional, carbon (N_C) and oxygen (N_O) number grid. The properties of each model species (e.g., reactivity (k_{OH}), volatility (C^*)) are parameterized based on their N_C and N_O. The SOM has five adjustable parameters that govern the oxidation chemistry and thermodynamic properties of the model species: (i-iv) $p_{f,1}$-$p_{f,4}$, the yields of four functionalized products that add one, two, three, and four oxygen atoms to the carbon backbone, respectively; (v) ΔLVP, the decrease in the C^* of the model species per addition of an oxygen atom. We did not model fragmentation reactions because O_3 was the only oxidant present in the chamber experiments. The TOMAS model tracks

the evolution of the aerosol number distribution and species-resolved mass distribution and simulates kinetic condensation/evaporation and coagulation. New particle formation in the nucleation experiments was specified based on the experimental data (Section B1 and Figure B1) and the SOM-TOMAS model was used to simulate vapor and size-dependent particle wall losses similar to that in previous work (Section B2). In this work, we used 60 size sections in TOMAS spanning dry diameters of 3-2000 nm.

Reaction intermediates formed during α-pinene ozonolysis (i.e., peroxy radicals) can autooxidize under low-NO_x conditions to rapidly form highly oxygenated organic molecules (HOM) (Bianchi et al., 2019). HOM have extremely low C^* values ($<10^{-4}$ μg m^{-3}) and high O/C ratios (~1) and are known to contribute to new particle formation and growth (Ehn et al., 2014; Jokinen et al., 2015; Kirkby et al., 2016). To account for this, we added an autooxidation pathway to the SOM-TOMAS model, where the α-pinene reaction with O_3 directly led to the formation of HOM with a fixed molar yield (f_{HOM}) and a C^* of 10^{-4} μg m^{-3}; species with volatilities this low are effectively nonvolatile. Based on the work of Jokinen et al. (Jokinen et al., 2015), we used a molar yield of 3.4%, or equivalently a mass yield of 7.9%, to model HOM formation from α-pinene ozonolysis. We ensured that the sum of $p_{f,1}$ through $p_{f,4}$ and f_{HOM} was exactly equal to 1.

This version of the SOM-TOMAS model, which included functionalization reactions and formation of HOMs, was updated to account for the influence of the particle phase state on kinetic gas/particle partitioning (Section 3.2.4). In this version, the D_b for the SOA was specified a priori and, hereafter, this is referred to as the prescribed-D_b version.

3.2.3. Endogenous-D_b Model and Updates for Particle Phase Reactions

We developed a separate endogenous-D_b version of the SOM-TOMAS model in which the D_b was calculated based on the simulated, evolving chemical composition of SOA. The D_b was

calculated following the semiempirical framework developed by Shiraiwa and co-workers (DeRieux et al., 2018; Shiraiwa et al., 2017; Li and Shiraiwa, 2019; Song et al., 2019), the equations for which are described in the Supporting Information (Section B3). Briefly, the molecular weights and O/C ratios of the condensed model species were used to estimate the glass-transition temperature (T_g) for the model species and these T_gs were weighted by their mass fraction to calculate the average $T_{g,org}$ for the SOA mixture. Using a fragility parameter set to 10, we estimated the viscosity (v) using Angell (Angell, 1995) and then D_b from v using the fractional Stokes-Einstein relation (Evoy et al., 2019). A single time-evolving D_b value was calculated for all SOA and applied to all particle size sections. A separate model was developed that calculated a size-dependent D_b and was used to perform sensitivity simulations.

High-molecular-weight oligomers have been frequently observed in SOA from α-pinene ozonolysis (D'Ambro et al., 2018; Sato et al., 2019) and are likely to exert a strong influence on the particle phase state. To account for the influence of oligomers on D_b, we included an oligomerization scheme in the endogenous-D_b model, with reversible oligomer formation and dissociation, characterized by a forward reaction rate (k_f, cm^3 $molecule^{-1}$ s^{-1}) and reverse reaction rate (k_r, s^{-1}), respectively. Only dimer formation and dissociation were included, assumed to represent general oligomer formation. Serving as monomers, the four functionalized oxidation products, in all combinations, were allowed to form dimers and we assumed that the dimers decomposed back into the same monomer pair that the dimer was formed from. Depending on the *ΔLVP*, the monomers included both semivolatile and low-volatility species. HOM were excluded from oligomerization reactions since there is little evidence for HOM participating in additional particle phase reactions (Bianchi et al., 2019). k_f was specified and k_r was treated as an adjustable

parameter. This oligomerization scheme was similar to that described in Trump and Donahue (2014) and the equations are as follows

$$\frac{dO_{i,j}}{dt} = \sum_k^{i_{max}} k_f \cdot M_{k,j} \cdot M_{i,j} - k_r \cdot O_{i,j} \qquad (3.1)$$

$$\frac{dM_{i,j}}{dt} = k_r \cdot O_{i,j} - \sum_k^{i_{max}} k_f \cdot M_{k,j} \cdot M_{i,j} \qquad (3.2)$$

where *M* and *O* are the monomer and dimer concentrations in the particle phase in molecules per cm^3 of particle volume, respectively; *i* and *k* are the species and *j* is the size bin. We also calculated the first-order loss rate of the condensing species in the particle phase to oligomerization reactions, $k_{i,j}^c$ (s^{-1}). $k_{i,j}^c$ is calculated assuming that the dimer mass is in pseudo-steady state with the monomer mass

$$k_{i,j}^c = \sum_k^{i_{max}} k_f \cdot M_{k,j} - k_r \cdot \frac{O_{i,j}}{M_{i,j}} \qquad (3.3)$$

3.2.4. Representing the Influence of Particle Phase State on Gas/Particle Partitioning

In the SOM-TOMAS model, the influence of D_b on the kinetic gas/particle partitioning of SOA was implemented using the diffusion-reactive framework of Zaveri et al. (2014). Depending on the first-order chemical loss rate ($k_{i,j}^c$) of the model species in the particle phase, the differential equations used to model the condensation and evaporation of a species *i*, for a polydisperse size distribution, can take on different forms. For a slow particle phase reaction ($k_{i,j}^c$<0.01 s^{-1})

$$\frac{dC_i^g}{dt} = -\sum_j 4\pi \cdot \left(R_j^p\right)^2 \cdot N_j^p \cdot K_{i,j} \cdot \left(C_i^g - \frac{C_{i,j}^p}{SOA_j} C_i^* S_j\right) \qquad (3.4)$$

$$\frac{dC_{i,j}^p}{dt} = 4\pi \cdot \left(R_j^p\right)^2 \cdot N_j^p \cdot K_{i,j} \cdot \left(C_i^g - \frac{C_{i,j}^p}{SOA_j} C_i^* S_j\right) \qquad (3.5)$$

where C_i^g is the gas-phase concentration of the species *i* in μg m^{-3}, $C_{i,j}^p$ is the particle-phase concentration of the species *i* in size bin *j* in μg m^{-3}, R_j^p is the radius of the particle in size bin *j* in m, N_j^p is the particle number concentration in size bin *j* m^{-3}, $K_{i,j}$ is the overall gas-side mass transfer

coefficient for species *i* in size bin *j* in m s^{-1}, SOA_j is the total SOA mass concentration in size bin *j* in μg m^{-3}, C_i^* is the effective saturation concentration of species *i* in μg m^{-3}, and S_j is the Kelvin ratio (Section B4). $K_{i,j}$ is calculated as follows:

$$\frac{1}{K_{i,j}} = \frac{1}{k_{i,j}^g} + \frac{1}{k_{i,j}^p}\left(\frac{C_i^*}{\rho_p}\right) \quad (3.6)$$

$$k_{i,j}^g = \frac{D_i^g \cdot FS_{i,j}}{R_j^p} \quad (3.7)$$

$$k_{i,j}^p = \frac{D_b}{R_j^p}\left(\frac{q_{i,j} \cdot coth(q_{i,j}) - 1}{1 - Q_{i,j}}\right) \quad (3.8)$$

$$q_{i,j} = R_j^p \cdot \sqrt{\frac{k_{i,j}^c}{D_b}} \quad (3.9)$$

$$Q_{i,j} = 3 \cdot \left(\frac{q_{i,j} \cdot coth(q_{i,j}) - 1}{q_{i,j}^2}\right) \quad (3.10)$$

where $k_{i,j}^g$ is the gas-side mass transfer coefficient for species *i* in size bin *j* in m s^{-1}, $k_{i,j}^p$ is the particle-side mass transfer coefficient in m s^{-1}, ρ_p is the SOA density in kg m^{-3}, $FS_{i,j}$ is the Fuchs-Sutugin correction factor (Section B4), $q_{i,j}$ is a unitless diffusion-reaction parameter for species *i* in size bin *j*, and $Q_{i,j}$ is the ratio of the average bulk concentration of species *i* to its concentration at the particle surface at steady state for size bin *j*. We should note that eq 3.8 shows the formulation of $k_{i,j}^p$ for a well-mixed particle where diffusion of the condensing species occurs across the entire particle radius. However, to simulate the seeded experiments, we derived an updated formula for $k_{i,j}^p$ where the diffusion of the condensing species occurred across an organic shell around an ammonium sulfate core (derivation in Section B5). For a fast particle phase reaction ($k_{i,j}^c$>0.01 s^{-1})

$$\frac{dC_i^g}{dt} = -\sum_j 4\pi \cdot \left(R_j^p\right)^2 \cdot N_j^p \cdot k_{i,j}^g \cdot \left(C_i^g - \frac{C_{i,j}^p}{SOA_j Q_{i,j}} C_i^* S_j\right) \quad (3.11)$$

$$\frac{dC_{i,j}^{p}}{dt} = 4\pi \cdot \left(R_j^p\right)^2 \cdot N_j^p \cdot k_{i,j}^{g} \cdot \left(C_i^g - \frac{C_{i,j}^{p}}{SOA_j Q_{i,j}} C_i^* S_j\right) \qquad (3.12)$$

For a liquid-like aerosol when D_b is greater than 10^{-10} cm^2 s^{-1}, eqs 5.4, 5.11 and 5.5, 5.12 resemble the condensation/evaporation equation equation expressed in the continuum regime (Pandis and Seinfeld, 2006).

3.2.5. Simulations

The following three sets of simulations were performed to constrain the D_b of the SOA formed from α-pinene ozonolysis. First, the SOM parameters ($p_{f,1\text{-}4}$ and ΔLVP with f_{HOM}=3.4%) were fit to reproduce the time-varying SOA mass concentrations in the nucleation experiments for a prescribed D_b value, that ranged between 10^{-6} and 10^{-19} cm^2 s^{-1}. Predictions of the SOA O/C and particle size distribution from these simulations were compared with measurements. Second, to determine an optimal fit, the SOM parameters ($p_{f,1\text{-}4}$ and ΔLVP with f_{HOM}=3.4%) and D_b were fit to simultaneously reproduce the time-varying SOA mass concentrations and particle size distribution in the nucleation experiments. Third, using the optimal SOM parameters determined in the second set of simulations, we simulated the nucleation experiments using the endogenous-D_b model. k_f was fixed at either 10^{-24} cm^3 molecule^{-1} s^{-1} (faster reaction) or 10^{-25} cm^3 molecule^{-1} s^{-1} (slower reaction), and k_r was adjusted to reproduce the time-varying SOA mass concentrations. In essence, we determined a k_f-k_r pair to optimize oligomer formation that then approximately produced the same D_b as that determined in the optimal fit. Finally, the endogenous-D_b model was used to study the impact of a size-dependent D_b on the evolution of the particle size distribution. For the first two sets, the simulations and their evaluations were done separately for the 100 and 500 ppbv O_3 experiments. The first set was also applied to simulate SOA formation in the seeded experiments. All model predictions were compared to measurements for the suspended aerosol

since the model inherently accounted for size-dependent losses of particles and losses of vapors to the chamber walls.

3.3 Results

Results from application of the prescribed-D_b version of the SOM-TOMAS model to the α-pinene ozonolysis nucleation experiment with 500 ppbv O_3 are presented in Figure 3.1. A unique set of SOM parameters ($p_{f,1-4}$ and ΔLVP with f_{HOM}=3.4%) was developed for each prescribed D_b that reproduced the time-varying SOA mass concentrations (Figure 3.1(a); solid lines); the SOM parameters from these fits are tabulated in Table B2. However, the use of different D_b values produced a significantly different evolution of the particle number size distribution. In Figure 3.1(b), we compare the predicted and measured number size distribution at 3 h after the start of the ozonolysis experiment. The simulations showed that the use of a higher D_b (>10^{-14} cm^2 s^{-1}) produced a broader distribution while a lower D_b (<10^{-15} cm^2 s^{-1}) produced a narrower distribution. As the D_b values varied between 10^{-14} and 10^{-15} cm^2 s^{-1}, the simulations produced a distribution that progressively transitioned between the broad and narrow number size distributions observed at the two extremes (Figure B2). These results can be explained by understanding the size-resolved dynamics of SOA condensation that changed with the different prescribed D_b values.

Smaller particles exhibit shorter timescales for bulk particle phase diffusion and hence condensation of SOA onto nucleation and Aitken mode sizes was not significantly affected by changes in D_b. For instance, for a 10 nm particle, τ_{diff} varies between 2.5 and 25 s for D_b values between 10^{-14} and 10^{-15} cm^2 s^{-1}, respectively. In contrast, larger particles exhibit longer timescales for bulk diffusion, which resulted in accumulation of the species at the particle surface and limited additional condensation for accumulation mode particles with the use of a lower D_b. For a 200 nm particle, τ_{diff} varies between 17 min and 3 h for D_b values between 10^{-14} and 10^{-15} cm^2 s^{-1},

respectively. Furthermore, the use of a lower D_b resulted in enhanced formation of lower-volatility species, which were necessary to reproduce the observed SOA formation under bulk diffusion limitations (Figure B3). Lower-volatility species, regardless of the D_b, condense irreversibly on all particle sizes with the diameter growth rate having no dependence on particle size in the kinetic regime and slowing with increasing size in the transition regime. Overall, a lower D_b resulted in a relatively faster diameter growth rate for the smaller particles compared to the larger particles and this produced the distinct number size distributions shown in Figure 3.1(b). This finding is generally consistent with previous theoretical and experimental studies that have observed a similar narrowing in the number size distribution with the use of a lower D_b and/or lower C^* of the condensing species (Zaveri et al., 2018, 2020, 2014; Pierce et al., 2011; Riipinen et al., 2010; Zhang et al., 2012; Shiraiwa et al., 2013b).

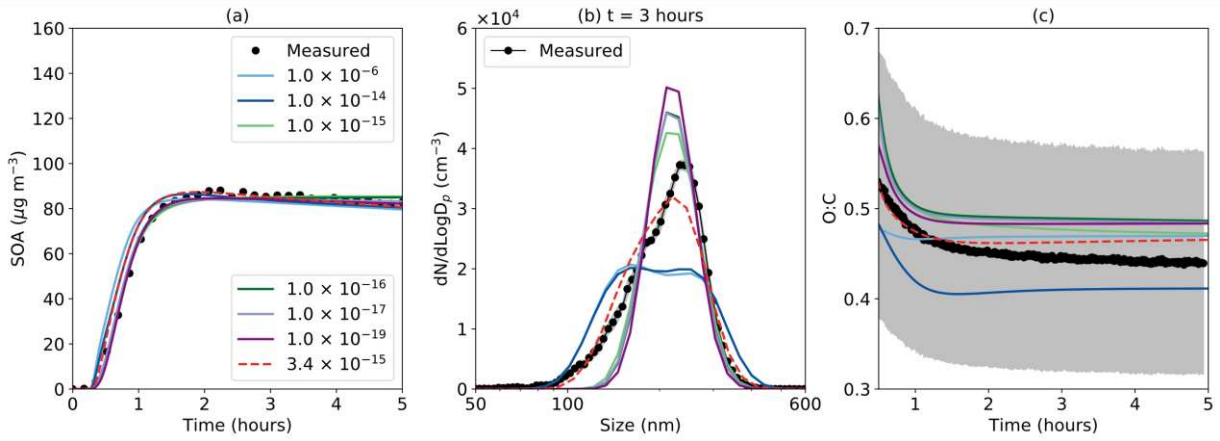

Figure 3.1: Results from the SOM-TOMAS model for (a) SOA mass concentration, (b) number size distribution at 3 h, and (c) O/C ratio compared to measurements for a range of prescribed D_b ($cm^2\ s^{-1}$) values. Results are for the 500 ppbv O_3, nucleation experiment. The dashed red line shows model predictions from the optimal fit when constrained to both the SOA mass concentration and number size distribution. The O/C data are only shown 30 min after the start of the experiment because the O/C measurements are fairly uncertain in the first 30 min when the SOA mass concentrations are quite low. The gray bands in (b) and (c) depict ± 1σ.

The prescribed-D_b simulations indicated that a D_b value between 10^{-15} and 10^{-14} $cm^2\ s^{-1}$, a range that reflects a semisolid particle phase state, might reproduce the observed evolution in the

number size distribution. When the SOM-TOMAS model was used to fit both the SOM and D_b to the time-varying SOA mass concentrations and number size distribution, the fitting produced a D_b of 3.4×10^{-15} cm^2 s^{-1}; model predictions based on this fit are shown as a dashed red line in Figure 3.1. Similar comparisons as shown in Figure 3.1(b) at other times (e.g., 0.5, 1, and 5 h) are presented in the Supporting Information (Figure B4), and these support the findings presented here.

Simulations based on parameters for the different D_b values did not seem to produce large differences in the SOA O/C ratio (Figure 3.1(c)), and the predictions were well within the bounds of the measurements. Model predictions with D_b values equal to or smaller than the optimal value (3.4×10^{-15} cm^2 s^{-1}) reproduced the general trend in the observed SOA O/C ratio: an initial decrease and a gradual flattening over time. We concluded that the SOA O/C data did not contain information that could be used to constrain the D_b further and hence the O/C data were not used as part of the fitting process. However, model predictions of the SOA O/C were found to be sensitive to HOM production. Simulations performed without the formation of HOM, but with fits that reproduced the time-varying SOA mass concentrations, resulted in an average SOA O/C of 0.39 between 2 and 5 h. Although still within the uncertainty range in the measurements, this was lower than the mean measured SOA O/C of 0.44 during the same time period. This suggests the need for HOM to be explicitly accounted for in models to ensure accurate predictions of SOA O/C.

Previous work has found that condensation of lower-volatility material (C^*<10^{-4} μg m^{-3}), including HOM, can produce a similar narrowing in the particle size distribution (Shiraiwa and Seinfeld, 2012; Riipinen et al., 2011; Pierce et al., 2011), as seen in Figure 3.1(b) with the use of a lower D_b. We investigated if the observations could only be explained by the production of low-volatility material (HOM in this case), but assuming a liquid-like SOA. For a D_b of 10^{-6} cm^2 s^{-1}, we determined SOM parameters ($p_{f,1\text{-}4}$, ΔLVP) for several predefined values of f_{HOM} (3.4, 7, 10,

and 20%) that reproduced the time-varying SOA mass concentrations. We found that while an increase in the production of HOM produced slight variations in the number size distribution at 3 h, none of the model predictions compared well with the observations (Figure B5). Further, the use of a larger f_{HOM} resulted in a relatively weaker comparison for the SOA mass concentration and O/C ratio. For the largest f_{HOM} (20%), the model formed SOA too rapidly and overpredicted the SOA O/C. These simulation results suggest that the SOA volatility was much less influential than the phase state in controlling the evolution of the particle size distribution and provided further evidence that α-pinene-derived SOA was semisolid with a D_b between 10^{-14} and 10^{-15} cm^2 s^{-1}.

In Figure 3.1, we chose not to present results from simulations performed with D_b values between 10^{-6} and 10^{-14} cm^2 s^{-1} because the model predictions for SOA mass concentration and number size distribution were nearly identical for any D_b between those bounds. Differences in model predictions of the number size distribution started to appear at D_b values lower than 10^{-14} cm^2 s^{-1}. While the literature has defined organic material with a D_b of 10^{-14} cm^2 s^{-1} and up to a D_b of 10^{-10} cm^2 s^{-1} as semisolid (Koop et al., 2011), these D_b values appeared to mimic the model response with a D_b strictly in the liquid range ($>10^{-10}$ cm^2 s^{-1}). This result suggests that the SOA condensation in nucleation experiments may not necessarily be limited by the particle phase state even when the SOA D_b is near the upper end (10^{-10}-10^{-14} cm^2 s^{-1}) of the semisolid range (10^{-10}-10^{-18} cm^2 s^{-1}). The "critical" D_b where the number size distribution evolution began to change (10^{-14} cm^2 s^{-1}, in this case) was likely to be lower in the nucleation experiment because the kinetics of SOA condensation was primarily driven by growth of nucleation and Aitken mode particles that are less susceptible to the effects of bulk diffusion. If the experiments were to be performed with absorbing seed particles in the accumulation mode that had the same D_b as the condensing SOA, the critical D_b would have very well been much higher ($>10^{-14}$ cm^2 s^{-1}).

The SOM-TOMAS model was applied to another α-pinene ozonolysis nucleation experiment performed at lower initial O_3 concentrations (100 ppbv; Figure B6). The findings from this application were very similar to those discussed above and an optimal D_b of 4.4×10^{-15} cm^2 s^{-1} was determined based on simultaneously fitting the SOA mass concentration and the evolution of the number size distribution. We explored the sensitivity in the optimal D_b by performing simulations and fits with the vapor wall loss rate, size-dependent particle wall loss rate, and f_{HOM}, all doubled and halved. This sensitivity analysis, presented in Figures B7-B9 for the 500 ppbv O_3 experiment, suggested that the optimal D_b was tightly constrained between 1.4×10^{-15} and 7.1×10^{-15} cm^2 s^{-1} for the uncertainty in these three inputs.

The technique used to constrain D_b in the nucleation experiments did not work with the seeded experiments due to the invariability in the predicted number size distribution with different prescribed D_b values. We attributed this to the relatively uniform SOA coating thickness around the ammonium sulfate core in these particular seeded experiments. The simulation results are shown in Figures B10-B12, and the results are described in Section B6.

The results from application of the endogenous-D_b version of the SOM-TOMAS model - where D_b was calculated from predictions of the SOA composition - to the α-pinene ozonolysis nucleation experiment with 500 ppbv O_3 are presented in Figure 3.2. To note, we used the optimal SOM parameters from Figure 3.1 and determined a k_f-k_r pair that reproduced the time-varying SOA mass concentrations. This, in essence, optimized the oligomer production to approximately reproduce the same SOA D_b as the optimal D_b identified in Figure 3.1.

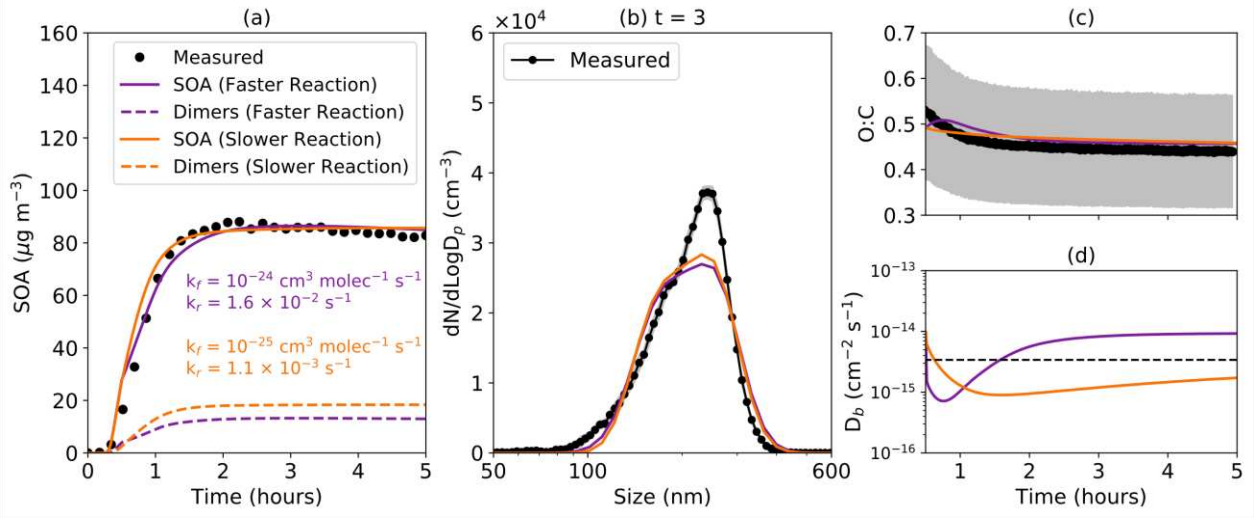

Figure 3.2: Results from the endogenous-D_b version of the SOM-TOMAS model for (a) SOA mass concentration, (b) number size distribution at 3 h, and (c) O/C ratio compared to measurements. (d) Model predictions of the time-varying D_b. Results are for the 500 ppbv O_3, nucleation experiment. Both the slower-reacting (orange lines) and faster-reacting (purple lines) cases use the SOM parameters from the optimal D_b fit in Figure 3.1 ($p_{f,1\text{-}4}$, ΔLVP, f_{HOM}=3.4%) but with different oligomer formation and dissociation rates. The O/C data are only shown 30 min after the start of the experiment because the O/C measurements are fairly uncertain in the first 30 min when the SOA mass concentrations are quite low. The gray bands in (b) and (c) depict ± 1σ.

The fitting resulted in k_r values of 1.1×10^{-3} s^{-1} and 1.6×10^{-2} s^{-1} for the slower and faster oligomerization schemes, respectively, and produced very similar predictions in the SOA O/C (Figure 3.2(c)) that agreed well with the measurements. Increasing the k_f to values larger than 10^{-24} cm^3 molecules s^{-1} produced too low of an initial D_b (<10^{-19} cm^2 s^{-1}) from a large oligomer fraction to condense any oxidation products apart from the HOM. A k_f value lower than 10^{-25} cm^3 molecules s^{-1} (and down to ~0) produced too high of an initial D_b (>10^{-13} cm^2 s^{-1}) from very few oligomers to agree with the evolution in the number size distribution. The model-measurement comparison for the SOA mass concentration and the number size distribution seemed to bound the k_f-k_r ranges, which were generally found to be consistent with those reported in the literature (Ziemann and Atkinson, 2012; Roldin et al., 2014; Bakker-Arkema and Ziemann, 2020). The oligomer mass concentrations and temporal profiles were consistent between the slower and faster schemes and the oligomers were between 15 and 21% of the total SOA by the end of the experiment. This

oligomer mass fraction, although slightly on the lower side, was consistent with previously measured oligomer fractions in α-pinene ozonolysis SOA in chamber and flow tube experiments (30-75%) (Zaveri et al., 2018; D'Ambro et al., 2018). In contrast to the results shown in Figure 3.1, where D_b was prescribed and remained constant throughout the experiment, D_b, shown in Figure 3.2d, changed with time but remained between 10^{-15} and 10^{-14} cm^2 s^{-1}. The average model-predicted D_b values during the first two hours of the simulations were 2.4×10^{-15} and 1.5×10^{-15} cm^2 s^{-1} for the slower and faster oligomerization schemes, respectively. In summary, by knowing the SOA D_b from earlier simulations and using the semiempirical approach proposed by Shiraiwa and co-workers (DeRieux et al., 2018; Shiraiwa et al., 2017; Li and Shiraiwa, 2019; Song et al., 2019), we were able to constrain the formation of high-molecular-weight oligomers that were contributing to the semisolid phase state of SOA. This finding would need to be validated in the future with explicit measurements of oligomers in SOA.

Additional simulations were performed with the size-dependent, endogenous-D_b model to study its impacts on SOA formation and the particle size distribution; the simulation results are shown in Figure B13. For the k_f-k_r pairs that reproduced the SOA mass concentrations, we found that these simulations failed to reproduce observations of the particle size distribution. For the slower k_f simulation, the size-dependent D_b favored SOA condensation onto smaller particle sizes and resulted in a very narrow particle size distribution. For the faster k_f simulation, the SOA seemed to condense on all sizes to produce a very broad particle size distribution. Although the slower and faster k_f simulations might give the impression that they bound the model's particle size distribution response, the model responded nonlinearly to all intermediate k_f and k_r values (not shown) with the actual response being sensitive to the size- and time-dependent HOM, monomer, and dimer composition. In this work, we were unable to model the size-dependent D_b while

reconciling both the mass and size distribution measurements. Future work, informed by more recent studies (Cheng et al., 2015; Petters and Kasparoglu, 2020), should aim to study this aspect in more detail.

3.4 Discussion

We used a chemistry, thermodynamics, and microphysics model to simulate the formation of fresh SOA formed from α-pinene ozonolysis in two nucleation experiments (Nah et al., 2016). We discovered that we were able to explain the SOA production and the evolution in the particle size distribution only if we assumed a semisolid SOA with a D_b between 1×10^{-15} and 7×10^{-15} cm^2 s^{-1}. This D_b was compared with historical D_b values estimated for α-pinene-derived SOA formed and/or sampled under dry conditions (RH<30%) in Table 3.1. The D_b range estimated in this work agreed with the value estimated by Zaveri et al. (2020) (2.5×10^{-15} cm^2 s^{-1}) who used a similar thermodynamic approach to constrain D_b, based on the varying growth rates observed for particles of different sizes. However, the D_b values in our work were found to be near the upper end of the observational range in Table 3.1 (10^{-21}-10^{-14} cm^2 s^{-1}), which was primarily inferred from measurements of viscosity. Furthermore, the Stokes-Einstein equation that allows for calculation of D_b from viscosity has been shown to underestimate D_b for highly viscous material (Evoy et al., 2019). Hence, our work tentatively suggests that the D_b for α-pinene-derived SOA inferred from the thermodynamic behavior might be much larger than that estimated in the literature based on its viscosity. While we demonstrate a novel technique to constrain D_b using historical chamber data, additional work is needed to reconcile the large differences in D_b and viscosity previously observed for this model system. Future work to constrain the particle phase state could be further complicated by recent observations of liquid-liquid phase separation at high relative humidity (Song et al., 2019) and the formation of surface crusts with chemical aging (Zhou et al., 2019).

Table 3.1: Estimates of D_b from this work compared to historical estimates under dry conditions for α-pinene-derived SOA. When not directly available, the D_b was estimated from the viscosity using the Stokes-Einstein equation. NM=not mentioned

Reference	*Oxidant*	*SOA formed in*	*RH*	*Max. SOA mass conc. ($\mu g\ m^{-3}$)*	*D_b ($cm^2\ s^{-1}$)*	*D_b estimated using*
This work	O_3	13 m^3 chamber at <5% RH	<5%	60-80	$1\text{-}7\times10^{-15}$	Evolution of the particle size distribution
Zaveri et al. (2020)	OH	10.6 m^3 chamber at 32 % RH	32%	110	2.5×10^{-15}	Growth of SOA on different sized particles
Abramson et al. (2013)	O_3	0.1 m^3 chamber at ~0% RH	~0%	NM	2.5×10^{-17}	Evaporation of pyrene trapped inside SOA
Zhou et al. (2013)	O_3	Flow tube at <5% RH	~0%	NM	2×10^{-14}	Oxidation of benzo[a]pyrene trapped inside SOA
Renbaum-Wolff et al. (2013)	O_3	Flow tube at <5% RH	0-30%	50	$<10^{-17}$	Flow properties of large SOA particles
Pajunoja et al. (2014)	O_3	6 m^3 chamber at 35% RH	<20%	3-15	$>3\times10^{-21}$	Coalescence time of individual particles
	OH				$<3\times10^{-21}$	
Zhang et al. (2015)	O_3	Flow tube at <5% RH	<5%	70	6×10^{-18}	Change in particle shape factor
Grayson et al. (2016)	O_3	Flow tube at <5% RH	0.5%	14000	2×10^{-15}-7×10^{-14}	Flow properties of large SOA particles
		Chamber at <5% RH	0.5%	121	6×10^{-17}-5×10^{-15}	

Water uptake at subsaturated and more atmospherically relevant conditions is known to have a plasticizing effect (O'Meara et al., 2016) that has been shown to dramatically alter the phase state of SOA (Bateman et al., 2015; Price et al., 2015; Song et al., 2015). Water vapor can also influence the oxidation chemistry to change the molecular composition of SOA and thus its phase state (Kidd et al., 2014). In two recent papers that compiled phase state data for SOA from different precursors (Reid et al., 2018; DeRieux et al., 2018), a change in RH from <5 to ~90% decreased the SOA viscosity by 7-10 orders of magnitude. DeRieux et al. (2018) showed that the semiempirical framework used in this work to calculate viscosity from the SOA composition was generally able to reproduce the observed changes in viscosity with RH for SOA derived from α-pinene, isoprene, and toluene. The D_b for α-pinene-derived SOA was estimated in this work based on chamber experiments performed under dry conditions (RH<5%). Hence, the models developed in this work, including the endogenous-D_b version, need to be used to explore the phase state of SOA in experiments performed under wet conditions. Since particle size distribution data are

routinely collected during laboratory experiments, our methods could easily be extended to historical unseeded data and potentially to seeded data.

The phase state has also been shown to affect the kinetics of SOA evaporation when perturbed with dilution, heating, or removing vapors in equilibrium with the SOA (Vaden et al., 2011; Yli-Juuti et al., 2017; D'Ambro et al., 2018; Sato et al., 2019; Trump and Donahue, 2014; Grieshop et al., 2007). To study the kinetics of SOA evaporation, we performed additional simulations with the SOA found at the end of the nucleation experiments. In these evaporation simulations, we instantaneously removed any vapors in the simulated chamber (but not particles) and studied the multihour evolution of the remaining SOA with the SOM-TOMAS model, where the D_b was prescribed (3.4×10^{-15} cm^2 s^{-1}) and or calculated endogenously from the chemical composition. The results from these simulations are shown in Figure 3.3, where we compare the normalized evolution of remaining SOA volume with historical data for SOA studies under dry conditions (different experiments than used for our simulations) (Yli-Juuti et al., 2017; Sato et al., 2019). The model with the prescribed D_b overestimated both the rate and net loss of SOA while the endogenous models appeared to bracket the observational range. As the D_b value for the SOA was roughly similar between all three simulations, these results suggest that models need to account for oligomers, in addition to representing the phase state and volatility distribution accurately, to reproduce the observed evaporation kinetics. Furthermore, this supports the general approach used in this work to first determine a D_b using a prescribed-D_b model and then using an endogenous-D_b model to constrain oligomer formation and dissociation. It is important to note that the SOA observations in Figure 3.3 were collated from several different studies with substantial differences in experimental details. Regardless, observations of the evaporation of SOA with

dilution or heating could provide additional constraints on the SOA composition and properties when used in conjunction with detailed process-based models (Tikkanen et al., 2019).

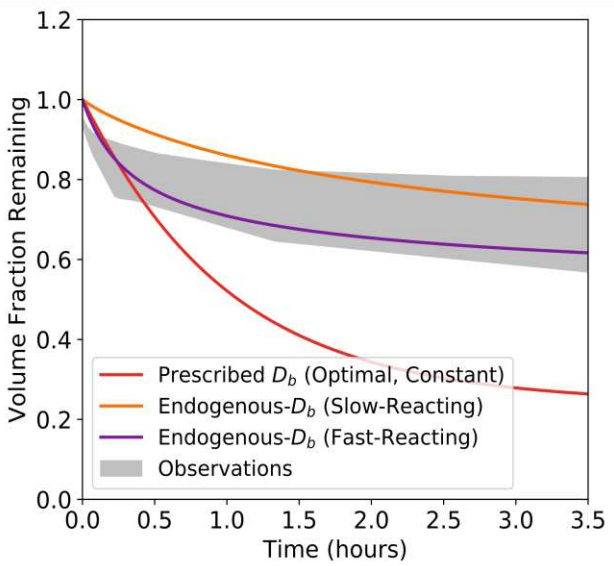

Figure 3.3: Simulated evaporation of the end-of-experiment SOA for the SOM-TOMAS model with D_b=3.4×10^{-15} cm^2 s^{-1} and the endogenous-D_b version of the model with slower and faster oligomerization rates. The observational range is adapted from the following studies: Sato et al. (2019), Grieshop et al. (2007), Vaden et al. (2011), Yli- Juuti et al. (2017), and D'Ambro et al. (2018).

Particle phase state is rarely, if at all, explicitly accounted for in aerosol modules present in atmospheric models to simulate the formulation and evolution of SOA or organic aerosol. This work suggests that a semisolid SOA, which is likely to be encountered at higher latitudes and altitudes (Shiraiwa et al., 2017), can have substantive effects on the evolution of the aerosol size distribution and subsequently exert an influence on aerosol-climate and aerosol-health interactions. We advocate for an explicit treatment of particle phase state in atmospheric models.

CHAPTER 4: Process-Level Modeling Can Simultaneously Explain Secondary Organic Aerosol Evolution in Chambers and Flow Reactors[3]

4.1 Introduction

Secondary organic aerosol (SOA), formed from the oxidation of volatile organic compounds (VOC), constitutes a large fraction of atmospheric fine particulate matter ($PM_{2.5}$), which has significant impacts on climate, air quality, and human health (Jimenez et al., 2009; Pachauri et al., 2014; Apte et al., 2018; Cohen et al., 2017; Shrivastava et al., 2017). Currently, there lacks a full understanding of SOA formation and evolution in the atmosphere, which has prevented us from accurately predicting its spatiotemporal distribution and properties, and assessing its environmental impacts (Pai et al., 2020; Hayes et al., 2015; Shrivastava et al., 2017).

Environmental chambers (ECs) and oxidation flow reactors (OFRs) are commonly used to study SOA formation over a wide range of photochemical ages. Most ECs are Teflon® bags with relatively large volumes (5-30 m^3), operated in batch or steady-state mode for several hours to up to a day (Ng et al., 2006; Hildebrandt et al., 2009; Zaveri et al., 2018; He et al., 2020). OFRs are small (~10 L) flow-through reactors that typically run in a steady state mode over short residence times (<2 minutes) (Kang et al., 2007; George et al., 2007; Lambe et al., 2011; Simonen et al., 2017; Xu and Collins, 2021). Photochemical aging timescales in ECs and OFRs are measured by the OH exposure, defined as the integrated OH concentration over experimental time. While ECs can typically simulate SOA formation up to about a day (OH exposure of 1.5×10^{11} molecules-s cm^{-3}), OFRs extend the formation and aging time to up to a few weeks by using higher oxidant concentrations (OH exposure of up to 2×10^{12} molecules-s cm^{-3}) (Kang et al., 2007; George et al., 2007; Smith et al., 2009; Lambe et al., 2011, 2015; Peng and Jimenez, 2020). Current atmospheric

[3] This work has been accepted at Environmental Science and Technology.

models predominantly rely on SOA mechanisms and parameterizations based on EC measurements of SOA properties (e.g., mass yield, composition, size distribution, hygroscopicity etc.) (Akherati et al., 2019; Pai et al., 2020), and only one study so far (Chen et al. (2013)) has used OFR data to validate these parameterizations. The synergistic use of EC and OFR data is challenging because: (1) the oxidation reactions and chemical pathways leading to SOA formation could vary between these reactors from differences in radical concentrations, (2) the timescales for gas- (i.e., homogeneous) and particle-phase (i.e., heterogeneous, condensed) chemistry, new particle formation, and gas/particle partitioning are very different in ECs and OFRs, and (3) both types of reactors exhibit experimental artifacts that bias SOA production, such as vapor and particle wall loss. Previous studies have shown that the oxidation pathways between ECs and OFRs are likely to be similar, despite differences in oxidant and radical concentrations (Bruns et al., 2015; Lambe et al., 2015; Peng and Jimenez, 2020). Here, we argue that a comprehensive and consistent treatment of the kinetic processes between ECs and OFRs will allow OFR data to be used to update and extend EC-based SOA parameterizations in atmospheric models.

The current treatment of the SOA-relevant kinetic processes in ECs and OFRs include: (1) particle and vapor wall loss (PWL and VWL); (2) gas/particle partitioning, which may be influenced by phase state; (3) heterogeneous oxidation; (4) new particle formation, or nucleation; and (5) condensed-phase reactions including particle-phase oligomerization. Both EC and OFR data are universally corrected for PWL (Ng et al., 2006, 2007; Chan et al., 2009; Hildebrandt et al., 2009; Chhabra et al., 2011; Bian et al., 2015; Nah et al., 2017; He et al., 2020; Akherati et al., 2020; He et al., 2021; Palm et al., 2016, 2018) but only a handful of studies have corrected for the influence of VWL in these reactors. For ECs, these studies have found that the VWL correction could increase SOA mass yields by a factor of four (Zhang et al., 2014). For OFRs, the influence

of VWL has been found small due to the short residence times (Palm et al., 2016). VOC oxidation under dry conditions has been shown to produce semi-solid/viscous SOA (Vaden et al., 2011; Virtanen et al., 2011; Abramson et al., 2013; Pajunoja et al., 2014), which can potentially slow down gas/particle partitioning and depress SOA formation (Zaveri et al., 2008; Shiraiwa and Seinfeld, 2012; Shiraiwa et al., 2017; Zaveri et al., 2018, 2020; He et al., 2021). This is of particular concern for OFR experiments where the timescales for partitioning for a semi-solid SOA might end up being much longer than the average residence time in the OFR. However, typical EC and OFR experiments uniformly assume a liquid phase state for SOA. Heterogeneous oxidation becomes important under higher OH exposures (>1 day) and has been shown to result in loss of aerosol mass in OFRs through fragmentation reactions followed by evaporation of the volatile products (Smith et al., 2009; Kroll et al., 2009; Palm et al., 2016; Hu et al., 2016; Ortega et al., 2016). While heterogeneous oxidation may be less important at the lower photochemical aging timescales employed in ECs (Hodshire et al., 2018), it needs to be accounted for over the multiday aging timescales attainable in OFRs. Nucleation is usually suppressed in seeded EC experiments, in large part owing to the use of substantial inorganic "seed" particle concentrations for SOA growth, but is important in both seeded and unseeded OFR experiments, where high oxidant concentrations and short residence times might create supersaturated conditions to initiate nucleation (Hodshire et al., 2018). Finally, oligomerization has been observed to contribute to SOA formation appreciably in EC experiments (Bakker-Arkema and Ziemann, 2020; Zaveri et al., 2020), and oligomers may contribute to semi-solid SOA phase state (Shiraiwa et al., 2017; He et al., 2021), but it is rarely considered in the development of EC-based SOA parameterizations, and rarely investigated in OFR studies. Furthermore, OFR studies rarely account for the interplay between oxidation chemistry and kinetic partitioning and their dynamic influence on nucleation.

In this study, we used a kinetic SOA model that simulates oxidation chemistry, thermodynamics, and microphysics (i.e., SOM-TOMAS (He et al., 2020; Akherati et al., 2020; He et al., 2021)) to comprehensively include the processes described above. To illustrate the utility of such a model approach, we applied the model to study SOA formation from α-pinene in both EC (Chhabra et al., 2010) and OFR (Lambe et al., 2015) experiments. We show that the gap between EC and OFR SOA mass yields, at least for this chemical system, can be bridged by accounting for these processes, and a single set of SOA parameters for photochemical aging can explain both EC and OFR SOA data.

4.2 Methods

4.2.1 SOM-TOMAS Model and Updates

The SOM-TOMAS model combines the Statistical Oxidation Model (SOM) (Cappa and Wilson, 2012; Jathar et al., 2015) and the TwO Moment Aerosol Sectional (TOMAS) model (Adams and Seinfeld, 2002). The SOM-TOMAS model simulates the gas-phase oxidation of the VOC and multi-generational gas- and particle-phase chemistry of the VOC's oxidation products and tracks the evolution of the particle size distribution subject to kinetic gas/particle partitioning, coagulation, wall loss, and nucleation. The gas-phase chemistry also includes direct formation of highly oxygenated organic molecules (HOM) to represent autoxidation reactions (Bianchi et al., 2019). Previously, the model has been extensively used to study SOA formation in EC and OFR experiments (He et al., 2021, 2020; Garofalo et al., 2021; Akherati et al., 2020; Eluri et al., 2018). Details of the SOM-TOMAS model have been described in these previous publications, but a brief model description is provided in Section C1 for completeness.

In this work, we updated the SOM-TOMAS model to account for heterogeneous reactions of SOA with the OH radical through the use of the reactive uptake coefficient (γ_{OH}), which

determines the fraction of collisions between OH radicals and particle surface which result in a chemical reaction. γ_{OH} can vary between 0 and up to 10 (Lambe et al., 2009; George and Abbatt, 2010), where values greater than 1 indicate conditions where the OH-initiated chain reactions in the particle phase result in the recycling of the OH radical (Hearn and Smith, 2006; George et al., 2007; Smith et al., 2009; Miracolo et al., 2010). As with gas-phase reactions, heterogeneous oxidation produces products from both functionalization (lower volatility) and fragmentation (higher volatility) reactions, with the latter able to evaporate. The detailed formulation for the loss rate of a particle-phase SOM species due to heterogeneous oxidation is described in the supporting information (Section C1).

We also updated the model to simulate nucleation in the OFR experiment (Lambe et al., 2015), where no seed aerosols were used and nucleation played a key role in SOA formation. Nucleation was modeled with four different schemes: (i) an instantaneous nucleation event at the beginning of the OFR simulation, (ii) a constant nucleation rate throughout the OFR simulation, (iii) a time-varying nucleation rate over the OFR simulation modeled as a Gaussian distribution, and (iv) a nucleation rate tied to the concentration of simulated extremely low-volatility organic compounds (ELVOCs; defined below). For (iii), we expected the nucleating species to initially increase in concentration to create supersaturated conditions that would drive nucleation, following which the nucleating species would decrease in concentration as it condensed onto the particles. We chose a Gaussian distribution to approximately mimic the increase and decrease in the nucleation species' concentrations. The time-varying nucleation rate (cm^{-3} s^{-1}) is expressed using the following equation:

$$J_{nuc} = \frac{T_{nuc}}{\sigma_{nuc}\sqrt{2\pi}} \cdot e^{-\frac{1}{2}\left(\frac{t-\mu nuc}{\sigma nuc}\right)^2} \qquad (4.1)$$

where t is the time since the entrance to the OFR in s, μ_{nuc} is the time corresponding to the peak nucleation rate in s, σ_{nuc} is the standard deviation of the distribution in s, and T_{nuc} is the total number of nucleating particles. These three parameters can be fitted to reproduce the observed particle size distributions in the OFR. The Gaussian shape was determined a priori. For (iv), the nucleation rate is determined using the following equation (Kirkby et al., 2016):

$$J_{nuc} = a_1 \cdot [ELVOC]^{a_2} \qquad (4.2)$$

where [*ELVOC*] is the gas-phase concentration of ELVOCs in 10^7 cm^{-3}, and a_1 and a_2 are adjustable parameters. Here, ELVOCs are limited to only include the gas-phase dimer species (C_{20}) formed from the oxidation of C_{10} SOM species at a molar yield of 0.2% (Zhao et al., 2018), as they are likely to be the main drivers for nucleation given their extremely low volatility ($<10^{-9}$ μg m^{-3}) (Heinritzi et al., 2020). The HOM monomers formed directly from autoxidation reactions were not included in the ELVOCs. The nucleated particles were always added to the smallest particle size bin in SOM-TOMAS (~1 nm) in all schemes.

4.2.2 α-Pinene SOA EC and OFR Data

We developed SOM-TOMAS parameters for α-pinene by simultaneously fitting the model to the measured SOA mass concentration and O:C ratio from an EC photooxidation experiment, performed and described in Chhabra et al. (2010). The EC photooxidation experiment, SOA data, and model fitting are briefly summarized in the supporting information (Section C2). The EC-based parameters were then used to simulate and evaluate the SOA formation and evolution in OFR α-pinene photooxidation experiments. We chose OFR experiments that were performed in the Potential Aerosol Mass (PAM) OFR (Lambe et al., 2015) since the results from these OFR experiments are generally consistent with other OFR studies on α-pinene for the SOA mass yield and chemical composition (Bruns et al., 2015; Friedman and Farmer, 2018).

The PAM OFR used in the studies described here is a 13 L pyrex cylindrical tube operated in continuous flow mode. In these OFR experiments, the residence time is distributed across 600 s with an average of 100 s, and OH radicals were generated inside the OFR by UV-photolysis of injected O_3 (λ=254 nm). The O_3 level inside the reactor was 15-30 ppmv and the RH was 30-40%. No NO_x was added to the reactor. No ammonium sulfate seed was used, so SOA was formed through nucleation and subsequent growth of pure SOA particles. The initial concentration of α-pinene was 50 ppbv, and six different OH exposures were achieved by stepping the UV light intensity. OH concentrations varied between 5.5×10^8 and 1.7×10^{10} molecules cm^{-3}, corresponding to OH exposures between 0.4 and 13.2 days of photochemical aging (assuming an OH concentration of 1.5×10^6 molecules cm^{-3}). Except for the lowest OH exposure, the OH concentrations were high enough compared to O_3 that α-pinene predominantly reacted with OH and not with O_3. At each OH exposure level, the SOA mass concentration, size distribution, and O:C ratio were quantified from measurements performed with a scanning mobility particle sizer (SMPS) and a high-resolution aerosol mass spectrometer (HR-AMS). The OH concentrations used in this work were updated from those reported in Lambe et al. (2015) by accounting for small amounts of OH suppression from the reactivity of the VOC (Section C3).

4.2.3 OFR Model Simulations and Sensitivity Tests

We systematically evaluated the influences from the different processes in OFR simulations by accounting for one process at a time, and the model configurations are listed in Table 4.1. Model A included gas-phase oxidation and kinetic gas/particle partitioning assuming a liquid D_b (10^{-10} m^2 s^{-1}). In models B through E, we progressively accounted for the following processes: PWL (model B), VWL (model C), semi-solid D_b (model D), oligomerization (model E), and heterogeneous oxidation (model F). Size-dependent PWL rates were estimated from

particle transmission efficiencies reported for the OFR (Section C4) (Lambe et al., 2011). The VWL rate ($k_{vap,on}$) in the OFR was assumed to be 2.5×10^{-3} s^{-1} (Palm et al., 2016). Assuming the vapors are lost to the pyrex walls of the OFR through adsorption instead of absorption into the surface, the release rate for vapors ($k_{vap,off}$) was assumed to be zero. The baseline D_b value for semi-solid α-pinene SOA was assumed to be 4×10^{-19} m^2 s^{-1}, consistent with those estimated recently through the use of kinetic models (Zaveri et al., 2020; He et al., 2021). The baseline γ_{OH} value for heterogeneous oxidation was assumed to be 1 (Kroll et al., 2009). Particle-phase oligomerization was simulated with the same baseline k_f and k_r values as those for the EC experiment (k_f =10^{-24} $molecules^{-1}$ cm^3 s^{-1}; k_r=1.6×10^{-2} s^{-1}) (He et al., 2021).

Nucleation was assumed to be instantaneous for models A through F and constant for model G. Models H and I use the time-dependent nucleation rates (J_{nuc}) calculated using equations 4.1 and 4.2, respectively. The nucleation rates for model A through G were tuned separately for each OH exposure to reproduce the measured total number concentrations. The J_{nuc} parameters in model H (μ_{nuc}, σ_{nuc}, *and* T_{nuc}) were optimized separately for each OH exposure to reproduce the measured number concentrations and number size distributions. The J_{nuc} parameters in model I (a_1 and a_2) were adjusted to optimize the model-measurement comparison for size distributions across all OH exposure levels simultaneously.

Table 4.1: Model configurations to simulate SOA in the OFR experiment. For Models A through F, processes of PWL, VWL, semi-solid D_b, oligomerization, and heterogeneous oxidation are progressively turned on/accounted for. For Model G through I, different J_{nuc} profiles are assigned. The normalized mean absolute errors (NMAE) for SOA mass yield, O:C and size distributions are shown.

Model	PWL	VWL	Semi-S.	Olig.	Het.	Nucleation	$NMAE_{Yield}$	$NMAE_{O:C}$	$NMAE_{Size}$
A	OFF	OFF	OFF	OFF	OFF	Instantaneous at t = 0	4.95	0.12	8.05
B	ON	OFF	OFF	OFF	OFF	Instantaneous at t = 0	1.57	0.16	1.66
C	ON	ON	OFF	OFF	OFF	Instantaneous at t = 0	1.36	0.18	1.54
D	ON	ON	ON	OFF	OFF	Instantaneous at t = 0	0.91	0.16	1.19
E	ON	ON	ON	ON	OFF	Instantaneous at t = 0	1.00	0.16	1.23
F	ON	ON	ON	ON	ON	Instantaneous at t = 0	0.28	0.11	0.93

G	ON	ON	ON	ON	ON	Constant over 100 s	0.24	0.12	0.76
H	ON	ON	ON	ON	ON	Equation 1 (Tuned)	0.16	0.15	0.53
I	ON	ON	ON	ON	ON	Equation 2 (Tuned)	0.22	0.13	0.68

The SOA at the OFR exit is a mixture of particle populations having experienced different residence times, as a result of the non-ideal flow inside the OFR. Therefore, we performed all model simulations for 600 s, and weighted the predictions by the observed residence time distribution (Lambe et al., 2011) to determine an average prediction for SOA mass, O:C ratio, and particle size distribution. All model-measurement comparisons in the results section were based on these weighted predictions. Also, using model I as the base case, we investigated model sensitivities with respect to the PWL and VWL rates, D_b, γ_{OH}, and oligomerization. The PWL and VWL rates were varied by a factor of three below and above the base values. D_b was varied between 10^{-10} m^2 s^{-1} (liquid-like) and 10^{-21} m^2 s^{-1} (nearly solid), as well as within the semi-solid range between 10^{-18} and 10^{-19} m^2 s^{-1}. γ_{OH} was varied between 0.1 and 5. k_f was increased by factors of 10 and 100 relative to the base value.

4.3 Results

4.3.1 Process-Level Contributions to SOA Mass, O:C, and Particle Size Distribution

The SOM-TOMAS model, with the EC-based SOA parameters, was run in different configurations to predict the SOA formation and evolution from α-pinene in the OFR photooxidation experiments. The various model predictions of the SOA mass yield, SOA O:C, and the evolving aerosol size distribution are compared against measurements in Figure 4.1. As described in Section 4.2.3, the different models, from A to F, additively captured the influence of a particular process/property (Table 4.1 for more information). The normalized mean absolute error (NMAE) values (mean of $(X_{mod} - X_{obs})/X_{obs}$, where X_{mod} and X_{obs} represent all modeled and

measured points, respectively) from the model-measurement comparison for SOA mass yield, O:C, and size distributions are also listed in Table 4.1.

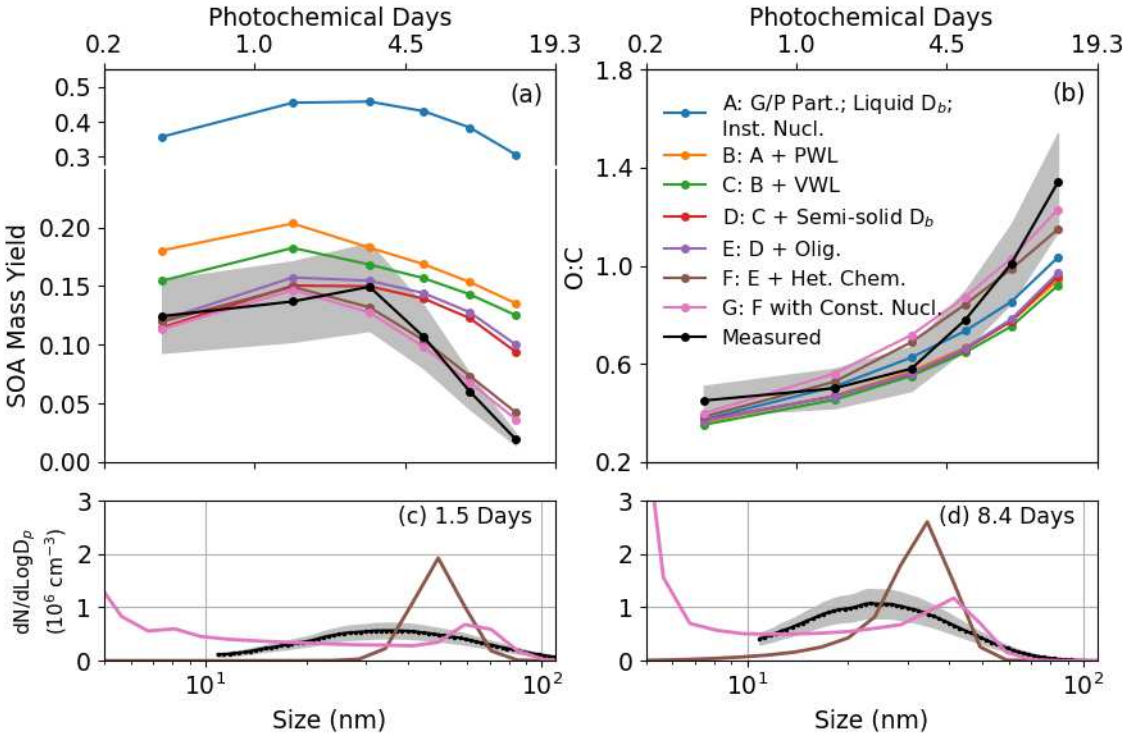

Figure 4.1: Simulated process-level contributions to OFR SOA and model-measurement comparisons for (a) SOA mass yield; (b) SOA O:C; (c, d) particle number size distributions at 1.5 and 8.4 days of photochemical aging, respectively. For the size distributions, only results from model F and G are shown to demonstrate the difference; the predicted size distributions from model A through E are similar in shape to that of F and shown in Figure C4. The grey bands represent the uncertainty shown as 1 standard deviation.

First, we consider models assuming a liquid-like SOA (D_b=10^{-10} m^2 s^{-1}) (A-C). Gas-phase chemistry and kinetic gas/particle partitioning (model A) overestimated the SOA mass yield over the six photochemical ages (factor of 3 at 0.4 days to a factor of 16 at 2 weeks of aging; NMAE=4.95). Including PWL (model B) reduced SOA formation by more than a factor of 3 on average (NMAE=1.57) compared to model A, in addition to slightly changing the trends with OH exposure. The SOA mass yields, however, were still overestimated on average by nearly a factor of 3 compared to the measurements. Accounting for VWL (model C) only marginally reduced SOA formation (<10%; NMAE=1.36). Taken together, models A through C suggest that wall

losses are an important artifact to consider when analyzing and modeling SOA mass yield, noting that in these experiments PWL was much more important than VWL in influencing SOA formation in OFRs.

The use of a semi-solid SOA (D_b=4×10^{-19} m^2 s^{-1}) in model D resulted in additional reduction in SOA formation (NMAE=0.91). This was presumably because a lower D_b resulted in a longer particle mixing timescale that slowed gas/particle partitioning and, in this case, the net condensation rate of SOA. For instance, for a 30 nm particle (representative of the number mode in the final particle size distribution measured in this work), the particle mixing timescale changes from 1 μs to 4 minutes as the D_b changes from 10^{-10} to 4×10^{-19} m^2 s^{-1}, respectively. Because the mixing timescales for a semi-solid aerosol are comparable to typical OFR residence times, SOA mass yield measurements in OFRs are potentially more sensitive to the SOA phase state than those in ECs, where similar changes in D_b (from 10^{-10} to 4×10^{-19} m^2 s^{-1}) have been shown to have a negligible effect (He et al., 2021; Jathar et al., 2021). Moreover, in the OFR simulations, the longer particle mixing timescales in the semi-solid SOA kept the condensable oxidation products in the gas phase for long enough that they were oxidized to form fragmented, more volatile products; the average O:C of the gas-phase products was 0.4 for the lowest OH exposure, for which the probability of fragmentation was 95%, based on the fitted SOM m_{frag} parameter (see Section C1 and Figure C1). This additional oxidation would tend to further reduce SOA mass yields. These results indicate that while a semi-solid aerosol may not be of much concern in ECs, where the experiments are sufficiently long for the gas and particles to reasonably equilibrate, a semi-solid aerosol might influence SOA formation in OFRs due to the short residence time experienced.

Accounting for oligomerization in model E slightly increased the SOA mass yields in comparison to model D (NMAE=0.91 to 1.00) where the oligomers accounted for between 14 and

25% of the total SOA over all OH exposures. The small increase in SOA mass yields was because the oxidation products in the condensed phase already had low volatilities, so oligomer formation did not additionally shift partitioning to the particle phase. These results suggest that although a modest fraction (14-20%) of SOA mass was composed of oligomers, which formed quickly in the OFR and was consistent with previous studies (Heaton et al., 2007, 2009; Zaveri et al., 2020; He et al., 2021), oligomerization was unlikely to shift gas/particle partitioning and affect total SOA formation in the OFR experiment.

The inclusion of heterogeneous oxidation in model F only marginally changed the SOA mass yields for the lower OH exposures (<2 days), but substantially reduced those at higher exposures (>2 days), resulting in close agreement with the measurements (NMAE=0.28). The decrease in the SOA mass yield principally stemmed from the oxidation of high O:C material in the particle phase that was susceptible to fragmentation, and which ultimately resulted in loss of SOA mass in the OFR. This is in line with Kroll et al. (2009), who also attributed observed OA mass reduction in OFRs at higher exposures to fragmentation reactions driven by heterogeneous oxidation. We should note that the model predicted an earlier decrease in the SOA mass yield compared to the measurements (1.5 versus 3 days), and slightly overestimated the O:C ratios in the same OH exposure range. This could possibly be due to uncertainties in the estimated OH concentrations (Section C3), as well as from the assumptions made for heterogeneous oxidation (i.e., γ_{OH}=1 and the same SOM parameters as those assumed for gas-phase oxidation). In Figure C3, we show the temporal evolution of SOA mass concentrations as a function of residence time at different OH exposures for simulations performed with model F. For higher OH exposures (>2 days), the model predicted the maximum SOA approximately one third of the way through the OFR and continued oxidation of the gas- and particle-phase material resulted in mass loss over the

remainder of the OFR. While fragmentation of gas-phase oxidation products does seem to decrease the SOA mass yield with OH exposure, as seen in predictions from models A through E, heterogeneous oxidation adds substantially to the mass loss and further steepens the decrease in SOA mass yield at higher OH exposures.

Models A through E predicted an increasing SOA O:C with OH exposure and the predictions of SOA O:C varied only marginally between models B through E (Figure 4.1(b)). The SOA formation and evolution in these simulations understandably followed very different chemical trajectories and, hence, it was interesting that they predicted roughly the same O:C evolution despite substantial differences in the predicted SOA mass yields. Generally speaking, these SOA O:C predictions for models A through E were slightly lower than the measured value at the lowest OH exposure (~0.4 day), consistent with measured values at intermediate OH exposures (~1 to 3 days), and lower than the measured values at the higher OH exposures (>4 days) (average NMAE=0.16). The SOA O:C predictions appeared to increasingly deviate from the measurements at higher OH exposures for models A through E. With the inclusion of heterogeneous oxidation, model F provided a better comparison with the measured O:C values (NMAE=0.11) although there were some differences in the shape of the predicted and measured change in O:C with OH exposure (Figure 4.1(b)); the predicted O:C increased somewhat linearly while the measured O:C increased exponentially over a logarithmic OH exposure scale.

With models A through F, we assumed nucleation to occur instantaneously at the beginning of the OFR simulation. Model G, which assumes nucleation occurs at a constant rate throughout the OFR residence time, predicted a nearly identical SOA mass yield and O:C as that from model F. However, Models F and G produced a very different evolution in the particle number size distribution, which is discussed in the paragraph below.

Figures 4.1(c) and 4.1(d) compare the modeled number size distributions from models F and G against the measurements at 1.5 and 8.4 days of photochemical aging. Predictions from models A through E and at other photochemical ages are omitted for visual clarity; the full comparison for all photochemical ages and model configurations is presented in Figures C4 and C5, for number and mass size distributions, respectively. Another reason for not showing the predictions for models A through E was that, on account of overestimating the SOA mass yield, the predicted number size distributions from these models were shifted to much larger sizes and therefore they did not compare well against the measurements. Model F resulted in much narrower number size distributions compared to measurements. This narrowing is characteristic of particle growth associated with low-volatility SOA and a semi-solid phase state, since both tend to contribute to the preferential growth of smaller over larger particles (Shiraiwa and Seinfeld, 2012; Zaveri et al., 2018, 2020; He et al., 2021). If instead we assumed constant nucleation throughout the OFR simulation, as in model G, the simulations predicted a bimodal number size distribution with a smaller mode that coincided with the size at which particles were assumed to nucleate in the model (1 nm) and a larger mode with a mode diameter that varied between 40 and 60 nm, depending on the OH exposure. For all OH exposures, the modeled number size distribution had a long leading edge that spanned between particle diameters of 5 nm and ~50 nm that was presumably a result of the constant nucleation and growth throughout the OFR. Regardless, none of the predicted number size distributions at any of the OH exposures from models F and G agreed with the measurements. Assuming that the results from models F and G approximately bound the influence of nucleation (instantaneous versus uniformly distributed), the following section investigates the effect of time-dependent nucleation on the model-measurement comparison.

4.3.2 Role of Nucleation on the Particle Size Distribution Evolution

In models H and I, we used a time-dependent nucleation profile (J_{nuc}) that was optimized in different ways to improve the model-measurement comparison with an emphasis on the particle number size distribution. Results from models H and I, in addition to those from models F and G, are shown in Figure 4.2. We only show the size distribution comparisons for photochemical ages of 1.5 and 8.4 days, and the full comparison for all six photochemical ages can be found in Figures C6 and C7, for number and mass size distributions, respectively.

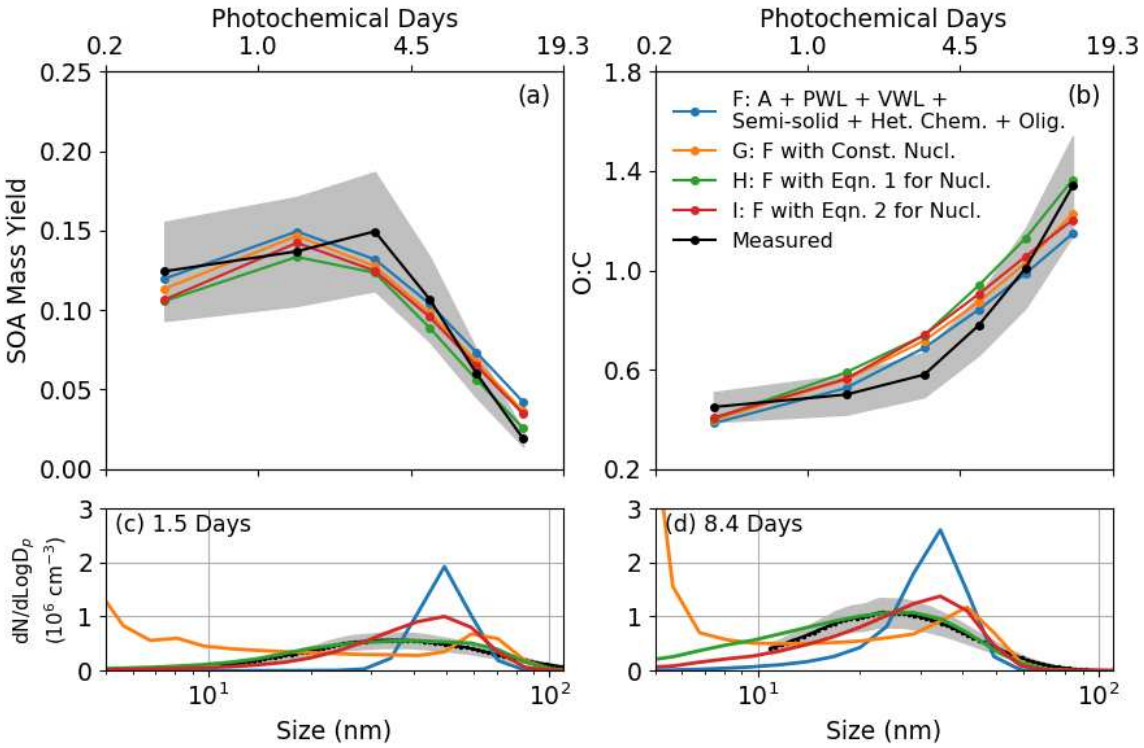

Figure 4.2: Influence of nucleation scheme on model predictions. Model-measurement comparisons are shown for (a) SOA mass yield; (b) O:C; (c) and (d) particle size distributions at 1.5 and 8.4 days of photochemical aging, respectively. The grey bands represent the uncertainty shown as 1 standard deviation.

In model H, we adjusted the J_{nuc} profile at each OH exposure to reproduce the observed evolution in the number size distribution. The optimal J_{nuc} profiles with the assumed Gaussian distribution are shown in Figure C6 and also in Figure C7. By design, simulations performed with model H resulted in vastly improved predictions of the number size distribution (Figures 4.2(c)

and 4.2(d)) (NMAE=0.53), compared to models F and G (NMAE=0.93 and 0.76, respectively). The optimal J_{nuc} profiles showed that the peak in nucleation was delayed in these OFR experiments ($\mu_{nuc} > 0$), with longer delays experienced at the lower OH exposures (e.g., 50 s at 0.4 days) and shorter delays at higher OH exposures (e.g., 17 s at 5.4 days and above) (Figure C10). An inverse relationship between the OH exposure and nucleation delay might suggest that higher OH concentrations are needed to produce lower-volatility oxidation products sooner that can subsequently aid to form new particles. Overall, these results highlight that the measurements of the evolution of the particle size distribution as a function of OH exposure can be used to constrain the timing and magnitude of nucleation in an OFR. However, the optimal timing of nucleation implied here was surprising, because it did not follow the gas-phase concentrations of HOM or the functionalized first-generation products from α-pinene oxidation ($C_{10}O_1$ through $C_{10}O_4$) (Figure C6). Since nucleation is expected to be highly correlated with the gas-phase concentration of the nucleating low-volatility species, our results indicate that the nucleating species are unlikely to be first-generation products but instead are products of multi-generational chemistry. Additionally, heterogeneous oxidation had a large impact on the final particle size distribution in the OFR at higher OH exposures. As shown in Figure C11, at the highest OH exposure, the SOA concentration first increased and then decayed away with time. The corresponding particle size distribution first grew to a larger size, and the larger particles quickly lost mass to make the size distribution shift to smaller particle sizes.

In model I, we linked J_{nuc} to ELVOC concentrations (as per equation 4.3) and manually adjusted the pre-factor (a_1) and exponent (a_2) values to best reproduce the observed evolution in the number size distribution; the optimal values for a_1 and a_2 were 20 and 1.7, respectively. The J_{nuc} profiles from model H and I are shown in Figure C7 alongside the ELVOC concentrations.

When compared to model H, the number size distribution predictions from model I were shifted to larger sizes for all OH exposures, and hence, these predictions did not agree as well with the measurements as those from model H. However, the predicted shape of the number size distribution from model I was much closer to the measurements than those from models F and G (NMAE=0.68). The shifts in the number size distribution to larger sizes for model I were directly related to the J_{nuc} profiles that peaked earlier compared to the optimal J_{nuc} profiles from model H (Figure C7). Our results provide evidence that the low-volatility, gas-phase dimers formed from functionalized products of α-pinene oxidation may be responsible for the formation and growth of new particles while also suggesting that the first-generation oxidation products, including HOMs, were relatively too volatile to initiate nucleation.

While the number size distribution data provided constraints on nucleation, models H and I had a relatively small impact on model predictions of SOA mass yield and O:C. When compared to models F and G, models H and I resulted in only 6-18% lower SOA mass yields at all OH exposures (Figure 4.2(a)) and produced slightly better agreement with the measurements (NMAE=0.19 and 0.26, respectively). Model H resulted in a higher SOA O:C compared to models F, G, and I and agreed less with the measurements (NMAE=0.15). The small SOA mass yield and O:C differences between models H and I and models F and G can be explained by examining the optimized J_{nuc} profiles. Since a delay in nucleation limited the condensational sink prior to nucleation, this delay resulted in continued gas-phase oxidation of the condensable products with high O:C, leading to the production of more fragmented, volatile, and oxygenated species. Thus, the nucleation delays in models H and I resulted in lower SOA mass yield and higher SOA O:C predictions compared to models F and G. We also note that the models (F, G, H, and I) performed less well in matching the mass size distributions, as shown in Figure C7, by overpredicting the

mass at smaller sizes (~50-100 nm) and underpredicting the mass at larger sizes (~100-200 nm). This potentially indicates an overestimation of the particle-phase diffusion limitation at the larger sizes, as a result of assuming a uniform D_b across all sizes. A size dependent D_b should be investigated in future work.

In summary, our model results showcased in Figure 4.2 support the hypothesis that a single set of SOA parameters can be used to describe SOA formation in ECs and OFRs if we consistently account for the influence of wall losses, aerosol phase state, oligomerization, heterogeneous oxidation, and nucleation. In contrast, overly simplistic SOA models (e.g., ones that assume liquid-like particles and instantaneous partitioning) inhibit translation of results between ECs and OFRs, and thus also complicate application in atmospheric models.

4.3.3 Model Sensitivity to the Kinetic Processes

Figure 4.3 shows the impacts of varying the key parameters investigated here: PWL and VWL rates, D_b, and γ_{OH}. PWL was especially important because the timescales for PWL for the Aitken mode particles (e.g., 100 s for 50 nm particles) were consistently shorter than those for VWL explored here (130 to 1200 s). The absolute influence of both diminished at higher OH exposures as other processes became more dominant (e.g., gas-phase and heterogeneous oxidation). The SOA O:C was mostly insensitive to varying the VWL and PWL rates, possibly because the O:C is primarily driven by the very high OH concentrations. A nearly-solid D_b reduced SOA mass yields by >50%. A liquid D_b only strongly increased SOA mass yields at lower OH exposures (<2 days), with higher exposures (>2 days) resulting in weak change in the SOA mass yield. This was likely because, at higher OH exposures, a liquid D_b allowed for more rapid evaporation of volatile SOA species formed from heterogeneous oxidation, which offset the increase in the SOA mass yield from condensation of gas-phase oxidation products. Varying the D_b within the semi-solid

range (10^{-18} to 10^{-19} m^2 s^{-1}) only resulted in small deviations in SOA mass yield (<20%) from the base case. The SOA O:C predictions were slightly more sensitive to D_b than to the PWL and VWL rates. Varying the γ_{OH} was extremely impactful at higher OH exposures (>3 days). This highlights the relatively important role of modeling heterogeneous oxidation in OFRs, especially at longer photochemical ages. As shown in Figure C9, the modeled SOA mass yields were only meaningfully sensitive to the treatment of oligomerization when k_f was at least 10 times faster than the base value of 10^{-24} cm^3 s^{-1}. These large k_f values are likely too fast and inconsistent with model-estimated (He et al., 2021) or measured (Bakker-Arkema and Ziemann, 2020) condensed-phase oligomerization rates, barring those when the aerosol is acidic (Roldin et al., 2014).

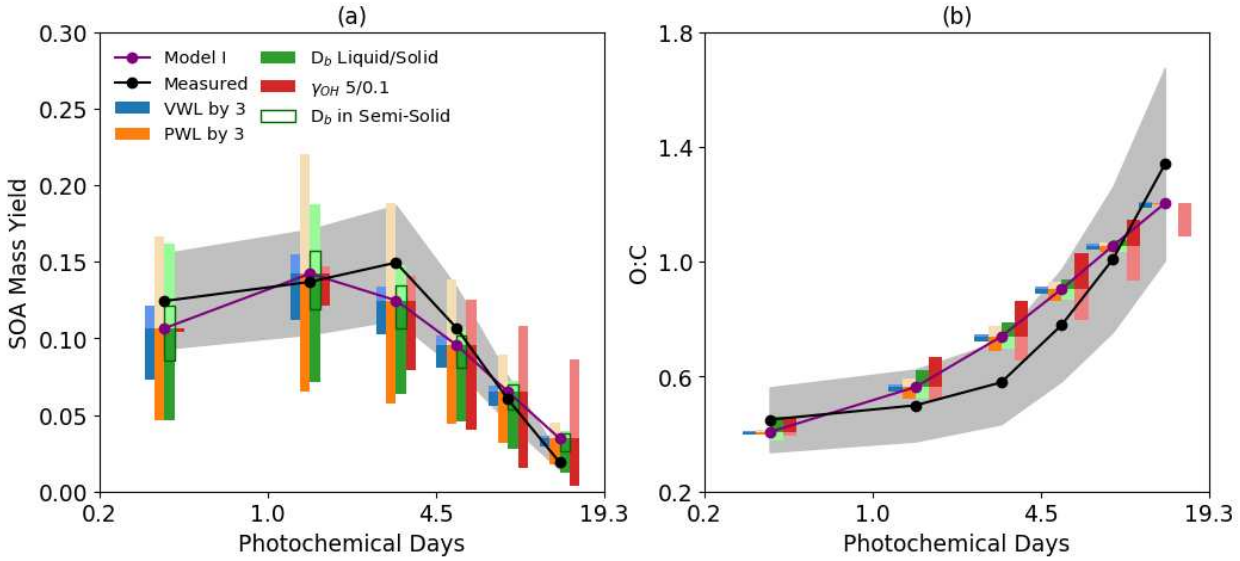

Figure 4.3: Sensitivity simulations based on model I with respect to variability in VWL and PWL rates by a factor of three, limiting cases for D_b under liquid (D_b=10^{-10} m^2 s^{-1}) and nearly solid (D_b=10^{-21} m^2 s^{-1}) phase states, as well as in the semi-solid range (D_b=10^{-18} and 10^{-19} m^2 s^{-1}), and limiting cases for γ_{OH} of 0.1 and 5. The darker bars represent increases in PWL and VWL rates, particle viscosity (i.e., lower D_b) and γ_{OH}, and the lighter bars represent the opposite. Model-measurement comparisons are shown for (a) SOA mass yield and (b) O:C. The grey bands represent the uncertainty shown as 1 standard deviation.

4.4. Discussion and Atmospheric Implications

In this work, through a synergistic use of EC and OFR data, we were able to develop a single set of parameters to explain the SOA processes in both reactors and, in turn, develop robust

parameterizations for use in atmospheric models for an important biogenic VOC (i.e., α-pinene). In future work, we will aim to use this framework to develop similar parameterizations for other important SOA precursors (e.g., isoprene, alkanes, aromatics) over oxidative aging timescales that are relevant in the atmosphere.

We were able to investigate the impact of various processes on SOA formation and aging in OFRs. Below, we discuss these impacts and, occasionally, compare these to those estimated in ECs. We found that the losses of particles to the walls (PWL) were very important in predicting the observed SOA mass yields in OFRs. Accounting for size-dependent PWL in OFRs affected the SOA mass yields by about a factor of 3, compared to a factor of ~1.2 in ECs (He et al., 2020). Hence, future OFR studies need to carefully characterize size-dependent PWL rates and account for those rates in estimating SOA mass yields and properties. In contrast, irreversible vapor losses to the walls of the OFR (VWL) were found to be much less important (~10% decrease in SOA mass yields), noting that reversible losses will tend to have an even smaller impact. The VWL rate used in this work was from Palm et al. (2016), who assumed a coefficient of eddy diffusivity (i.e., k_e) of 0.0036 s^{-1}. Scaling the k_e up by a factor of 10 would only result in about a three-fold increase in the VWL rate (the VWL rate scales with the square root of k_e (McMurry and Grosjean, 1985a)), which is unlikely to strongly affect the SOA formation and evolution, as shown in Figure 4.3. This finding for OFRs contrasts with large estimated VWL effects on SOA mass yields in EC studies (Zhang et al., 2014).

A semi-solid D_b between 10^{-18} and 10^{-19} m^2 s^{-1}, which typically has a very small impact on the SOA mass yields in an EC (He et al., 2021), meaningfully reduced SOA mass yields in the OFR (~30% decrease), indicating that aerosol phase state is an important property to account for when estimating SOA mass yields in OFR experiments. Also, the semi-solid phase state of aerosols

was found to resist the growth of SOA through condensation and resist SOA loss at higher OH exposures through heterogeneous oxidation and evaporation. This interplay between physical and chemical properties to control the SOA fate highlights the need for a process-level representation of phase state in OA and aerosol models.

Heterogeneous oxidation, much more so than gas-phase fragmentation, was vital in explaining the observed loss in SOA mass and the increase in SOA O:C at higher OH exposures in the OFR (>3 days). Based on this result, one would expect heterogeneous oxidation to be equally important in determining the abundance and properties of global OA, knowing that OA has a lifetime between 1 and 2 weeks (Hodzic et al., 2016; Pai et al., 2020). The parameters developed in this work to represent heterogeneous oxidation could be valuable in examining the influence of this process in three-dimensional models.

Nucleation and its timing inside the OFR were found to be critical in reproducing the shape and evolution of the particle size distribution. However, the optimal timing for nucleation was delayed with respect to the peak gas-phase concentrations of the first-generation oxidation products and HOM, the latter of which have been implicated in aiding nucleation (Bianchi et al., 2019). It is possible that the elevated HO_2 levels in the OFR suppressed autoxidation reactions and HOM production and this might be one reason why HOM did not contribute to nucleation in these OFR experiments. Our work suggests that the ELVOCs responsible for nucleation are likely formed from multiple generations of oxidation, as opposed to being a first-generation autooxidation product. This is consistent with Henrtizi et al. (2020), who pointed to the gas-phase C_{20} dimers from *a*-pinene oxidation as the main contributor to nucleation. These C_{20} dimers may take multiple generations to form in the OFR when autooxidation is suppressed.

The interplay between individual processes was found to be quite important. For example, the semi-solid phase state of aerosols was found to resist the growth of SOA through condensation and resist SOA loss at higher OH exposures through heterogeneous oxidation and evaporation. Also, the fast photooxidation and heterogeneous oxidation rates at the higher OH exposures were found to diminish the impact of the wall loss processes. This interplay between different processes to control the SOA fate highlights the need for a process-level representation of OA in aerosol models. Some previous studies have used kinetic models to examine the interplay between these processes (Shiraiwa and Seinfeld, 2012; Shiraiwa et al., 2013a), but more future studies will be needed to clarify the coupled effects, especially in OFRs.

In this work, we assumed the OH-driven oxidation chemistry (specifically, the gas-phase reaction products and their yields) leading to SOA formation to be similar between the EC and OFR. There is indirect evidence for this in the literature that has shown favorable comparisons between HR-AMS mass spectra for SOA formed in an EC and OFR (Lambe et al., 2015; Bruns et al., 2015) and consistency in the modeled fates of the peroxy radicals (RO_2) in theoretical EC and OFR simulations (Peng and Jimenez, 2020). That the same set of parameters were able to simulate the observed SOA formation in both EC and OFR experiments provides additional evidence for the oxidation chemistry to be similar in these two reactors. To study the fate of RO_2 radicals in the EC and OFR experiments used in this work, we performed additional simulations with the Master Chemical Mechanism (v3.3) model (Section C3). We found that in both the EC and OFR experiments, the RO_2 fate was dominated by RO_2+HO_2 reactions (>95% for EC and 55-75% for OFR) and RO_2 loss was negligibly controlled by RO_2+RO_2 or RO_2+OH reactions (Figure C13). In these simulations, we did not account for RO_2 isomerization reactions that could compete with RO_2+HO_2 reactions, noting that RO_2 isomerization might be more important in ECs over OFRs.

Furthermore, we assumed α-pinene to exclusively react with OH, but competition from O_3 was found to be significant at the lowest OH exposure (Figure C14). We performed simulations at the lowest OH exposure to additionally model SOA formation from α-pinene+O_3 using parameters published in our previous work (He et al., 2021). These simulations assumed that the first-generation oxidation products from α-pinene+O_3 were further oxidized by OH. We found that including α-pinene+O_3 reactions resulted in a small change in the SOA mass yield (Figure C15) likely because the first-generation oxidation products from OH and O_3 oxidation were likely very similar. The SOM-TOMAS model currently does not account for aqueous processing (McNeill, 2015) or photolysis (Zawadowicz et al., 2020) of organic compounds and the influence of these processes needs to be examined in the future.

To investigate the influence of various process-level assumptions on the SOA mass yield in the atmosphere, we performed pseudo atmospheric (PA) simulations using the final set of parameters informed by model I, as shown in Figure 4.4; details for these simulations are in the supporting information (Section C5). Condensation of SOA to a liquid-like background aerosol (PA1) resulted in an SOA mass yield that varied between 0.18 and 0.3. The use of a semi-solid aerosol (PA2) produced a lower SOA mass yield over the first few hours of photochemical aging but the predictions ultimately converged with those for the liquid-like aerosol after about 8 hours of aging, consistent with Jathar et al. (2021) When heterogeneous oxidation was turned on (PA3), the SOA mass yield was similar to the PA2 case for 1 day of photochemical aging but resulted in a rapid decrease thereafter. For an absorbing seed aerosol in the Aitken mode (instead of the accumulation mode assumed in PA1 through PA3), the effect of heterogeneous oxidation on the SOA mass yield and O:C was even more pronounced. Although idealized, these pseudo atmospheric simulations clearly highlight the important role phase state, heterogeneous oxidation,

and background particles play in controlling the SOA abundance and properties over short and long photochemical ages.

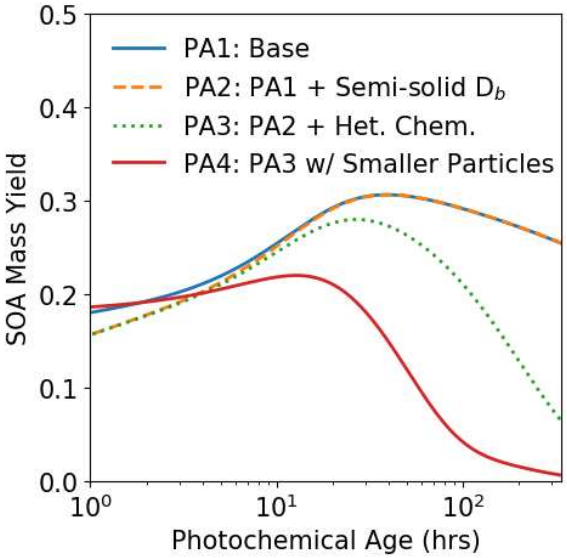

Figure 4.4: Pseudo atmospheric simulations to predict SOA mass yield under different scenarios. PA1 assumed only gas-phase oxidation and liquid aerosol; PA2 used a semi-solid phase state (D_b=4×10^{-19} m^2 s^{-1}); PA3 turned on heterogeneous oxidation; and PA4 is a variant of PA3 with smaller particles (30 nm vs. 100 nm) while conserving the background OA loading.

It is well understood that the timescales for various aerosol processes, and therefore the formation, evolution, and properties of SOA in ECs, OFRs, and in the real atmosphere, are quite different. Hence, it follows that SOA yields and properties from ECs and OFRs may not be directly comparable even if compared at the same oxidant exposures. In the future, we recommend it would be prudent to use kinetic models, such as those used in this work, to interpret experimental results from ECs and OFRs before those data are translated for use in atmospheric models.

CHAPTER 5: Vapors Are Lost to Walls, Not to Particles on the Wall: Development of Artifact-Corrected Parameters from Chamber Experiments and Implications for Global Secondary Organic Aerosol[4]

5.1 Introduction

Secondary organic aerosol (SOA), formed through the atmospheric oxidation of volatile organic compounds (VOCs), makes up a significant fraction of fine particulate matter ($PM_{2.5}$) (Jimenez et al., 2009; Shrivastava et al., 2017) and consequently has adverse impacts on climate, air quality, and human health (Apte et al., 2018; Stocker et al., 2013). Chemical transport models (CTMs) typically account for SOA formation using simplified parameterizations, derived from environmental chambers that are subject to experimental artifacts (Charan et al., 2019). The wall-related artifacts include (1) losses of particles to the walls (PWL), (2) losses of vapors to the particles on the wall (V2PWL), and (3) losses of vapors to the wall directly (VWL) (Figure 5.1). While all pathways may impact SOA formation in the chamber, PWL is the only pathway that is routinely accounted for. V2PWL is frequently accounted for with key assumptions but only a handful have accounted for VWL (Charan et al., 2019).

PWL rates, modulated by particle size, particle charge, and chamber conditions, can be directly measured under dark conditions (Pierce et al., 2008; Nah et al., 2017; Charan et al., 2018). The measured loss rates are then used to estimate the amount of SOA deposited on the wall. Subsequently, the PWL estimate is added to the suspended SOA measurements to determine the corrected SOA mass concentrations. Some have speculated that condensable SOA vapors can also be lost to wall-deposited particles (i.e., V2PWL) (Weitkamp et al., 2007; Hildebrandt et al., 2009; Liu et al., 2015). These and many earlier chamber studies have assumed that there are no mass

[4] Dr. Kelsey Bilsback and I equally contributed to this work. This work will be submitted to Environmental Science and Technology.

transfer limitations for V2PWL. Therefore, SOA mass concentrations are corrected by assuming that the gas-particle partitioning to particles on the wall proceeds in a manner similar to partitioning on suspended particles (Hildebrandt et al., 2009).

VWL is an important loss process for vapors across a wide range of volatilities (C^* of 1 to 10^6 μg m^{-3}) (Matsunaga and Ziemann, 2010; McVay et al., 2014; Zhang et al., 2014; Krechmer et al., 2016; Nah et al., 2016; Huang et al., 2018). These losses, which likely scale with the surface-area-to-volume ratio of the chamber and the presence of active mixing, tend to depress SOA formation (Brune, 2019). Measured timescales (e-folding) of VWL rates vary from more than five minutes (5-10 m^3 chamber) (Krechmer et al., 2016) to up to an hour (~30 m^3 chamber) (Zhang et al., 2014). Using process-based models, several studies have simulated VWL to develop VWL-corrected SOA parameters (Zhang et al., 2014; Nah et al., 2016; Bertrand et al., 2018; He et al., 2020). When used in 3D models, Cappa et al. (2016) and Akherati et al. (2019) showed that VWL-corrected parameters increased SOA mass concentrations by factors of ~2-10 and brought model predictions closer to ambient measurements in southern California. Similarly, Hodzic et al. (2016) demonstrated that accounting for VWL increased global OA estimates by up to ~10 μg m^{-3} in heavily forested regions.

Correctly accounting for chamber artifacts is critical to modeling the evolution and impacts of SOA and OA in the atmosphere. In this work, we present a systematic method for developing artifact-corrected SOA parameters from chamber studies and demonstrate the impacts of updating the parameters in GEOS-Chem. First, we used the Statistical Oxidation Model (SOM) with a TwO-Moment Aerosol Sectional (TOMAS) model and data from chamber experiments to develop artifact-corrected SOA parameters for important precursors (i.e., terpenes, aromatics, and intermediate volatility organic compounds (IVOCs)) (Section 5.2). Second, we ran pseudo

'atmospheric' simulations using the artifact-corrected SOA parameters and used the output to develop volatility basis set (VBS) parameters at atmospherically relevant OA mass concentrations (Section 5.3). Third, we implemented the updated VBS parameters in GEOS-Chem to evaluate how artifact corrections impact global OA and model-measurement agreement (Section 5.4). Sections 5.2-5.4 include both a description of the Methods as well as the Results & Discussion for each of the models, while Section 5.5 describes the implications of our results for future atmospheric SOA modeling. Our study highlights that VWL impacts SOA formation in environmental chambers to a much greater extent than PWL and that V2PWL can likely be ignored.

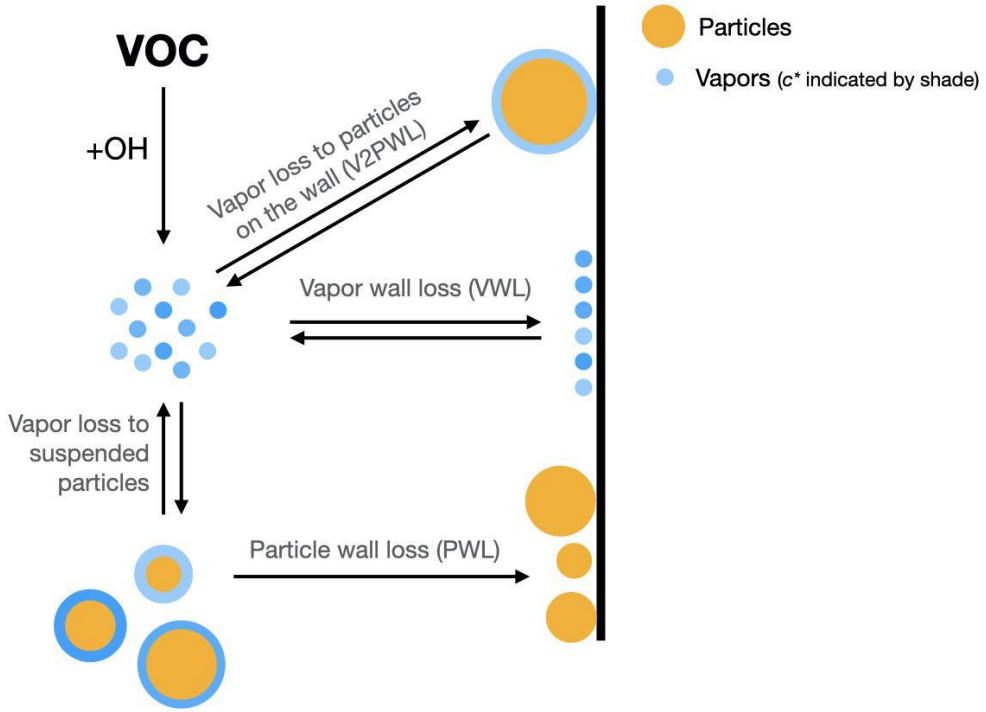

Figure 5.1: Schematic demonstrating experimental artifacts that impact particles and vapors in chamber experiments.

5.2 Artifact-corrected SOA Parameters Developed with SOM-TOMAS

We used SOM-TOMAS to model previously published chamber experiments (Chan et al., 2009; Chhabra et al., 2011; Ng et al., 2006, 2007). SOM-TOMAS has been described in detail in

previous work (Akherati et al., 2020; He et al., 2020, 2021). Briefly, SOM uses a statistical approach to represent the multi-generational oxidation chemistry of VOCs and their oxidation products and calculates the thermodynamic properties needed to inform gas-particle partitioning (Cappa and Wilson, 2012; Jathar et al., 2015). SOM tracks the chemistry using a two-dimensional grid for carbon and oxygen number. The carbon numbers on the grid are limited to the carbon number of the VOC and the oxygen numbers are limited to 7. The properties of each model species (e.g. reactivity (k_{OH}), volatility (C^*)) are parameterized based on the compound's carbon and oxygen numbers. TOMAS, meanwhile, tracks the number and mass moments of the aerosol size distribution using a sectional approach. TOMAS simulates nucleation, coagulation, condensation, and evaporation (Adams and Seinfeld, 2002; Pierce and Adams, 2007). In this work, the particle-phase species from SOM are tracked in 36 TOMAS size sections between 3 and 1,000 nm.

In SOM-TOMAS, PWL is simulated using a size-dependent kernel based on measurements of the loss of ammonium sulfate seed particles to the chamber wall (Ng et al., 2007). The same size-dependent kernel was used to model PWL for all chamber experiments (details below) since the kernels from different chamber studies were found to be nearly identical to each other (Figure D1). All of the chamber experiments used in this work were performed in the same set of chambers at the California Institute of Technology (Caltech) over a five-year period.

Historically, V2PWL has been accounted for empirically by assuming that the condensable SOA vapors inside the chamber partition to both the suspended SOA and the SOA deposited on the walls, following the same physics. This assumes that there are no mass transfer limitations for the SOA vapors to condense to the wall-deposited SOA. Theoretically, the condensation of vapors onto suspended particles is controlled by the condensational sink offered by the suspended particles, while the kinetics of vapors condensing onto wall-deposited particles is controlled by the

coefficient of eddy diffusion and the condensational sink offered by the wall-deposited particles. Using this postulation, we derive two equations to represent the flux rate of V2PWL with and without the mass transfer limitation. In our 'unrealistic' formulation, we assume that vapors partition to the wall-deposited particles as if they were suspended and that there is no mass transfer limitation, while in our 'realistic' formulation, we describe the loss rate of vapors to wall-deposited particles with the mass transfer limitation included. For simplicity, we assume that the particles deposited to the walls retain their spherical size and morphology (SOA coating on an ammonium sulfate seed particle) and have point contact with the wall; model sensitivity simulations and results that test the validity of the point-contact assumption are described later in this section. The governing equations and model implementation for the realistic formulation are described in detail in the supporting information (D1).

VWL is simulated in SOM-TOMAS as described in our earlier work (He et al., 2020; Akherati et al., 2020) and based on the methods presented in Matsunaga et al. (2010), Zhang et al. (2014), and Krechmer et al. (2016). Briefly, the first-order uptake of vapors to the chamber walls is assumed to be equal to $k_{vap,on}$ and the release of vapors from the walls is modeled using absorptive partitioning theory with the Teflon wall serving as an absorbing mass with an effective mass concentration of C_w in mg m^{-3}. $k_{vap,on}$ is assumed to be 4×10^{-4} s^{-1} for the Caltech chamber following Huang et al. (2018). Based on the observations of Krechmer et al. (2016), C_w is varied with the C^* of the model species, with higher values used for more volatile species (e.g., C_w=10 mg m^{-3} for $C^*>10^4$ µg m^{-3}) and vice versa (e.g., C_w=0.016 mg m^{-3} for $C^*<1$ µg m^{-3}).

We used SOM-TOMAS to model SOA formation in photooxidation experiments for seven SOA precursors performed in environmental chambers: α-pinene was from Chhabra et al. (2011); limonene and β-caryophyllene were from Ng et al. (2006); benzene, toluene, and m-xylene were

from Ng et al. (2007); and naphthalene was from Chan et al. (2009). The details of these experiments are in Table D2. We chose to include these seven precursors because they are represented in GEOS-Chem using VBS parameters. We modeled both low- and high-NO_x experiments for all precursors except limonene, where only high-NO_x experiments were conducted. For the low-NO_x experiments, we additionally included the formation of highly oxygenated organic molecules (HOMs) formed via autoxidation reactions in SOM-TOMAS. HOM yields were directly specified (i.e., not fit) based on the compilation of studies reported by Bianchi et al. (2019); 7.3% for α-pinene, 3.8% for β-caryophyllene, 0.5% for benzene, 0.2% for toluene, 3.1% for m-xylene, and 4.1% for naphthalene.

While fitting the measurements of suspended SOA, we modeled three configurations that employed the artifact corrections shown in Figure 5.1, additively. For 'PWL', we corrected for losses of particles to the walls of the chamber. For 'PWL+V2PWL', we corrected for PWL and losses of vapors to the wall-deposited particles. For 'PWL+V2PWL+VWL', we corrected for PWL, V2PWL, and vapor wall losses. We chose this sequence because PWL are routinely accounted for, while V2PWL and VWL are accounted for less frequently. All three of the aforementioned configurations used the 'realistic' formulation for V2PWL described above (i.e., included the mass transfer limitation). We also modeled 'PWL+V2PWL(unrealistic)' and 'PWL+V2PWL+VWL(unrealistic)', which did not account for mass transfer limitations for V2PWL. We added these configurations to demonstrate the errors incurred by incorrectly assuming that vapors condense onto wall-deposited particles as if they were suspended.

SOM-TOMAS results for the four configurations are in Figure 5.2 for α-pinene; the other compounds are in Figures D2-7. At the end of the α-pinene chamber experiments, we find that correcting for PWL increased estimated SOA mass concentrations by 23% for high NO_x and 35%

for low NO_x, while PWL+V2PWL was negligibly different from PWL (<1% for both high and low NO_x). Adding VWL had the largest impact, increasing SOA mass yields by 162% for high NO_x and 175% for low NO_x, relative to PWL+V2PWL (or PWL). Generally, we saw similar trends across all SOA precursors. PWL increased SOA mass concentrations by 8-39% for high NO_x and 10-37% for low NO_x, V2PWL had a negligible impact relative to PWL, and VWL increased SOA mass concentrations by 36-680% for high NO_x and 55-250% for low NO_x relative to PWL+V2PWL (or PWL).

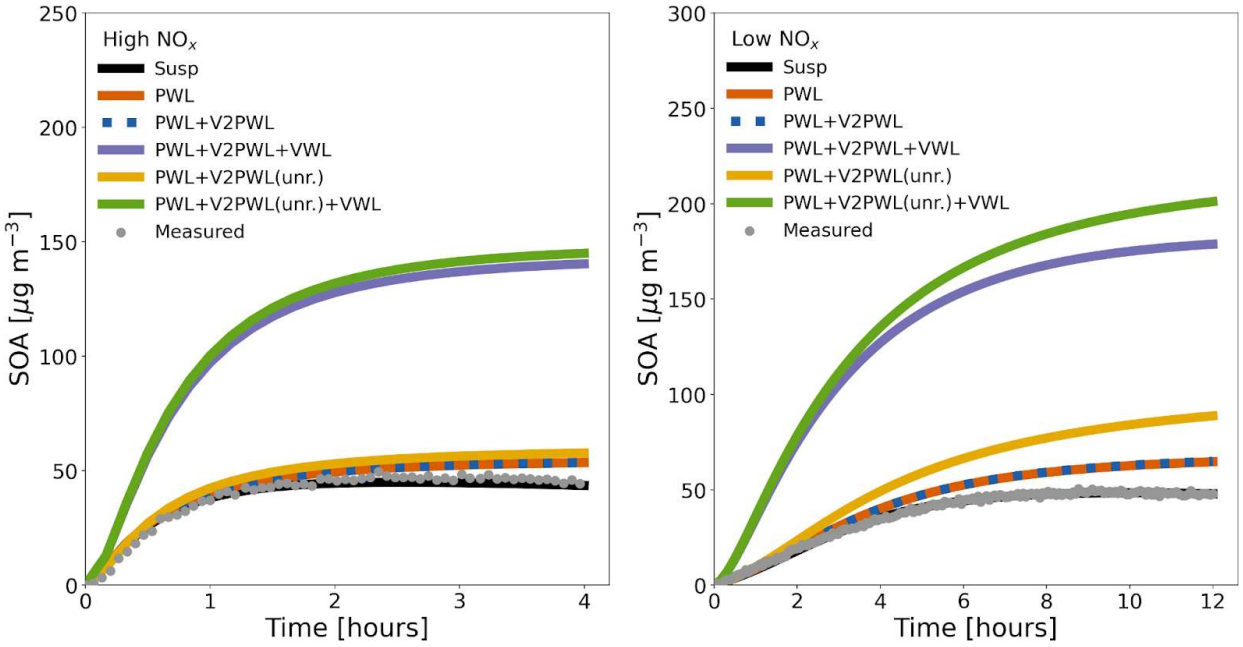

Figure 5.2: SOM-TOMAS estimates of secondary organic aerosol (SOA) mass concentration of α-pinene chamber experiments under high-NO_x (left panel) and low-NO_x (right panel) conditions. SOA measurements are shown in the gray dots (Chhabra et al., 2011). The black line shows the SOM-TOMAS model fit for the SOA mass concentration. The colored lines show the three artifact-corrected SOA estimates (PWL: orange, PWL+V2PWL: blue (dashed), PWL+V2PWL+VWL: purple). These artifact corrections are based on our 'realistic' V2PWL formulation, which correctly accounts for the mass transfer limitation. The PWL+V2PWL(unrealistic) (yellow) and PWL+V2PWL(unrealistic)+VWL (green) are based on our 'unrealistic' formulation, which does not account for the mass transfer limitation.

Correcting for V2PWL had a marginal impact on SOA mass concentrations because the vapors condensing on the suspended particles and those lost to the walls (i.e., VWL) were much faster processes. The V2PWL process is inherently much slower than the VWL process because

the particles on the wall present a much smaller surface area compared to the walls. For example, in this α-pinene experiment, the total surface area offered by the wall (55 m^2) dwarfed that offered by the particles on the wall (0.01 m^2) by the end of the experiment. McMurry and Grosjean (1985a) argue that the loss rate of vapors to the particles on the wall or directly to the wall is only proportional to the surface area offered by these two substrates, as long as the mass accommodation coefficient for the vapors (to the wall or the particles on the wall) is larger than 10^{-6}. Overall, by the end of this experiment, the timescales for vapor loss to the suspended particles, particles on the wall, and wall were 40 (inverse of the condensation sink), 7×10^6 (inverse of $k_{vap,j,on}$), and 2400 (inverse of $k_{vap,wall,on}$) s, respectively. These timescales highlight the weak influence particles on the wall exert on vapor loss. Since the SOA parameters were nearly identical in our PWL and PWL+V2PWL configuration, moving forward we will only show the results from the PWL and PWL+V2PWL+VWL scenarios.

There are two reasons why we assumed point contact for the particles lost to the wall. First, SOA formed under such dry chamber conditions (RH<20%) has been shown to be semi-solid/viscous, with plenty of evidence for α-pinene SOA (diffusion coefficient ~10^{-19} m^2 s^{-1}) (DeRieux et al., 2018; Zaveri et al., 2020; He et al., 2021). If this is true, we would expect the SOA-coated ammonium sulfate particle to retain its shape after colliding and adhering to the chamber wall, specifically over the duration of the chamber experiment (<12 hours). Second, 'flattening' the particle to distribute the wall-deposited SOA over the chamber wall would tend to increase the surface area available for uptake of condensable vapors. In sensitivity simulations performed for the α-pinene case (Figure D8), we found that the SOA surface area had to be increased by three orders of magnitude to witness even a 2% increase in the V2PWL-corrected SOA mass concentrations. To note, if all of the SOA at the end of the experiment were spread out

over the chamber wall as a single monolayer, it would result in less than a two order of magnitude increase in surface area.

Importantly, we find that across all precursors if V2PWL is modeled without considering the mass-transfer limitation SOA mass yields PWL+V2PWL(unrealistic) erroneously increases the SOA mass yields by 2.8-8.7% for high NO_x and 4-46% for low NO_x, relative to PWL. Further, we find that when PWL+V2PWL(unrealistic)+VWL is used rather than PWL+ V2PWL(unrealistic)+VWL, the final SOA mass yields will have a -6.6 to +3.3% error for high NO_x and a +1.2 to +14.4% error low NO_x, depending on the SOA precursor (Figure 5.2, D2-7).

5.3 VBS_{SOM} Parameters Developed Using 'Atmospheric' Simulations

The SOM-TOMAS model is too computationally intensive to be included in a CTM such as GEOS-Chem. Therefore, we ran pseudo 'atmospheric' simulations using the artifact-corrected SOA parameters described in Section 5.2 and used the SOM-TOMAS model output to develop volatility basis set (VBS) parameters. In our 'atmospheric' simulations, a trace amount of SOA precursor (~1 pptv) was oxidized to form SOA at a fixed OH concentration (1.5×10^6 molecules cm^{-3}) for 168 hours (7 days). SOM-TOMAS was run at OA mass concentrations of 0.1, 1, and 10 $\mu g\ m^{-3}$ to capture the concentration range observed in the atmosphere (Porter et al., 2021). Our approach loosely followed Hodzic et al. (2016). However, we expanded on this approach by fitting our VBS parameters across a range of OA mass concentrations (0.1, 1, and 10 $\mu g\ m^{-3}$) and constraining those parameters to the average SOM-TOMAS-predicted SOA mass yield over 2 to 7 days of photochemical aging. In comparison, Hodzic et al. (2016) only fit the VBS parameters at one OA mass concentration (10 $\mu g\ m^{-3}$) and constrained the parameters to the SOM-predicted SOA mass yield at 3 days of photochemical aging.

The results of the 'atmospheric' simulations are shown in solid lines in Figures 5.3(a) and 5.3(d) for α-pinene under high NO_x and low NO_x, respectively, and for the PWL and PWL+V2PWL+VWL artifact-corrected configurations described in Section 5.2. (We did not include the PWL+V2PWL scenario because there was a negligible difference from PWL). Results for all other precursors are in Figures D8-13. Generally, we found that large changes in the SOM-TOMAS modeled SOA mass yields happened within the first few simulated hours but that the SOA mass yields were nearly constant after 48 hours (2 days) or slightly decreasing thereafter. The decrease in SOA mass yields after 48 hours was a result of fragmentation reactions in the gas phase followed by evaporation from the particle phase. Since our GEOS-Chem simulations were run at 2°×2.5° resolution (Section 5.4), we argue that only the SOA mass yields at longer atmospheric timescales (>48 hours) are relevant for inclusion in a global CTM.

The SOM-TOMAS 'atmospheric' simulation results were used to inform the SOA parameters for a VBS model, we call VBS_{SOM}. The SOM-TOMAS-modeled SOA mass yields were simultaneously fit at all OA mass concentrations (i.e., 0.1, 1, and 10 $\mu g\ m^{-3}$) between 48 and 168 hours to determine the parameters for each precursor. The VBS_{SOM} model predictions are dashed lines in Figures 5.3(a) and 5.3(d) for α-pinene (Figures D8-13 for other precursors). We did not include multi-generational, gas-phase aging in the VBS_{SOM} model because SOM-TOMAS predicted relatively constant SOA mass yields after 48 hours of photochemical aging. Multi-generational gas-phase aging will need to be considered when performing air quality or chemical transport modeling at higher spatial resolution (e.g., 4 km).

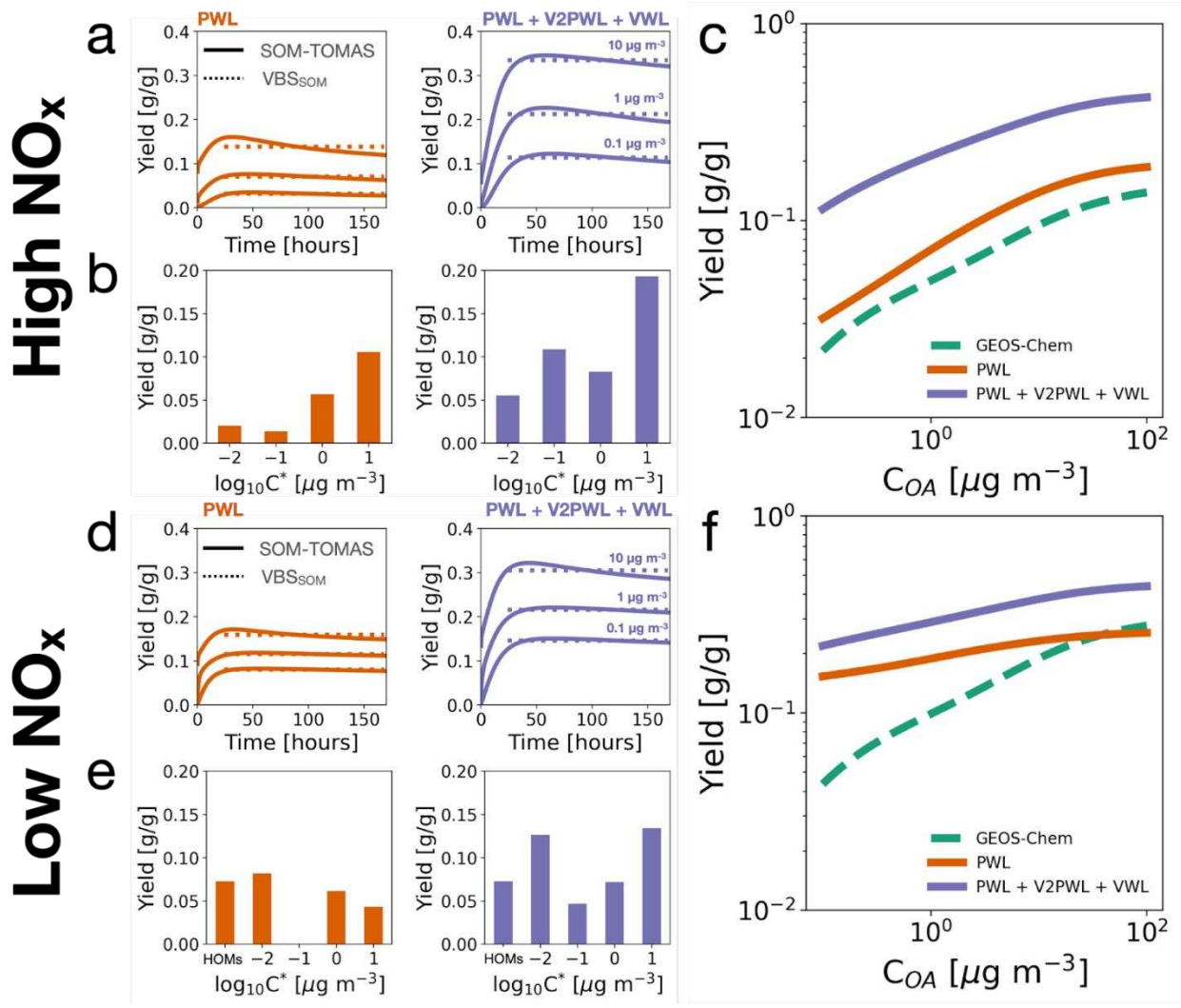

Figure 5.3: (a) Evolution of α-pinene secondary organic aerosol (SOA) mass yields as a function of atmospheric photochemical age at three different organic aerosol (OA) mass concentrations under high-NO_x conditions. Solid lines are the 'atmospheric' simulation results from SOM-TOMAS, while the dashed lines are the VBS_{SOM} model predictions. (b) VBS_{SOM} fit parameters resulting from (a). Parameters were fit for C^* = 0.1, 1, 10, 100 μg m^{-3}. (c) SOA mass yields across a range of OA mass concentrations based on the parameters in (b). (d, e, f) Are the same as panels (a, b, c), respectively, but for low-NO_x conditions. A bin was added for highly oxygenated molecules (HOMs) at C^* = 10^{-6} μg m^{-3} for the low-NO_x conditions. The HOMs yields are from Bianchi et al. (2019).

VBS_{SOM} fit four sequential C^* bins for each of the seven precursors (i.e., α-pinene, limonene, β-caryophyllene, benzene, toluene, *m*-xylene, naphthalene). The C^* bins ranged from 0.001 to 100 μg m^{-3}, depending on which range provided the best fit. The same C^* bins were used for fitting the SOA parameters under both high- and low-NO_x conditions for the same precursor.

For limonene, no data were available under low-NO_x conditions, so the same VBS parameters were used for both NO_x conditions. Under low-NO_x conditions for all precursors (except for limonene), an additional $C^* = 10^{-6}$ μg m^{-3} bin was added to represent the production of HOMs from autoxidation reactions. The HOM yields were directly prescribed and were the same as those used in the SOM-TOMAS modeling. We note that this C^* bin for HOMs was not included when determining the VBS_{SOM} parameters.

Generally, the VBS_{SOM} model predictions agreed well with SOM-TOMAS-modeled data for the precursors and OA mass concentrations explored here in part because we focused on SOA mass yields at longer timescales (>48 hours), while the shorter timescales are likely harder to capture with the VBS_{SOM} model. Trends are summarized in Figures 5.3(c) (high NO_x) and 5.3(f) (low NO_x), where the SOA mass yields for each of the artifact-corrected configurations are shown as a function of OA mass concentration (Figures D8-13 for the other precursors). While there were some exceptions (e.g., β-caryophyllene at high OA concentrations), we generally found that both PWL and PWL+V2PWL+VWL had higher yields than those in GEOS-Chem across OA mass concentrations.

Figure D14 shows the SOA mass yield enhancement ratios between PWL+V2PWL +VWL and PWL by VOC precursor, NO_x condition, and OA concentration. Overall, the SOA mass yields were greater for PWL+V2PWL+VWL than for PWL; however, the PWL+V2PWL+VWL:PWL ratio were dependent on the precursor VOC; suspended OA, OH, and NO_x concentration; and chamber conditions. Under low NO_x, the PWL+V2PWL +VWL:PWL mass yield enhancement ratios tend to be the highest for aromatics (i.e., benzene, toluene, naphthalene), while for high NO_x and *m*-xylene, the ratio is an order of magnitude larger than other species.

5.4 Artifact-corrected Global Organic Aerosol Estimates from GEOS-Chem

We used the GEOS-Chem v13.0.0 model (2021) to simulate the spatiotemporal distribution and concentrations of OA globally (www.geos-chem.org). We ran global simulations following GEOS-Chem's tropospheric chemistry ("tropchem") configuration for 2017. Simulations were driven by MERRA-2 meteorology from NASA's Global Modeling and Assimilation Office (GMAO) at 2°×2.5° resolution with 47 vertical layers. For anthropogenic emissions, we used an update to the Community Emissions Data System inventory (CEDSGBD-MAPS (McDuffie et al., 2020)). For biomass burning emissions, we used Global Fire Emissions Database v4 (Randerson et al., 2015). We used the Jaeglé et al. (2011) and the Zender et al. (2003) configurations for sea salt and mineral dust emissions, respectively. We used the Model of Emissions of Gases and Aerosols from Nature (MEGAN) v2.1 configuration for biogenic emissions with modifications from Guenther et al. (2012).

We updated the 'complex' SOA configuration in GEOS-Chem to test the impacts of the artifact-corrected configurations described in Section 5.2 on global OA. Pai et al. (2020) recently described the complex SOA configuration in depth. Briefly, SOA is formed from eight different precursors and the SOA formation is parameterized using the VBS framework. The VBS mass yields under high- and low-NO_x conditions are from Pye et al. (2010). The precursors include terpenes (α-pinene, limonene, other monoterpenes, sesquiterpenes), aromatics (benzene, toluene, xylene), and IVOCs (naphthalene). The products are eventually grouped into terpenes (TSOA) and aromatics + IVOCs (ASOA). The complex SOA configuration also includes a reversible, semi-volatile treatment of primary OA (POA) and a mechanistic treatment of isoprene (Fisher et al., 2016; Marais et al., 2016; Pye et al., 2010). The treatment for POA and isoprene has not been modified in this work as the effects of VWL on their treatment are unclear.

The VBS parameters from Pye et al. (2010) were derived from several different chamber studies that did not comprehensively deal with chamber artifacts. The VBS parameters included PWL corrections but did not include corrections for V2PWL or VWL. We did not update this set of VBS parameters by correcting for V2PWL and VWL artifacts because we did not have ready access to all of the chamber data used to develop the original VBS parameters. Instead, we used a different set of chamber experiments with some overlap with the original set of experiments to develop a completely new set of VBS parameters.

We added several C^* bins to implement our updated VBS parameters in GEOS-Chem. Tables D3-D9 summarized how we mapped the precursors from the chamber experiments to the parent hydrocarbons in GEOS-Chem and lists the VBS parameters by C^* bin. Our updated version of GEOS-Chem included six C^* bins for both TSOA and ASOA (10^{-6}, 0.01, 0.1, 1, 10, 100 μg m^{-3}). We also ran a 'BASE' simulation that followed GEOS-Chem's default complex SOA configuration.

The global-average surface-level changes in TSOA, ASOA, and total OA are shown in Figure 5.4. PWL+V2PWL+VWL lead to a 0.25 μg m^{-3} (24%) increase in global-average OA relative to PWL, demonstrating that VWL is an influential loss pathway to account for when developing VBS parameters for atmospheric models. PWL+V2PWL+VWL also increased global-average OA by 0.37 μg m^{-3} (40%) compared to the BASE simulation. While some of the differences between the PWL+V2PWL+VWL and BASE simulations might result from using a different set of chamber experiments to develop the SOA parameters, the higher global burden of OA in PWL+V2PWL+VWL relative to PWL demonstrates that the impacts of chamber artifacts are likely underestimated in the default complex SOA configuration.

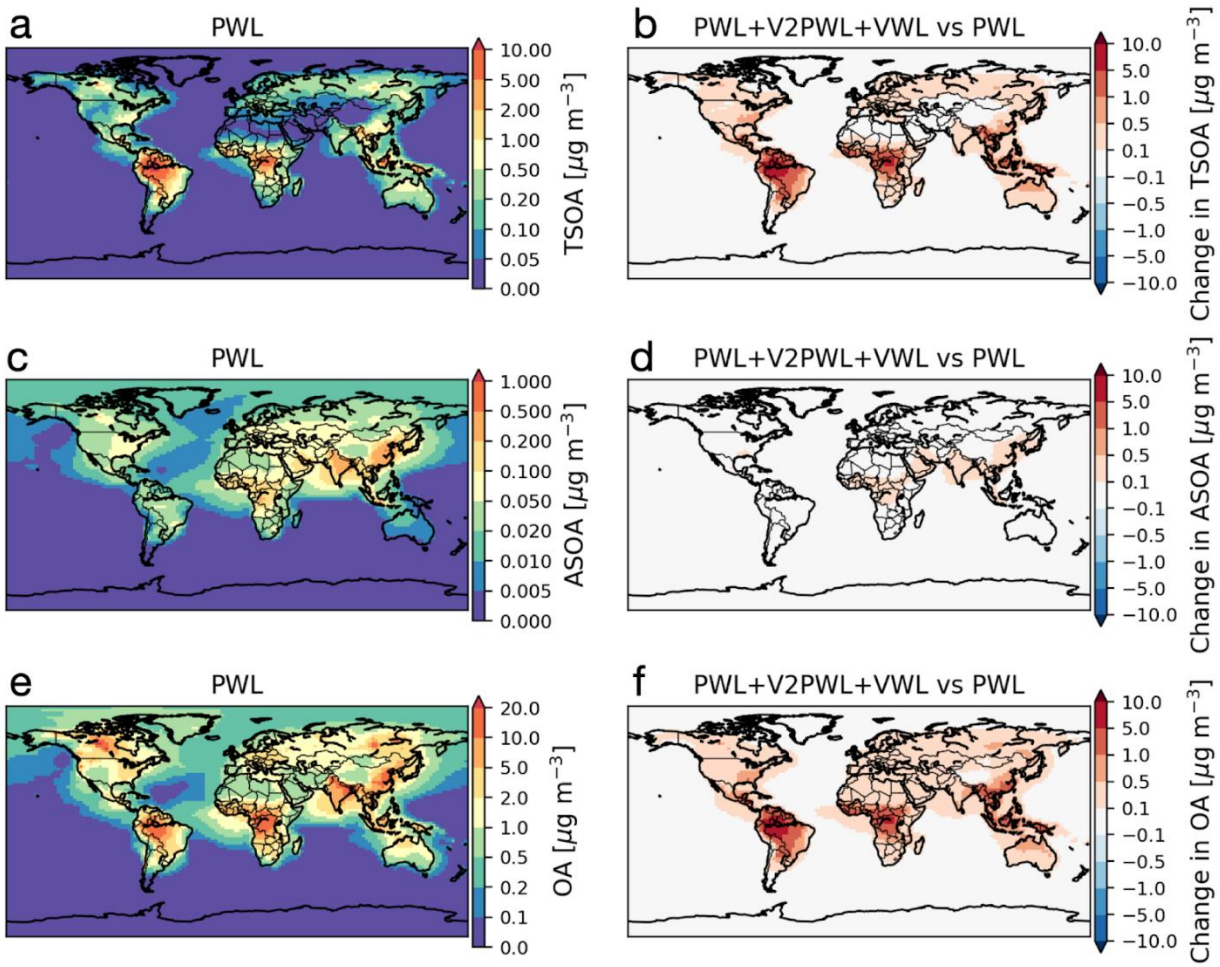

Figure 5.4: (a) Simulated annual-mean surface-layer terpene secondary organic aerosol (TSOA) mass concentrations for the PWL scenario. (b) Change in TSOA mass concentration for the PWL+V2PWL+VWL scenario relative to PWL. Red hues indicate an increase relative to PWL. (c) Change in TSOA mass concentrations for the PWL+V2PWL+VWL scenario relative to the BASE GEOS-Chem scheme. Red hues indicate an increase relative to the BASE scheme. (d, e, f) The same as for (a, b, c), respectively, but for aromatic + IVOC secondary organic aerosol (ASOA). (g, h, i) The same as for (a, b, c), respectively, but for total organic aerosol (OA).

The regional changes in TSOA, ASOA, and OA were much larger than the global average changes. For example, when comparing PWL+V2PWL+VWL to PWL, OA increased by up to 9.0 μg m^{-3} (130%), TSOA increased by up to 8.9 μg m^{-3} (170%), and ASOA increased by 0.5 μg m^{-3} (213%). The largest changes for TSOA and ASOA were near source regions. TSOA increased over forested areas, and ASOA increased near population centers. The changes in TSOA contributed to most of the overall changes in OA.

Given the importance of OA for $PM_{2.5}$, we compared $PM_{2.5}$ estimates from the GEOS-Chem simulations to $PM_{2.5}$ estimates from Hammer et al. (2020) (Figures D17-D18). These $PM_{2.5}$ estimates combine satellite observations of aerosol optical depth (AOD) from multiple instruments and algorithms with a simulation of the AOD to $PM_{2.5}$ relationship and with in-situ measurements and are widely used as exposure estimates for global $PM_{2.5}$ (GBD 2017 Risk Factor Collaborators, 2018). The comparison was conducted by aggregating the Hammer et al. (2020) estimates to our model resolution (2°×2.5°). The BASE simulation had the largest normalized mean bias (NMB=-12%) and the poorest agreement with the Hammer et al. (2020) $PM_{2.5}$ values (r^2=0.825), while the PWL+V2PWL+VWL had the smallest normalized mean bias (-6.3%) and the best agreement (r^2=0.849). The PWL+V2PWL+VWL simulation led to the greatest improvements in model-measurement comparisons in regions with heavy biogenic emissions (South America, sub-Saharan Africa). Thus, accurately accounting for chamber artifacts in VBS parametrizations will likely lead to better exposure estimates and may lead to a better understanding of how specific sources impact exposure and health.

Finally, we compared OA estimates from the GEOS-Chem simulations to OA measurements from the Atmospheric Tomography Mission (ATom) (Figures D19-20). ATom consisted of four campaigns that tracked the vertical profile of a suite of trace gases and aerosols over the remote Pacific and Atlantic. Overall, we found that the OA estimates for GEOS-Chem were within the interquartile range of the ATom OA measurements and that the OA estimates in the remote troposphere were not strongly sensitive to the SOA parameterizations investigated here, likely because there are other processes that contribute greater uncertainty (e.g., aerosol deposition, sources of marine OA). We propose that a more detailed characterization of the GEOS-Chem predictions for artifact-corrected OA mass and composition be undertaken in future work.

5.5 Implications for Atmospheric Secondary Organic Aerosol Modeling

Here, we present a novel methodology to correct for chamber artifacts and develop VBS parameterizations to model SOA formation in global CTMs. The VBS parameters are fit to reproduce average week-long SOA mass yields across a range of atmospherically relevant OA concentrations. As part of our chamber and 3D modeling, we also include the production of HOMs from autoxidation reactions, which are typically not accounted for in 3D models.

In this work, we quantified the impacts of chamber artifacts, including PWL, V2PWL, and VWL. We found that VWL led to the largest increase in SOA mass yield (high NO_x: 36-680%; low NO_x: 55-250%), followed by PWL (high NO_x: 3-39%; low NO_x: 10-37%), while V2PWL had a negligible impact. Thus, accounting for PWL but failing to account for VWL will lead to a substantial underestimate of the SOA mass yield. Further, we strongly recommend that chamber practitioners, both experimentalists and modelers, refrain from correcting chamber data for losses of vapors to the particles on the wall while assuming no mass transfer limitations to this process.

Finally, we find that accurately accounting for chamber artifacts improves surface estimates of $PM_{2.5}$. Further, failing to account for VWL will lead global-average surface-level OA to be underestimated by 24% (0.25 $\mu g\ m^{-3}$) or up to 130% (9.0 $\mu g\ m^{-3}$) in regions of high biogenic or anthropogenic activity. We recommend that future modeling studies include VBS parameters that account for VWL (in addition to PWL) to more accurately assess the impacts of SOA formation on air quality, health, and climate.

CHAPTER 6: Conclusions and Discussions

Traditional SOA parameterizations used in CTMs assume a static product distribution (e.g., two-product model (Odum et al., 1996) and one-dimensional volatility basis set (VBS) (Donahue et al., 2006)) for the oxidation of VOCs and instantaneous gas/particle partitioning of the oxidation products, while simplifying or neglecting many other physical/chemical processes that may influence SOA formation in both laboratory experiments and the real atmosphere (Pye and Pouliot, 2012; Murphy et al., 2017; Shrivastava et al., 2019; Pai et al., 2020). However, the results in this dissertation clearly showed that the traditional assumptions may have been oversimplified and inaccurate, and a few examples include: (1) the SOA mass yield of VOCs is not static, but rather it changes with photochemical age as a result of both gas-phase oxidation and heterogeneous oxidation of the particles; at higher aging times, the effect of heterogeneous oxidation can even be dominant; (2) the wall loss processes, especially vapor wall loss, can bias SOA mass yields substantially; (3) neither chamber nor atmospheric SOA particles are always liquid, but they can be semi-solid or nearly solid to various degrees depending on the temperature, relative humidity, and SOA chemical composition; thus assuming liquid SOA in both cases may distort SOA mass yield predictions in CTMs (Shiraiwa et al., 2017; Jathar et al., 2021). The complexity of the processes governing SOA formation and evolution necessitates the use of sophisticated kinetic SOA models to develop robust SOA parameterizations. Future work should focus on comprehensively representing all of the processes while simplifying the formulations to improve computational efficiency. The initial development of such a simplified and comprehensive model framework from our group has been published in Jathar et al. (2021).

In a recent study (Pai et al., 2020), questions have been raised about using more complex representations of SOA formation in CTMs, because such a complex SOA scheme was apparently

outperformed by a simpler SOA scheme in reducing model bias in OA prediction with respect to observations. Specifically, the complex scheme considered the reversible gas/particle partitioning of the SOA and POA species, following the VBS approach (Pye et al., 2010), and the simpler scheme assumed non-volatile POA and fixed yields for SOA. While the complex scheme better reflected the dynamics of the gas/particle partitioning of the SOA species, it is also clear from this dissertation that there are many more processes that can control the formation and evolution of SOA in the atmosphere. Thus, the "complex" scheme may still have fallen short of truthfully representing all the relevant processes, which may be the reason why it was outperformed by the simpler scheme. Based on this dissertation, we think considering the formation of oligomers, and therefore explicitly simulating the phase state of SOA particles may improve the performance of the complex scheme, as frequently encountered semi-solid phase state in the real atmosphere can substantially slow down the gas/particle partitioning timescale of the SOA species. Also, heterogeneous oxidation may play an important role in improving model predictions given the large geographical range and long time period covered in Pai et al. (2020) where SOA can go through long photochemical aging. These hypotheses will need to be evaluated in future works where we would integrate comprehensive and efficient SOA kinetic parameterizations with CTMs.

The development of SOA parameterizations from laboratory experiments relies on the prescription of a number of SOA and reactor properties, including vapor and particle wall loss rates, particle bulk diffusivity D_b, heterogeneous uptake coefficient γ_{OH}, and the oligomerization rates, for example. Thus, the accuracy of these quantities, mostly measured in separate, dedicated experiments, are a pillar to the SOA parameterizations developed subsequently. However, there are still uncertainties surrounding some of these values. For example, although particle wall loss rates are routinely accounted for in most experiments, the experiment-to-experiment variations in

the loss rates due to reactor wall charge effects (McMurry and Grosjean, 1985) have never been taken into account. Future works should improve the experimental procedures or reactor designs to reduce the charge effect, or measure the particle wall loss rates before each experiment. Also, the estimation of D_b in flow reactor experiments is complicated by their short residence times, which may prevent the SOA species, as well as water molecules, to come to full equilibrium of mixing. Future studies employing radially resolved multi-layer SOA particle models (Shiraiwa et al., 2012) could be helpful to elucidate this issue.

Despite its ability to capture laboratory and atmospheric SOA behavior, there still remain a few shortcomings with our model. First, the SOM-TOMAS framework does not represent aqueous-phase reactions, so the model may not accurately capture the SOA formation mechanism when such reactions are important (e.g., cloud processing of SOA (Ervens et al., 2011)). Second, for systems with peculiar uptake mechanisms (e.g., isoprene-epoxydiols (IEPOX) uptake in isoprene oxidation systems (Hu et al., 2016)), the model is currently failing to represent those pathways. Third, the SOM-TOMAS model does not explicitly account for the influence of NO_x on SOA formation, but rather relies on separate SOA parameterizations for low- and high-NO_x regimes; for future work, it could be beneficial to explicitly account for the radical chemistry between RO_2, NO_x and HO_2 in the model framework to consistently account for the influence of NO_x. Fourth, the current model framework assumes the aging of the VOCs is independent from each other and there is no cross-reactions between the products; however, studies (Peng and Jimenez, 2019; Heinritzi et al., 2020) have shown that RO_2 radicals from different VOCs do react with each other and may change the product distribution of the oxidation reactions. This is especially important when simulating VOC mixtures of high concentrations; an explicit representation of the RO_2 fate would be beneficial. Lastly, each time a new VOC needs to be

parameterized, chamber experiments (plus the procedure above) have to be repeated; the amount of work could be tremendous considering the large number of new VOCs recently identified and classified as VCPs (McDonald et al., 2018). Thus, for future work, it would be beneficial to develop parameterizations for SOA atmospheric mass yields based on VOC properties (such as carbon and oxygen numbers), which can be used to quickly estimate and test SOA yields of new VOCs.

References

Abramson, E., Imre, D., Beránek, J., Wilson, J., and Zelenyuk, A.: Experimental determination of chemical diffusion within secondary organic aerosol particles, Phys. Chem. Chem. Phys., 15, 2983–2991, 2013.

Adams, P. J. and Seinfeld, J. H.: Predicting global aerosol size distributions in general circulation models, J. Geophys. Res., 107, 4370, 2002.

Akherati, A., Cappa, C. D., Kleeman, M. J., Docherty, K. S., Jimenez, J. L., Griffith, S. M., Dusanter, S., Stevens, P. S., and Jathar, S. H.: Simulating secondary organic aerosol in a regional air quality model using the statistical oxidation model – Part 3: Assessing the influence of semi-volatile and intermediate-volatility organic compounds and NO x, Atmos. Chem. Phys., 19, 4561–4594, 2019.

Akherati, A., He, Y., Coggon, M. M., Koss, A. R., Hodshire, A. L., Sekimoto, K., Warneke, C., de Gouw, J., Yee, L., Seinfeld, J. H., Onasch, T. B., Herndon, S. C., Knighton, W. B., Cappa, C. D., Kleeman, M. J., Lim, C. Y., Kroll, J. H., Pierce, J. R., and Jathar, S. H.: Oxygenated Aromatic Compounds are Important Precursors of Secondary Organic Aerosol in Biomass-Burning Emissions, Environ. Sci. Technol., 54, 8568–8579, 2020.

Aljawhary, D., Lee, A. K. Y., and Abbatt, J. P. D.: High-resolution chemical ionization mass spectrometry (ToF-CIMS): application to study SOA composition and processing, Atmospheric Measurement Techniques, 6, 3211–3224, 2013.

Al-Naiema, I. M., Roppo, H. M., and Stone, E. A.: Quantification of furandiones in ambient aerosol, Atmos. Environ., 153, 41–46, 2017.

Angell, C. A.: Formation of glasses from liquids and biopolymers, Science, 267, 1924–1935, 1995.

Apte, J. S., Brauer, M., Cohen, A. J., Ezzati, M., and Pope, C. A.: Ambient PM2.5 Reduces Global and Regional Life Expectancy, Environ. Sci. Technol. Lett., 5, 546–551, 2018.

Athanasopoulou, E., Vogel, H., Vogel, B., Tsimpidi, A. P., Pandis, S. N., Knote, C., and Fountoukis, C.: Modeling the meteorological and chemical effects of secondary organic aerosols during an EUCAARI campaign, Atmos. Chem. Phys., 13, 625–645, 2013.

Atkinson, R. and Arey, J.: Atmospheric degradation of volatile organic compounds, Chem. Rev., 103, 4605–4638, 2003.

Aumont, B., Szopa, S., and Madronich, S.: Modelling the evolution of organic carbon during its gas-phase tropospheric oxidation: development of an explicit model based on a self generating approach, Atmos. Chem. Phys., 5, 2497–2517, 2005.

Bakker-Arkema, J. G. and Ziemann, P. J.: Measurements of Kinetics and Equilibria for the Condensed Phase Reactions of Hydroperoxides with Carbonyls to Form Peroxyhemiacetals, ACS Earth Space Chem., 4, 467–475, 2020.

Bateman, A. P., Bertram, A. K., and Martin, S. T.: Hygroscopic Influence on the Semisolid-to-Liquid Transition of Secondary Organic Materials, J. Phys. Chem. A, 119, 4386–4395, 2015.

Berkemeier, T., Shiraiwa, M., Pöschl, U., and Koop, T.: Competition between water uptake and ice nucleation by glassy organic aerosol particles, Atmos. Chem. Phys., 14, 12513–12531, 2014.

Bertrand, A., Stefenelli, G., Jen, C. N., Pieber, S. M., Bruns, E. A., Ni, H., Temime-Roussel, B., Slowik, J. G., Goldstein, A. H., El Haddad, I., Baltensperger, U., Prévôt, A. S. H., Wortham, H., and Marchand, N.: Evolution of the chemical fingerprint of biomass burning organic aerosol during aging, Atmos. Chem. Phys., 18, 7607–7624, 2018.

Bian, Q., May, A. A., Kreidenweis, S. M., and Pierce, J. R.: Investigation of particle and vapor wall-loss effects on controlled wood-smoke smog-chamber experiments, Atmos. Chem. Phys., 15, 11027–11045, 2015.

Bianchi, F., Kurtén, T., Riva, M., Mohr, C., Rissanen, M. P., Roldin, P., Berndt, T., Crounse, J. D., Wennberg, P. O., Mentel, T. F., Wildt, J., Junninen, H., Jokinen, T., Kulmala, M., Worsnop, D. R., Thornton, J. A., Donahue, N., Kjaergaard, H. G., and Ehn, M.: Highly Oxygenated Organic Molecules (HOM) from Gas-Phase Autoxidation Involving Peroxy Radicals: A Key Contributor to Atmospheric Aerosol, Chem. Rev., 119, 3472–3509, 2019.

Bilsback, K. R., He, Y., Chan, A. W. H., Croft, B., Pierce, J. R., Ng, N. L., Seinfeld, J., and Jathar, S. H.: Vapors are Lost to Walls, Not to Particles on the Wall: Development of Artifact-Corrected Parameters from Chamber Experiments and Implications for Global Secondary Organic Aerosol, n.d.

Bloss, C., Wagner, V., Jenkin, M. E., Volkamer, R., Bloss, W. J., Lee, J. D., Heard, D., Wirtz, K., Martin-Reviejo, M., Rea, G., and Others: Development of a detailed chemical mechanism (MCMv3. 1) for the atmospheric oxidation of aromatic hydrocarbons, Atmos. Chem. Phys., 5, 641–664, 2005.

Boyd, C. M., Sanchez, J., Xu, L., Eugene, A. J., Nah, T., Tuet, W. Y., Guzman, M. I., and Ng, N. L.: Secondary organic aerosol formation from the β-pinene+NO_3 system: effect of humidity and peroxy radical fate, Atmos. Chem. Phys., 15, 7497–7522, 2015.

Brune, W. H.: The Chamber Wall Index for Gas-Wall Interactions in Atmospheric Environmental Enclosures, Environ. Sci. Technol., 53, 3645–3652, 2019.

Bruns, E. A., El Haddad, I., Keller, A., Klein, F., Kumar, N. K., Pieber, S. M., Corbin, J. C., Slowik, J. G., Brune, W. H., Baltensperger, U., and Prévôt, A. S. H.: Inter-comparison of laboratory smog chamber and flow reactor systems on organic aerosol yield and composition, Atmospheric Measurement Techniques, 8, 2315–2332, 2015.

Bruns, E. A., El Haddad, I., Slowik, J. G., Kilic, D., Klein, F., Baltensperger, U., and Prévôt, A. S. H.: Identification of significant precursor gases of secondary organic aerosols from residential wood combustion, Sci. Rep., 6, 27881, 2016.

Canagaratna, M. R., Jimenez, J. L., Kroll, J. H., Chen, Q., Kessler, S. H., Massoli, P., Hildebrandt Ruiz, L., Fortner, E., Williams, L. R., Wilson, K. R., Surratt, J. D., Donahue, N. M., Jayne, J. T., and Worsnop, D. R.: Elemental ratio measurements of organic compounds using aerosol mass spectrometry: characterization, improved calibration, and implications, Atmos. Chem. Phys., 15, 253–272, 2015.

Cappa, C. D. and Wilson, K. R.: Multi-generation gas-phase oxidation, equilibrium partitioning, and the formation and evolution of secondary organic aerosol, Atmos. Chem. Phys., 12, 9505–9528, 2012.

Cappa, C. D., Jathar, S. H., Kleeman, M. J., Docherty, K. S., Jimenez, J. L., Seinfeld, J. H., and Wexler, A. S.: Simulating secondary organic aerosol in a regional air quality model using the statistical oxidation model--Part 2: Assessing the influence of vapor wall losses, Atmos. Chem. Phys., 16, 3041–3059, 2016.

Carslaw, H. S. and Jaeger, J. C.: Conduction of Heat in Solids, Clarendon Press, 510 pp., 1986.

Carter, W. P. L.: Implementation of the SAPRC-99 chemical mechanism into the models-3 framework, 29, 2000.

Carter, W. P. L.: Development of the SAPRC-07 chemical mechanism, Atmos. Environ., 44, 5324–5335, 2010.

Chacon-Madrid, H. J., Henry, K. M., and Donahue, N. M.: Photo-oxidation of pinonaldehyde at low NO_x: from chemistry to organic aerosol formation, Atmos. Chem. Phys., 13, 3227–3236, 2013.

Chan, A. W. H., Kautzman, K. E., Chhabra, P. S., Surratt, J. D., Chan, M. N., Crounse, J. D., Kürten, A., Wennberg, P. O., Flagan, R. C., and Seinfeld, J. H.: Secondary organic aerosol formation from photooxidation of naphthalene and alkylnaphthalenes: implications for oxidation of intermediate volatility organic compounds (IVOCs), Atmos. Chem. Phys., 9, 3049–3060, 2009.

Charan, S. M., Kong, W., Flagan, R. C., and Seinfeld, J. H.: Effect of particle charge on aerosol dynamics in Teflon environmental chambers, Aerosol Sci. Technol., 52, 854–871, 2018.

Charan, S. M., Huang, Y., and Seinfeld, J. H.: Computational Simulation of Secondary Organic Aerosol Formation in Laboratory Chambers, Chem. Rev., 119, 11912–11944, 2019.

Chen, S., Brune, W. H., Lambe, A. T., Davidovits, P., and Onasch, T. B.: Modeling organic aerosol from the oxidation of α-pinene in a Potential Aerosol Mass (PAM) chamber, Atmos. Chem. Phys., 13, 5017–5031, 2013.

Chen, T., Liu, Y., Chu, B., Liu, C., Liu, J., Ge, Y., Ma, Q., Ma, J., and He, H.: Differences of the oxidation process and secondary organic aerosol formation at low and high precursor concentrations, J. Environ. Sci. , 79, 256–263, 2019a.

Chen, T., Liu, Y., Liu, C., Liu, J., Chu, B., and He, H.: Important role of aromatic hydrocarbons in SOA formation from unburned gasoline vapor, Atmos. Environ., 201, 101–109, 2019b.

Cheng, Y., Su, H., Koop, T., Mikhailov, E., and Pöschl, U.: Size dependence of phase transitions in aerosol nanoparticles, Nat. Commun., 6, 5923, 2015.

Chhabra, P. S., Flagan, R. C., and Seinfeld, J. H.: Elemental analysis of chamber organic aerosol using an aerodyne high-resolution aerosol mass spectrometer, Atmos. Chem. Phys., 10, 4111–4131, 2010.

Chhabra, P. S., Ng, N. L., Canagaratna, M. R., Corrigan, A. L., Russell, L. M., Worsnop, D. R., Flagan, R. C., and Seinfeld, J. H.: Elemental composition and oxidation of chamber organic aerosol, Atmos. Chem. Phys., 11, 8827–8845, 2011.

Cohen, A. J., Brauer, M., Burnett, R., Anderson, H. R., Frostad, J., Estep, K., Balakrishnan, K., Brunekreef, B., Dandona, L., Dandona, R., Feigin, V., Freedman, G., Hubbell, B., Jobling, A., Kan, H., Knibbs, L., Liu, Y., Martin, R., Morawska, L., Pope, C. A., 3rd, Shin, H., Straif, K., Shaddick, G., Thomas, M., van Dingenen, R., van Donkelaar, A., Vos, T., Murray, C. J. L., and Forouzanfar, M. H.: Estimates and 25-year trends of the global burden of disease attributable to ambient air pollution: an analysis of data from the Global Burden of Diseases Study 2015, Lancet, 389, 1907–1918, 2017.

Crump, J. G. and Seinfeld, J. H.: Turbulent deposition and gravitational sedimentation of an aerosol in a vessel of arbitrary shape, J. Aerosol Sci., 12, 405–415, 1981.

D'Ambro, E. L., Schobesberger, S., Zaveri, R. A., Shilling, J. E., Lee, B. H., Lopez-Hilfiker, F. D., Mohr, C., and Thornton, J. A.: Isothermal Evaporation of α-Pinene Ozonolysis SOA: Volatility, Phase State, and

Oligomeric Composition, ACS Earth Space Chem., 2, 1058–1067, 2018.

Danckwerts, P. V.: Absorption by simultaneous diffusion and chemical reaction into particles of various shapes and into falling drops, Trans. Faraday Soc., 47, 1014–1023, 1951.

DeRieux, W.-S. W., Li, Y., Lin, P., Laskin, J., Laskin, A., Bertram, A. K., Nizkorodov, S. A., and Shiraiwa, M.: Predicting the glass transition temperature and viscosity of secondary organic material using molecular composition, Atmos. Chem. Phys., 18, 6331–6351, 2018.

Dickerson, R. R., Anderson, D. C., and Ren, X.: On the use of data from commercial NOx analyzers for air pollution studies, Atmos. Environ., 214, 116873, 2019.

Donahue, N. M., Robinson, A. L., Stanier, C. O., and Pandis, S. N.: Coupled partitioning, dilution, and chemical aging of semivolatile organics, Environ. Sci. Technol., 40, 2635–2643, 2006.

van Donkelaar, A., Martin, R. V., Brauer, M., Kahn, R., Levy, R., Verduzco, C., and Villeneuve, P. J.: Global estimates of ambient fine particulate matter concentrations from satellite-based aerosol optical depth: development and application, Environ. Health Perspect., 118, 847–855, 2010.

Dunlea, E. J., Herndon, S. C., Nelson, D. D., Volkamer, R. M., San Martini, F., Sheehy, P. M., Zahniser, M. S., Shorter, J. H., Wormhoudt, J. C., Lamb, B. K., Allwine, E. J., Gaffney, J. S., Marley, N. A., Grutter, M., Marquez, C., Blanco, S., Cardenas, B., Retama, A., Ramos Villegas, C. R., Kolb, C. E., Molina, L. T., and Molina, M. J.: Evaluation of nitrogen dioxide chemiluminescence monitors in a polluted urban environment, Atmos. Chem. Phys., 7, 2691–2704, 2007.

Ehn, M., Thornton, J. A., Kleist, E., Sipilä, M., Junninen, H., Pullinen, I., Springer, M., Rubach, F., Tillmann, R., Lee, B., Lopez-Hilfiker, F., Andres, S., Acir, I.-H., Rissanen, M., Jokinen, T., Schobesberger, S., Kangasluoma, J., Kontkanen, J., Nieminen, T., Kurtén, T., Nielsen, L. B., Jørgensen, S., Kjaergaard, H. G., Canagaratna, M., Maso, M. D., Berndt, T., Petäjä, T., Wahner, A., Kerminen, V.-M., Kulmala, M., Worsnop, D. R., Wildt, J., and Mentel, T. F.: A large source of low-volatility secondary organic aerosol, Nature, 506, 476–479, 2014.

Eluri, S., Cappa, C. D., Friedman, B., Farmer, D. K., and Jathar, S. H.: Modeling the formation and composition of secondary organic aerosol from diesel exhaust using parameterized and semi-explicit chemistry and thermodynamic models, Atmos. Chem. Phys., 18, 13813–13838, 2018.

EPA: Estimation programs interface suite™ for microsoft® windows, v 4.11, 2012.

Evoy, E., Maclean, A. M., Rovelli, G., Li, Y., Tsimpidi, A. P., Karydis, V. A., Kamal, S., Lelieveld, J., Shiraiwa, M., Reid, J. P., and Bertram, A. K.: Predictions of diffusion rates of large organic molecules in secondary organic aerosols using the Stokes–Einstein and fractional Stokes–Einstein relations, Atmos. Chem. Phys., 19, 10073–10085, 2019.

Farrell, J. T., Wagner, R., Gaspar, D., and Moen, C.: Co-Optimization of Fuels & Engines: FY18 Year in Review, National Renewable Energy Lab.(NREL), Golden, CO (United States), 2019.

Fisher, J. A., Jacob, D. J., Travis, K. R., Kim, P. S., Marais, E. A., Miller, C. C., Yu, K., Zhu, L., Yantosca, R. M., Sulprizio, M. P., Mao, J., Wennberg, P. O., Crounse, J. D., Teng, A. P., Nguyen, T. B., St Clair, J. M., Cohen, R. C., Romer, P., Nault, B. A., Wooldridge, P. J., Jimenez, J. L., Campuzano-Jost, P., Day, D. A., Hu, W., Shepson, P. B., Xiong, F., Blake, D. R., Goldstein, A. H., Misztal, P. K., Hanisco, T. F., Wolfe, G. M., Ryerson, T. B., Wisthaler, A., and Mikoviny, T.: Organic nitrate chemistry and its implications for nitrogen budgets in an isoprene- and monoterpene-rich atmosphere: constraints from

aircraft (SEAC^{4}RS) and ground-based (SOAS) observations in the Southeast US, Atmos. Chem. Phys., 16, 5969–5991, 2016.

Forstner, H. J. L., Flagan, R. C., and Seinfeld, J. H.: Secondary Organic Aerosol from the Photooxidation of Aromatic Hydrocarbons: Molecular Composition, Environ. Sci. Technol., 31, 1345–1358, 1997.

Friedman, B. and Farmer, D. K.: SOA and gas phase organic acid yields from the sequential photooxidation of seven monoterpenes, Atmos. Environ., 187, 335–345, 2018.

Fröhlich, R., Cubison, M. J., Slowik, J. G., Bukowiecki, N., Prévôt, A. S. H., Baltensperger, U., Schneider, J., Kimmel, J. R., Gonin, M., Rohner, U., Worsnop, D. R., and Jayne, J. T.: The ToF-ACSM: a portable aerosol chemical speciation monitor with TOFMS detection, https://doi.org/10.5194/amtd-6-6767-2013, 2013.

Fuzzi, S., Baltensperger, U., Carslaw, K., Decesari, S., Denier van der Gon, H., Facchini, M. C., Fowler, D., Koren, I., Langford, B., Lohmann, U., Nemitz, E., Pandis, S., Riipinen, I., Rudich, Y., Schaap, M., Slowik, J. G., Spracklen, D. V., Vignati, E., Wild, M., Williams, M., and Gilardoni, S.: Particulate matter, air quality and climate: lessons learned and future needs, Atmos. Chem. Phys., 15, 8217–8299, 2015.

Garofalo, L. A., He, Y., Jathar, S. H., Pierce, J. R., Fredrickson, C. D., Palm, B. B., Thornton, J. A., Mahrt, F., Crescenzo, G. V., Bertram, A. K., Draper, D. C., Fry, J. L., Orlando, J., Zhang, X., and Farmer, D. K.: Heterogeneous nucleation drives particle size segregation in sequential ozone and nitrate radical oxidation of catechol, Environ. Sci. Technol., 55, 15637–15645, 2021.

GBD 2017 Risk Factor Collaborators: Global, regional, and national comparative risk assessment of 84 behavioural, environmental and occupational, and metabolic risks or clusters of risks for 195 countries and territories, 1990-2017: a systematic analysis for the Global Burden of Disease Study 2017, Lancet, 392, 1923–1994, 2018.

Gentner, D. R., Isaacman, G., Worton, D. R., Chan, A. W. H., Dallmann, T. R., Davis, L., Liu, S., Day, D. A., Russell, L. M., Wilson, K. R., Weber, R., Guha, A., Harley, R. A., and Goldstein, A. H.: Elucidating secondary organic aerosol from diesel and gasoline vehicles through detailed characterization of organic carbon emissions, Proc. Natl. Acad. Sci. U. S. A., 109, 18318–18323, 2012.

George, I. J. and Abbatt, J. P. D.: Heterogeneous oxidation of atmospheric aerosol particles by gas-phase radicals, Nat. Chem., 2, 713–722, 2010.

George, I. J., Vlasenko, A., Slowik, J. G., Broekhuizen, K., and Abbatt, J. P. D.: Heterogeneous oxidation of saturated organic aerosols by hydroxyl radicals: uptake kinetics, condensed-phase products, and particle size change, Atmos. Chem. Phys., 7, 4187–4201, 2007.

de Gouw, J. A., Middlebrook, A. M., Warneke, C., Goldan, P. D., Kuster, W. C., Roberts, J. M., Fehsenfeld, F. C., Worsnop, D. R., Canagaratna, M. R., Pszenny, A. A. P., Keene, W. C., Marchewka, M., Bertman, S. B., and Bates, T. S.: Budget of organic carbon in a polluted atmosphere: Results from the New England Air Quality Study in 2002, J. Geophys. Res. D: Atmos., 110, https://doi.org/10.1029/2004JD005623, 2005.

Grayson, J. W., Zhang, Y., Mutzel, A., Renbaum-Wolff, L., Böge, O., Kamal, S., Herrmann, H., Martin, S. T., and Bertram, A. K.: Effect of varying experimental conditions on the viscosity of α-pinene derived secondary organic material, Atmos. Chem. Phys., 16, 6027–6040, 2016.

Grieshop, A. P., Donahue, N. M., and Robinson, A. L.: Is the gas-particle partitioning in alpha-pinene

secondary organic aerosol reversible?, Geophys. Res. Lett., 34, 305, 2007.

Grosjean, D.: Wall loss of gaseous pollutants in outdoor Teflon chambers, Environ. Sci. Technol., 19, 1059–1065, 1985.

Guenther, A. B., Jiang, X., Heald, C. L., Sakulyanontvittaya, T., Duhl, T., Emmons, L. K., and Wang, X.: The Model of Emissions of Gases and Aerosols from Nature version 2.1 (MEGAN2.1): an extended and updated framework for modeling biogenic emissions, Geosci. Model Dev., 5, 1471–1492, 2012.

Hammer, M. S., van Donkelaar, A., Li, C., Lyapustin, A., Sayer, A. M., Hsu, N. C., Levy, R. C., Garay, M. J., Kalashnikova, O. V., Kahn, R. A., Brauer, M., Apte, J. S., Henze, D. K., Zhang, L., Zhang, Q., Ford, B., Pierce, J. R., and Martin, R. V.: Global Estimates and Long-Term Trends of Fine Particulate Matter Concentrations (1998-2018), Environ. Sci. Technol., 54, 7879–7890, 2020.

Hatch, L. E., Luo, W., Pankow, J. F., Yokelson, R. J., Stockwell, C. E., and Barsanti, K. C.: Identification and quantification of gaseous organic compounds emitted from biomass burning using two-dimensional gas chromatography–time-of-flight mass spectrometry, https://doi.org/10.5194/acp-15-1865-2015, 2015.

Hayes, P. L., Carlton, A. G., Baker, K. R., Ahmadov, R., Washenfelder, R. A., Alvarez, S., Rappenglück, B., Gilman, J. B., Kuster, W. C., de Gouw, J. A., Zotter, P., Prévôt, A. S. H., Szidat, S., Kleindienst, T. E., Offenberg, J. H., Ma, P. K., and Jimenez, J. L.: Modeling the formation and aging of secondary organic aerosols in Los Angeles during CalNex 2010, Atmos. Chem. Phys., 15, 5773–5801, 2015.

He, Y., King, B., Pothier, M., Lewane, L., Akherati, A., Mattila, J., Farmer, D. K., McCormick, R. L., Thornton, M., Pierce, J. R., Volckens, J., and Jathar, S. H.: Secondary organic aerosol formation from evaporated biofuels: comparison to gasoline and correction for vapor wall losses, Environ. Sci. Process. Impacts, 22, 1461–1474, 2020.

He, Y., Akherati, A., Nah, T., Ng, N. L., Garofalo, L. A., Farmer, D. K., Shiraiwa, M., Zaveri, R. A., Cappa, C. D., Pierce, J. R., and Jathar, S. H.: Particle Size Distribution Dynamics Can Help Constrain the Phase State of Secondary Organic Aerosol, Environ. Sci. Technol., 55, 1466–1476, 2021.

Hearn, J. D. and Smith, G. D.: A mixed-phase relative rates technique for measuring aerosol reaction kinetics, Geophys. Res. Lett., 33, https://doi.org/10.1029/2006gl026963, 2006.

Heaton, K. J., Dreyfus, M. A., Wang, S., and Johnston, M. V.: Oligomers in the early stage of biogenic secondary organic aerosol formation and growth, Environ. Sci. Technol., 41, 6129–6136, 2007.

Heaton, K. J., Sleighter, R. L., Hatcher, P. G., Hall, W. A., 4th, and Johnston, M. V.: Composition domains in monoterpene secondary organic aerosol, Environ. Sci. Technol., 43, 7797–7802, 2009.

Heinritzi, M., Dada, L., Simon, M., Stolzenburg, D., Wagner, A. C., Fischer, L., Ahonen, L. R., Amanatidis, S., Baalbaki, R., Baccarini, A., Bauer, P. S., Baumgartner, B., Bianchi, F., Brilke, S., Chen, D., Chiu, R., Dias, A., Dommen, J., Duplissy, J., Finkenzeller, H., Frege, C., Fuchs, C., Garmash, O., Gordon, H., Granzin, M., El Haddad, I., He, X., Helm, J., Hofbauer, V., Hoyle, C. R., Kangasluoma, J., Keber, T., Kim, C., Kürten, A., Lamkaddam, H., Laurila, T. M., Lampilahti, J., Lee, C. P., Lehtipalo, K., Leiminger, M., Mai, H., Makhmutov, V., Manninen, H. E., Marten, R., Mathot, S., Mauldin, R. L., Mentler, B., Molteni, U., Müller, T., Nie, W., Nieminen, T., Onnela, A., Partoll, E., Passananti, M., Petäjä, T., Pfeifer, J., Pospisilova, V., Quéléver, L. L. J., Rissanen, M. P., Rose, C., Schobesberger, S., Scholz, W., Scholze, K., Sipilä, M., Steiner, G., Stozhkov, Y., Tauber, C., Tham, Y. J., Vazquez-Pufleau, M., Virtanen, A., Vogel, A. L., Volkamer, R., Wagner, R., Wang, M., Weitz, L., Wimmer, D., Xiao, M., Yan, C., Ye, P., Zha, Q., Zhou, X., Amorim, A., Baltensperger, U., Hansel, A., Kulmala, M., Tomé, A.,

Winkler, P. M., Worsnop, D. R., Donahue, N. M., Kirkby, J., and Curtius, J.: Molecular understanding of the suppression of new-particle formation by isoprene, Atmos. Chem. Phys., 20, 11809–11821, 2020.

Hildebrandt, L., Donahue, N. M., and Pandis, S. N.: High formation of secondary organic aerosol from the photo-oxidation of toluene, Atmos. Chem. Phys., 9, 2973–2986, 2009.

Hinds, W. C.: Aerosol Technology: Properties, Behavior, and Measurement of Airborne Particles, John Wiley & Sons, 504 pp., 1999.

Hodshire, A. L., Palm, B. B., Alexander, M. L., Bian, Q., Campuzano-Jost, P., Cross, E. S., Day, D. A., de Sá, S. S., Guenther, A. B., Hansel, A., Hunter, J. F., Jud, W., Karl, T., Kim, S., Kroll, J. H., Park, J.-H., Peng, Z., Seco, R., Smith, J. N., Jimenez, J. L., and Pierce, J. R.: Constraining nucleation, condensation, and chemistry in oxidation flow reactors using size-distribution measurements and aerosol microphysical modeling, 28, 12433, 2018.

Hodzic, A., Kasibhatla, P. S., Jo, D. S., Cappa, C. D., Jimenez, J. L., Madronich, S., and Park, R. J.: Rethinking the global secondary organic aerosol (SOA) budget: stronger production, faster removal, shorter lifetime, Atmos. Chem. Phys., 16, 7917–7941, 2016.

Hu, W., Palm, B. B., Day, D. A., Campuzano-Jost, P., Krechmer, J. E., Peng, Z., de Sá, S. S., Martin, S. T., Alexander, M. L., Baumann, K., Hacker, L., Kiendler-Scharr, A., Koss, A. R., de Gouw, J. A., Goldstein, A. H., Seco, R., Sjostedt, S. J., Park, J.-H., Guenther, A. B., Kim, S., Canonaco, F., Prévôt, A. S. H., Brune, W. H., and Jimenez, J. L.: Volatility and lifetime against OH heterogeneous reaction of ambient isoprene-epoxydiols-derived secondary organic aerosol (IEPOX-SOA), Atmos. Chem. Phys., 16, 11563–11580, 2016.

Huang, Y., Zhao, R., Charan, S. M., Kenseth, C. M., Zhang, X., and Seinfeld, J. H.: Unified Theory of Vapor-Wall Mass Transport in Teflon-Walled Environmental Chambers, Environ. Sci. Technol., 52, 2134–2142, 2018.

Isaacman-VanWertz, G., Massoli, P., O'Brien, R. E., Nowak, J. B., Canagaratna, M. R., Jayne, J. T., Worsnop, D. R., Su, L., Knopf, D. A., Misztal, P. K., Arata, C., Goldstein, A. H., and Kroll, J. H.: Using advanced mass spectrometry techniques to fully characterize atmospheric organic carbon: current capabilities and remaining gaps, Faraday Discuss., 200, 579–598, 2017.

Jaeglé, L., Quinn, P. K., Bates, T. S., Alexander, B., and Lin, J.-T.: Global distribution of sea salt aerosols: new constraints from in situ and remote sensing observations, Atmos. Chem. Phys., 11, 3137–3157, 2011.

Jathar, S. H., Miracolo, M. A., Tkacik, D. S., Donahue, N. M., Adams, P. J., and Robinson, A. L.: Secondary organic aerosol formation from photo-oxidation of unburned fuel: experimental results and implications for aerosol formation from combustion emissions, Environ. Sci. Technol., 47, 12886–12893, 2013.

Jathar, S. H., Donahue, N. M., Adams, P. J., and Robinson, A. L.: Testing secondary organic aerosol models using smog chamber data for complex precursor mixtures: influence of precursor volatility and molecular structure, Atmos. Chem. Phys., 14, 5771–5780, 2014.

Jathar, S. H., Cappa, C. D., Wexler, A. S., Seinfeld, J. H., and Kleeman, M. J.: Multi-generational oxidation model to simulate secondary organic aerosol in a 3-D air quality model, 2553–2567, 2015.

Jathar, S. H., Cappa, C. D., Wexler, A. S., Seinfeld, J. H., and Kleeman, M. J.: Simulating secondary

organic aerosol in a regional air quality model using the statistical oxidation model--Part 1: Assessing the influence of constrained multi-generational ageing, Atmos. Chem. Phys., 16, 2309–2322, 2016.

Jathar, S. H., Cappa, C. D., He, Y., Pierce, J. R., Chuang, W., Bilsback, K. R., Seinfeld, J. H., Zaveri, R. A., and Shrivastava, M.: A computationally efficient model to represent the chemistry, thermodynamics, and microphysics of secondary organic aerosols (simpleSOM): model development and application to α-pinene SOA, Environ. Sci.: Atmos., 1, 372–394, 2021.

Jenkin, M. E., Saunders, S. M., Wagner, V., and Pilling, M. J.: Protocol for the development of the Master Chemical Mechanism, MCM v3 (Part B): tropospheric degradation of aromatic volatile organic compounds, 3, 181–193, 2003.

Jenkin, M. E., Young, J. C., and Rickard, A. R.: The MCM v3.3.1 degradation scheme for isoprene, Atmos. Chem. Phys., 15, 11433–11459, 2015.

Jimenez, J. L., Canagaratna, M. R., Donahue, N. M., Prevot, A. S. H., Zhang, Q., Kroll, J. H., DeCarlo, P. F., Allan, J. D., Coe, H., Ng, N. L., Aiken, A. C., Docherty, K. S., Ulbrich, I. M., Grieshop, A. P., Robinson, A. L., Duplissy, J., Smith, J. D., Wilson, K. R., Lanz, V. A., Hueglin, C., Sun, Y. L., Tian, J., Laaksonen, A., Raatikainen, T., Rautiainen, J., Vaattovaara, P., Ehn, M., Kulmala, M., Tomlinson, J. M., Collins, D. R., Cubison, M. J., Dunlea, E. J., Huffman, J. A., Onasch, T. B., Alfarra, M. R., Williams, P. I., Bower, K., Kondo, Y., Schneider, J., Drewnick, F., Borrmann, S., Weimer, S., Demerjian, K., Salcedo, D., Cottrell, L., Griffin, R., Takami, A., Miyoshi, T., Hatakeyama, S., Shimono, A., Sun, J. Y., Zhang, Y. M., Dzepina, K., Kimmel, J. R., Sueper, D., Jayne, J. T., Herndon, S. C., Trimborn, A. M., Williams, L. R., Wood, E. C., Middlebrook, A. M., Kolb, C. E., Baltensperger, U., and Worsnop, D. R.: Evolution of organic aerosols in the atmosphere, Science, 326, 1525–1529, 2009.

Jokinen, T., Berndt, T., Makkonen, R., Kerminen, V.-M., Junninen, H., Paasonen, P., Stratmann, F., Herrmann, H., Guenther, A. B., Worsnop, D. R., Kulmala, M., Ehn, M., and Sipilä, M.: Production of extremely low volatile organic compounds from biogenic emissions: Measured yields and atmospheric implications, Proc. Natl. Acad. Sci. U. S. A., 112, 7123–7128, 2015.

Joo, T., Rivera-Rios, J. C., Takeuchi, M., Alvarado, M. J., and Ng, N. L.: Secondary Organic Aerosol Formation from Reaction of 3-Methylfuran with Nitrate Radicals, ACS Earth Space Chem., 3, 922–934, 2019.

Kang, E., Root, M. J., Toohey, D. W., and Brune, W. H.: Introducing the concept of Potential Aerosol Mass (PAM), Atmos. Chem. Phys., 7, 5727–5744, 2007.

Kidd, C., Perraud, V., Wingen, L. M., and Finlayson-Pitts, B. J.: Integrating phase and composition of secondary organic aerosol from the ozonolysis of α-pinene, Proc. Natl. Acad. Sci. U. S. A., 111, 7552–7557, 2014.

Kirkby, J., Duplissy, J., Sengupta, K., Frege, C., Gordon, H., Williamson, C., Heinritzi, M., Simon, M., Yan, C., Almeida, J., Tröstl, J., Nieminen, T., Ortega, I. K., Wagner, R., Adamov, A., Amorim, A., Bernhammer, A.-K., Bianchi, F., Breitenlechner, M., Brilke, S., Chen, X., Craven, J., Dias, A., Ehrhart, S., Flagan, R. C., Franchin, A., Fuchs, C., Guida, R., Hakala, J., Hoyle, C. R., Jokinen, T., Junninen, H., Kangasluoma, J., Kim, J., Krapf, M., Kürten, A., Laaksonen, A., Lehtipalo, K., Makhmutov, V., Mathot, S., Molteni, U., Onnela, A., Peräkylä, O., Piel, F., Petäjä, T., Praplan, A. P., Pringle, K., Rap, A., Richards, N. A. D., Riipinen, I., Rissanen, M. P., Rondo, L., Sarnela, N., Schobesberger, S., Scott, C. E., Seinfeld, J. H., Sipilä, M., Steiner, G., Stozhkov, Y., Stratmann, F., Tomé, A., Virtanen, A., Vogel, A. L., Wagner, A. C., Wagner, P. E., Weingartner, E., Wimmer, D., Winkler, P. M., Ye, P., Zhang, X., Hansel, A., Dommen, J., Donahue, N. M., Worsnop, D. R., Baltensperger, U., Kulmala, M., Carslaw, K. S., and

Curtius, J.: Ion-induced nucleation of pure biogenic particles, Nature, 533, 521–526, 2016.

Knote, C., Barré, J., and Eckl, M.: BEATBOX v1.0: Background Error Analysis Testbed with Box Models, https://doi.org/10.5194/gmd-11-561-2018, 2018.

Koop, T., Bookhold, J., Shiraiwa, M., and Pöschl, U.: Glass transition and phase state of organic compounds: dependency on molecular properties and implications for secondary organic aerosols in the atmosphere, Phys. Chem. Chem. Phys., 13, 19238–19255, 2011.

Koss, A. R., Sekimoto, K., Gilman, J. B., Selimovic, V., Coggon, M. M., Zarzana, K. J., Yuan, B., Lerner, B. M., Brown, S. S., Jimenez, J. L., and Others: Non-methane organic gas emissions from biomass burning: identification, quantification, and emission factors from PTR-ToF during the FIREX 2016 laboratory experiment, Atmos. Chem. Phys., 18, 3299–3319, 2018.

Krechmer, J. E., Pagonis, D., Ziemann, P. J., and Jimenez, J. L.: Quantification of Gas-Wall Partitioning in Teflon Environmental Chambers Using Rapid Bursts of Low-Volatility Oxidized Species Generated in Situ, Environ. Sci. Technol., 50, 5757–5765, 2016.

Kroll, J. H., Smith, J. D., Che, D. L., Kessler, S. H., Worsnop, D. R., and Wilson, K. R.: Measurement of fragmentation and functionalization pathways in the heterogeneous oxidation of oxidized organic aerosol, Phys. Chem. Chem. Phys., 11, 8005–8014, 2009.

Lambe, A. T., Miracolo, M. A., Hennigan, C. J., Robinson, A. L., and Donahue, N. M.: Effective rate constants and uptake coefficients for the reactions of organic molecular markers (n-alkanes, hopanes, and steranes) in motor oil and diesel primary organic aerosols with hydroxyl radicals, Environ. Sci. Technol., 43, 8794–8800, 2009.

Lambe, A. T., Ahern, A. T., Williams, L. R., Slowik, J. G., Wong, J. P. S., Abbatt, J. P. D., Brune, W. H., Ng, N. L., Wright, J. P., Croasdale, D. R., Worsnop, D. R., Davidovits, P., and Onasch, T. B.: Characterization of aerosol photooxidation flow reactors: heterogeneous oxidation, secondary organic aerosol formation and cloud condensation nuclei activity measurements, Atmospheric Measurement Techniques, 4, 445–461, 2011.

Lambe, A. T., Chhabra, P. S., Onasch, T. B., Brune, W. H., Hunter, J. F., Kroll, J. H., Cummings, M. J., Brogan, J. F., Parmar, Y., Worsnop, D. R., Kolb, C. E., and Davidovits, P.: Effect of oxidant concentration, exposure time, and seed particles on secondary organic aerosol chemical composition and yield, Atmos. Chem. Phys., 15, 3063–3075, 2015.

Lee, B. H., Lopez-Hilfiker, F. D., Mohr, C., Kurtén, T., Worsnop, D. R., and Thornton, J. A.: An iodide-adduct high-resolution time-of-flight chemical-ionization mass spectrometer: application to atmospheric inorganic and organic compounds, Environ. Sci. Technol., 48, 6309–6317, 2014.

Lewis, A. C., Carslaw, N., Marriott, P. J., Kinghorn, R. M., Morrison, P., Lee, A. L., Bartle, K. D., and Pilling, M. J.: A larger pool of ozone-forming carbon compounds in urban atmospheres, Nature, 405, 778–781, 2000.

Li, L., Tang, P., Nakao, S., and Cocker, D. R., III: Impact of molecular structure on secondary organic aerosol formation from aromatic hydrocarbon photooxidation under low-NO x conditions, Atmos. Chem. Phys., 16, 10793–10808, 2016.

Li, W., Li, L., Chen, C.-L., Kacarab, M., Peng, W., Price, D., Xu, J., and Cocker, D. R.: Potential of select intermediate-volatility organic compounds and consumer products for secondary organic aerosol and

ozone formation under relevant urban conditions, Atmos. Environ., 178, 109–117, 2018.

Li, Y. and Shiraiwa, M.: Timescales of secondary organic aerosols to reach equilibrium at various temperatures and relative humidities, Atmos. Chem. Phys., 19, 5959–5971, 2019.

Lim, Y. B. and Ziemann, P. J.: Effects of molecular structure on aerosol yields from OH radical-initiated reactions of linear, branched, and cyclic alkanes in the presence of NOx, Environ. Sci. Technol., 43, 2328–2334, 2009.

Liu, T., Wang, X., Deng, W., Hu, Q., Ding, X., Zhang, Y., He, Q., Zhang, Z., Lü, S., Bi, X., Chen, J., and Yu, J.: Secondary organic aerosol formation from photochemical aging of light-duty gasoline vehicle exhausts in a smog chamber, Atmos. Chem. Phys., 15, 9049–9062, 2015.

Lopez-Hilfiker, F. D., Mohr, C., D'Ambro, E. L., Lutz, A., Riedel, T. P., Gaston, C. J., Iyer, S., Zhang, Z., Gold, A., Surratt, J. D., and Others: Molecular composition and volatility of organic aerosol in the Southeastern US: implications for IEPOX derived SOA, Environ. Sci. Technol., 50, 2200–2209, 2016.

Loza, C. L., Chhabra, P. S., Yee, L. D., Craven, J. S., Flagan, R. C., and Seinfeld, J. H.: Chemical aging of *m*-xylene secondary organic aerosol: laboratory chamber study, Atmos. Chem. Phys., 12, 151–167, 2012.

Loza, C. L., Craven, J. S., Yee, L. D., Coggon, M. M., Schwantes, R. H., Shiraiwa, M., Zhang, X., Schilling, K. A., Ng, N. L., Canagaratna, M. R., Ziemann, P. J., Flagan, R. C., and Seinfeld, J. H.: Secondary organic aerosol yields of 12-carbon alkanes, Atmos. Chem. Phys., 14, 1423–1439, 2014.

Lunderman, S., Fioroni, G. M., McCormick, R. L., Nimlos, M. R., Rahimi, M. J., and Grout, R. W.: Screening Fuels for Autoignition with Small-Volume Experiments and Gaussian Process Classification, Energy Fuels, 32, 9581–9591, 2018.

Marais, E. A., Jacob, D. J., Jimenez, J. L., Campuzano-Jost, P., Day, D. A., Hu, W., Krechmer, J., Zhu, L., Kim, P. S., Miller, C. C., Fisher, J. A., Travis, K., Yu, K., Hanisco, T. F., Wolfe, G. M., Arkinson, H. L., Pye, H. O. T., Froyd, K. D., Liao, J., and McNeill, V. F.: Aqueous-phase mechanism for secondary organic aerosol formation from isoprene: application to the Southeast United States and co-benefit of SO2 emission controls, Atmos. Chem. Phys., 16, 1603–1618, 2016.

Matsunaga, A. and Ziemann, P. J.: Gas-Wall Partitioning of Organic Compounds in a Teflon Film Chamber and Potential Effects on Reaction Product and Aerosol Yield Measurements, Aerosol Sci. Technol., 44, 881–892, 2010.

May, A. A., Nguyen, N. T., Presto, A. A., Gordon, T. D., Lipsky, E. M., Karve, M., Gutierrez, A., Robertson, W. H., Zhang, M., Brandow, C., Chang, O., Chen, S., Cicero-Fernandez, P., Dinkins, L., Fuentes, M., Huang, S.-M., Ling, R., Long, J., Maddox, C., Massetti, J., McCauley, E., Miguel, A., Na, K., Ong, R., Pang, Y., Rieger, P., Sax, T., Truong, T., Vo, T., Chattopadhyay, S., Maldonado, H., Maricq, M. M., and Robinson, A. L.: Gas- and particle-phase primary emissions from in-use, on-road gasoline and diesel vehicles, Atmos. Environ., 88, 247–260, 2014.

McCormick, R. L., Fioroni, G., Fouts, L., Christensen, E., Yanowitz, J., Polikarpov, E., Albrecht, K., Gaspar, D. J., Gladden, J., and George, A.: Selection Criteria and Screening of Potential Biomass-Derived Streams as Fuel Blendstocks for Advanced Spark-Ignition Engines, 10, 442–460, 2017.

McDonald, B. C., de Gouw, J. A., Gilman, J. B., Jathar, S. H., Akherati, A., Cappa, C. D., Jimenez, J. L., Lee-Taylor, J., Hayes, P. L., McKeen, S. A., Cui, Y. Y., Kim, S.-W., Gentner, D. R., Isaacman-

VanWertz, G., Goldstein, A. H., Harley, R. A., Frost, G. J., Roberts, J. M., Ryerson, T. B., and Trainer, M.: Volatile chemical products emerging as largest petrochemical source of urban organic emissions, Science, 359, 760–764, 2018.

McDuffie, E. E., Smith, S. J., O'Rourke, P., Tibrewal, K., Venkataraman, C., Marais, E. A., Zheng, B., Crippa, M., Brauer, M., and Martin, R. V.: A global anthropogenic emission inventory of atmospheric pollutants from sector- and fuel-specific sources (1970–2017): an application of the Community Emissions Data System (CEDS), Earth Syst. Sci. Data, 12, 3413–3442, 2020.

McMurry, P. H. and Grosjean, D.: Gas and aerosol wall losses in Teflon film smog chambers, Environ. Sci. Technol., 19, 1176–1182, 1985a.

McMurry, P. H. and Grosjean, D.: Photochemical formation of organic aerosols: Growth laws and mechanisms, https://doi.org/10.1016/0004-6981(85)90282-3, 1985b.

McNeill, V. F.: Aqueous organic chemistry in the atmosphere: sources and chemical processing of organic aerosols, Environ. Sci. Technol., 49, 1237–1244, 2015.

McVay, R. C., Cappa, C. D., and Seinfeld, J. H.: Vapor-wall deposition in chambers: theoretical considerations, Environ. Sci. Technol., 48, 10251–10258, 2014.

Middlebrook, A. M., Bahreini, R., Jimenez, J. L., and Canagaratna, M. R.: Evaluation of Composition-Dependent Collection Efficiencies for the Aerodyne Aerosol Mass Spectrometer using Field Data, Aerosol Sci. Technol., 46, 258–271, 2012.

Miracolo, M. A., Presto, A. A., Lambe, A. T., Hennigan, C. J., Donahue, N. M., Kroll, J. H., Worsnop, D. R., and Robinson, A. L.: Photo-oxidation of low-volatility organics found in motor vehicle emissions: production and chemical evolution of organic aerosol mass, Environ. Sci. Technol., 44, 1638–1643, 2010.

Monks, P. S., Archibald, A. T., Colette, A., Cooper, O., Coyle, M., Derwent, R., Fowler, D., Granier, C., Law, K. S., Mills, G. E., Stevenson, D. S., Tarasova, O., Thouret, V., von Schneidemesser, E., Sommariva, R., Wild, O., and Williams, M. L.: Tropospheric ozone and its precursors from the urban to the global scale from air quality to short-lived climate forcer, 15, 8889–8973, 2015.

Morrison, G. M., Yeh, S., Eggert, A. R., Yang, C., Nelson, J. H., Greenblatt, J. B., Isaac, R., Jacobson, M. Z., Johnston, J., Kammen, D. M., Mileva, A., Moore, J., Roland-Holst, D., Wei, M., Weyant, J. P., Williams, J. H., Williams, R., and Zapata, C. B.: Comparison of low-carbon pathways for California, Clim. Change, 131, 545–557, 2015.

Mu, Q., Shiraiwa, M., Octaviani, M., Ma, N., Ding, A., Su, H., Lammel, G., Pöschl, U., and Cheng, Y.: Temperature effect on phase state and reactivity controls atmospheric multiphase chemistry and transport of PAHs, Sci Adv, 4, eaap7314, 2018.

Murphy, B. N., Woody, M. C., Jimenez, J. L., Carlton, A. M. G., Hayes, P. L., Liu, S., Ng, N. L., Russell, L. M., Setyan, A., Xu, L., Young, J., Zaveri, R. A., Zhang, Q., and Pye, H. O. T.: Semivolatile POA and parameterized total combustion SOA in CMAQv5.2: impacts on source strength and partitioning, Atmos. Chem. Phys., 17, 11107–11133, 2017.

Murray, B. J., Wilson, T. W., Dobbie, S., Cui, Z., Al-Jumur, S. M. R. K., Möhler, O., Schnaiter, M., Wagner, R., Benz, S., Niemand, M., Saathoff, H., Ebert, V., Wagner, S., and Kärcher, B.: Heterogeneous nucleation of ice particles on glassy aerosols under cirrus conditions, Nat. Geosci., 3, 233–237, 2010.

Nah, T., McVay, R. C., Zhang, X., Boyd, C. M., Seinfeld, J. H., and Ng, N. L.: Influence of seed aerosol surface area and oxidation rate on vapor wall deposition and SOA mass yields: a case study with α-pinene ozonolysis, Atmos. Chem. Phys., 16, 9361–9379, 2016.

Nah, T., McVay, R. C., Pierce, J. R., Seinfeld, J. H., and Ng, N. L.: Constraining uncertainties in particle-wall deposition correction during SOA formation in chamber experiments, Atmos. Chem. Phys., 17, 2297–2310, 2017.

Narula, C. K., Li, Z., Casbeer, E. M., Geiger, R. A., Moses-Debusk, M., Keller, M., Buchanan, M. V., and Davison, B. H.: Heterobimetallic Zeolite, InV-ZSM-5, Enables Efficient Conversion of Biomass Derived Ethanol to Renewable Hydrocarbons, Sci. Rep., 5, 16039, 2015.

Ng, N. L., Kroll, J. H., Keywood, M. D., Bahreini, R., Varutbangkul, V., Flagan, R. C., Seinfeld, J. H., Lee, A., and Goldstein, A. H.: Contribution of first- versus second-generation products to secondary organic aerosols formed in the oxidation of biogenic hydrocarbons, Environ. Sci. Technol., 40, 2283–2297, 2006.

Ng, N. L., Kroll, J. H., Chan, A. W. H., Chhabra, P. S., Flagan, R. C., and Seinfeld, J. H.: Secondary organic aerosol formation from m-xylene, toluene, and benzene, Atmos. Chem. Phys., 7, 3909–3922, 2007.

Ng, N. L., Herndon, S. C., Trimborn, A., Canagaratna, M. R., Croteau, P. L., Onasch, T. B., Sueper, D., Worsnop, D. R., Zhang, Q., Sun, Y. L., and Jayne, J. T.: An Aerosol Chemical Speciation Monitor (ACSM) for Routine Monitoring of the Composition and Mass Concentrations of Ambient Aerosol, Aerosol Sci. Technol., 45, 780–794, 2011.

Odum, J. R., Hoffmann, T., Bowman, F., Collins, D., Flagan, R. C., and Seinfeld, J. H.: Gas/particle partitioning and secondary organic aerosol yields, Environ. Sci. Technol., 30, 2580–2585, 1996.

Odum, J. R., Jungkamp, T. P. W., Griffin, R. J., Forstner, H. J. L., Flagan, R. C., and Seinfeld, J. H.: Aromatics, Reformulated Gasoline, and Atmospheric Organic Aerosol Formation, Environ. Sci. Technol., 31, 1890–1897, 1997.

O'Meara, S., Topping, D. O., and McFiggans, G.: The rate of equilibration of viscous aerosol particles, Atmos. Chem. Phys., 16, 5299–5313, 2016.

Ortega, A. M., Hayes, P. L., Peng, Z., Palm, B. B., Hu, W., Day, D. A., Li, R., Cubison, M. J., Brune, W. H., Graus, M., Warneke, C., Gilman, J. B., Kuster, W. C., de Gouw, J., Gutiérrez-Montes, C., and Jimenez, J. L.: Real-time measurements of secondary organic aerosol formation and aging from ambient air in an oxidation flow reactor in the Los Angeles area, Atmos. Chem. Phys., 16, 7411–7433, 2016.

Pachauri, R. K., Allen, M. R., Barros, V. R., Broome, J., Cramer, W., Christ, R., Church, J. A., Clarke, L., Dahe, Q., Dasgupta, P., Dubash, N. K., Edenhofer, O., Elgizouli, I., Field, C. B., Forster, P., Friedlingstein, P., Fuglestvedt, J., Gomez-Echeverri, L., Hallegatte, S., Hegerl, G., Howden, M., Jiang, K., Jimenez Cisneroz, B., Kattsov, V., Lee, H., Mach, K. J., Marotzke, J., Mastrandrea, M. D., Meyer, L., Minx, J., Mulugetta, Y., O'Brien, K., Oppenheimer, M., Pereira, J. J., Pichs-Madruga, R., Plattner, G.-K., Pörtner, H.-O., Power, S. B., Preston, B., Ravindranath, N. H., Reisinger, A., Riahi, K., Rusticucci, M., Scholes, R., Seyboth, K., Sokona, Y., Stavins, R., Stocker, T. F., Tschakert, P., van Vuuren, D., and van Ypserle, J.-P.: Climate Change 2014: Synthesis Report. Contribution of Working Groups I, II and III to the Fifth Assessment Report of the Intergovernmental Panel on Climate Change, 151, 2014.

Pai, S. J., Heald, C. L., Pierce, J. R., Farina, S. C., Marais, E. A., Jimenez, J. L., Campuzano-Jost, P.,

Nault, B. A., Middlebrook, A. M., Coe, H., Shilling, J. E., Bahreini, R., Dingle, J. H., and Vu, K.: An evaluation of global organic aerosol schemes using airborne observations, Atmos. Chem. Phys., 20, 2637–2665, 2020.

Pajunoja, A., Malila, J., Hao, L., Joutsensaari, J., Lehtinen, K. E. J., and Virtanen, A.: Estimating the Viscosity Range of SOA Particles Based on Their Coalescence Time, Aerosol Sci. Technol., 48, i–iv, 2014.

Palm, B. B., Campuzano-Jost, P., Ortega, A. M., Day, D. A., Kaser, L., Jud, W., Karl, T., Hansel, A., Hunter, J. F., Cross, E. S., Kroll, J. H., Peng, Z., Brune, W. H., and Jimenez, J. L.: In situ secondary organic aerosol formation from ambient pine forest air using an oxidation flow reactor, Atmos. Chem. Phys., 16, 2943–2970, 2016.

Palm, B. B., de Sá, S. S., Day, D. A., Campuzano-Jost, P., Hu, W., Seco, R., Sjostedt, S. J., Park, J.-H., Guenther, A. B., Kim, S., Brito, J., Wurm, F., Artaxo, P., Thalman, R., Wang, J., Yee, L. D., Wernis, R., Isaacman-VanWertz, G., Goldstein, A. H., Liu, Y., Springston, S. R., Souza, R., Newburn, M. K., Alexander, M. L., Martin, S. T., and Jimenez, J. L.: Secondary organic aerosol formation from ambient air in an oxidation flow reactor in central Amazonia, Atmos. Chem. Phys., 18, 467–493, 2018.

Pandis, S. N. and Seinfeld, J. H.: Atmospheric chemistry and physics: From air pollution to climate change, Wiley, 2006.

Peng, Z. and Jimenez, J. L.: Modeling of the chemistry in oxidation flow reactors with high initial NO, Atmos. Chem. Phys., 17, 11991–12010, 2017.

Peng, Z. and Jimenez, J. L.: Radical chemistry in oxidation flow reactors for atmospheric chemistry research, Chem. Soc. Rev., 49, 2570–2616, 2020.

Petters, M. and Kasparoglu, S.: Predicting the influence of particle size on the glass transition temperature and viscosity of secondary organic material, Sci. Rep., 10, 15170, 2020.

Pierce, J. R. and Adams, P. J.: Efficiency of cloud condensation nuclei formation from ultrafine particles, Atmos. Chem. Phys., 7, 1367–1379, 2007.

Pierce, J. R., Chen, K., and Adams, P. J.: Contribution of primary carbonaceous aerosol to cloud condensation nuclei: processes and uncertainties evaluated with a global aerosol microphysics model, Atmos. Chem. Phys., 7, 5447–5466, 2007.

Pierce, J. R., Engelhart, G. J., Hildebrandt, L., Weitkamp, E. A., Pathak, R. K., Donahue, N. M., Robinson, A. L., Adams, P. J., and Pandis, S. N.: Constraining Particle Evolution from Wall Losses, Coagulation, and Condensation-Evaporation in Smog-Chamber Experiments: Optimal Estimation Based on Size Distribution Measurements, https://doi.org/10.1080/02786820802389251, 2008.

Pierce, J. R., Riipinen, I., Kulmala, M., Ehn, M., Petäjä, T., Junninen, H., Worsnop, D. R., and Donahue, N. M.: Quantification of the volatility of secondary organic compounds in ultrafine particles during nucleation events, Atmos. Chem. Phys., 11, 9019–9036, 2011.

Porter, W. C., Jimenez, J. L., and Barsanti, K. C.: Quantifying Atmospheric Parameter Ranges for Ambient Secondary Organic Aerosol Formation, ACS Earth Space Chem., 5, 2380–2397, 2021.

Presto, A. A., Miracolo, M. A., Donahue, N. M., and Robinson, A. L.: Secondary organic aerosol formation from high-NO(x) photo-oxidation of low volatility precursors: n-alkanes, Environ. Sci.

Technol., 44, 2029–2034, 2010.

Price, H. C., Mattsson, J., Zhang, Y., Bertram, A. K., Davies, J. F., Grayson, J. W., Martin, S. T., O'Sullivan, D., Reid, J. P., Rickards, A. M. J., and Murray, B. J.: Water diffusion in atmospherically relevant α-pinene secondary organic material, Chem. Sci., 6, 4876–4883, 2015.

Pye, H. O. T. and Pouliot, G. A.: Modeling the role of alkanes, polycyclic aromatic hydrocarbons, and their oligomers in secondary organic aerosol formation, Environ. Sci. Technol., 46, 6041–6047, 2012.

Pye, H. O. T., Chan, A. W. H., Barkley, M. P., and Seinfeld, J. H.: Global modeling of organic aerosol: the importance of reactive nitrogen (NO_x and NO_3), Atmos. Chem. Phys., 10, 11261–11276, 2010.

Randerson, J. T., Van Der Werf, G. R., Giglio, L., Collatz, G. J., and Kasibhatla, P. S.: Global Fire Emissions Database, Version 4.1 (GFEDv4), https://doi.org/10.3334/ORNLDAAC/1293, 2015.

Reid, J. P., Bertram, A. K., Topping, D. O., Laskin, A., Martin, S. T., Petters, M. D., Pope, F. D., and Rovelli, G.: The viscosity of atmospherically relevant organic particles, Nat. Commun., 9, 956, 2018.

Renbaum-Wolff, L., Grayson, J. W., and Bertram, A. K.: Technical Note: New methodology for measuring viscosities in small volumes characteristic of environmental chamber particle samples, Atmos. Chem. Phys., 13, 791–802, 2013.

Riipinen, I., Pierce, J. R., Donahue, N. M., and Pandis, S. N.: Equilibration time scales of organic aerosol inside thermodenuders: Evaporation kinetics versus thermodynamics, Atmos. Environ., 44, 597–607, 2010.

Riipinen, I., Pierce, J. R., Yli-Juuti, T., Nieminen, T., Häkkinen, S., Ehn, M., Junninen, H., Lehtipalo, K., Petäjä, T., Slowik, J., Chang, R., Shantz, N. C., Abbatt, J., Leaitch, W. R., Kerminen, V.-M., Worsnop, D. R., Pandis, S. N., Donahue, N. M., and Kulmala, M.: Organic condensation: a vital link connecting aerosol formation to cloud condensation nuclei (CCN) concentrations, Atmos. Chem. Phys., 11, 3865–3878, 2011.

Robinson, A. L., Donahue, N. M., Shrivastava, M. K., Weitkamp, E. A., Sage, A. M., Grieshop, A. P., Lane, T. E., Pierce, J. R., and Pandis, S. N.: Rethinking organic aerosols: semivolatile emissions and photochemical aging, Science, 315, 1259–1262, 2007.

Roldin, P., Eriksson, A. C., Nordin, E. Z., Hermansson, E., Mogensen, D., Rusanen, A., Boy, M., Swietlicki, E., Svenningsson, B., Zelenyuk, A., and Pagels, J.: Modelling non-equilibrium secondary organic aerosol formation and evaporation with the aerosol dynamics, gas- and particle-phase chemistry kinetic multilayer model ADCHAM, Atmos. Chem. Phys., 14, 7953–7993, 2014.

Sato, K., Takami, A., Kato, Y., Seta, T., Fujitani, Y., Hikida, T., Shimono, A., and Imamura, T.: AMS and LC/MS analyses of SOA from the photooxidation of benzene and 1,3,5-trimethylbenzene in the presence of NO_x: effects of chemical structure on SOA aging, Atmos. Chem. Phys., 12, 4667–4682, 2012.

Sato, K., Fujitani, Y., Inomata, S., Morino, Y., Tanabe, K., Hikida, T., Shimono, A., Takami, A., Fushimi, A., Kondo, Y., Imamura, T., Tanimoto, H., and Sugata, S.: A study of volatility by composition, heating, and dilution measurements of secondary organic aerosol from 1,3,5-trimethylbenzene, Atmos. Chem. Phys., 19, 14901–14915, 2019.

Saunders, S. M., Jenkin, M. E., Derwent, R. G., and Pilling, M. J.: Protocol for the development of the Master Chemical Mechanism, MCM v3 (Part A): tropospheric degradation of non-aromatic volatile

organic compounds, Atmos. Chem. Phys., 3, 161–180, 2003.

Shakya, K. M. and Griffin, R. J.: Secondary Organic Aerosol from Photooxidation of Polycyclic Aromatic Hydrocarbons, Environ. Sci. Technol., 44, 8134–8139, 2010.

Shilling, J. E., Chen, Q., King, S. M., Rosenoern, T., Kroll, J. H., Worsnop, D. R., DeCarlo, P. F., Aiken, A. C., Sueper, D., Jimenez, J. L., and Martin, S. T.: Loading-dependent elemental composition of α-pinene SOA particles, Atmos. Chem. Phys., 8, 15343–15373, 2008.

Shiraiwa, M. and Seinfeld, J. H.: Equilibration timescale of atmospheric secondary organic aerosol partitioning, Geophys. Res. Lett., 39, https://doi.org/10.1029/2012GL054008, 2012.

Shiraiwa, M., Ammann, M., Koop, T., and Pöschl, U.: Gas uptake and chemical aging of semisolid organic aerosol particles, Proc. Natl. Acad. Sci. U. S. A., 108, 11003–11008, 2011.

Shiraiwa, M., Zuend, A., Bertram, A. K., and Seinfeld, J. H.: Gas-particle partitioning of atmospheric aerosols: interplay of physical state, non-ideal mixing and morphology, Phys. Chem. Chem. Phys., 15, 11441–11453, 2013a.

Shiraiwa, M., Yee, L. D., Schilling, K. A., Loza, C. L., Craven, J. S., Zuend, A., Ziemann, P. J., and Seinfeld, J. H.: Size distribution dynamics reveal particle-phase chemistry in organic aerosol formation, Proc. Natl. Acad. Sci. U. S. A., 110, 11746–11750, 2013b.

Shiraiwa, M., Li, Y., Tsimpidi, A. P., Karydis, V. A., Berkemeier, T., Pandis, S. N., Lelieveld, J., Koop, T., and Pöschl, U.: Global distribution of particle phase state in atmospheric secondary organic aerosols, Nat. Commun., 8, 15002, 2017.

Shrivastava, M., Zhao, C., Easter, R. C., Qian, Y., Zelenyuk, A., Fast, J. D., Liu, Y., Zhang, Q., and Guenther, A.: Sensitivity analysis of simulated SOA loadings using a variance-based statistical approach, J. Adv. Model. Earth Syst., 8, 499–519, 2016.

Shrivastava, M., Cappa, C. D., Fan, J., Goldstein, A. H., Guenther, A. B., Jimenez, J. L., Kuang, C., Laskin, A., Martin, S. T., Ng, N. L., Petaja, T., Pierce, J. R., Rasch, P. J., Roldin, P., Seinfeld, J. H., Shilling, J., Smith, J. N., Thornton, J. A., Volkamer, R., Wang, J., Worsnop, D. R., Zaveri, R. A., Zelenyuk, A., and Zhang, Q.: Recent advances in understanding secondary organic aerosol: Implications for global climate forcing, Rev. Geophys., 55, 509–559, 2017.

Shrivastava, M., Andreae, M. O., Artaxo, P., Barbosa, H. M. J., Berg, L. K., Brito, J., Ching, J., Easter, R. C., Fan, J., Fast, J. D., Feng, Z., Fuentes, J. D., Glasius, M., Goldstein, A. H., Alves, E. G., Gomes, H., Gu, D., Guenther, A., Jathar, S. H., Kim, S., Liu, Y., Lou, S., Martin, S. T., McNeill, V. F., Medeiros, A., de Sá, S. S., Shilling, J. E., Springston, S. R., Souza, R. A. F., Thornton, J. A., Isaacman-VanWertz, G., Yee, L. D., Ynoue, R., Zaveri, R. A., Zelenyuk, A., and Zhao, C.: Urban pollution greatly enhances formation of natural aerosols over the Amazon rainforest, Nat. Commun., 10, 1046, 2019.

Simonen, P., Saukko, E., Karjalainen, P., Timonen, H., Bloss, M., Aakko-Saksa, P., Rönkkö, T., Keskinen, J., and Dal Maso, M.: A new oxidation flow reactor for measuring secondary aerosol formation of rapidly changing emission sources, Atmospheric Measurement Techniques, 10, 1519–1537, 2017.

Smith, J. D., Kroll, J. H., Cappa, C. D., Che, D. L., Liu, C. L., Ahmed, M., Leone, S. R., Worsnop, D. R., and Wilson, K. R.: The heterogeneous reaction of hydroxyl radicals with sub-micron squalane particles: a model system for understanding the oxidative aging of ambient aerosols, Atmos. Chem. Phys., 9, 3209–3222, 2009.

Song, C., Na, K., Warren, B., Malloy, Q., and Cocker, D. R.: Secondary organic aerosol formation from the photooxidation of p- and o-xylene, Environ. Sci. Technol., 41, 7403–7408, 2007.

Song, M., Liu, P. F., Hanna, S. J., Li, Y. J., Martin, S. T., and Bertram, A. K.: Relative humidity-dependent viscosities of isoprene-derived secondary organic material and atmospheric implications for isoprene-dominant forests, Atmos. Chem. Phys., 15, 5145–5159, 2015.

Song, M., Maclean, A. M., Huang, Y., Smith, N. R., Blair, S. L., Laskin, J., Laskin, A., DeRieux, W.-S. W., Li, Y., Shiraiwa, M., Nizkorodov, S. A., and Bertram, A. K.: Liquid–liquid phase separation and viscosity within secondary organic aerosol generated from diesel fuel vapors, Atmos. Chem. Phys., 19, 12515–12529, 2019.

Stocker, T. F., Qin, D., Plattner, G.-K., Tignor, M. M. B., Allen, S. K., Boschung, J., Nauels, A., Xia, Y., Bex, V., Midgley, P. M., Alexander, L. V., Bindoff, N. L., Breon, F.-M., Church, J. A., Cubasch, U., Emori, S., Forster, P., Friedlingstein, P., Gillett, N., Gregory, J. M., Hartmann, D. L., Jansen, E., Kirtman, B., Knutti, R., Kumar Kanikicharla, K., Lemke, P., Marotzke, J., Masson-Delmotte, V., Meehl, G. A., Mokhov, I. I., Piao, S., Dahe, Q., Ramaswamy, V., Randall, D., Rhein, M., Rojas, M., Sabine, C., Shindell, D., Talley, L. D., Vaughan, D. G., Xie, S.-P., Allen, M. R., Boucher, O., Chambers, D., Hesselbjerg Christensen, J., Ciais, P., Clark, P. U., Collins, M., Comiso, J. C., Vasconcellos de Menezes, V., Feely, R. A., Fichefet, T., Fiore, A. M., Flato, G., Fuglestvedt, J., Hegerl, G., Hezel, P. J., Johnson, G. C., Kaser, G., Kattsov, V., Kennedy, J., Klein Tank, A. M. G., Le Quere, C., Myhre, G., Osborn, T., Payne, A. J., Perlwitz, J., Power, S., Prather, M., Rintoul, S. R., Rogelj, J., Rusticucci, M., Schulz, M., Sedlacek, J., Stott, P. A., Sutton, R., Thorne, P. W., and Wuebbles, D.: Climate Change 2013. The Physical Science Basis. Working Group I Contribution to the Fifth Assessment Report of the Intergovernmental Panel on Climate Change - Abstract for decision-makers, 2013.

Stockwell, C. E., Veres, P. R., Williams, J., and Yokelson, R. J.: Characterization of biomass burning emissions from cooking fires, peat, crop residue, and other fuels with high-resolution proton-transfer-reaction time-of-flight mass spectrometry, Atmos. Chem. Phys., 15, 845–865, 2015.

Strollo, C. M. and Ziemann, P. J.: Products and mechanism of secondary organic aerosol formation from the reaction of 3-methylfuran with OH radicals in the presence of NOx, Atmos. Environ., 77, 534–543, 2013.

The International GEOS-Chem User Community: geoschem/GCClassic: GEOS-Chem 13.0.0, https://doi.org/10.5281/zenodo.4618180, 2021.

Tikkanen, O.-P., Hämäläinen, V., Rovelli, G., Lipponen, A., Shiraiwa, M., Reid, J. P., Lehtinen, K. E. J., and Yli-Juuti, T.: Optimization of process models for determining volatility distribution and viscosity of organic aerosols from isothermal particle evaporation data, Atmos. Chem. Phys., 19, 9333–9350, 2019.

Tkacik, D. S., Presto, A. A., Donahue, N. M., and Robinson, A. L.: Secondary organic aerosol formation from intermediate-volatility organic compounds: cyclic, linear, and branched alkanes, Environ. Sci. Technol., 46, 8773–8781, 2012.

Tröstl, J., Chuang, W. K., Gordon, H., Heinritzi, M., Yan, C., Molteni, U., Ahlm, L., Frege, C., Bianchi, F., Wagner, R., Simon, M., Lehtipalo, K., Williamson, C., Craven, J. S., Duplissy, J., Adamov, A., Almeida, J., Bernhammer, A.-K., Breitenlechner, M., Brilke, S., Dias, A., Ehrhart, S., Flagan, R. C., Franchin, A., Fuchs, C., Guida, R., Gysel, M., Hansel, A., Hoyle, C. R., Jokinen, T., Junninen, H., Kangasluoma, J., Keskinen, H., Kim, J., Krapf, M., Kürten, A., Laaksonen, A., Lawler, M., Leiminger, M., Mathot, S., Möhler, O., Nieminen, T., Onnela, A., Petäjä, T., Piel, F. M., Miettinen, P., Rissanen, M. P., Rondo, L., Sarnela, N., Schobesberger, S., Sengupta, K., Sipilä, M., Smith, J. N., Steiner, G., Tomè,

A., Virtanen, A., Wagner, A. C., Weingartner, E., Wimmer, D., Winkler, P. M., Ye, P., Carslaw, K. S., Curtius, J., Dommen, J., Kirkby, J., Kulmala, M., Riipinen, I., Worsnop, D. R., Donahue, N. M., and Baltensperger, U.: The role of low-volatility organic compounds in initial particle growth in the atmosphere, Nature, 533, 527–531, 2016.

Trump, E. R. and Donahue, N. M.: Oligomer formation within secondary organic aerosols: equilibrium and dynamic considerations, Atmos. Chem. Phys., 14, 3691–3701, 2014.

Tsigaridis, K., Daskalakis, N., Kanakidou, M., Adams, P. J., Artaxo, P., Bahadur, R., Balkanski, Y., Bauer, S. E., Bellouin, N., Benedetti, A., Bergman, T., Berntsen, T. K., Beukes, J. P., Bian, H., Carslaw, K. S., Chin, M., Curci, G., Diehl, T., Easter, R. C., Ghan, S. J., Gong, S. L., Hodzic, A., Hoyle, C. R., Iversen, T., Jathar, S., Jimenez, J. L., Kaiser, J. W., Kirkevåg, A., Koch, D., Kokkola, H., Lee, Y. H., Lin, G., Liu, X., Luo, G., Ma, X., Mann, G. W., Mihalopoulos, N., Morcrette, J.-J., Müller, J.-F., Myhre, G., Myriokefalitakis, S., Ng, N. L., O'Donnell, D., Penner, J. E., Pozzoli, L., Pringle, K. J., Russell, L. M., Schulz, M., Sciare, J., Seland, Ø., Shindell, D. T., Sillman, S., Skeie, R. B., Spracklen, D., Stavrakou, T., Steenrod, S. D., Takemura, T., Tiitta, P., Tilmes, S., Tost, H., van Noije, T., van Zyl, P. G., von Salzen, K., Yu, F., Wang, Z., Wang, Z., Zaveri, R. A., Zhang, H., Zhang, K., Zhang, Q., and Zhang, X.: The AeroCom evaluation and intercomparison of organic aerosol in global models, Atmos. Chem. Phys., 14, 10845–10895, 2014.

Vaden, T. D., Imre, D., Beránek, J., Shrivastava, M., and Zelenyuk, A.: Evaporation kinetics and phase of laboratory and ambient secondary organic aerosol, Proc. Natl. Acad. Sci. U. S. A., 108, 2190–2195, 2011.

Virtanen, A., Kannosto, J., Kuuluvainen, H., Arffman, A., Joutsensaari, J., Saukko, E., Hao, L., Yli-Pirilä, P., Tiitta, P., Holopainen, J. K., Keskinen, J., Worsnop, D. R., Smith, J. N., and Laaksonen, A.: Bounce behavior of freshly nucleated biogenic secondary organic aerosol particles, Atmos. Chem. Phys., 11, 8759–8766, 2011.

Volkamer, R., Jimenez, J. L., San Martini, F., Dzepina, K., Zhang, Q., Salcedo, D., Molina, L. T., Worsnop, D. R., and Molina, M. J.: Secondary organic aerosol formation from anthropogenic air pollution: Rapid and higher than expected, Geophys. Res. Lett., 33, https://doi.org/10.1029/2006GL026899, 2006.

Wang, B., Laskin, A., Roedel, T., Gilles, M. K., Moffet, R. C., Tivanski, A. V., and Knopf, D. A.: Heterogeneous ice nucleation and water uptake by field-collected atmospheric particles below 273 K, J. Geophys. Res., 117, https://doi.org/10.1029/2012JD017446, 2012.

Weitkamp, E. A., Sage, A. M., Pierce, J. R., Donahue, N. M., and Robinson, A. L.: Organic aerosol formation from photochemical oxidation of diesel exhaust in a smog chamber, Environ. Sci. Technol., 41, 6969–6975, 2007.

Xu, N. and Collins, D. R.: Design and characterization of a new oxidation flow reactor for laboratory and long-term ambient studies, Atmos. Meas. Tech., 14, 2891–2906, 2021.

Yee, L. D., Kautzman, K. E., Loza, C. L., Schilling, K. A., Coggon, M. M., Chhabra, P. S., Chan, M. N., Chan, A. W. H., Hersey, S. P., Crounse, J. D., Wennberg, P. O., Flagan, R. C., and Seinfeld, J. H.: Secondary organic aerosol formation from biomass burning intermediates: phenol and methoxyphenols, Atmos. Chem. Phys., 13, 8019–8043, 2013.

Yli-Juuti, T., Pajunoja, A., Tikkanen, O., Buchholz, A., Faiola, C., Väisänen, O., Hao, L., Kari, E., Peräkylä, O., Garmash, O., Shiraiwa, M., Ehn, M., Lehtinen, K., and Virtanen, A.: Factors controlling the evaporation of secondary organic aerosol from α-pinene ozonolysis, Geophys. Res. Lett., 44, 2562–2570,

2017.

Zaveri, R. A., Easter, R. C., Fast, J. D., and Peters, L. K.: Model for Simulating Aerosol Interactions and Chemistry (MOSAIC), J. Geophys. Res., 113, 1591, 2008.

Zaveri, R. A., Easter, R. C., Shilling, J. E., and Seinfeld, J. H.: Modeling kinetic partitioning of secondary organic aerosol and size distribution dynamics: representing effects of volatility, phase state, and particle-phase reaction, Atmos. Chem. Phys., 14, 5153–5181, 2014.

Zaveri, R. A., Shilling, J. E., Zelenyuk, A., Liu, J., Bell, D. M., D'Ambro, E. L., Gaston, C. J., Thornton, J. A., Laskin, A., Lin, P., Wilson, J., Easter, R. C., Wang, J., Bertram, A. K., Martin, S. T., Seinfeld, J. H., and Worsnop, D. R.: Growth Kinetics and Size Distribution Dynamics of Viscous Secondary Organic Aerosol, Environ. Sci. Technol., 52, 1191–1199, 2018.

Zaveri, R. A., Shilling, J. E., Zelenyuk, A., Zawadowicz, M. A., Suski, K., China, S., Bell, D. M., Veghte, D., and Laskin, A.: Particle-Phase Diffusion Modulates Partitioning of Semivolatile Organic Compounds to Aged Secondary Organic Aerosol, Environ. Sci. Technol., 54, 2595–2605, 2020.

Zawadowicz, M. A., Lee, B. H., Shrivastava, M., Zelenyuk, A., Zaveri, R. A., Flynn, C., Thornton, J. A., and Shilling, J. E.: Photolysis Controls Atmospheric Budgets of Biogenic Secondary Organic Aerosol, Environ. Sci. Technol., 54, 3861–3870, 2020.

Zender, C. S., Bian, H., and Newman, D.: Mineral Dust Entrainment and Deposition (DEAD) model: Description and 1990s dust climatology, J. Geophys. Res. D: Atmos., 108, https://doi.org/10.1029/2002JD002775, 2003.

Zhang, Q., Jimenez, J. L., Canagaratna, M. R., Allan, J. D., Coe, H., Ulbrich, I., Alfarra, M. R., Takami, A., Middlebrook, A. M., Sun, Y. L., Dzepina, K., Dunlea, E., Docherty, K., DeCarlo, P. F., Salcedo, D., Onasch, T., Jayne, J. T., Miyoshi, T., Shimono, A., Hatakeyama, S., Takegawa, N., Kondo, Y., Schneider, J., Drewnick, F., Borrmann, S., Weimer, S., Demerjian, K., Williams, P., Bower, K., Bahreini, R., Cottrell, L., Griffin, R. J., Rautiainen, J., Sun, J. Y., Zhang, Y. M., and Worsnop, D. R.: Ubiquity and dominance of oxygenated species in organic aerosols in anthropogenically-influenced Northern Hemisphere midlatitudes, Geophys. Res. Lett., 34, https://doi.org/10.1029/2007GL029979, 2007.

Zhang, R., Wang, G., Guo, S., Zamora, M. L., Ying, Q., Lin, Y., Wang, W., Hu, M., and Wang, Y.: Formation of urban fine particulate matter, Chem. Rev., 115, 3803–3855, 2015a.

Zhang, X., Pandis, S. N., and Seinfeld, J. H.: Diffusion-Limited Versus Quasi-Equilibrium Aerosol Growth, Aerosol Sci. Technol., 46, 874–885, 2012.

Zhang, X., Cappa, C. D., Jathar, S. H., McVay, R. C., Ensberg, J. J., Kleeman, M. J., and Seinfeld, J. H.: Influence of vapor wall loss in laboratory chambers on yields of secondary organic aerosol, Proc. Natl. Acad. Sci. U. S. A., 111, 5802–5807, 2014.

Zhang, X., McVay, R. C., Huang, D. D., Dalleska, N. F., Aumont, B., Flagan, R. C., and Seinfeld, J. H.: Formation and evolution of molecular products in α-pinene secondary organic aerosol, Proc. Natl. Acad. Sci. U. S. A., 112, 14168–14173, 2015b.

Zhao, Y., Thornton, J. A., and Pye, H. O. T.: Quantitative constraints on autoxidation and dimer formation from direct probing of monoterpene-derived peroxy radical chemistry, Proc. Natl. Acad. Sci. U. S. A., 115, 12142–12147, 2018.

Zhou, S., Shiraiwa, M., McWhinney, R. D., Pöschl, U., and Abbatt, J. P. D.: Kinetic limitations in gas-particle reactions arising from slow diffusion in secondary organic aerosol, Faraday Discuss., 165, 391–406, 2013.

Zhou, S., Hwang, B. C. H., Lakey, P. S. J., Zuend, A., Abbatt, J. P. D., and Shiraiwa, M.: Multiphase reactivity of polycyclic aromatic hydrocarbons is driven by phase separation and diffusion limitations, Proc. Natl. Acad. Sci. U. S. A., 116, 11658–11663, 2019.

Ziemann, P. J. and Atkinson, R.: Kinetics, products, and mechanisms of secondary organic aerosol formation, Chem. Soc. Rev., 41, 6582–6605, 2012.

Appendix A: Supplementary Information for Chapter 2

A1 HONO Synthesis

Measurements performed with a time-of-flight chemical ionization mass spectrometer (Tofwerk AG, Switzerland and Aerodyne Research Inc., MA) with an iodide reagent ion (Iodide-ToFCIMS) (Aljawhary et al., 2013; Lee et al., 2014; Lopez-Hilfiker et al., 2016) showed that the 'wet' HONO synthesis process of Ng et al. (2007) produced significantly higher concentrations of NO relative to HONO (NO:HONO~0.33 ppbv:a.u.) in the first 30 minutes, with much lower NO concentrations later (NO:HONO~0.06 ppbv:a.u.) (Figure A2(a)). As the HONO concentrations peaked later than those for NO and were relatively flat between 40 and 60 minutes, venting the bubbler output for the first ~30 minutes and injecting for the next ~30 minutes meant that the initial NO (and also NO_2^*) concentrations during the chamber experiment were substantially lower with very little effect on the HONO concentrations. In our experiments, our NO and NO_2^* before lights were turned on was 46±15 and 160±60 ppbv, respectively, significantly lower than those in historical experiments that have used this synthesis process (Ng et al., 2007; Presto et al., 2010). Dropwise addition of $NaNO_2$ into a H_2SO_4 solution can also lead to reduced NO and NO_2 production but perhaps not to the same degree to the technique used in this work (Ng et al., 2007). We also experimented with bubbling clean air at ~1.3 L min^{-1} through 80 mL of 10% H_2SO_4 and directing the H_2SO_4 vapors over solid $NaNO_2$ crystals before injecting the stream into the chamber. This synthesis process yielded a nearly 10-fold decrease in HONO emissions but with little to no NO production (Figure A2(b)). This 'dry' synthesis process might allow for HONO to be used as an OH precursor without coproduction of NO and NO_2^*, but will need to be explored in future work. Experiments performed with HCl as a substitute to H_2SO_4 resulted in relatively little to no HONO production.

A2 SAPRC Modeling

We were unable to measure VOC concentrations and its decay during the fuel experiments and this prevented us from quantifying the OH concentrations during those experiments. Instead, we relied on OH concentrations predicted by the SAPRC99 gas-phase chemical mechanism. The ability of the model to predict OH was first demonstrated with dedicated chamber measurements performed with toluene, before being used to determine OH for the fuel experiments.

We performed four chamber experiments with toluene, identical to the methods used in the fuel experiments. However, in these experiments, we used a gas chromatograph photoionization detector (GC-PID; SRI Instruments, CA) to measure the decay of toluene and estimate OH concentrations and exposures. As shown in Figure A3, the average OH exposure at the end of the experiment over those four toluene experiments was $(1.9\pm0.2)\times10^{7}$ molecules-h cm^{-3}. SAPRC99 was run using an offline version of the BOXMOX platform developed by Knote et al. (2018). Chamber simulations were performed by specifying initial concentrations of NO, O_3, toluene (as ARO1), and HONO, photolysis rates for all species in SAPRC99, and the chamber temperature and relative humidity. Since the HONO synthesis method typically produces equal amounts of NO and NO_2 concentrations (Zhang et al., 2014), we assumed the initial NO_2 to be equal to NO, although this assumption was not found to affect the findings from the SAPRC modeling. The photolysis rates for the chamber simulation were determined by scaling photolysis rates representative of UV-A lights (shared by Xuan Zhang, NCAR) to match the photolysis rate of NO_2 estimated from chemical actinometry experiments (0.25 min^{-1}; see Figure A1). Since we did not measure HONO concentrations, we adjusted the initial HONO concentration till the model predictions agreed with the observations of O_3 and NO. We did not attempt to match the model predictions of NO_2 because the measurements were likely to include reactive nitrogen species other

than NO_2 that were produced during the chamber experiment (e.g., nitric acid, peroxyacetyl nitrates). In Figure A4, we show the model-measurement comparison for the OH exposure and the O_3 and NO concentrations for four toluene experiments. We found that our approach to model the gas-phase chemistry by constraining the model predictions to O_3 and NO seemed to reproduce the observed OH exposure in the toluene experiments.

Based on our success with modeling the toluene experiments, we used the same approach to model the gas-phase chemistry in the fuel experiments. The SAPRC simulations required us to map the VOC species in the fuels to appropriate surrogates in SAPRC99. This was done using published assignments suggested by William Carter (SpecDB.xls found at https://intra.engr.ucr.edu/~carter/emitdb/). While the assignments were relatively trivial for the alkanes, aromatics, and alkenes found in gasoline and ETH, SAPRC99 does not have appropriate surrogates to model the gas-phase chemistry of cyclopentanone, diisobutylene, 2-methylfuran, and dimethylfuran. Based on SpecDB.xls, cyclopentanone was modeled as MEK (methyl ethyl ketone), diisobutylene was modeled as OLE2 (alkenes with k_{OH}>4.77×10^{-11} cm^3 $molecule^{-1}$ s^{-1}), and furans were modeled as ARO2 (aromatics with k_{OH}>1.36×10^{-11} cm^3 $molecule^{-1}$ s^{-1}). Results for O_3 and NO from simulations performed on a representative ETH experiment are shown in Figure A5(a) and predictions of OH exposure for all the fuel experiments are shown in Figure A5(b). The OH exposure seemed to vary with the fuel, the amount of fuel injected, and the reactivity of the fuel. Generally, the OH exposure for the relatively less reactive fuels, cyclopentanone, gasoline, and ETH, was within the bounds of the OH exposures measured with the toluene experiments but the OH exposure was substantially lower for the more reactive fuels, diisobutylene (factor of ~2) and the alkylfuran mixture (factor of ~5).

In the future, we recommend the use of a proton transfer reaction - time of flight - mass

spectrometer (PTR-ToF-MS) or a chemical ionization mass spectrometer (CIMS) to measure similar VOCs and their decay in the chamber experiments (Isaacman-VanWertz et al., 2017). Alternatively, or in addition, we suggest that simulations be performed with an explicit gas-phase chemical mechanism, the likes of MCM (Saunders et al., 2003; Jenkin et al., 2003) or GECKO-A (Aumont et al., 2005), to validate the OH data.

A3 Coefficient of Eddy Diffusion

We used the Aerosol Parameter Estimation (APE) model of Pierce et al. (2008) with the scanning mobility particle sizer (SMPS, GRIMM Aerosol Technik, Austria) data to determine the coagulation-corrected, size-resolved wall loss rate ($k_{par,j}$, where j is the size bin) for particles up to 100 nm during the dark portions of the experiment when no SOA was being formed. The calculations were only performed on data from six chamber experiments where we had access to sufficient SMPS data before the lights were turned on (minimum of 10 SMPS scans that showed uniform loss in particle number concentrations). We limited the calculations to particle sizes up to 100 nm because loss rates for larger sizes up to 1000 nm are strongly affected by the charge distribution on the particles and the Teflon® walls (McMurry and Grosjean, 1985a, b). These dark portions, over the six experiments, varied between 50 and 130 minutes. The $k_{par,j}$ values were then compiled together for all experiments to fit a study-wide $k_{w,p0}$ and k_e according to the following equation (Crump and Seinfeld, 1981):

$$k_{par,j} = \frac{1}{L}\left[\frac{8\sqrt{k_e D_j}}{\pi} + v_{s,j} \cdot coth\left(\frac{x}{2}\right)\right], where\ x = \frac{\pi v_{s,j}}{2\sqrt{k_e D_j}} \qquad \text{(A1)}$$

where D_j is the diffusion coefficient of the particle of size j in $m^2\ s^{-1}$, L is one of the sides of the chamber assuming a cubical chamber in m (2.15 m) and $\nu_{s,j}$ is the gravitational settling velocity of the particle of size j in $m\ s^{-1}$ (Hinds, 1999). The $k_{par,j}$ for all the experiments performed in this work and the ensemble fit are shown in Figure A6.

A4 Electronic Archive

† Electronic supplementary information is available at: https://github.com/yicongh/He-2020Arch

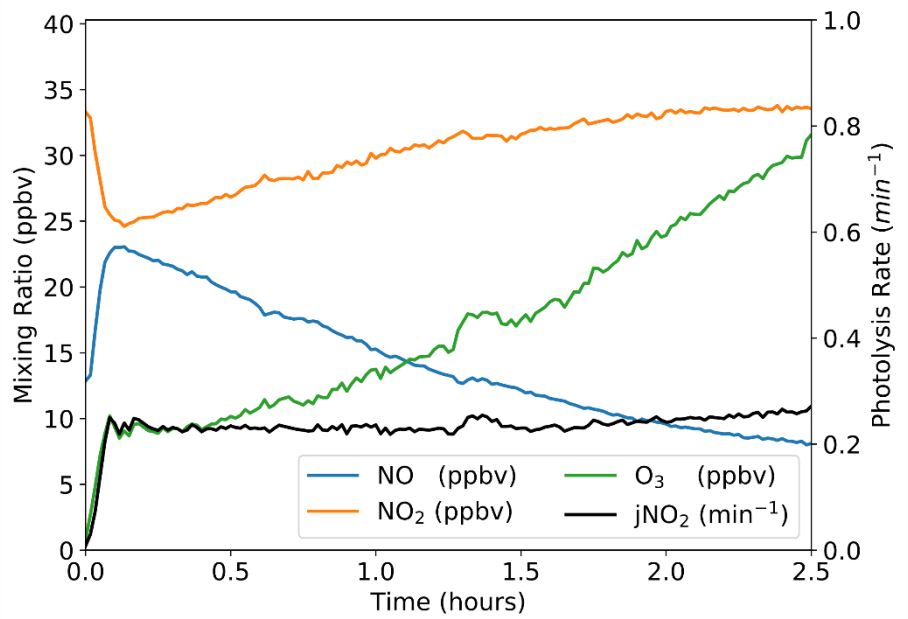

Figure A1: NO, NO_2 and O_3 concentrations and the NO_2 photolysis rate during the chemical actinometry experiment performed on May 20, 2016.

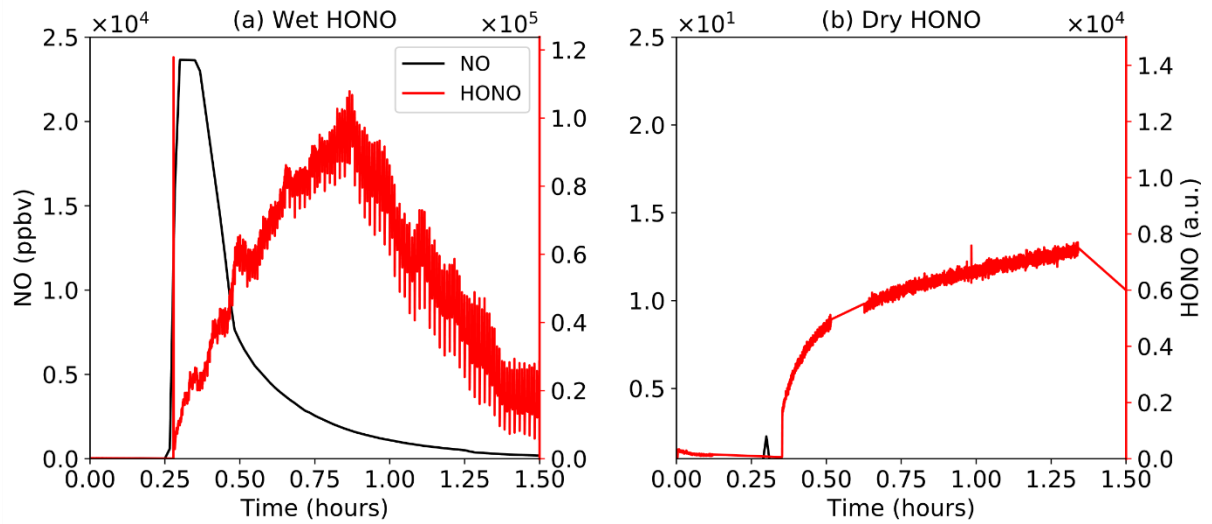

Figure A2: NO (ppbv) and HONO (arbitrary units) concentrations during the (a) wet and (b) dry HONO synthesis processes.

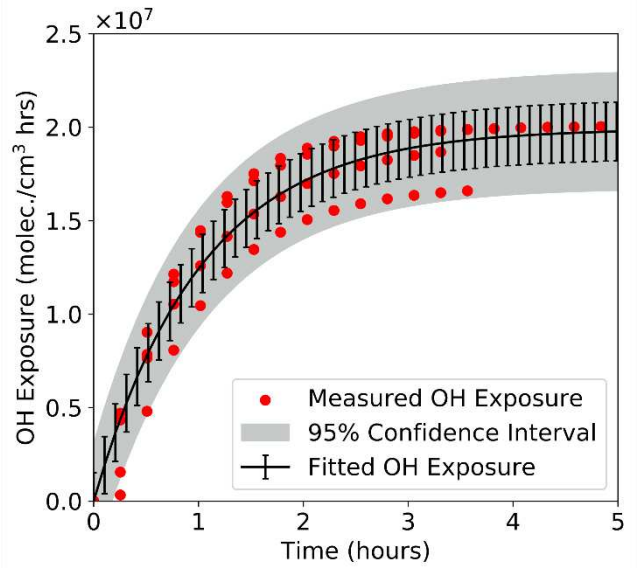

Figure A3: OH exposure calculated based on the decay of toluene in four separate experiments (red circles), along with the fit to the combined data (black lines).

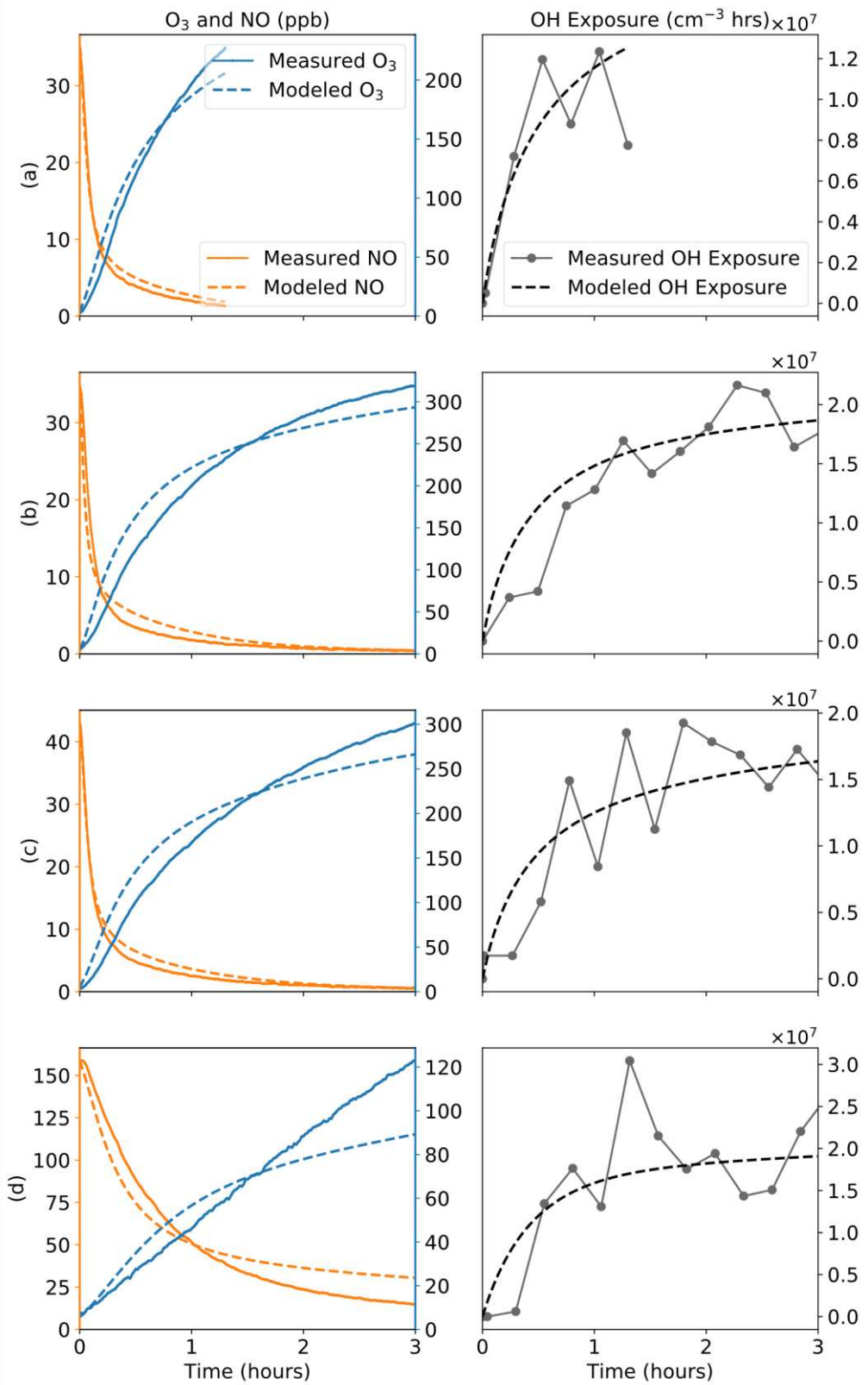

Figure A4: SAPRC model predictions of OH exposure compared to measurements when the model is constrained to O_3 and NO measurements for the four toluene experiments.

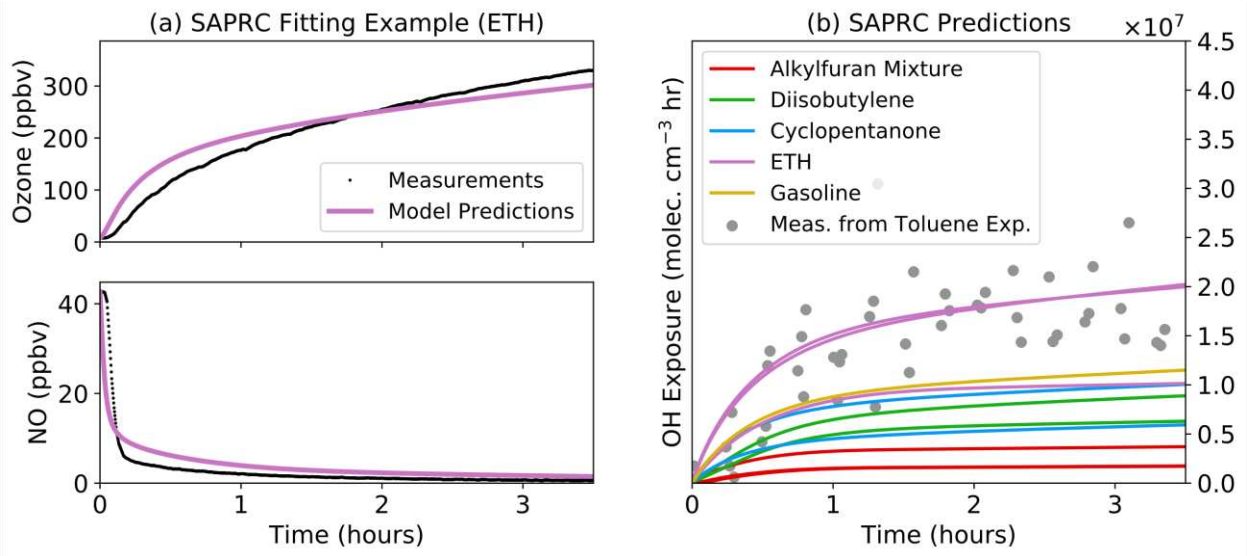

Figure A5: SAPRC model predictions of OH exposures when constrained to O_3 and NO measurements. An example of fitting the model is shown in panel (a). The predicted OH exposures for all fuel experiments are shown in panel (b).

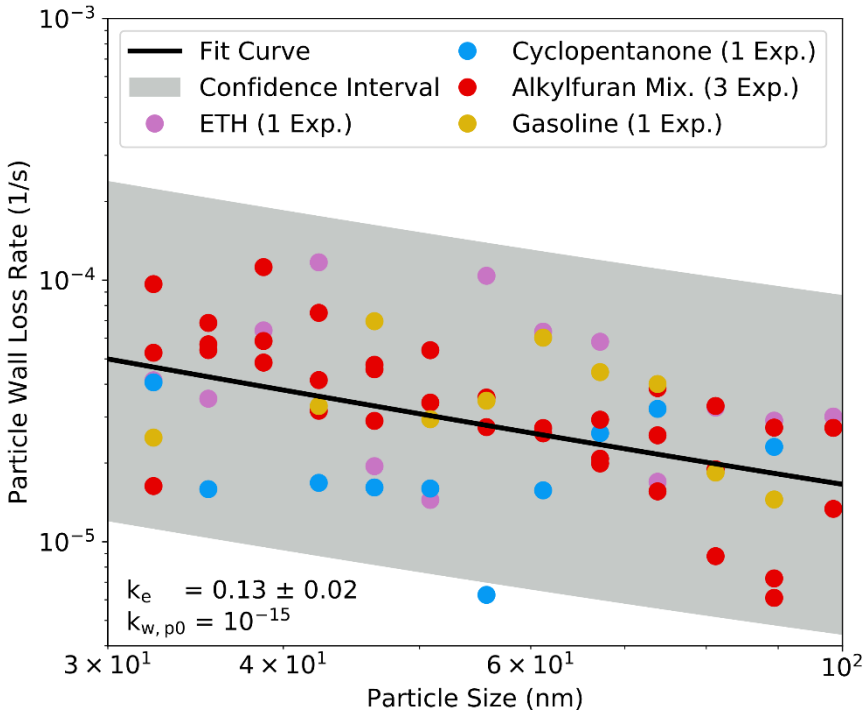

Figure A6: Particle wall loss rates calculated for particle sizes up to 100 nm for six experiments performed in this work. The solid black line represents the best fit to the data while the grey bands represent the 95 percent confidence interval.

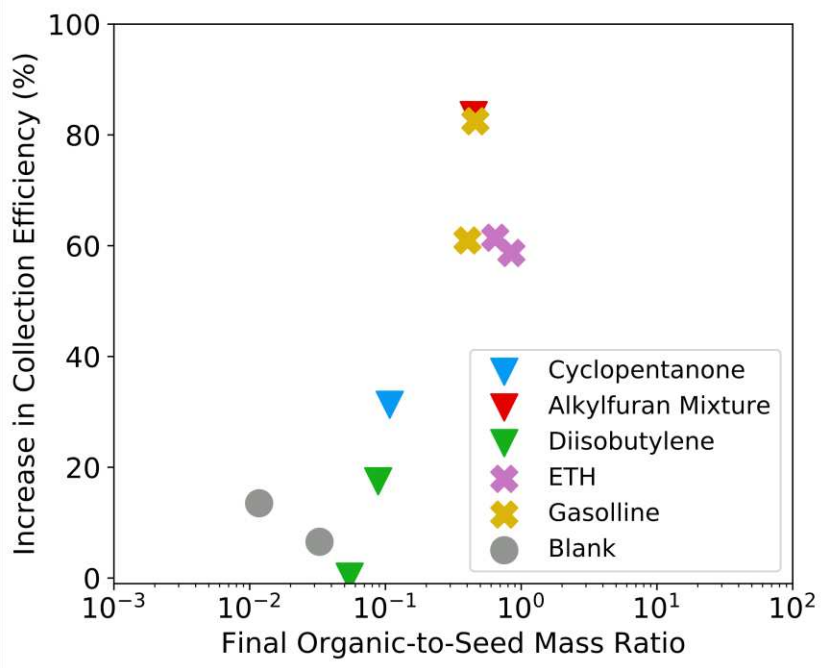

Figure A7: Scaling factor as a function of the organic-to-seed mass ratio for all experiments performed in this work where we had access to the SMPS and ACSM data.

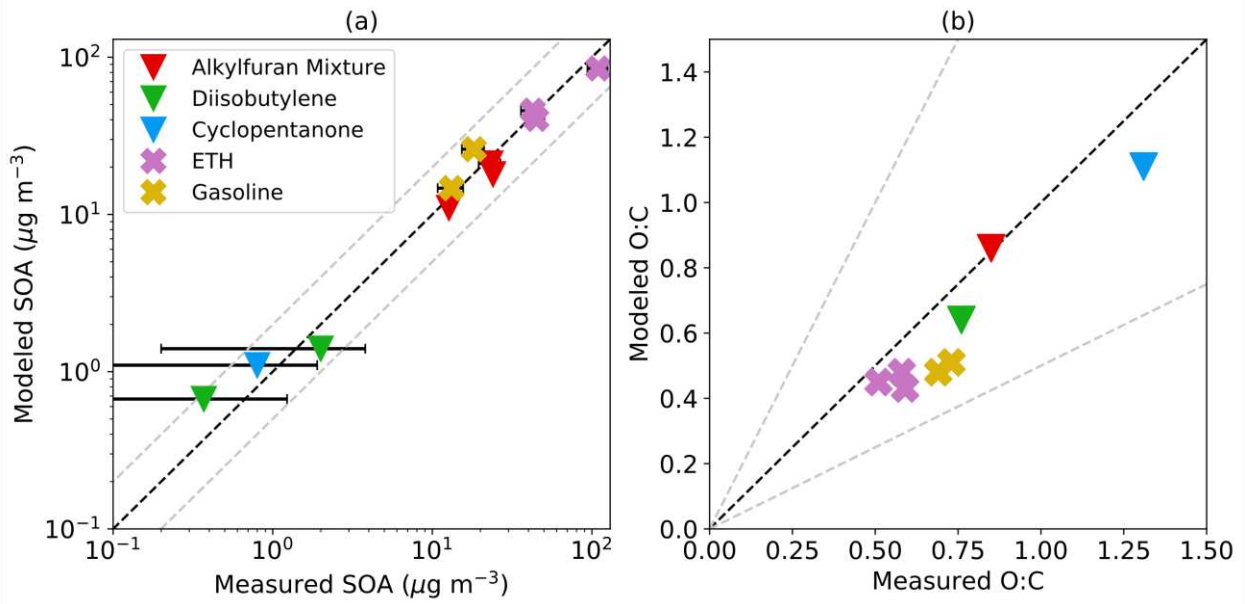

Figure A8: Scatter plot comparing the modeled and measured SOA mass concentrations and O:C for experiments performed in this work.

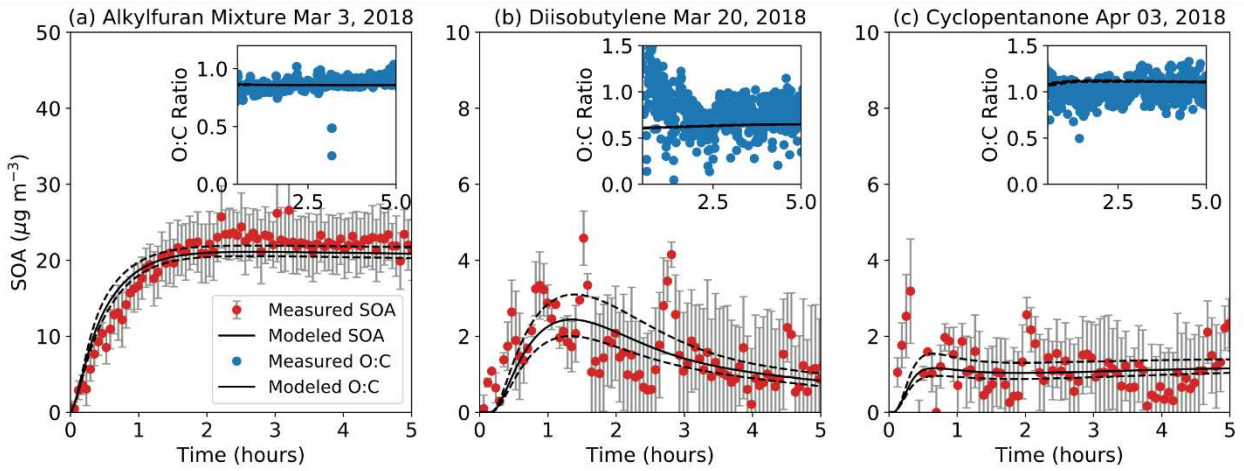

Figure A9: Same as Figure 2.2 but includes SOM-TOMAS predictions based on a k_e of 0.09 (upper bound) and 0.17 (lower bound) s^{-1}.

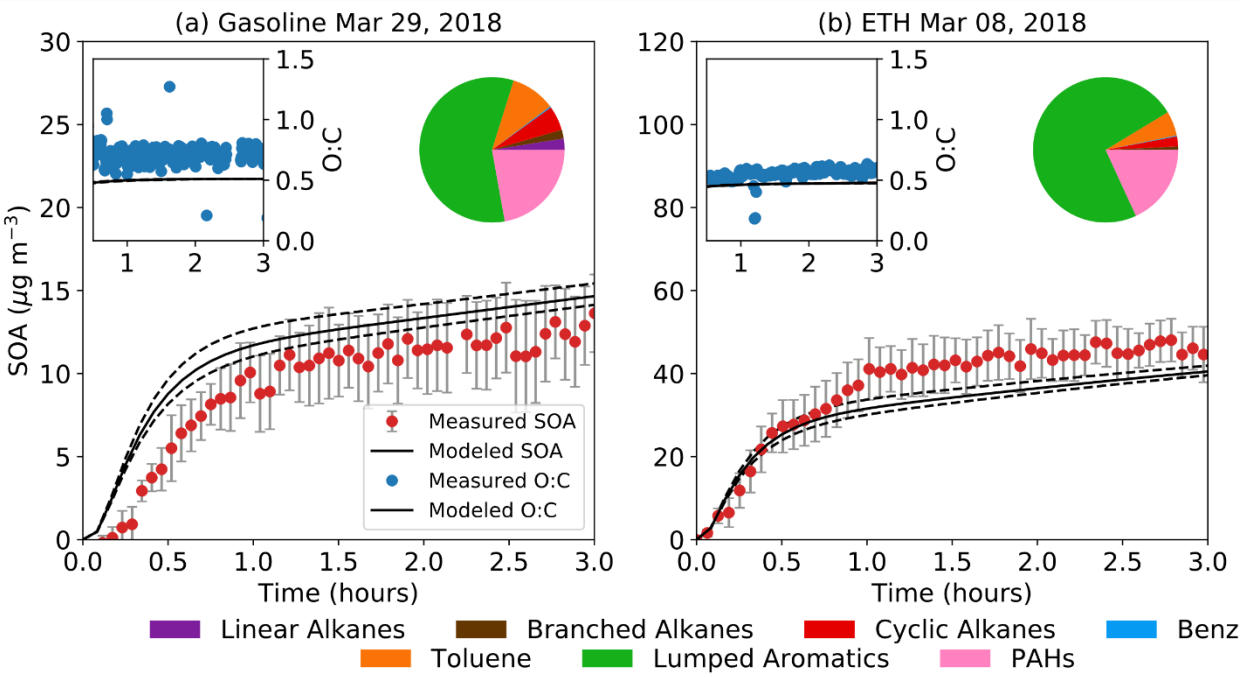

Figure A10: Same as Figure 2.3 but includes SOM-TOMAS predictions based on k_e of 0.09 (upper bound) and 0.17 (lower bound) s^{-1}.

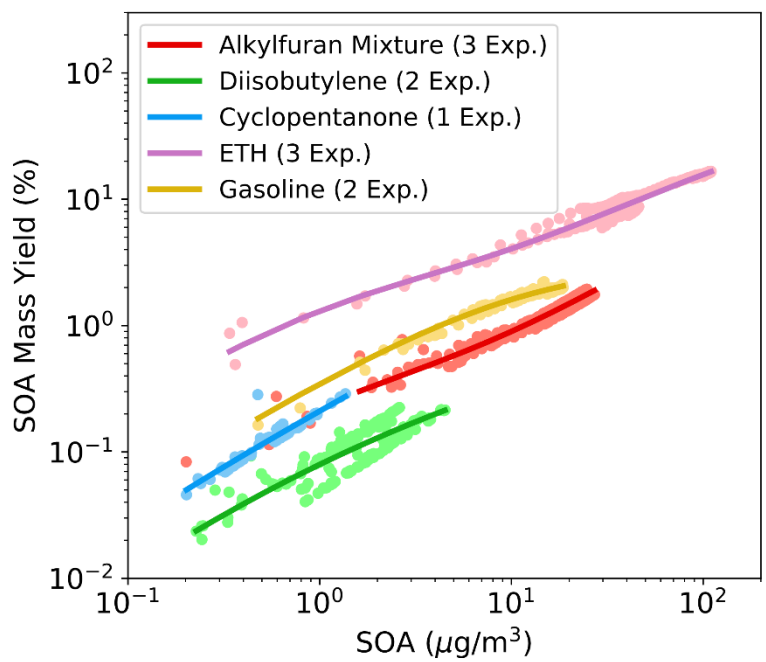

Figure A11: Plot showing the SOA mass yields estimated from the chamber experiments plotted against the SOA mass concentrations for all the experiments performed in this work. The dark solid lines show the fuel-specific volatility basis set (VBS) fits to the data.

Table A1: SOM grids, surrogate species, and parameters used to model the SOA formation from gasoline and ETH. These parameters have been developed based on data from earlier work (Zhang et al., 2014; Cappa et al., 2016).

SOM Grid	Surrogate	m_{frag}	ΔLVP	p_{f1}	p_{f2}	p_{f3}	p_{f4}	Reference
Linear Alkanes	n-dodecane	0.2627	1.4629	0.9657	0.0010	0.0020	0.0314	Loza et al.[19]
Branched Alkanes	methylundecane	0.2042	0.9679	0.3169	0.1804	0.4760	0.0267	Loza et al.[19]
Cyclic Alkanes	hexylcyclohexane	0.2717	1.7950	0.9589	0.0007	0.0014	0.0390	Loza et al.[19]
Benzene	benzene	0.7895	1.5495	0.0743	0.0213	0.8963	0.0081	Ng et al.[4]
Toluene	toluene	1.3064	1.4169	0.5634	0.3413	0.0016	0.0937	Zhang et al.[6]
Lumped Aromatics	m-xylene	0.0736	1.4601	0.1418	0.2971	0.4571	0.1040	Ng et al.[4]
Lumped Aromatics	o-xylene	0.0590	1.3930	0.1260	0.0490	0.7690	0.0570	Song et al.[18]
PAHs	naphthalene	0.7673	1.4922	0.8138	0.0072	0.0635	0.1155	Chan et al.[20]

Appendix B: Supplementary Information for Chapter 3

B1 New Particle Formation

In the nucleation experiments, SOA was formed through nucleation and growth of new particles. We used the scanning mobility particle sizer (SMPS) data to model the rate and timing of new particle formation. This was done by first calculating the linear change in the total suspended number concentration from the start of the nucleation event (~10 minutes after the start of the ozonolysis experiment) to the end of the nucleation event (~35 minutes after the start of the ozonolysis experiment) where the total suspended number concentration plateaued. This change in the number concentration was then divided by the time period over which nucleation occurred to calculate a nucleation rate in cm^{-3} s^{-1}. The use of this nucleation rate in the SOM-TOMAS model simulations was able to accurately predict the observed change in total suspended number concentration over time (Figure B1 for 500 ppbv O_3 experiment). The offline calculation of the nucleation rate described above did not account for losses of the new particles to the chamber walls or to coagulation. The good model-measurement agreement shown in Figure B1 suggests that neither of these loss processes were as important over the time scale for nucleation.

B2 Chamber Wall Losses

Loss of vapors of the model species to the chamber walls was modeled in SOM-TOMAS following the methods described in previous publications (He et al., 2020; Akherati et al., 2020). Briefly, the first-order uptake of the vapors to the walls was assumed to be equal to $k_{w,on}$ and the release of vapors from the walls, $k_{w,off}$, was modeled using absorptive partitioning theory with the Teflon® wall serving as an absorbing mass with an effective mass concentration of C_w mg m^{-3}. $k_{w,on}$ for a model species was calculated using the following equation that assumes that the mass accommodation coefficient of the vapor with the wall was larger than 10^{-6} (McMurry and Grosjean,

1985b):

$$k_{w,on} = \frac{2}{\pi} \cdot \frac{A}{V} \cdot \sqrt{k_e D_v} \qquad \text{(B1)}$$

where A/V is the surface area to volume ratio for the Teflon® chamber, k_e is the coefficient of eddy diffusion, and D_v is the gas-phase diffusion coefficient of the vapor molecule. $k_{w,off}$ was calculated using the following equation (Matsunaga and Ziemann, 2010):

$$k_{w,off} = k_{w,on} \cdot \frac{C^*}{C_w} \qquad \text{(B2)}$$

Nah et al. (Nah et al., 2016) used a k_e of 0.03 s^{-1} and a $k_{w,on}$ of 6.1×10^{-4} s^{-1} for the GTEC chamber. Based on the observations of Krechmer et al. (2016), C_w was varied with the C^* of the model species, with higher values used for more volatile species (e.g., C_w=10 mg m^{-3} for $C^*>10^4$ μg m^{-3}) and vice versa (e.g., C_w=0.016 mg m^{-3} for $C^*<1$ μg m^{-3}). Losses of particles to the chamber walls were modeled using the size-dependent loss rate, β in s^{-1}, determined in Nah et al. (2016). β was determined from analyzing number size distribution data gathered by the SMPS using an aerosol dynamics model that accounted for the influence of coagulation (Pierce et al., 2008).

B3 Calculation of D_b Based on the Predicted SOA Composition

We used the semi-empirical approach described by Shiraiwa and coworkers (Shiraiwa et al., 2017) to calculate the D_b value from the model-predicted composition of SOA. First, we calculated the glass transition temperature (T_g) for each model species as follows:

$$T_{g,i} = A + B \cdot M_i + C \cdot M_i^2 + D \cdot O{:}C_i + E \cdot M_i \cdot O{:}C_i \qquad \text{(B3)}$$

where M_i is the molecular weight of the species i (g mol^{-1}) and $O{:}C_i$ is the elemental oxygen-to-carbon ratio of species i. The coefficients have values of A=-21.57 (K), B=1.51 (K mol g^{-1}), C=-1.7×10^{-3} (K mol^2 g^{-2}), D=131.40 (K) and E=-0.25 (K mol g^{-1}). Next, we calculated the glass transition temperature of the SOA mixture as follows:

$$T_{g,org} = \sum_{i=1}^{n} f_i \cdot T_{g,i} \qquad \text{(B4)}$$

where n is the total number of model species and f_i is the mass fraction of species i. The viscosity of the SOA was calculated using the following equation proposed by Angell (Angell, 1995):

$$\eta = \eta_0 \cdot e^{\frac{D}{(1+D/39.15)\cdot(T/T_{g,org})-1}} \qquad \text{(B5)}$$

where η_0 is the viscosity of the fluid at infinite temperature (10^{-5} Pa·s), D is the fragility parameter (10) (DeRieux et al., 2018), and T is the ambient temperature (298 K). Finally, the D_b value was calculated using the fractional Stokes-Einstein equation as proposed by Evoy et al. (Evoy et al., 2019):

$$D_b = \frac{k_B T}{6\pi d\cdot\eta_C} \cdot \left(\frac{\eta_C}{\eta}\right)^{\xi} \qquad \text{(B6)}$$

where η_C is the reference viscosity (10^{-3} Pa·s), ξ is an empirically-determined exponent (0.93), d is the effective molecular diameter of the model species (0.7 nm), and k_B is the Boltzmann constant (1.38×10^{-23} m^2 kg s^{-2} K^{-1}).

B4 Kelvin Ratio and Fuchs-Sutugin Correction Factor

The Kelvin Ratio (KR) was calculated as follows:

$$KR = e^{\frac{\gamma M_i}{\rho RT\cdot D_{p,j}}} \qquad \text{(B7)}$$

where γ is the surface tension (0.025 N m^{-1}), ρ is the particle density in kg m^{-3}, R is the universal gas constant (8.314 J mol^{-1} K^{-1}), T is the ambient temperature (298 K), and $D_{p,j}$ is the particle diameter of size bin j in m. The Fuchs-Sutugin (FS) correction factor was calculated as follows (Pandis and Seinfeld, 2006):

$$FS = \frac{0.75\cdot\alpha\cdot(1+Kn)}{Kn^2+Kn+0.283\cdot\alpha\cdot Kn+0.75\cdot\alpha} \qquad \text{(B8)}$$

where Kn is the Knudsen number ($Kn = \frac{2\lambda_{AB}}{D_{p,j}}$), α is the mass accommodation coefficient (assumed to be 1) and λ_{AB} is the mean free path of the organic molecule in air in m.

B5 Derivation of $k_{i,j}^{p}$ for Core-Shell Morphology

We derived an analytical equation for $k_{i,j}^{p}$ for a core-shell morphology, following methods analogous to those presented in Zaveri et al. (2014). We started with the mass diffusion equation in a spherical particle in radial coordinates:

$$\frac{\partial T}{\partial t} = k\left(\frac{\partial^2 T}{\partial r^2} + \frac{2}{r}\frac{\partial T}{\partial r}\right) \qquad \text{(B9)}$$

where A is the mass concentration of the diffusing species, D_b is the diffusion coefficient in the particle phase, and r is the radial position. For a particle with a solid core, the gradient of A at the core surface is zero, and therefore the boundary conditions are:

$$\frac{\partial T}{\partial r}(R_c, t) = 0 \qquad \text{(B10)}$$

$$T\left(R_p, t\right) = T_s \qquad \text{(B11)}$$

$$T(r, 0) = 0 \qquad \text{(B12)}$$

where R_c is the core radius, R_p is the particle radius, and A_s is the concentration of the species at the particle surface, which is assumed to be constant. The solution to equation (B9), with boundary conditions listed in equations B10 through B12, is (Carslaw and Jaeger, 1986):

$$\frac{A}{A_s} = 1 + \frac{2R_p}{r}\sum_1^\infty \frac{(\beta_n^2+L^2)\sin\left(\beta_n\frac{r-R_p}{R_p-R_c}\right)}{\beta_n\left(L+L^2+\beta_n^2\right)} \cdot \exp\left(-\frac{\beta_n^2 D_b t}{\left(R_p-R_c\right)^2}\right) \qquad \text{(B13)}$$

where $L = \left(R_p - R_c\right)/R_c$ and β_ns are the successive members of the infinite number of solutions to $\beta_n \cot(\beta_n) + L = 0$. This solution can be extended to include first-order chemical decay within the aerosol following the methods of Danckwerts (1951), which yields:

$$\frac{A}{A_s} = 1 + \frac{2R_p}{r}\sum_1^\infty \frac{(\beta_n^2+L^2)\sin\left(\beta_n\frac{r-R_p}{R_p-R_c}\right)q^2}{\beta_n\left(L+L^2+\beta_n^2\right)\left(\beta_n^2+q^2\right)} + \frac{2R_p}{r}\sum_1^\infty \frac{\beta_n(\beta_n^2+L^2)\sin\left(\beta_n\frac{r-R_p}{R_p-R_c}\right)}{\left(L+L^2+\beta_n^2\right)\left(\beta_n^2+q^2\right)} \cdot \exp\left(-\left(\frac{\beta_n^2 D_b}{\left(R_p-R_c\right)^2} + k_c\right)t\right) \qquad \text{(B14)}$$

where $q = \left(R_p - R_c\right)\cdot\sqrt{k_c/D_b}$, where k_c is the first-order chemical loss rate. Now, we can relate the bulk-average concentration, $\bar{A}$, to the surface concentration A_s:

$$\frac{\bar{A}}{A_s} = \frac{\int_{R_c}^{R_p} 4\pi r^2 (A/A_s) dr}{(4/3)\pi(R_p^3 - R_c^3)} = Q - U \qquad \text{(B15)}$$

where Q is a constant factor and U is a transient factor, as shown below:

$$Q = 1 + \frac{6R_p(R_p - R_c)}{R_p^3 - R_c^3} \sum_1^\infty \frac{(\beta_n^2 + L^2) q^2 G}{\beta_n^3 (L + L^2 + \beta_n^2)(\beta_n^2 + q^2)} \qquad \text{(B16)}$$

$$U = \frac{6R_p(R_p - R_c)}{R_p^3 - R_c^3} \sum_1^\infty \frac{(\beta_n^2 + L^2) G}{\beta_n (L + L^2 + \beta_n^2)(\beta_n^2 + q^2)} \cdot \exp\left\{ -\left[\frac{\beta_n^2 D_b}{(R_p - R_c)^2} + k_c \right] t \right\} \qquad \text{(B17)}$$

Following methods in Zaveri et al. (2014), we found the $k_{i,j}^p$ for a core-shell aerosol, assuming slow reaction.

$$k_{i,j}^p = \frac{R_p^3 - R_c^3}{3R_p^2} \cdot \frac{k_c \cdot Q}{1 - Q} \qquad \text{(B18)}$$

Substituting Q and taking the limit of k_c to zero, we get

$$k_{i,j}^p = \frac{R_p^3 - R_c^3}{3R_p^2} \cdot \frac{-D_b(R_p^3 - R_c^3)}{6R_p(R_p - R_c)^3 \sum \frac{(\beta_n^2 + L^2) G}{\beta_n^5 (L + L^2 + \beta_n^2)}} \qquad \text{(B19)}$$

B6 Application of the SOM-TOMAS Model to Seeded Experiments

Results from application of the SOM-TOMAS model to the higher-seed-concentration (~3000 μm^2 cm^3) α-pinene ozonolysis experiment with 500 ppbv O_3 are presented in Figure B10. Note that for the seeded experiments, we used a formulation of the particle-side mass transfer coefficient ($k_{i,j}^p$) derived specifically for the core-shell case (Section B5). Similar to the nucleation experiments, a unique set of SOM parameters ($p_{f,1\text{-}4}$, ΔLVP) was developed for each prescribed D_b value and these produced good agreement with the time-varying SOA mass concentrations, as shown in Figure B10(a). SOM parameters from these fits are tabulated in Table B3. These SOM parameters produced a nearly identical number size distribution 3 hours after the start of the ozonolysis experiment, all of which agreed reasonably well with the measured number size distribution (Figure B10(b)). The use of different D_b values produced a similar evolution in the number size distribution because, unlike in the nucleation simulations, bulk diffusion limitations

had little to no influence on the size-dependent partitioning of SOA. The reason for this effect is explained below.

The suspended ammonium sulfate seed concentrations were still ~3 times the suspended SOA mass concentrations at the end of the experiment and hence the maximum SOA coatings at the end of the experiment were still quite thin (e.g., a 30% increase in mass results in a 10% increase in particle diameter or radius). For instance, output from the SOM-TOMAS model (from any of the simulations for the seeded experiments) indicated that the SOA coating varied between 10 and 20 nm for the particle size range of 70-1000 nm that accounted for 95% of the SOA mass at the end of the experiment (Figure B11(b)). The coating thickness varied with particle size because the SOA mass condensed as per the Fuchs-corrected surface area, which shifted the SOA mass size distribution to smaller sizes with respect to the seed mass size distribution (Figure B11(a)). The relative uniformity in the SOA coating thickness with particle size meant that the length scales and timescales for bulk diffusion were nearly identical between the different particle sizes. Hence, in contrast to the nucleation simulations where the growth rates varied significantly between the particle sizes, simulations with the seeded experiments resulted in little to no variation in the growth of the different particle sizes across a range of D_b values. The model predictions of SOA O:C for the different D_b values in the seeded experiment (Figure B10(c)) were much more variable than those seen for the nucleation experiment, but the predictions lay well within the uncertainty of the measurements. Overall, these results suggest that the technique used to constrain D_b in the nucleation experiment is unlikely to work with the seeded experiment where the SOA coating thickness is much smaller than the solid core radius. A similar analysis was performed for experiments where the initial seed was smaller than that presented in Figure B10 (Figure B12), yet the findings were nearly identical to those presented here.

We ran the SOM-TOMAS model using the optimal parameters developed in the nucleation experiment to predict the SOA formation in the seeded experiment. These results are shown as a solid red curve in Figure B10. These parameters seemed to reasonably reproduce the SOA O:C, and number size distribution but overestimated the SOA mass concentration by slightly less than 30%. The overestimation in the SOA mass concentration is very likely due to experiment-to-experiment variability in the nucleation and seeded experiments since both were performed identically, within experimental variability, except for the use of the seed.

Table B1: Details on the instrumentation used to perform measurements during the α-pinene ozonolysis experiments.

Species/Data Measured	***Instrument***	***Notes***
α-pinene	Gas Chromatograph-Flame Ionization Detector (GC-FID; Agilent 7890A)	NA
O_3	Gas Analyzer (Teledyne T400)	NA
NO_X	Gas Analyzer (Teledyne 200EU)	NA
Particle size distribution	Scanning Mobility Particle Sizer (SMPS, TSI)	Used to determine size-dependent particle wall loss rates and SOA mass concentrations
Bulk aerosol mass and composition	High-Resolution Aerosol Mass Spectrometer (HR-AMS; Aerodyne Research, Inc.)	Processed with SQUIRREL v1.63 and PIKA v1.23 in Igor Pro 7.07 (WaveMetrics) to determine O:C

Table B2: SOM parameters determined from fitting the SOA mass concentration in the nucleation experiment with 500 ppbv O_3 for different prescribed D_b values. The last row contains the optimal fit where the SOA mass concentration and number size distribution were both used to fit the SOM parameters and D_b.

D_b (m^2 s^{-1})	ΔLVP	f_{HOM}	p_{f1}	p_{f2}	p_{f3}	p_{f4}
10^{-10}	1.860	0.034	0.234	0.570	0.000	0.161
10^{-18}	2.127	0.034	0.000	0.857	0.000	0.109
10^{-19}	1.514	0.034	0.309	0.209	0.214	0.234
10^{-20}	1.750	0.034	0.253	0.463	0.001	0.248
10^{-21}	2.014	0.034	0.309	0.209	0.214	0.235
10^{-23}	2.486	0.034	0.266	0.169	0.265	0.266
$^{*}3.4\times10^{-19}$	1.555	0.034	0.245	0.286	0.270	0.165

Table B3: SOM parameters determined from fitting the SOA mass concentration in the seeded experiment with 500 ppbv O_3 for different prescribed D_b values.

D_b (m^2 s^{-1})	ΔLVP	f_{HOM}	p_{f1}	p_{f2}	p_{f3}	p_{f4}
10^{-10}	1.902	0.034	0.000	0.854	0.001	0.110
10^{-18}	1.918	0.034	0.104	0.750	0.000	0.112
10^{-19}	2.027	0.034	0.146	0.718	0.000	0.102
10^{-20}	2.266	0.034	0.000	0.902	0.001	0.063
10^{-21}	2.740	0.034	0.001	0.964	0.000	0.001
10^{-23}	2.552	0.034	0.063	0.665	0.126	0.112

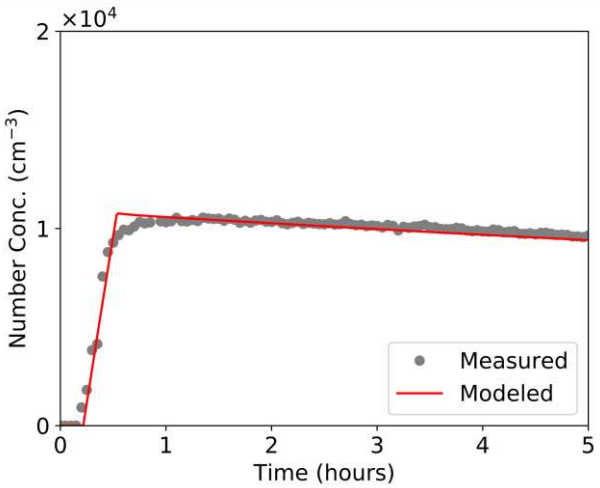

Figure B1: Modeled and measured total particle number concentrations in the nucleation experiment with 500 ppbv O_3.

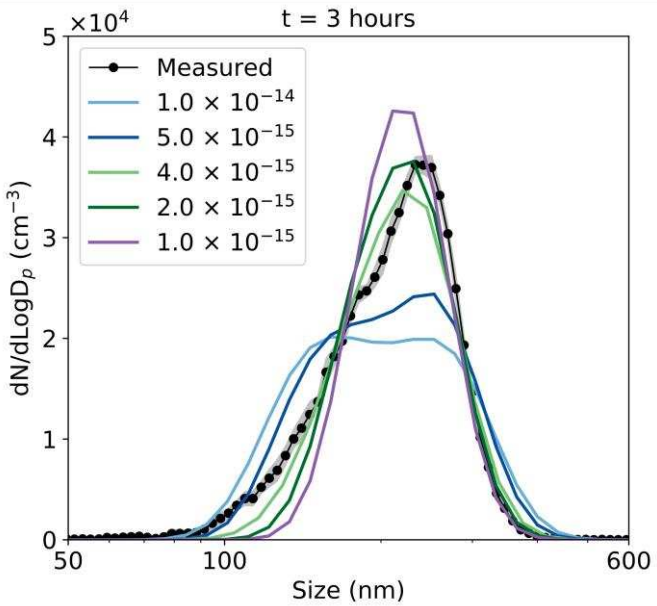

Figure B2: Results from the SOM-TOMAS model for number size distribution at 3 hours compared to measurements for a range of prescribed D_b (cm^2 s^{-1}) values. Results are for the 500 ppbv O_3, nucleation experiment. The grey band depicts ± 1σ.

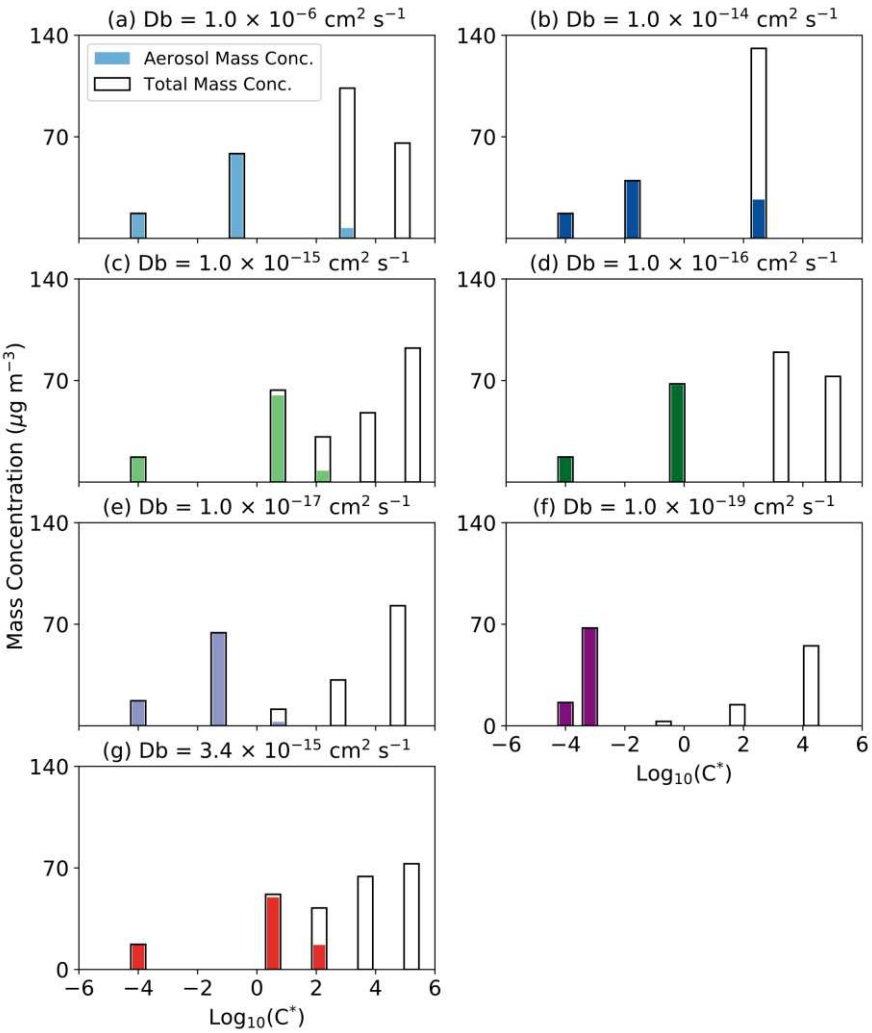

Figure B3: Model-predicted volatility distributions of SOA from the simulations performed for the 500 ppbv O_3, nucleation experiment at different D_b values. All volatility distributions are at 3 hours after the start of the ozonolysis experiment.

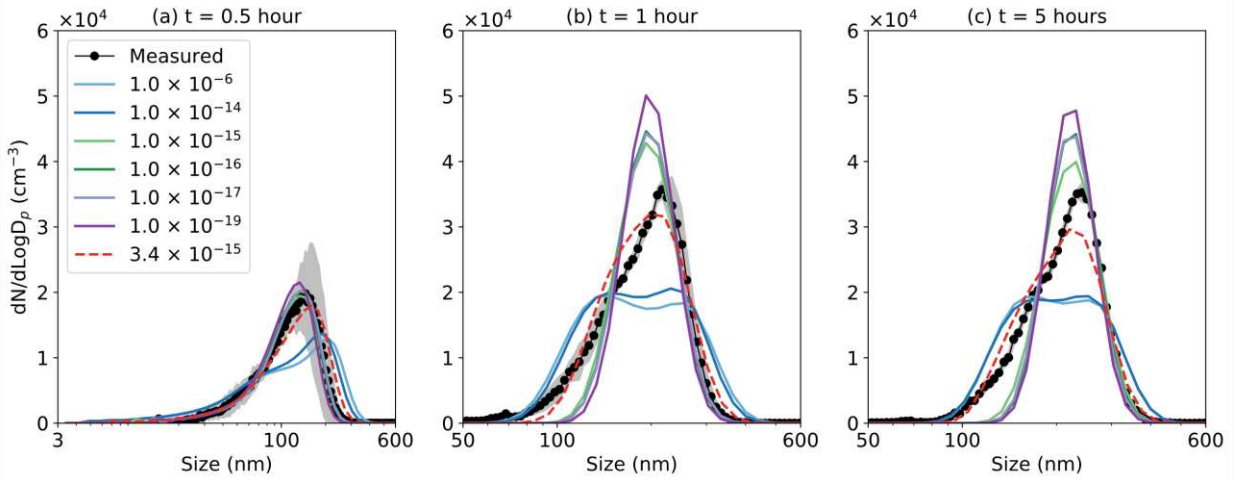

Figure B4: Results from the SOM-TOMAS model for number size distribution at (a) 0.5, (b) 1, and (c) 5 hours compared to measurements for a range of prescribed D_b (cm^2 s^{-1}) values. Results are for the 500 ppbv O_3, nucleation experiment. The grey band depicts ± 1σ.

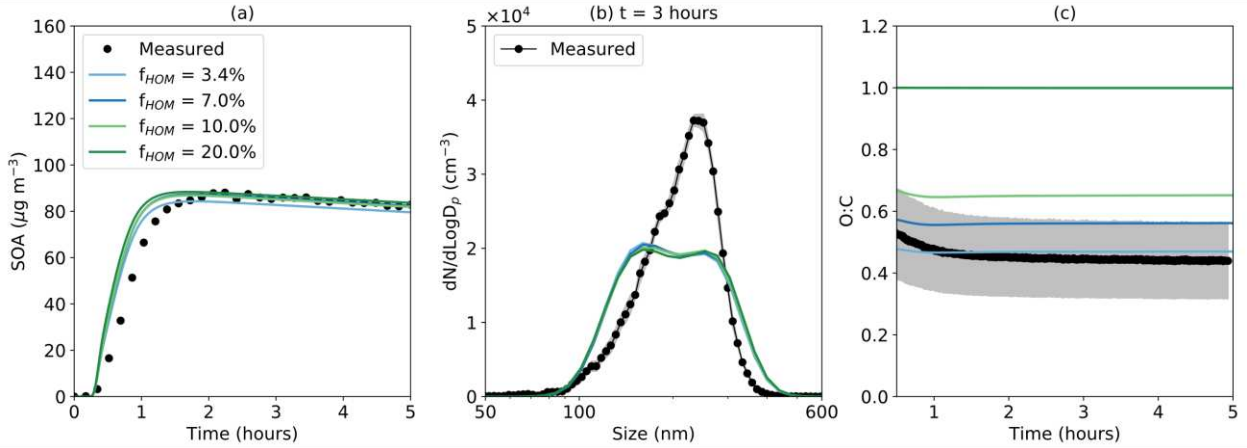

Figure B5: Results from the SOM-TOMAS model for (a) SOA mass concentration, (b) number size distribution at 3 hours, and (c) O:C ratio compared to measurements. Results are for the 500 ppbv O_3, nucleation experiment. All simulations used a liquid-like D_b of 10^{-10} m^2 s^{-1} with different molar yields for HOMs. The O:C data are only shown 30 minutes after the start of the experiment because the O:C measurements are fairly uncertain in the first 30 minutes when the SOA mass concentrations are quite low. The grey band in the panels (b) and (c) depicts ± 1σ.

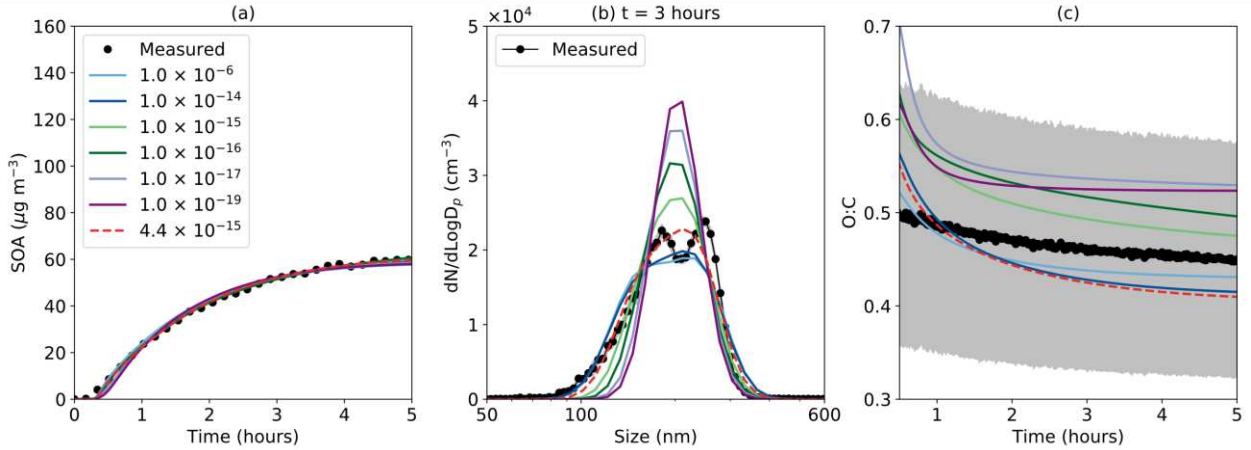

Figure B6: Results from the SOM-TOMAS model for (a) SOA mass concentration, (b) number size distribution at 3 hours, and (c) O:C ratio compared to measurements for a range of prescribed D_b ($cm^2\ s^{-1}$) values. Results are for the 100 ppbv O_3, nucleation experiment. The dashed red line shows model predictions from the optimal fit when constrained to both the SOA mass concentration and number size distribution. The O:C data are only shown 30 minutes after the start of the experiment because the O:C measurements are fairly uncertain in the first 30 minutes when the SOA mass concentrations are quite low. The grey band in panels (b) and (c) depicts ± 1σ.

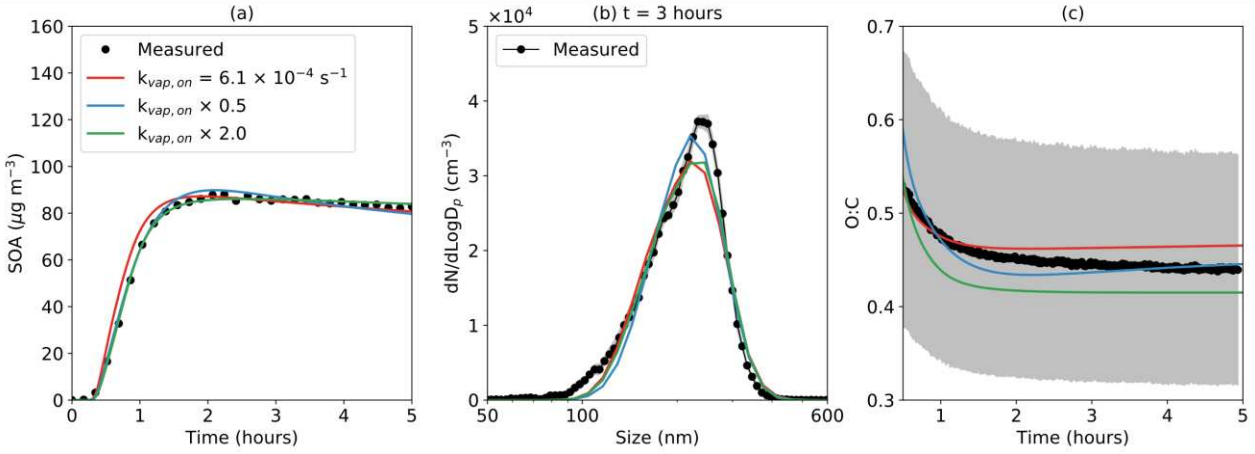

Figure B7: Results from simulations performed to assess sensitivity in the optimal D_b for uncertainty in the vapor wall loss rate ($k_{vap,on}$). Results are for the 500 ppbv O_3, nucleation experiment. The grey band in panels (b) and (c) depicts ± 1σ. The optimal D_b for the $k_{vap,on}$×0.5 and $k_{vap,on}$×2.0 were 2.7×10^{-15} and 7.1×10^{-15} m^2 s^{-1}.

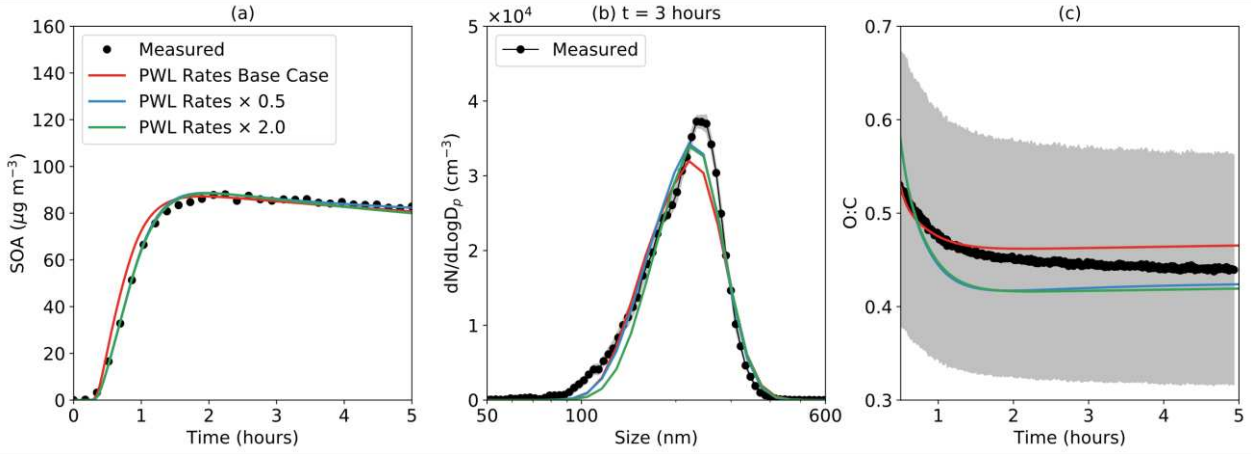

Figure B8: Results from simulations performed to assess sensitivity in the optimal D_b for uncertainty in the size-dependent particle wall loss rate (PWL). Results are for the 500 ppbv O_3, nucleation experiment. The grey band in panels (b) and (c) depicts ± 1σ. The optimal D_b for the PWL×0.5 and PWL×2.0 were 4.5×10^{-15} and 3.9×10^{-15} m^2 s^{-1}.

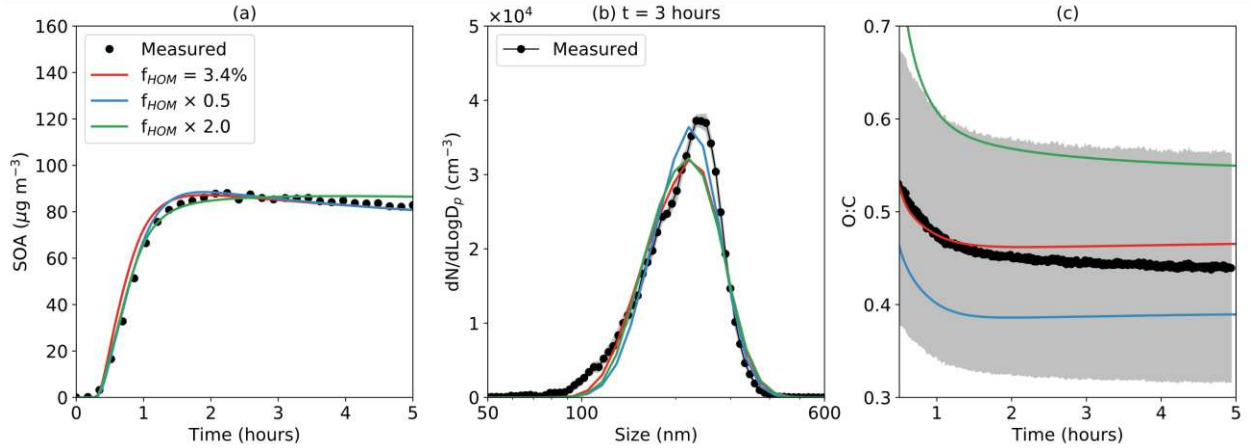

Figure B9: Results from simulations performed to assess sensitivity in the optimal D_b for uncertainty in the molar yield for HOM (f_{HOM}). Results are for the 500 ppbv O_3, nucleation experiment. The grey band in panels (b) and (c) depicts ± 1σ. The optimal D_b for the f_{HOM}×0.5 and f_{HOM}×2.0 were 3.9×10^{-15} and 1.4×10^{-15} m^2 s^{-1}.

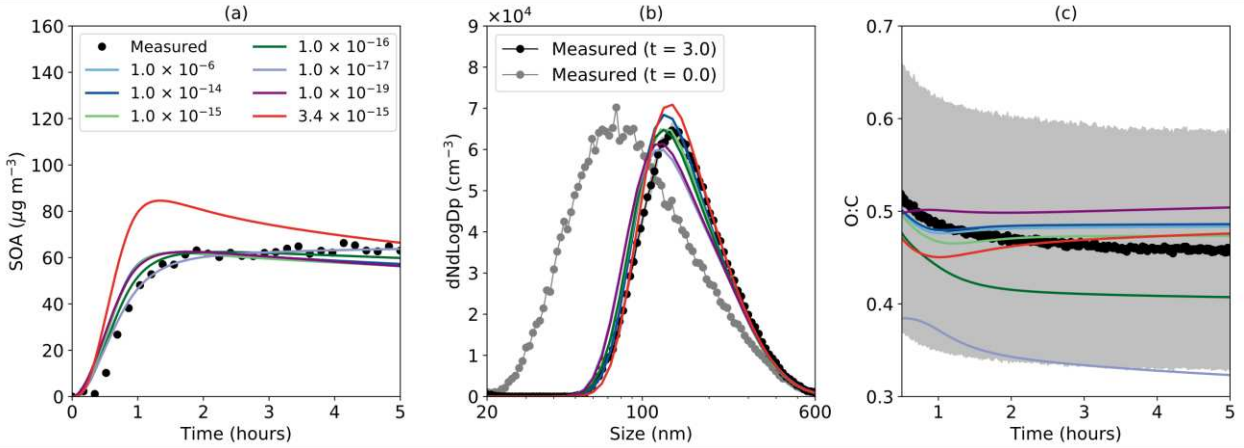

Figure B10: Results from the SOM-TOMAS model for (a) SOA mass concentration, (b) number size distribution at 3 hours, and (c) O:C ratio compared to measurements for a range of prescribed D_b ($cm^2\ s^{-1}$) values. Results are for the 500 ppbv O_3, higher-seed-concentration (~3000 $\mu m^2\ cm^3$) experiment. The solid red line shows model predictions from the optimal fit from Figure 3.1. The O:C data are only shown 30 minutes after the start of the experiment because the O:C measurements are fairly uncertain in the first 30 minutes when the SOA mass concentrations are quite low. The grey band in the panels (b) and (c) depicts $\pm 1\sigma$.

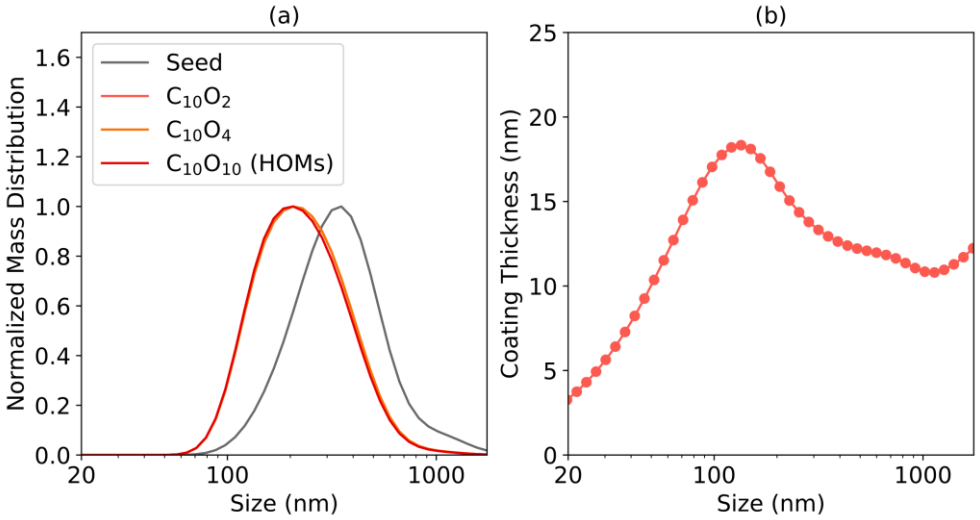

Figure B11: (a) Normalized mass size distributions for the ammonium sulfate seed and the three most abundant SOA model species at 3 hours after the start of the experiment. (b) SOA coating thickness as a function of particle size at the end of the experiment. Results are for the 500 ppbv O_3, higher-seed-concentration (~3000 μm^2 cm^3) experiment.

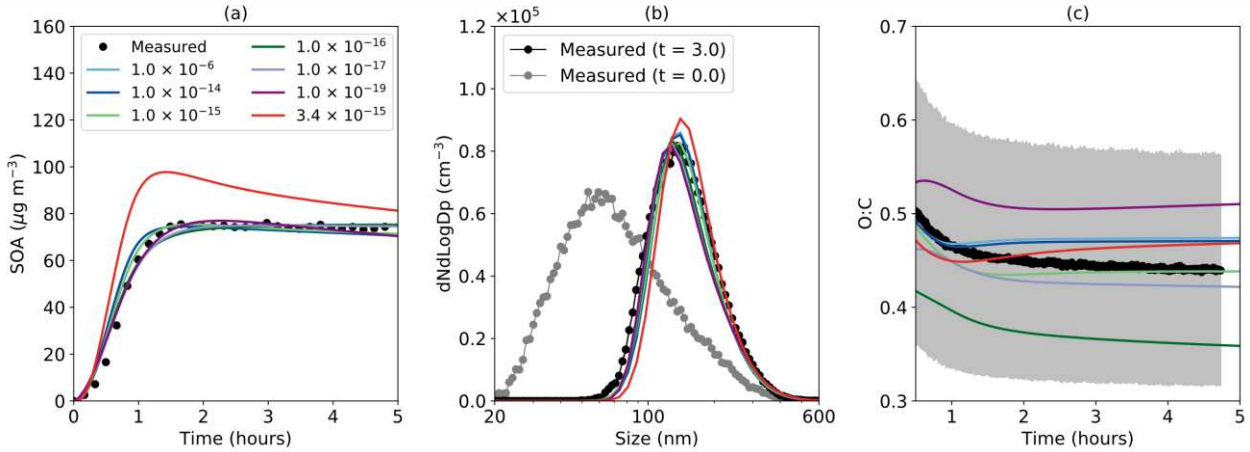

Figure B12: Results from the SOM-TOMAS model for (a) SOA mass concentration, (b) number size distribution at 3 hours, and (c) O:C ratio compared to measurements for a range of prescribed D_b ($cm^2\ s^{-1}$) values. Results are for the 500 ppbv O_3, lower-seed-concentration (~1000 $\mu m^2\ cm^3$) experiment. The solid red line shows model predictions from the optimal fit from Figure 3.1. The O:C data are only shown 30 minutes after the start of the experiment because the O:C measurements are fairly uncertain in the first 30 minutes when the SOA mass concentrations are quite low. The grey band in the panels (b) and (c) depicts $\pm 1\sigma$.

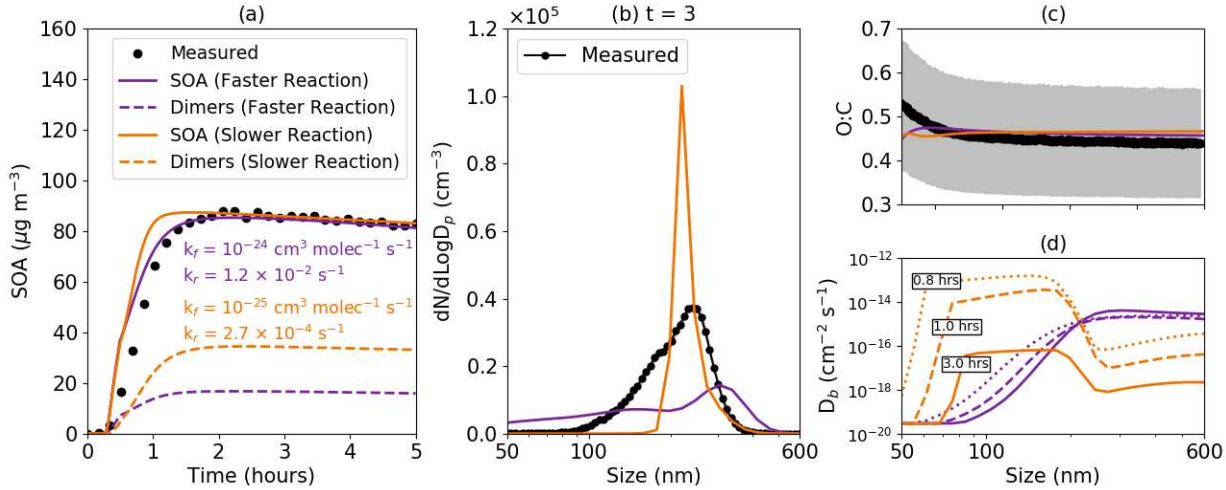

Figure B13: Results from the size-dependent, endogenous-D_b version of the SOM-TOMAS model for (a) SOA mass concentration, (b) number size distribution at 3 hours, and (c) O:C ratio compared to measurements. Model predictions of the size- and time-varying D_b are shown in panel (d). Results are for the 500 ppbv O_3, nucleation experiment. Both the slower-reacting (orange lines) and faster-reacting (purple lines) cases use the SOM parameters from the optimal D_b fit in Figure 3.1 ($p_{f,1\text{-}4}$, ΔLVP, f_{HOM}=3.4%) but with different oligomer formation and dissociation rates. The O:C data are only shown 30 minutes after the start of the experiment because the O:C measurements are fairly uncertain in the first 30 minutes when the SOA mass concentrations are quite low. The grey band in panels (b) and (c) depict ± 1σ.

Appendix C: Supplementary Information for Chapter 4

C1 SOM-TOMAS Model and Updates

SOM represents the VOC oxidation chemistry statistically using a two-dimensional carbon-oxygen grid where the properties of each model species, defined by its carbon (N_C) and oxygen (N_O) number, are parameterized based on N_C and N_O (e.g., reactivity (k_{OH}); volatility (C^*)). The SOM species can participate in multi-generational oxidation in the gas phase and gas/particle partitioning based on their C^* (Donahue et al., 2006). SOM employs a total of six free parameters to describe these processes: (1) m_{frag} controls the overall fragmentation and functionalization probabilities; (2) p_1-p_4 control the probabilities of gaining one to four oxygen atoms per functionalization reaction; and (3) ΔLVP controls the C^* of the SOM species based on their N_C and N_O. TOMAS uses a sectional approach to track the dynamics of the number and mass moments of the particle size distribution, as governed by the microphysical processes of nucleation, coagulation, particle wall loss, and condensation/evaporation. The particle-phase species in SOM are tracked in the 36 TOMAS size sections that span dry diameters between 1 to 1,000 nm. The condensation/evaporation processes in SOM-TOMAS are simulated kinetically using the reactive-diffusive framework described in Zaveri et al. (2014), which incorporates the influence of particle phase state on gas-particle partitioning through the particle bulk diffusivity (D_b) (He et al., 2021). SOM-TOMAS also accounts for the formation of highly oxygenated organic molecules (HOMs), formed via autoxidation reactions at a fixed molar yield from reaction of the VOC with the OH radical (Bianchi et al., 2019). The molar yield of HOMs is simulated with a prescribed parameter p_{HOM}.

All SOM species in the particle phase can be oxidized through heterogeneous oxidation reactions driven by the OH radical. Heterogeneous oxidation happens when the gas-phase OH

radicals collide with the particle surface and react with particle-phase SOM species at the surface. The loss rate of particle-phase SOM species due to heterogeneous oxidation is given by the following equation:

$$\frac{dC_{i,j}^{p}}{dt} = -\gamma_{OH} \cdot \frac{[OH] \cdot \bar{C}_{OH}}{4} \cdot FS_j \cdot \pi d_j^2 N_j \cdot \frac{C_{i,j}^{p}}{\sum_k C_{i,k}^{p}} \qquad \text{(C1)}$$

where $C_{i,j}^{p}$ is the particle-phase mass concentration in μg m^{-3} for species *i* in size bin *j*; γ_{OH} is the reactive uptake coefficient of OH; $[OH]$ is the gas-phase concentration of OH in molecules m^{-3}; $\bar{C}_{OH}$ is the mean speed of OH molecules in m s^{-1}; FS_j is the Fuchs-Sutugin correction factor (Pandis and Seinfeld, 2006); d_j is the particle diameter for size bin *j* in m; and N_j is the number concentration for particles in size bin *j* in m^{-3}. The oxidation chemistry of the SOM species from heterogeneous reactions is kept the same as the oxidation chemistry in the gas-phase. This includes functionalization reactions where 1 to 4 oxygen atoms are added to the SOM species and a probability of fragmentation that is dictated by the O:C ratio of the SOM species (i.e., $P_{frag} = (O:C)^{m_{frag}}$, m_{frag} is an adjustable parameter).

We employed the oligomerization scheme developed in He et al. (2021), where we simulated oligomer formation by tracking the particle-phase monomer concentrations (M) and the concentrations of monomer units that existed in dimer form (O). Any two monomers can react through forward reactions with a rate constant k_f in cm^3 molecules^{-1} s^{-1} to convert a fraction of each to its corresponding dimer form. Each dimer form can decay back into its monomer form through reverse reactions with a first-order rate constant k_r in s^{-1}. The governing equations are:

$$\frac{dO_{i,j}}{dt} = \sum_k^{i_{max}} k_f \cdot M_{k,j} \cdot M_{i,j} - k_r \cdot O_{i,j} \qquad \text{(C2)}$$

$$\frac{dM_{i,j}}{dt} = k_r \cdot O_{i,j} - \sum_k^{i_{max}} k_f \cdot M_{k,j} \cdot M_{i,j} \qquad \text{(C3)}$$

where k and i are indices for the species, and j for the size bins. The influence of oligomerization on gas/particle partitioning is represented through the first-order decay rate of the particle-phase species $k_{i,j}^{c}$ (s^{-1}) (Zaveri et al., 2014), calculated assuming pseudo steady state between M and O species:

$$k_{i,j}^{c} = \sum_{k}^{i_{max}} k_f \cdot M_{k,j} - k_r \cdot \frac{O_{i,j}}{M_{i,j}} \qquad \text{(C4)}$$

C2 α-Pinene SOA EC Data and Parameterizations

We developed SOM-TOMAS parameters to simulate the SOA formation and evolution from photooxidation of α-pinene in an EC experiment. These parameters were developed from data gathered from an EC experiment performed under low-NO_X conditions by Chhabra et al. (2010). Parameterizations based on these data have been reported previously (Jathar et al., 2016, 2021), and these parameterizations have been used in 3D models to simulate SOA formation from monoterpenes in a regional model (Cappa et al., 2016; Akherati et al., 2019; Bilsback et al., n.d.).

Briefly, these experiments were performed in the 30 m^3 EC at the California Institute of Technology (Caltech) under relatively dry conditions (RH<20%). Ammonium sulfate seeds were used to provide a surface area for SOA condensation (1670 μm^2 cm^3) and hydrogen peroxide was used as the source for hydroxyl radicals (OH) (~1.9×10^6 molecules cm^{-3}). The initial α-pinene concentration was 45 ppbv, and the total OH exposure was 9×10^{10} molecules-s cm^{-3}, or 0.7 day of atmospheric photochemical aging (assuming an OH concentration of 1.5×10^6 molecules cm^{-3}), spread over 13 hours, and the NO and NO_2 concentrations throughout the experiment were below the instrument detection limit (<2 ppbv). The particle volume, mass, and composition were monitored via a custom scanning mobility particle sizer (SMPS) and high-resolution aerosol mass spectrometer (HR-AMS).

Several SOM-TOMAS parameters were prescribed a priori based on what we know about α-pinene SOA formed in EC experiments. The model simulates production of HOMs from autoxidation reactions under low-NO_X conditions (Ehn et al., 2014). Based on the work of Bianchi et al. (2019), we assumed a direct HOM yield of 0.44% from reaction of α-pinene with OH. Furthermore, we assumed that the SOA formed under these EC conditions was semi-solid with a bulk diffusion coefficient (D_b) of 4×10^{-19} m^2 s^{-1}. Recently, Zaveri et al (2020) and He et al. (2021) were able to constrain the D_b for α-pinene SOA between 10^{-19} and 10^{-18} m^2 s^{-1} by applying kinetic models to EC SOA data. This semi-solid phase state is consistent with other laboratory observations of α-pinene SOA formed in photooxidation experiments (e.g., Pajunoja et al. (2014)). We also simulated heterogeneous oxidation with a γ_{OH} of 1 (Kroll et al., 2009), which had negligible impact on the model predictions due to the relatively low OH exposure. Finally, we modeled oligomerization reactions by specifying a dimer formation rate of 10^{-24} cm^3 $molecules^{-1}$ s^{-1} and a dimer dissociation rate of 1.6×10^{-2} s^{-1}, based on recent work by He et al. (2021).

The SOM-TOMAS parameters were fit to reproduce measurements of SOA mass concentration and the oxygen-to-carbon (O:C) ratio (Figure C1). The fit parameters are provided in the figure caption. Model predictions were able to track the measurements over the entire EC experiment suggesting, similar to the point we have made in earlier work, that the SOM-TOMAS model is able to adequately represent the chemistry and thermodynamic properties of the VOC and its oxidation products.

C3 Accounting for OH Suppression

We accounted for OH modulation in the OFR experiment from adding *a*-pinene using the MCMv3.3 (Master Chemical Mechanism) box model (Jenkin et al., 2015) distributed with the BOXMOX kinetic preprocessor manager (Knote et al., 2018). Briefly, we first constrained the O_3

(23 ppmv) and H_2O (RH=35%) levels in the MCM model and tuned a uniform scaling factor for the photolysis rate of O_3 and other species to match the reported OH exposures with no α-pinene addition. Then, we introduced α-pinene (50 ppbv; OH reactivity of ~60 s^{-1}) to recalculate the OH concentrations. Compared to those reported in Lambe et al. (2015), the OH concentrations were reduced by around a factor of two for the six OH exposures, with the largest reduction at the lowest exposure (2.8) and smallest reduction at the highest exposure (1.2). The OH reductions were found to be similar if we used the spreadsheet model of Peng and Jimenez (2017).

C4 Calculation of PWL Rates

Assuming that the particles followed a first-order loss rate in the OFR and were minimally influenced by coagulation (only relevant for timescales >1 hr), the PWL rates were calculated as:

$$\beta_j = -\frac{ln(\eta_j)}{\Delta t} \qquad \text{(C2)}$$

Where β_j is the first-order PWL rate for size bin j in s^{-1}, η_j is the particle transmission efficiency for size bin j, and Δt is the residence time (100 s). The estimated PWL rates and the log-linear fits are shown in Figure C2. For particles smaller than 50 nm, we assumed the PWL rates to be equal to that of the 50 nm particles.

C5 Pseudo-Atmospheric Simulations

The pseudo-atmospheric simulations followed the same methodology from our previous studies (He et al., 2020; Jathar et al., 2021), where we assumed background OA mass loading to be 10 μg m^{-3}, OH to be 1.5×10^6 cm^{-3}, and VOC to be 1 pptv. The simulations were run for 2 weeks to assess the evolution of the SOA mass yield over its typical atmospheric lifetime. The use of a small initial VOC allowed the OA mass loading to stay constant and the effect of aging to be separated. In PA1, we assumed gas-phase oxidation and liquid D_b. In PA2, we enabled semi-solid D_b. In PA3, we turned on heterogeneous oxidation, and PA4, we enhanced the effect of

heterogeneous oxidation by decreasing background OA particle sizes while conserving the mass concentration of 10 μg m^{-3}.

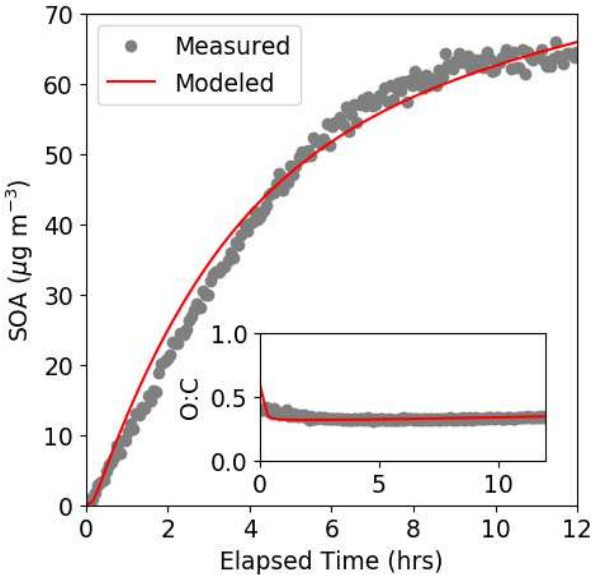

Figure C1: SOM-TOMAS model predictions of SOA mass concentration (main) and SOA O:C (inset) compared against measurements from a photooxidation chamber experiment performed on α-pinene (Chhabra et al., 2011). The fit parameters are: ΔLVP = 2.080, m_{frag} = 0.049, p_{f1} = 0.244, p_{f2} = 0.613, p_{f3} = 0.142, and p_{f4} = 0.000. Prescribed parameters include p_{HOM} = 0.0044, D_b = 4×10^{-19} m^2 s^{-1}, k_f = 10^{-24} $molecules^{-1}$ cm^3 $molecules^{-1}$ s^{-1} and k_r = 1.6×10^{-2} s^{-1}.

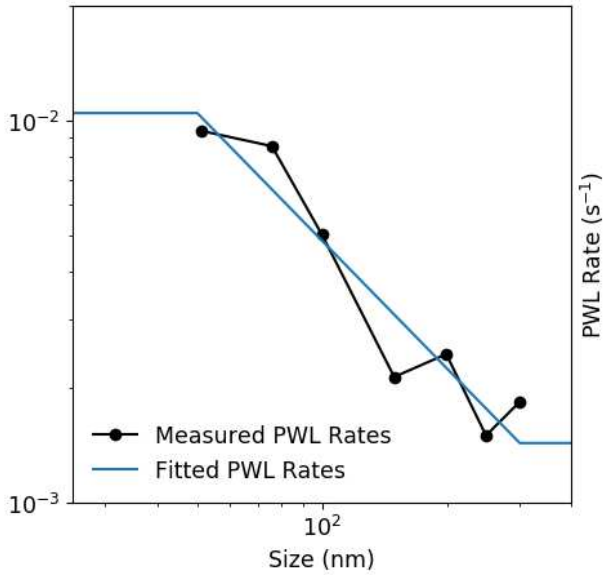

Figure C2: PWL rates in the OFR estimated from measured particle transmission efficiencies from Lambe et al. (2011) and the log-linear fit. The fitted curve assumes the same values of the measured lower and upper bounds, for particle diameters outside the measured size range.

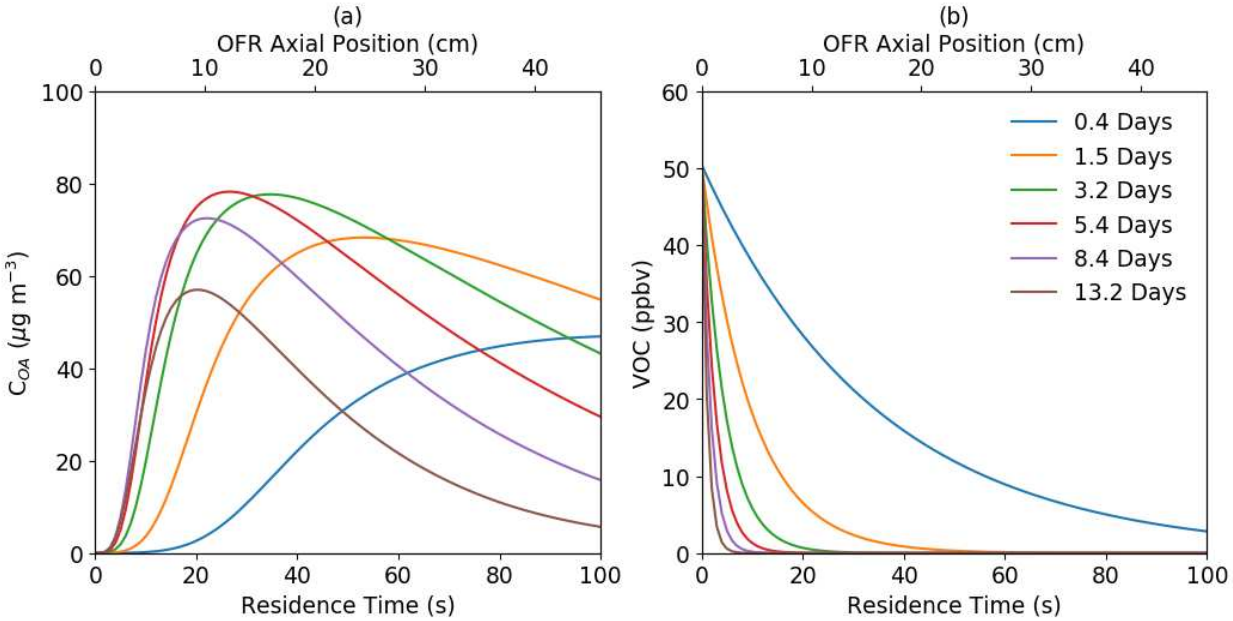

Figure C3: (a) SOA mass concentrations and (b) α-pinene mixing ratios inside the OFR for six different OH exposures simulated with heterogeneous oxidation using model F. Horizontal axis is shown with both the residence time and OFR axial position.

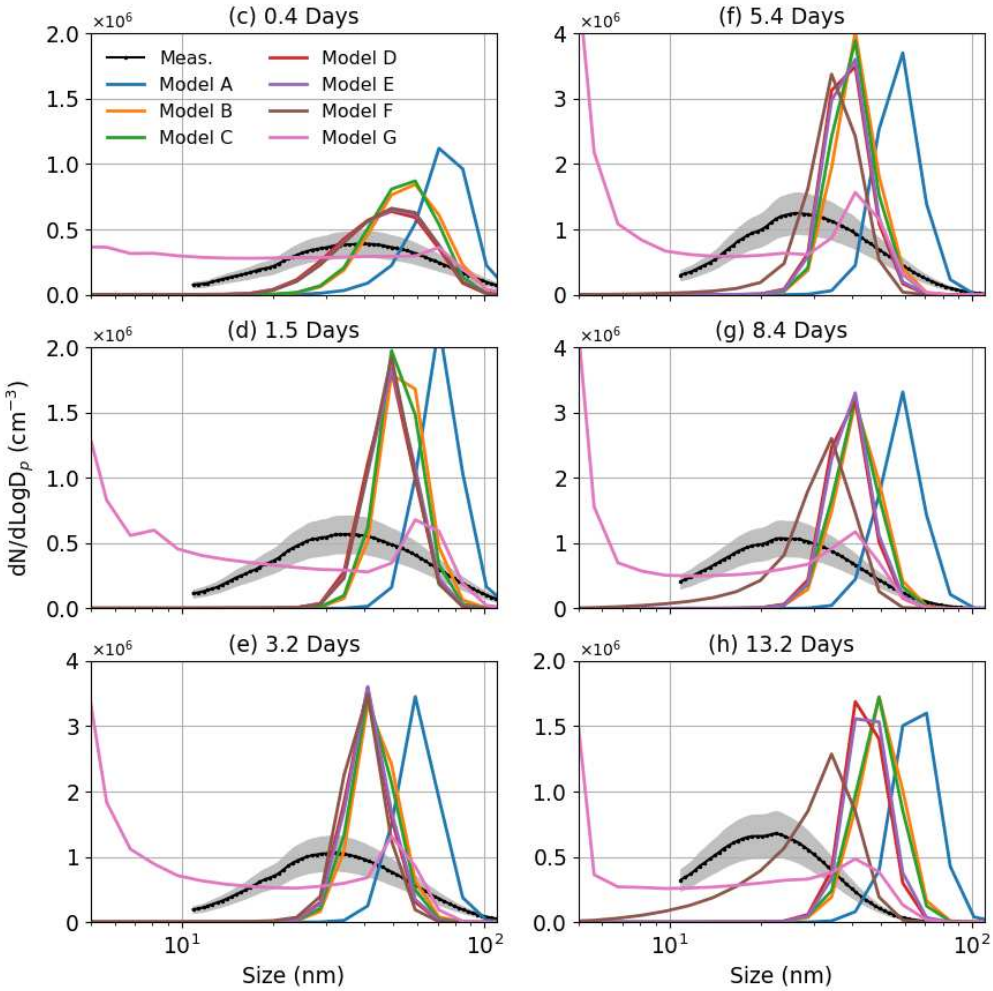

Figure C4: Simulated particle number size distributions from models A through G for the six different OH exposures.

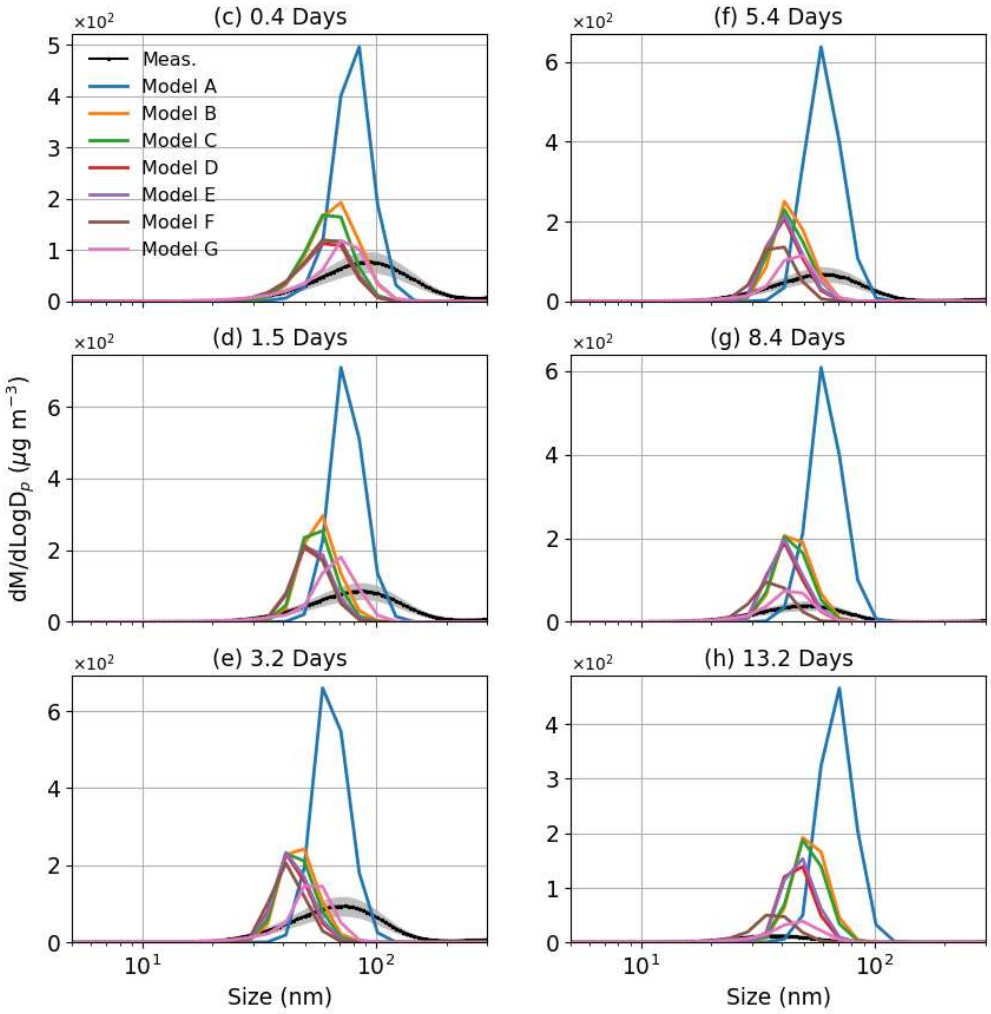

Figure C5: Simulated particle mass size distributions from models A through G for the six different OH exposures. The grey bands represent the uncertainty shown as 1 standard deviation.

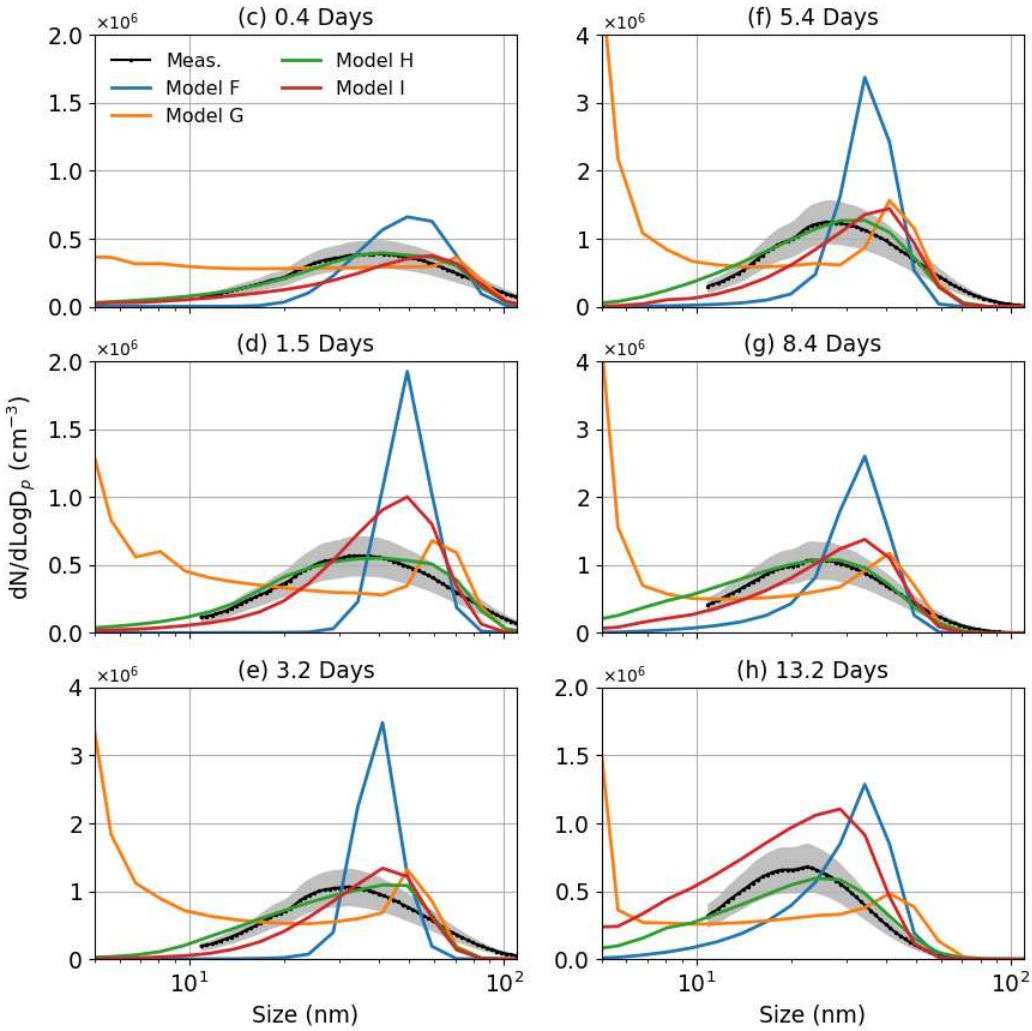

Figure C6: Simulated particle number size distributions from models F through I for the six different OH exposures.

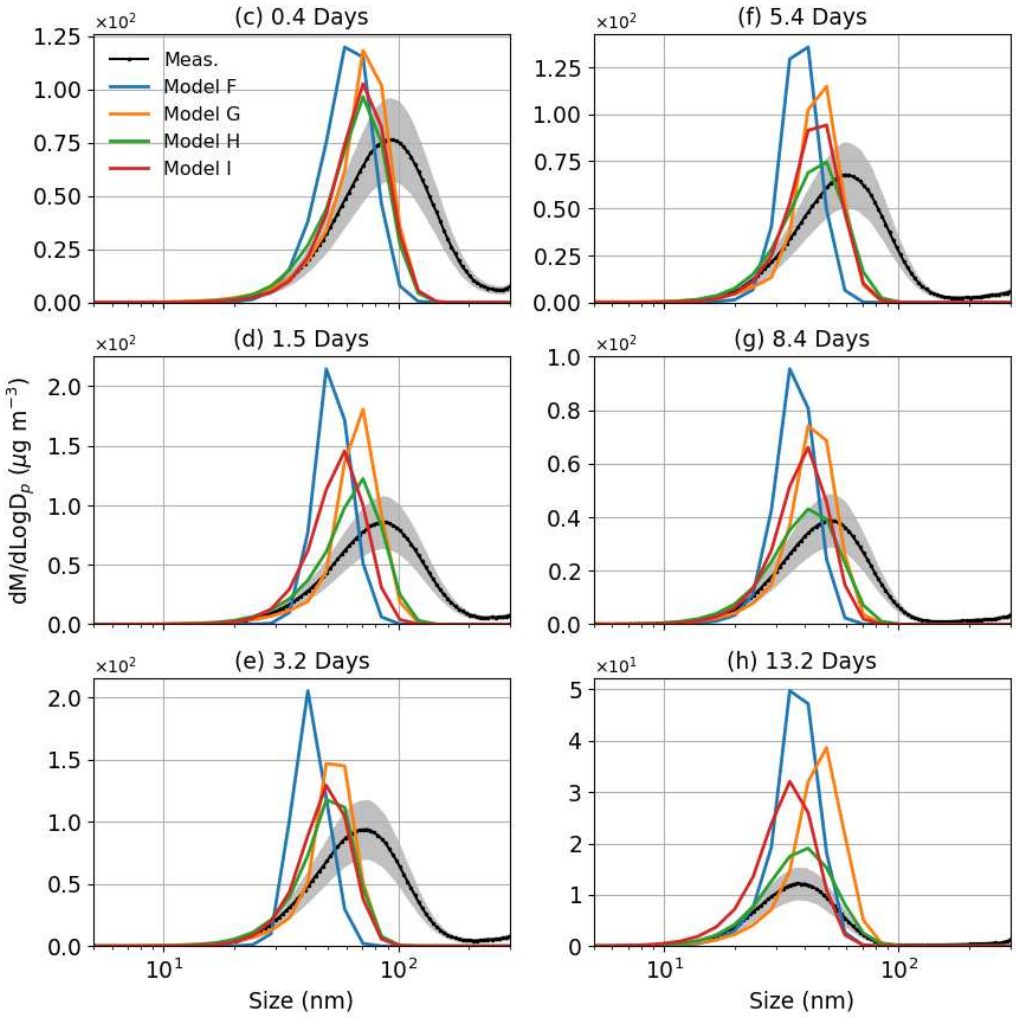

Figure C7: Simulated particle number size distributions from models F through I for the six different OH exposures. The grey bands represent the uncertainty shown as 1 standard deviation.

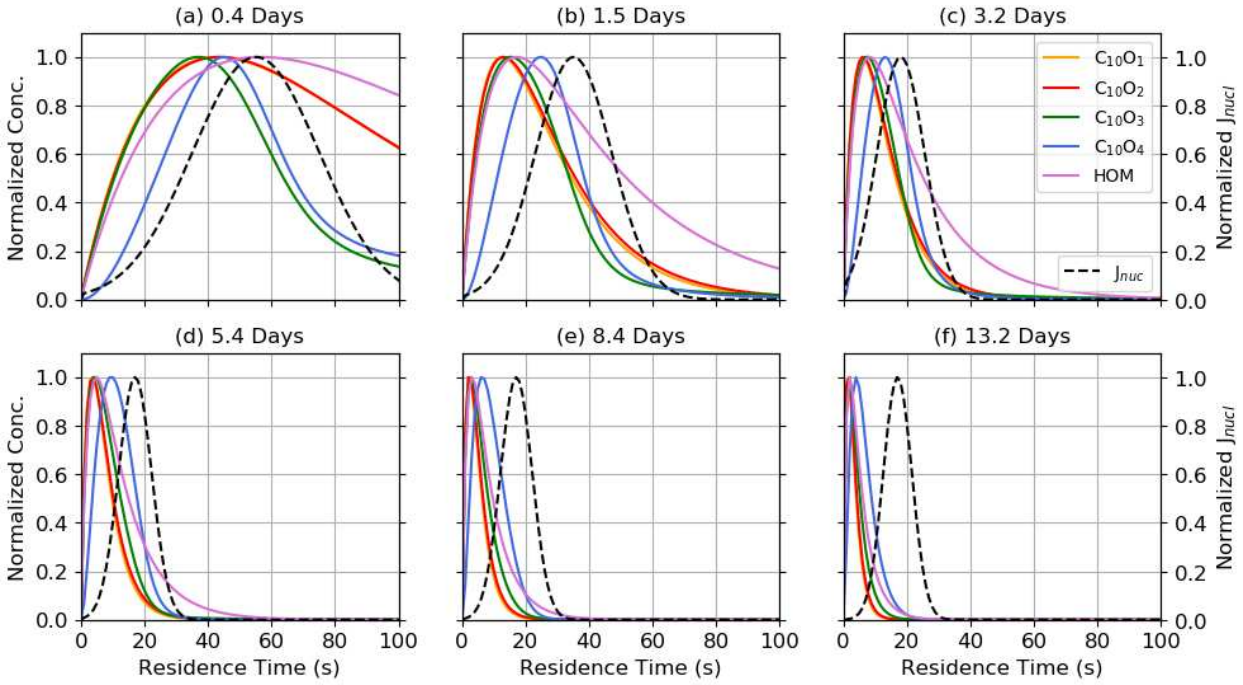

Figure C8: Normalized optimal J_{nuc} profiles from model H in comparison to normalized concentration profiles of gas-phase oxidation products ($C_{10}O_1$ through $C_{10}O_4$ and HOM).

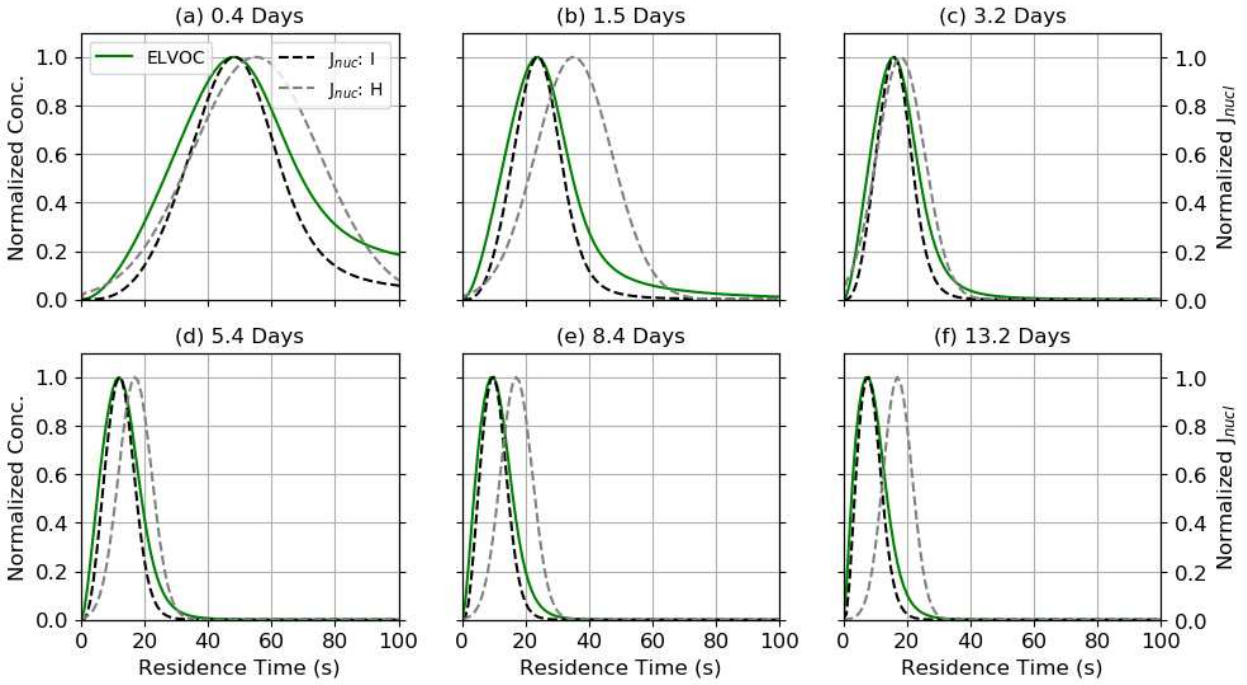

Figure C9: Normalized optimal J_{nuc} profiles from model H and I and normalized concentration profile of the nucleating ELVOC species.

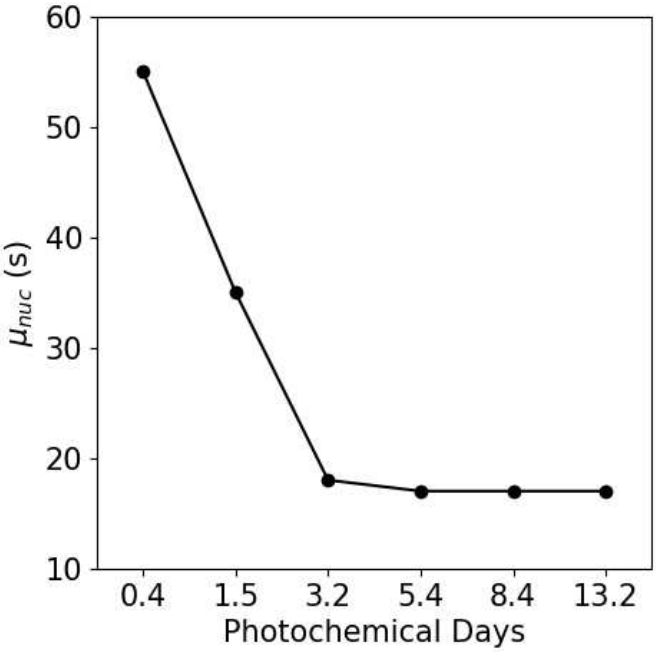

Figure C10: Optimal peak positions (μ_{nuc}) for the Gaussian J_{nuc} profiles for model H as a function of OH exposure.

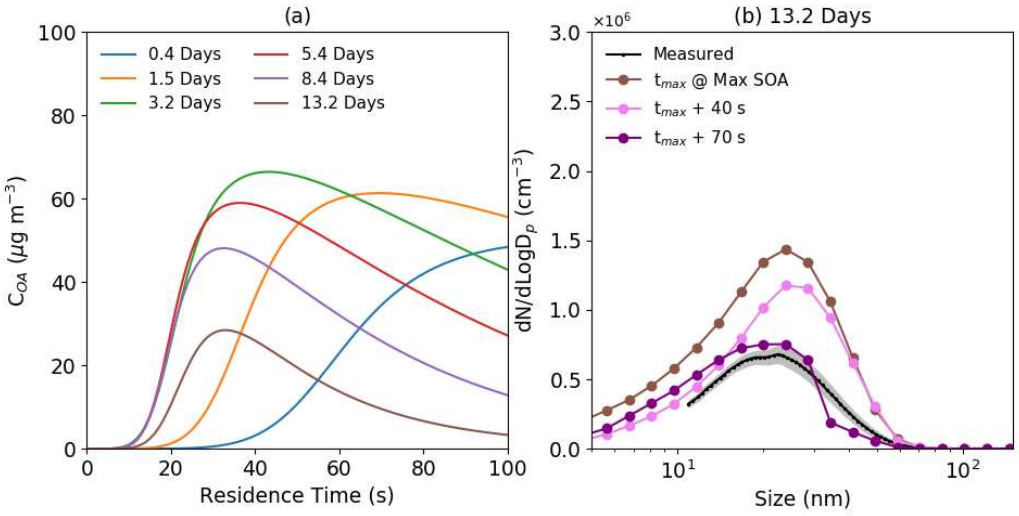

Figure C11: (a) SOA mass concentration inside the OFR from model H at six different OH exposures and (b) evolution of the particle size distribution at 13.2 days of OH exposure, starting from the time of maximal SOA concentration. The grey bands represent the uncertainty shown as 1 standard deviation.

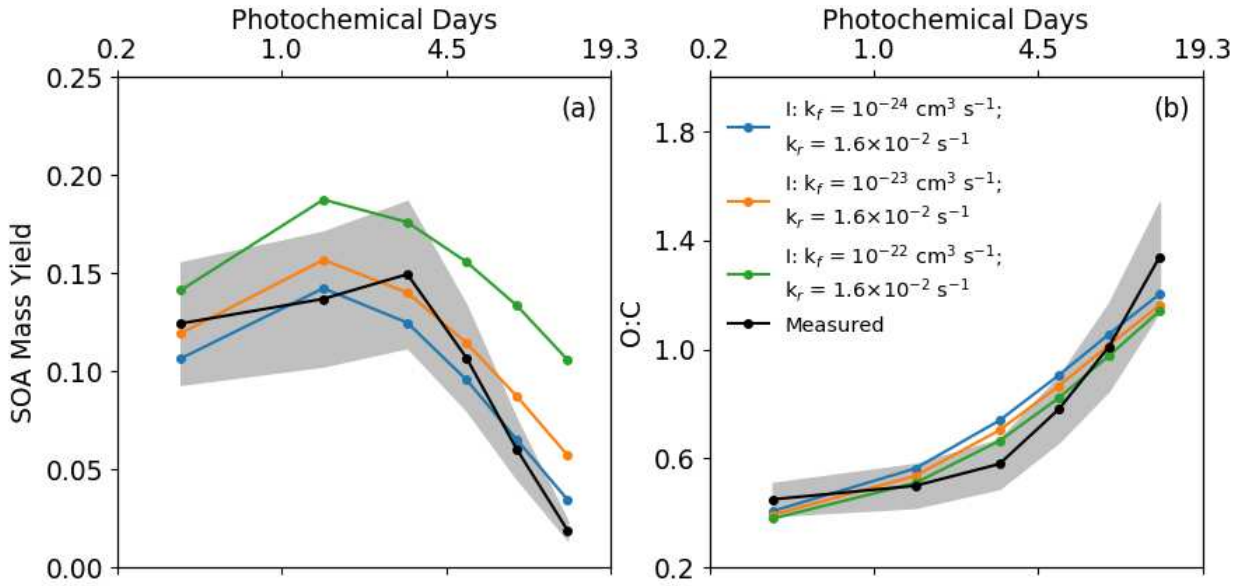

Figure C12: Sensitivity simulations using model I where we varied oligomer formation rates (k_f). Large changes were only realized when the k_f was above 10 times the base value.

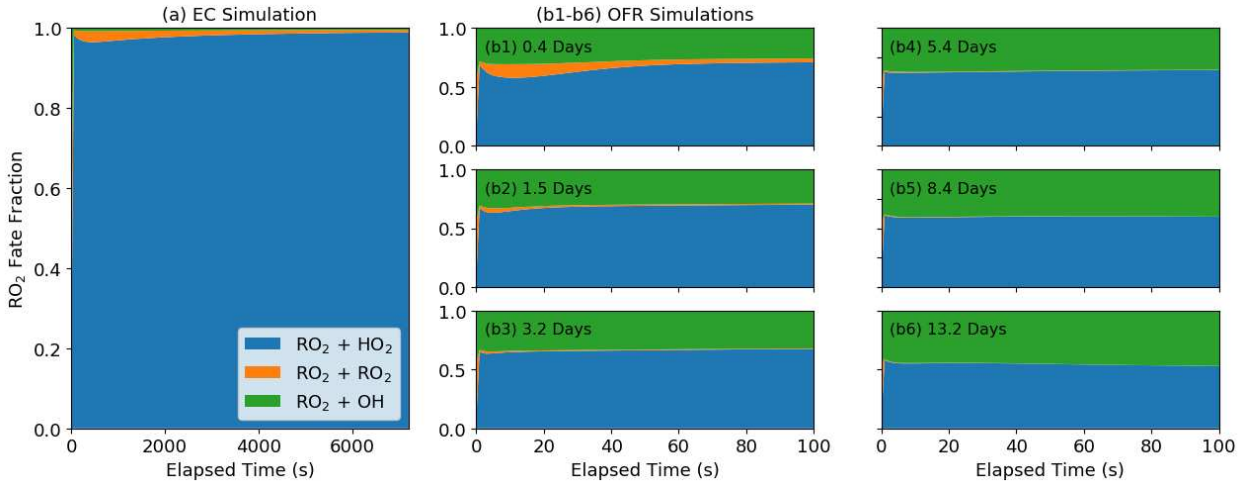

Figure C13: MCM-simulated RO_2 fate for (a) the EC experiment and (b1-b6) the OFR experiments.

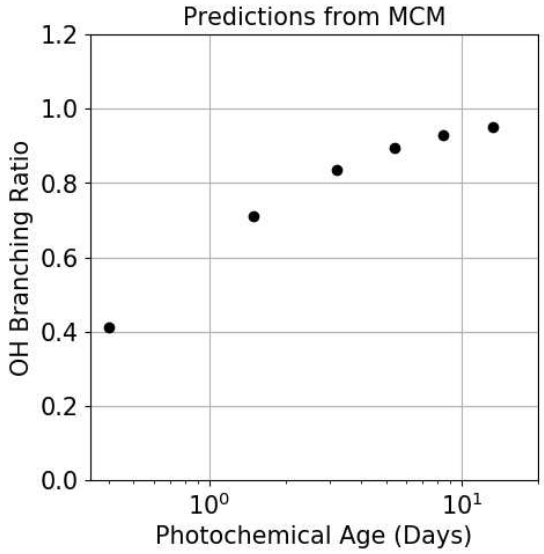

Figure C14: MCM-simulated α-pinene+OH branching ratio with respect to the sum of α-pinene+OH and α-pinene+O_3 reactions as a function of OH exposure.

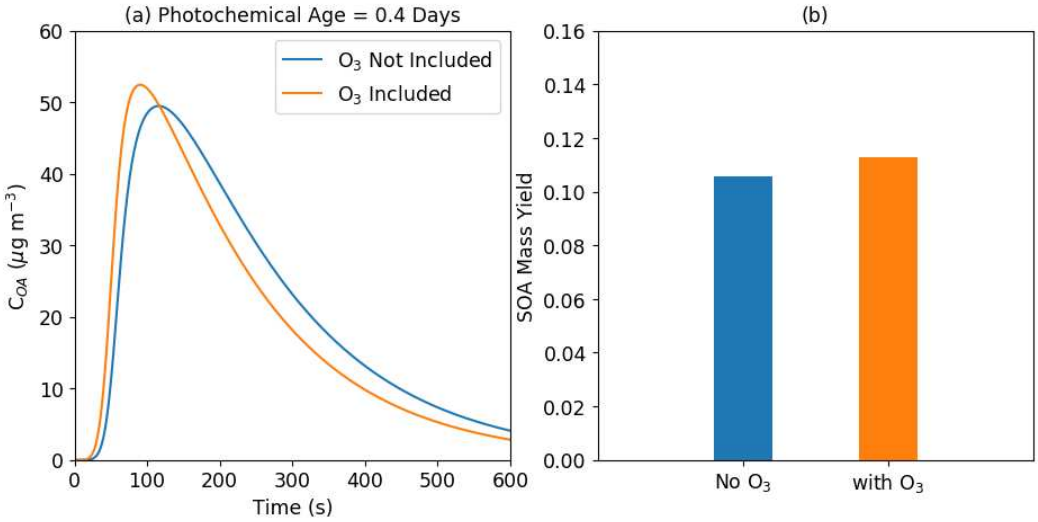

Figure C15: (a) Model-simulated OA mass concentrations inside the OFR for the lowest OH exposure (0.4 days) with and without α-pinene reaction with O_3 and (b) average SOA mass yields weighted by the residence time distribution.

Appendix D: Supplementary Information for Chapter 5

D1 Vapor Losses to Particles on the Wall

Here, we describe the mathematical formulation used to simulate vapor loss to deposited particles (V2PWL). We start with Eqn 5 from McMurry and Grosjean (1985a), which describes the change of vapor concentration with respect to loss to the walls.

$$-\frac{1}{C_1}\cdot\frac{dC_1}{dt}=\left(\frac{A}{V}\right)\cdot\frac{\alpha\bar{v}/4}{1+(\pi/2)\cdot\alpha\bar{v}/\left(4\cdot\sqrt{k_eD}\right)} \qquad \text{(D1)}$$

where C_1 is the gas-phase concentration of a species; A is the reactor surface area; V is the reactor volume; α is the mass accommodation coefficient; $\bar{v}$ is the mean thermal velocity of the gas-phase molecules; k_e is the eddy diffusion coefficient; and D is the Brownian diffusion coefficient. If we rearrange Eqn D1,

$$-\frac{VdC_1}{dt}=A\cdot\frac{\alpha\bar{v}/4}{1+(\pi/2)\cdot\alpha\bar{v}/\left(4\cdot\sqrt{k_eD}\right)}\cdot C_1 \qquad \text{(D2)}$$

we see that Eqn D2 is a statement of the mass conservation principle in the form of

$$-\frac{dm}{dt}=A\cdot J \qquad \text{(D3)}$$

where J is the flux of the vapor to the chamber walls. Thus, the formulation for J is

$$J=\frac{\alpha\bar{v}/4}{1+(\pi/2)\cdot\alpha\bar{v}/\left(4\cdot\sqrt{k_eD}\right)}\cdot C_1 \qquad \text{(D4)}$$

when α is sufficiently large, Eqn D4 becomes (McMurry and Grosjean, 1985a)

$$J=\frac{2\sqrt{k_eD}}{\pi}\cdot C_1 \qquad \text{(D5)}$$

This represents the same flux term that we need to use when simulating V2PWL, where we make one modification by including the vapor concentration at the particle surface (C_s).

$$J_{V2PWL}=\frac{2\sqrt{k_eD}}{\pi}\cdot(C_1-C_s) \qquad \text{(D6)}$$

Now we compare Eqn D5 to the SOA condensation flux, shown as follows.

$$J_{cond}=K_p\cdot(C_1-C_s) \qquad \text{(D7)}$$

where K_p is the overall mass transfer coefficient with respect to the suspended particles. We can note that Eqn D5 and D6 have similar forms and the first factor in Eqn D5 constitutes a mass transfer coefficient, which we name K_{V2PWL}.

$$K_{V2PWL} = \frac{2\sqrt{k_e D}}{\pi} \quad \text{(D8)}$$

Thus, we now have two equations for calculating vapor flux to particles: for suspended particles (i.e. SOA condensation; Eqn D9a) and deposited particles (Eqn D9b), respectively.

$$J_{cond} = K_p \cdot (C_1 - C_s) \quad \text{(D9a)}$$

$$J_{V2PWL} = K_{V2PWL} \cdot (C_1 - C_s) \quad \text{(D9b)}$$

Based on Eqn D9a and D9b, we have two equations to describe condensational particle growth for suspended and deposited particles, respectively.

$$\frac{dm}{dt} = A \cdot J_{cond} \quad \text{(D10a)}$$

$$\frac{dm}{dt} = 0.5 \cdot A \cdot J_{V2PWL} \quad \text{(D10b)}$$

Note that in Eqn D10b, the factor of 0.5 is used to account for flux to the exposed side of the deposited particles. Also, when simulating V2PWL without diffusion limitation, we would use Eqn D10a.

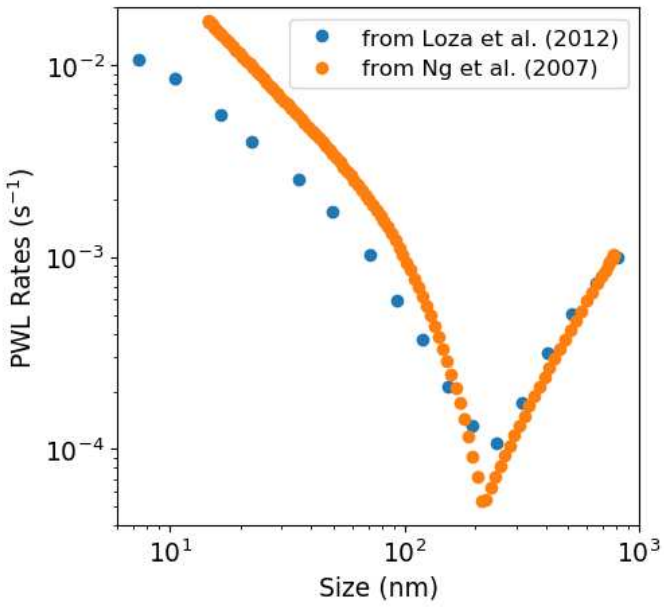

Figure D1: Comparison of particle wall loss kernels from chamber studies (Ng et al., 2007; Loza et al., 2012).

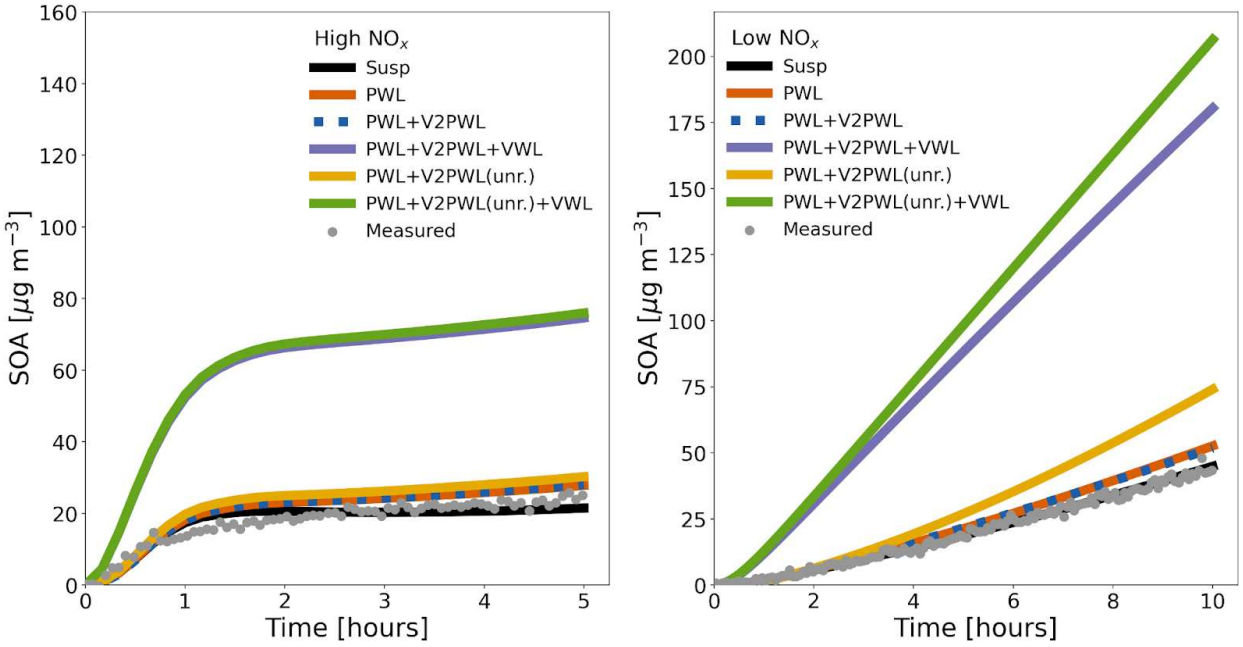

Figure D2: SOM-TOMAS estimates of secondary organic aerosol (SOA) mass concentration of benzene chamber experiments under high-NO_x (left panel) and low-NO_x (right panel) conditions. SOA measurements are shown in the gray dots (Ng et al., 2006). The black line shows the SOM-TOMAS model fit for the SOA mass concentration. The colored lines show the three artifact-corrected SOA estimates (PWL: orange, PWL+V2PWL: blue, PWL+V2PWL+VWL: purple). These artifact corrections are based on our 'realistic' V2PWL formulation, which correctly accounts for the mass transfer limitation. The PWL+V2PWL(unrealistic) and PWL+V2PWL(unrealistic)+VWL are based on our 'unrealistic' formulation, which does not account for the mass transfer limitation.

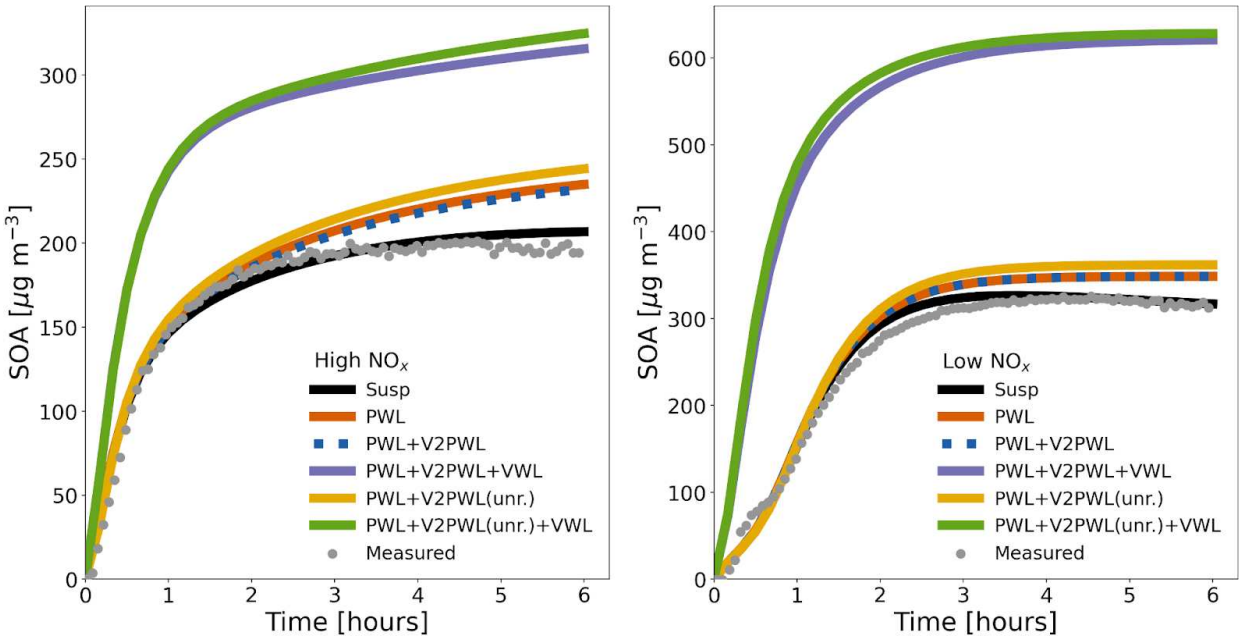

Figure D3: The same as for Figure D2 but for β-caryophyllene (Ng et al., 2006).

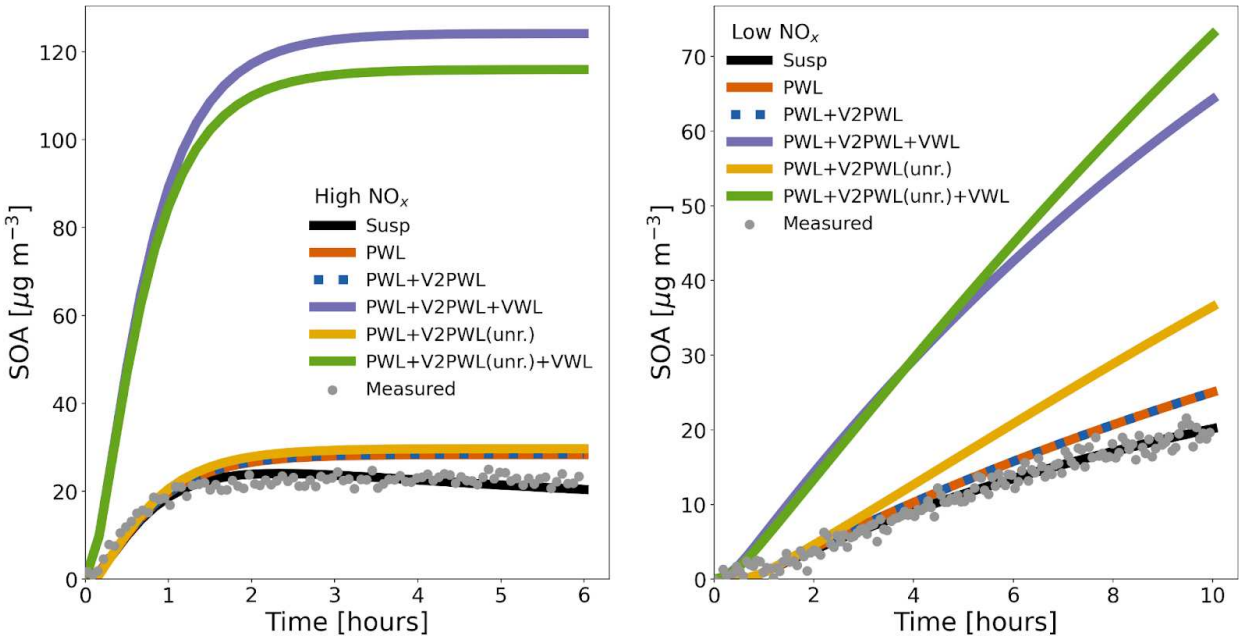

Figure D4: The same as for Figure D2 but for toluene (Ng et al., 2007).

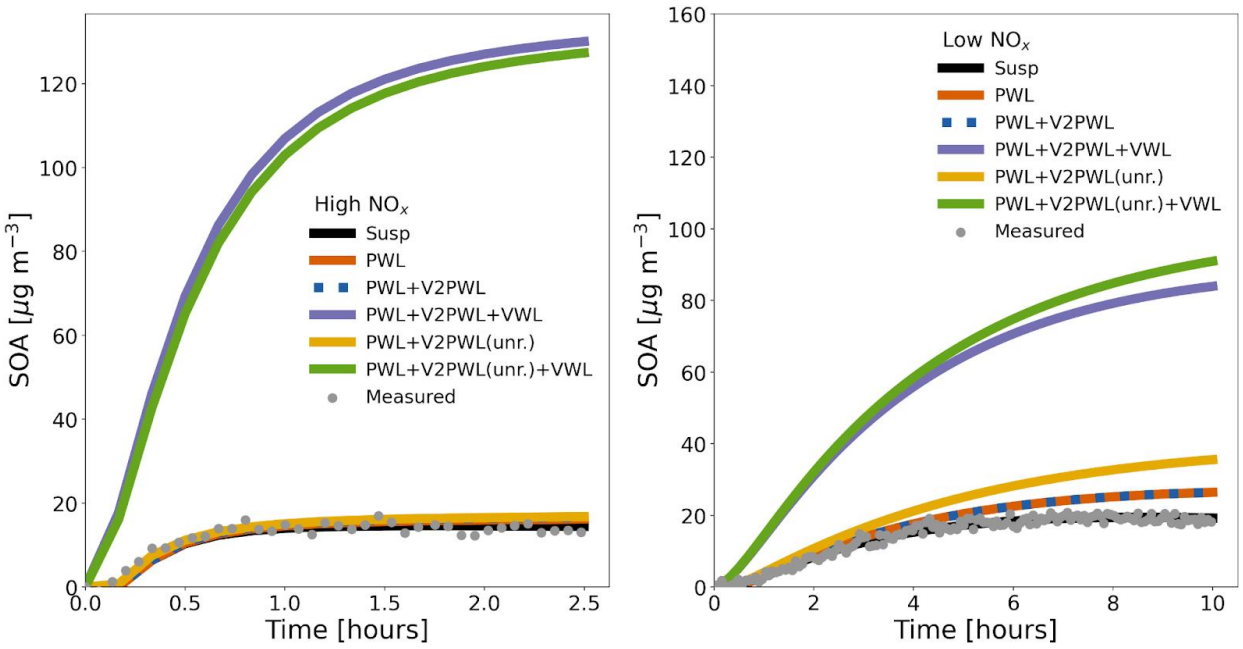

Figure D5: The same as for Figure D2 but for *m*-xylene (Ng et al., 2007).

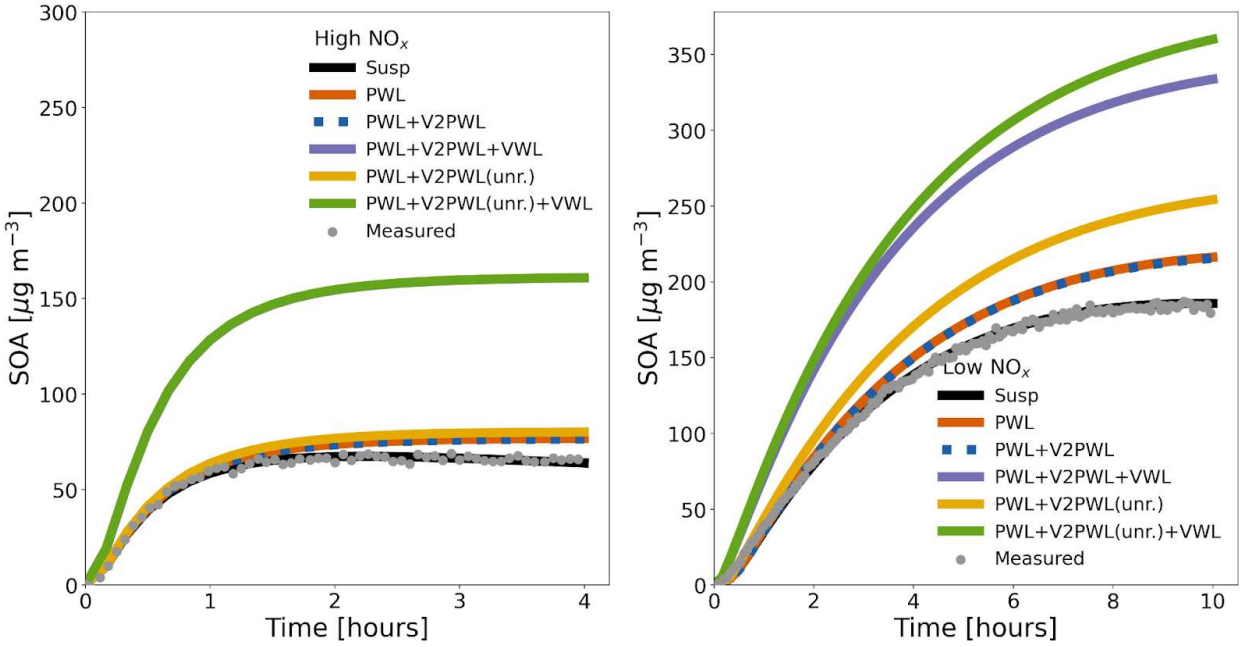

Figure D6: The same as for Figure D2 but for naphthalene (Chan et al., 2009).

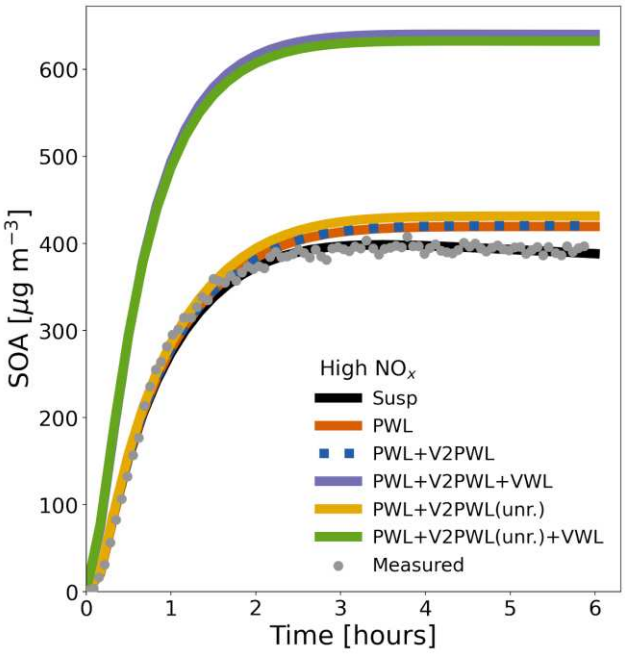

Figure D7: The same as for Figure D2 but for limonene (Ng et al., 2006).

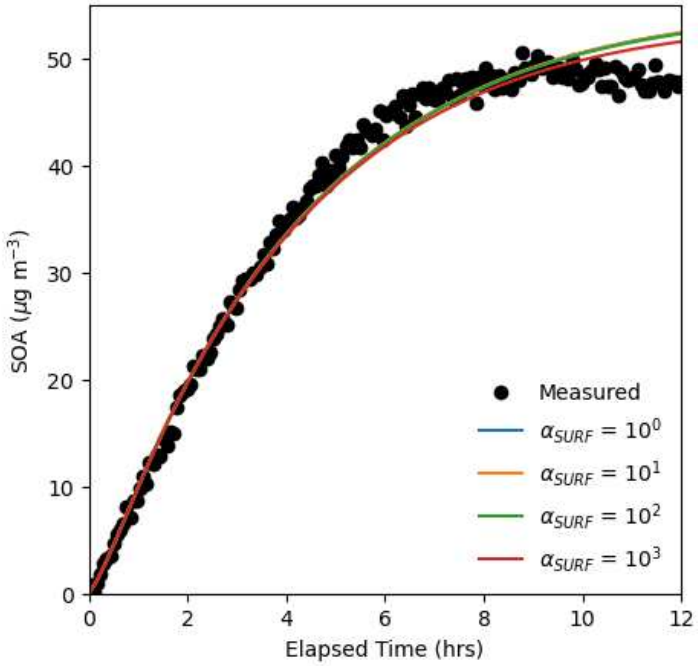

Figure D8: Sensitivity simulations on particle flattening for the *a*-pinene low-NO_x experiment. The flattening of the particles is characterized by the a_{SURF} parameter, which represents the scaling factor to the particle surface area when flattened. Higher a_{SURF} indicates greater flattening.

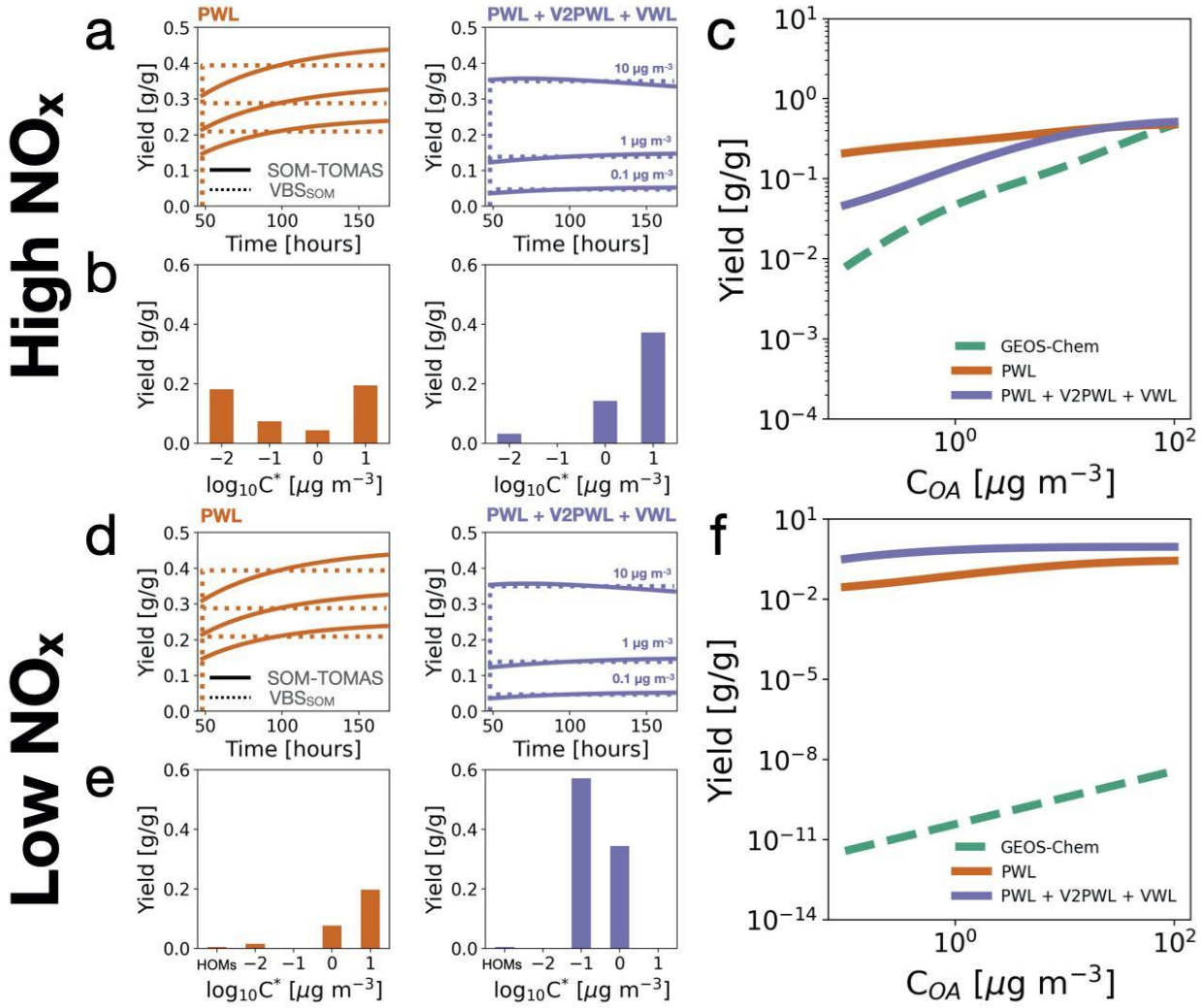

Figure D9: Panel a: Evolution of benzene secondary organic aerosol (SOA) mass yields as a function of atmospheric photochemical age at three different organic aerosol (OA) mass concentrations under high-NO_x conditions. Solid lines are the 'atmospheric' simulation results from SOM-TOMAS, while the dashed lines are the VBS_{SOM} model predictions. Panel b: VBS_{SOM} fit parameters resulting from panel a. Parameters were fit for C^*=0.1, 1, 10, 100 μg m^{-3}. Panel c: SOA mass yields across a range of OA mass concentrations based on the parameters in panel b. Panels d, e, and f: Are the same as panels a, b, and c, respectively, but for low-NO_x conditions. A bin was added for highly oxygenated molecules (HOMs) at C^*=10^{-6} μg m^{-3} for the low-NO_x conditions. The HOMs yields are from Bianchi et al. (2019).

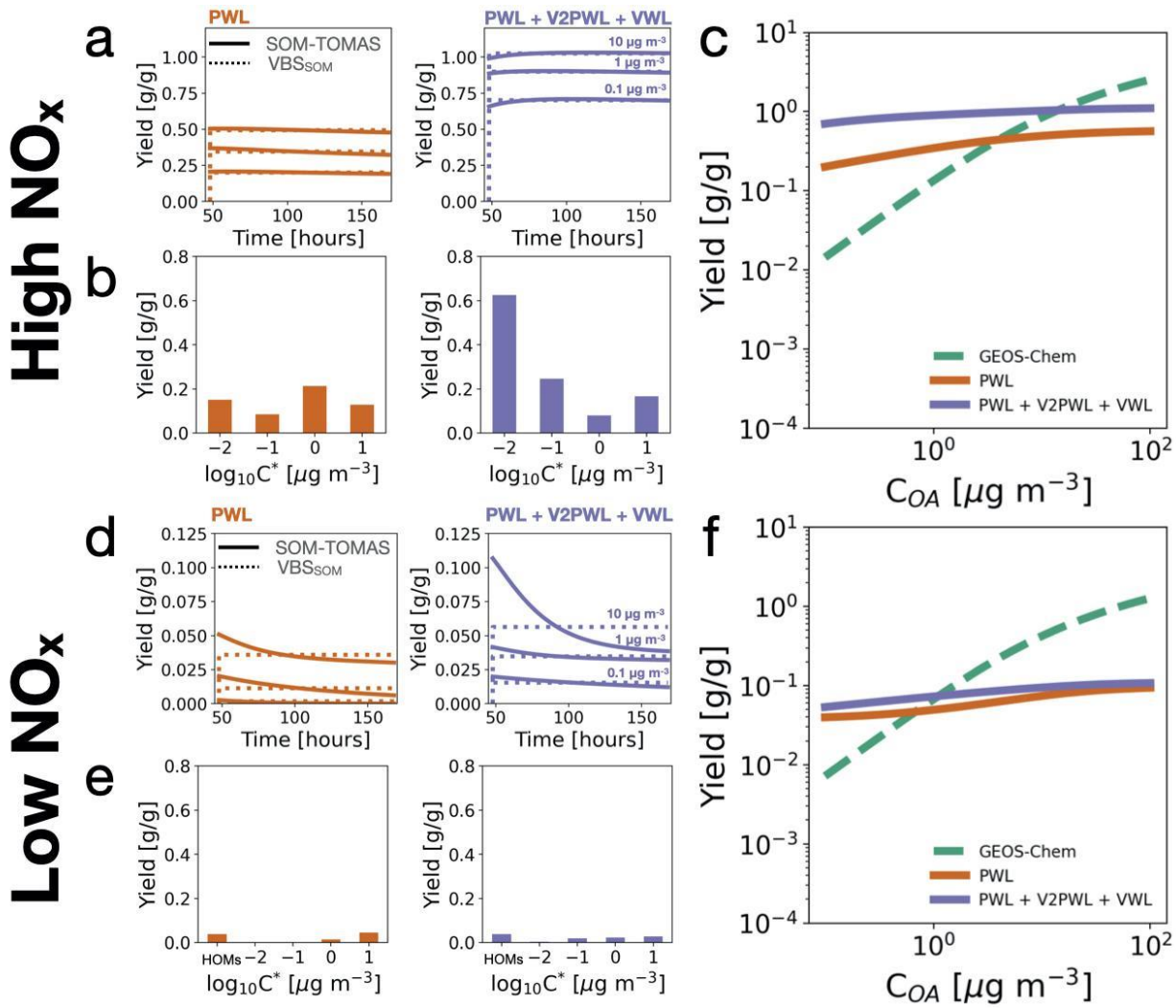

Figure D10: The same as for Figure D8 but for β-caryophyllene.

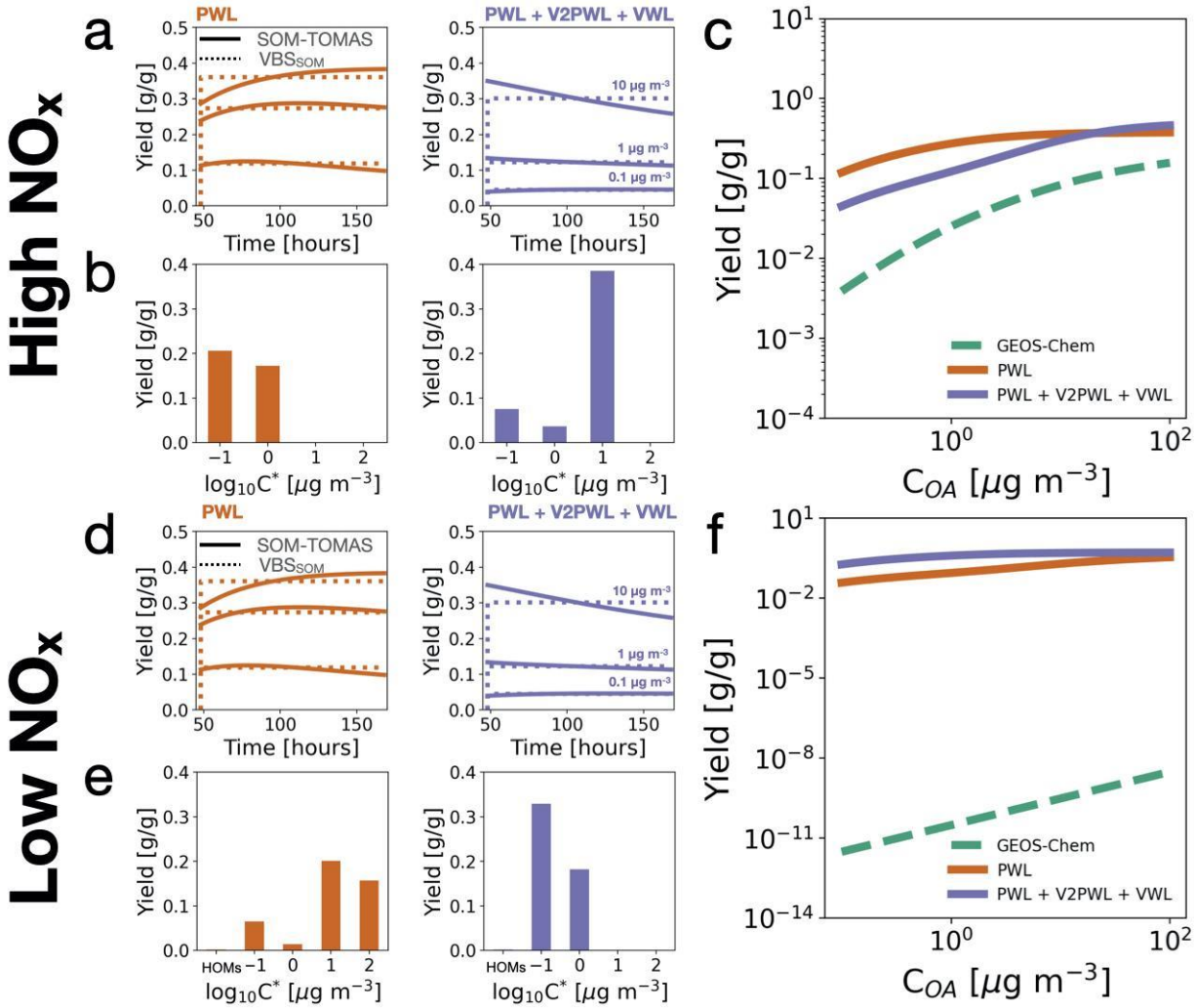

Figure D11: The same as for Figure D8 but for toluene.

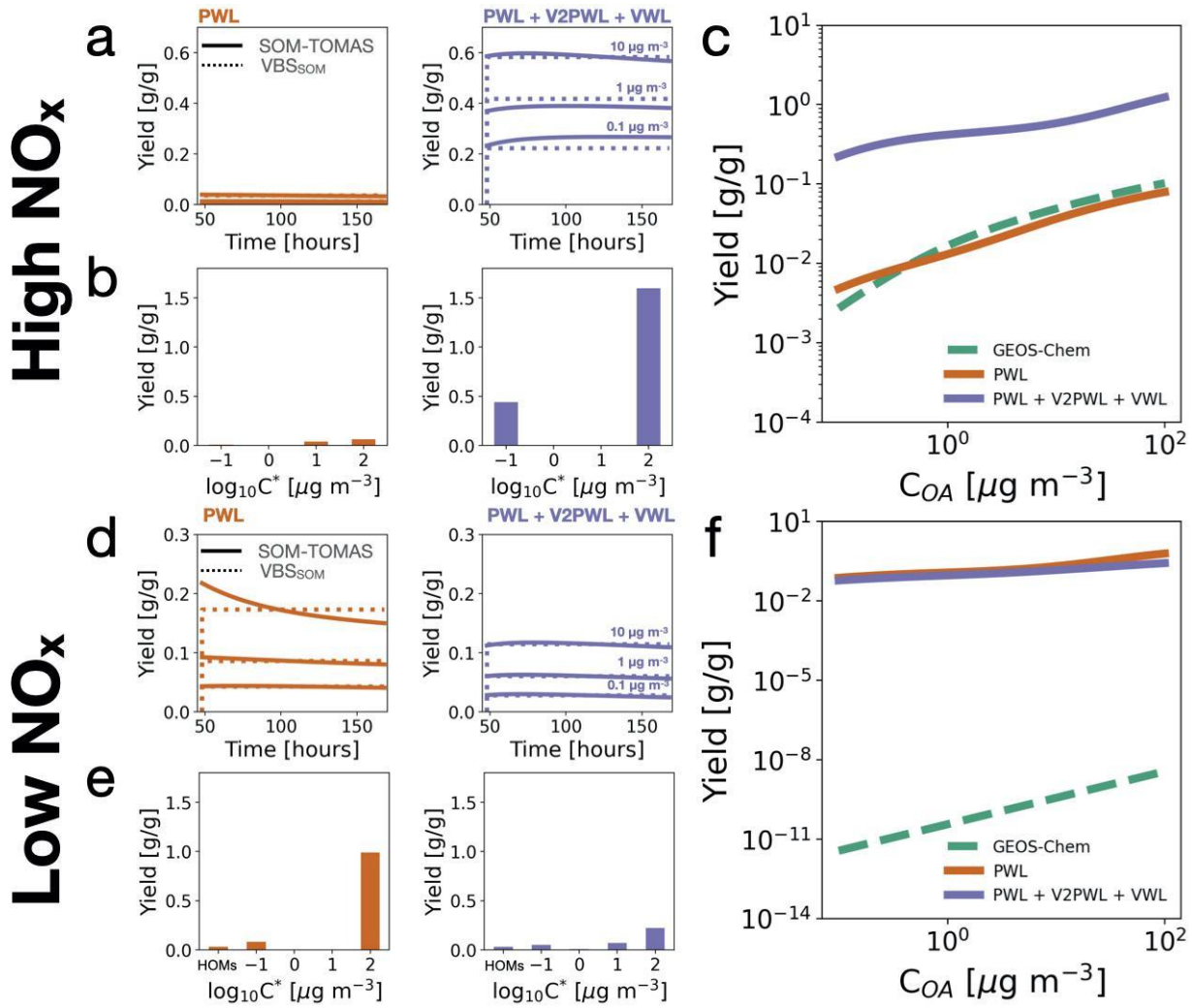

Figure D12: The same as for Figure D8 but for *m*-xylene.

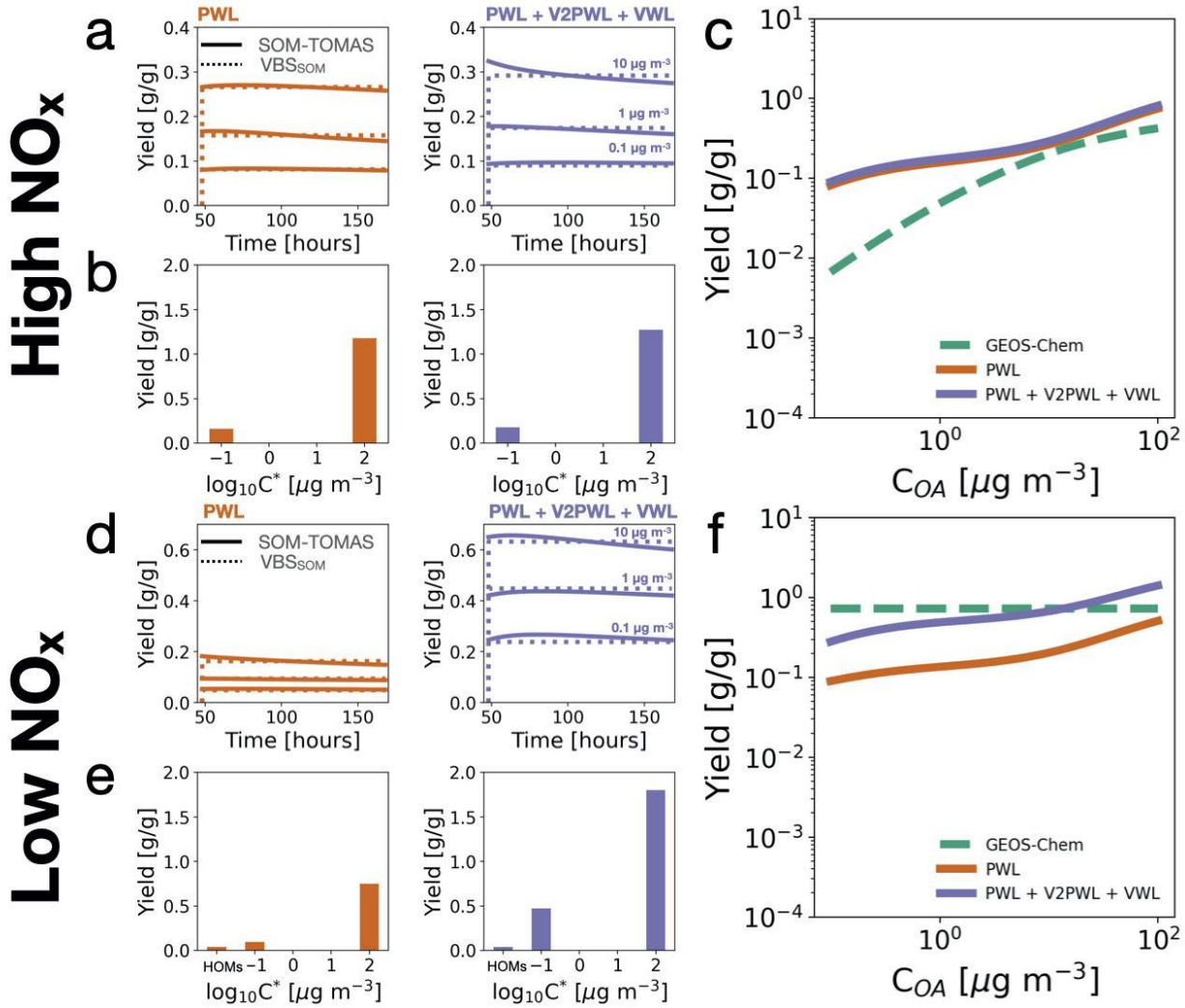

Figure D13: The same as for Figure D8 but for naphthalene.

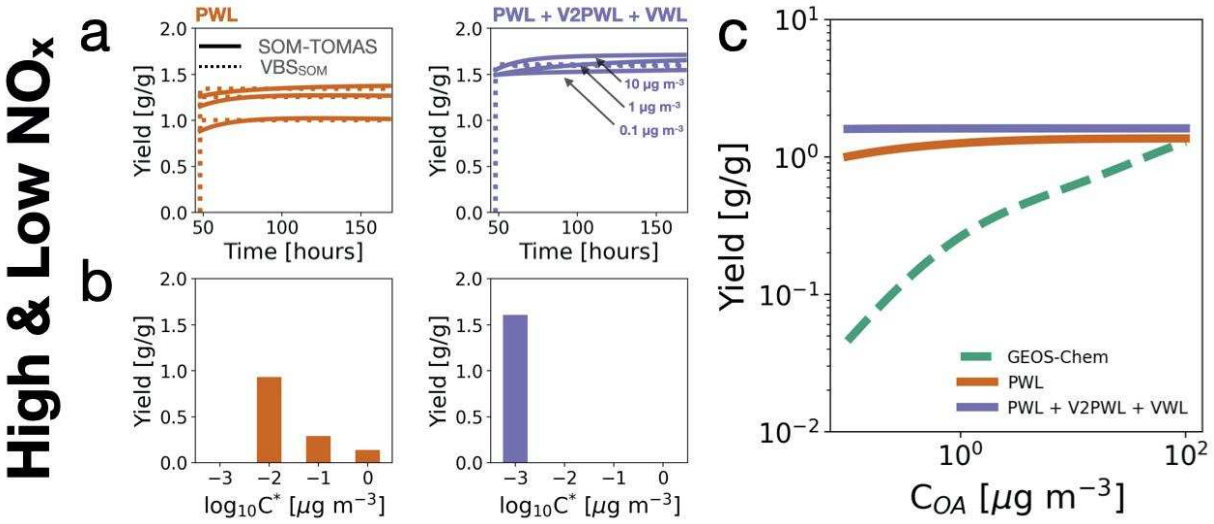

Figure D14: The same as for Figure D8 but for limonene. Note high- and low-NO_x parameters are the same for limonene.

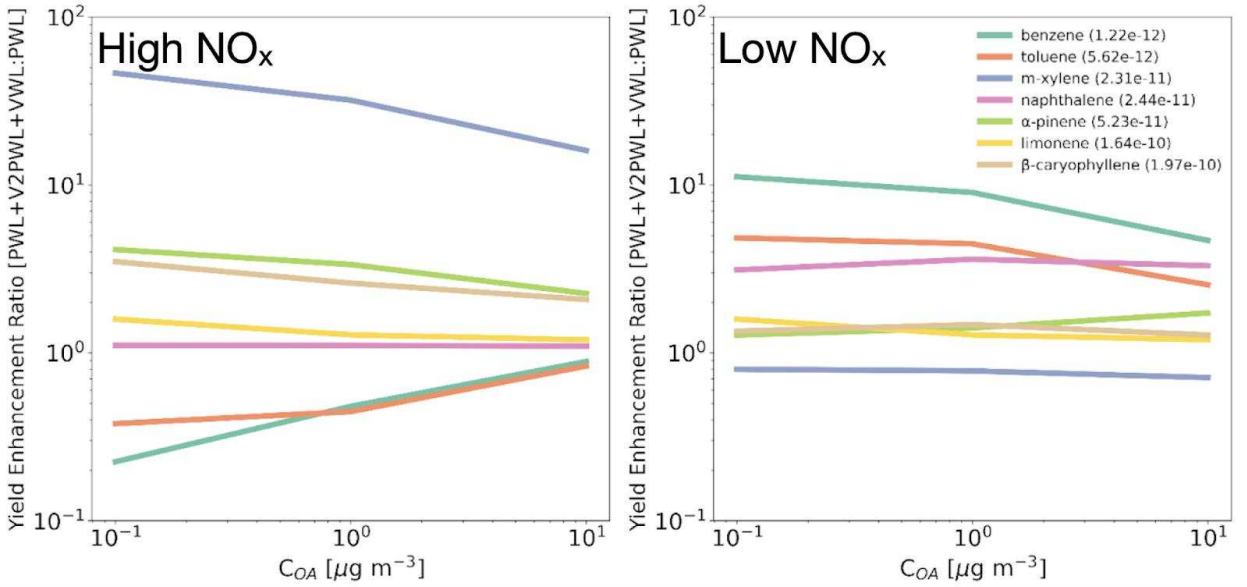

Figure D15: Yield enhancement ratio (YER) between PWL+V2PWL+VWL and PWL by VOC precursor, NO_x condition, and OA concentration. Reactivity (k_{OH}) is given in parentheses for each species.

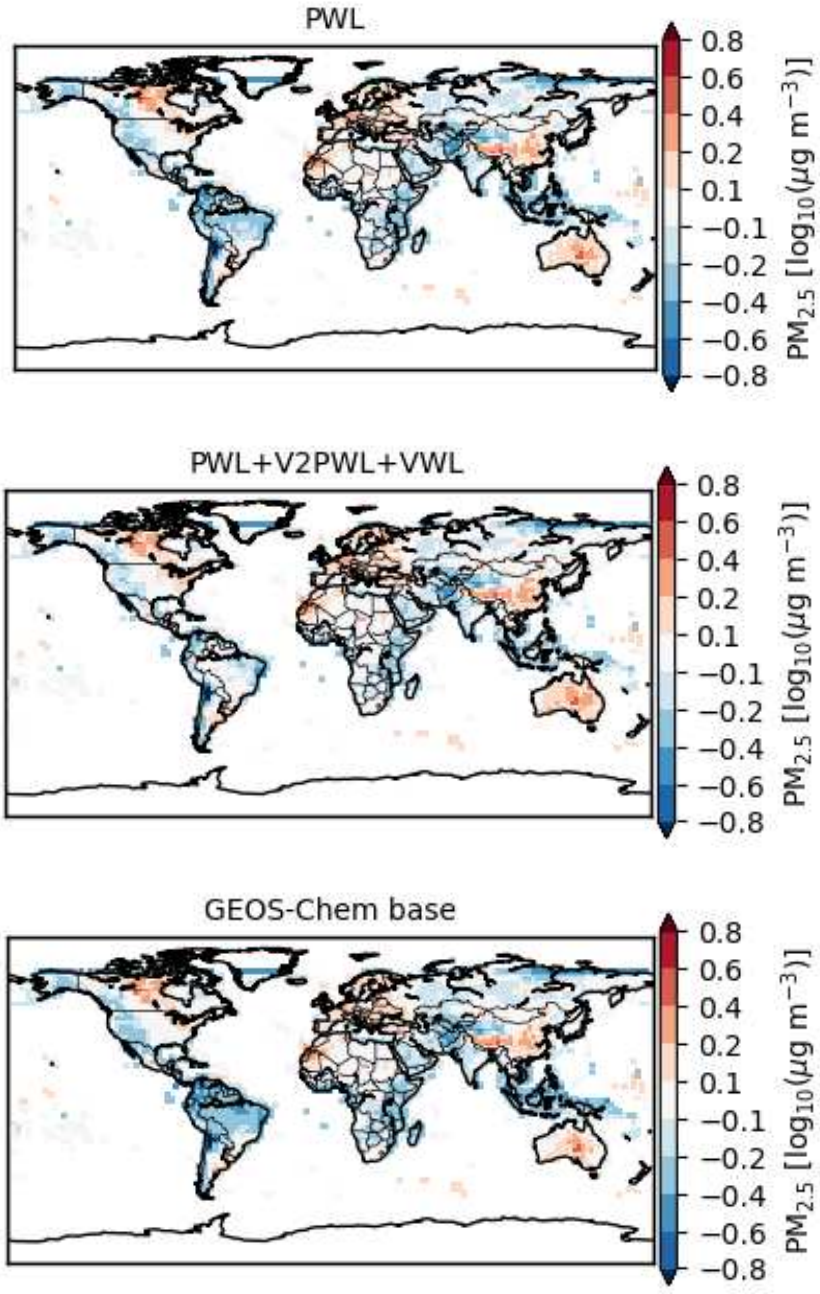

Figure D16: Maps showing the differences in fine particulate matter ($PM_{2.5}$) estimates from Hammer et al. (2020) vs $PM_{2.5}$ estimates from GEOS-Chem. GEOS-Chem estimates are from the PWL simulation, the PWL+V2PWL+VWL simulation, and the BASE simulation, which uses the default complex SOA scheme. Blues indicate the GEOS-Chem simulation is biased low, while reds indicate the GEOS-Chem simulation is biased high. White indicates that there is no bias between the GEOS-Chem simulation and Hammer et al. (2020).

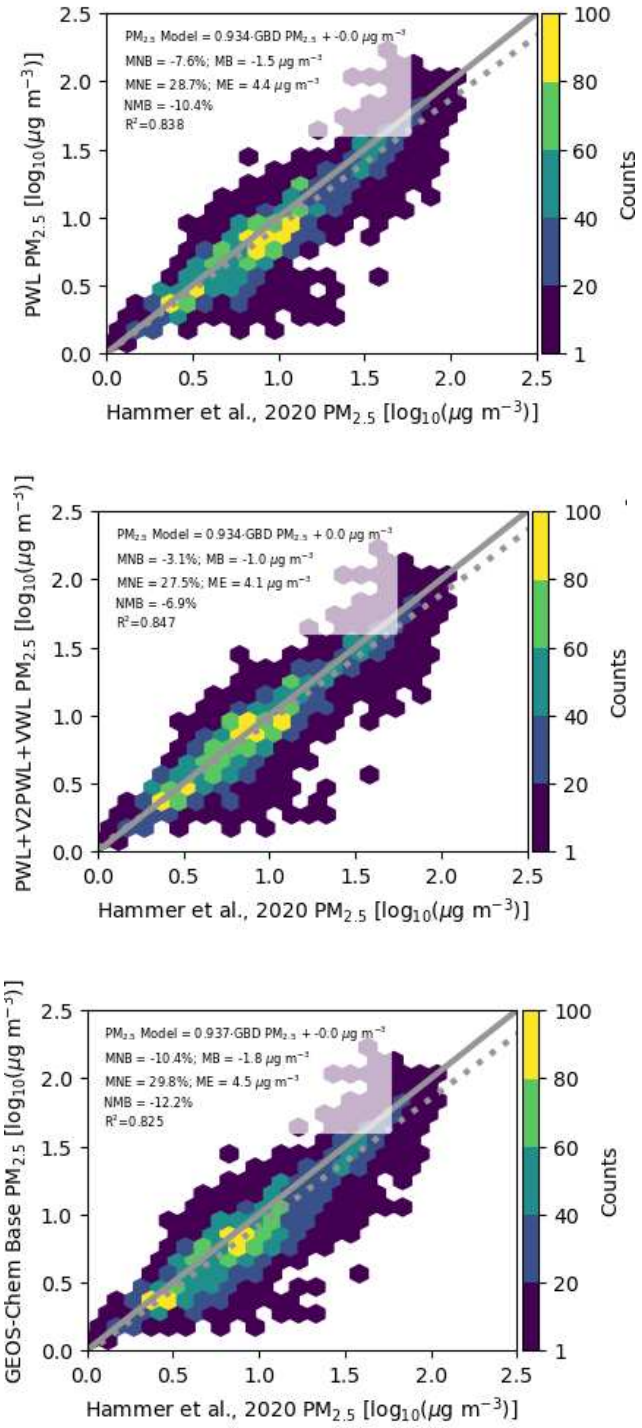

Figure D17: Fine particulate matter ($PM_{2.5}$) estimates from Hammer et al. (2020) vs $PM_{2.5}$ estimates from GEOS-Chem. GEOS-Chem estimates are from the PWL simulation, the PWL+V2PWL+VWL simulation, and the BASE simulation, which uses the default complex SOA scheme.

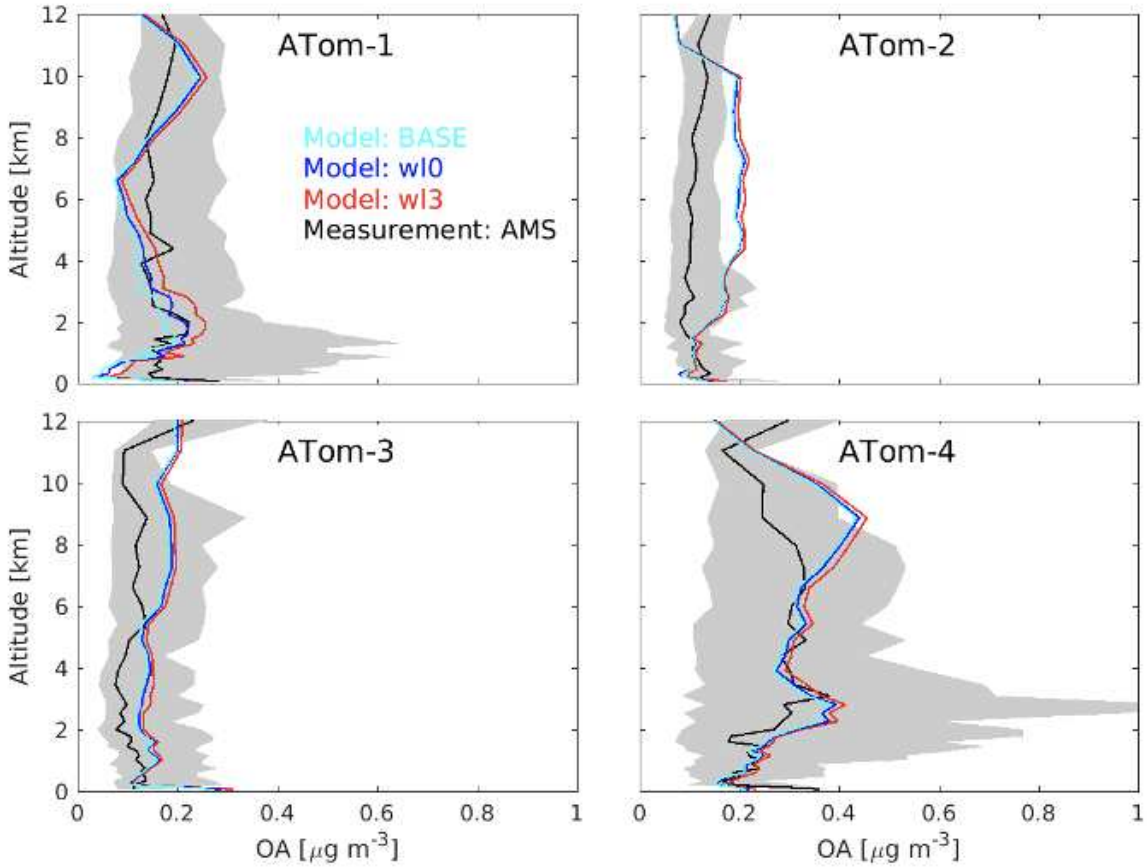

Figure D18: Northern Hemisphere median OA along Atmospheric Tomography Mission (ATom) campaign tracks from the aerosol mass spectrometer (AMS) (in black) compared to the three GEOS-Chem simulations, BASE (in cyan), PWL (wl0; in blue) and PWL+V2PWL+VWL (wl3; in red). The 25th to 75th percentile of the OA measurements are shaded in grey. (The dates of the field campaigns are as follows: Atom-1: 29 July 2016 to 23; August 2016 Atom-2: 26 Jan 2017 to 21 Feb 2017; ATom-3: 14 Sept 2017 to 27 Oct 2017; Atom-4: 10 Apr 2018 to 21 May 2018.)

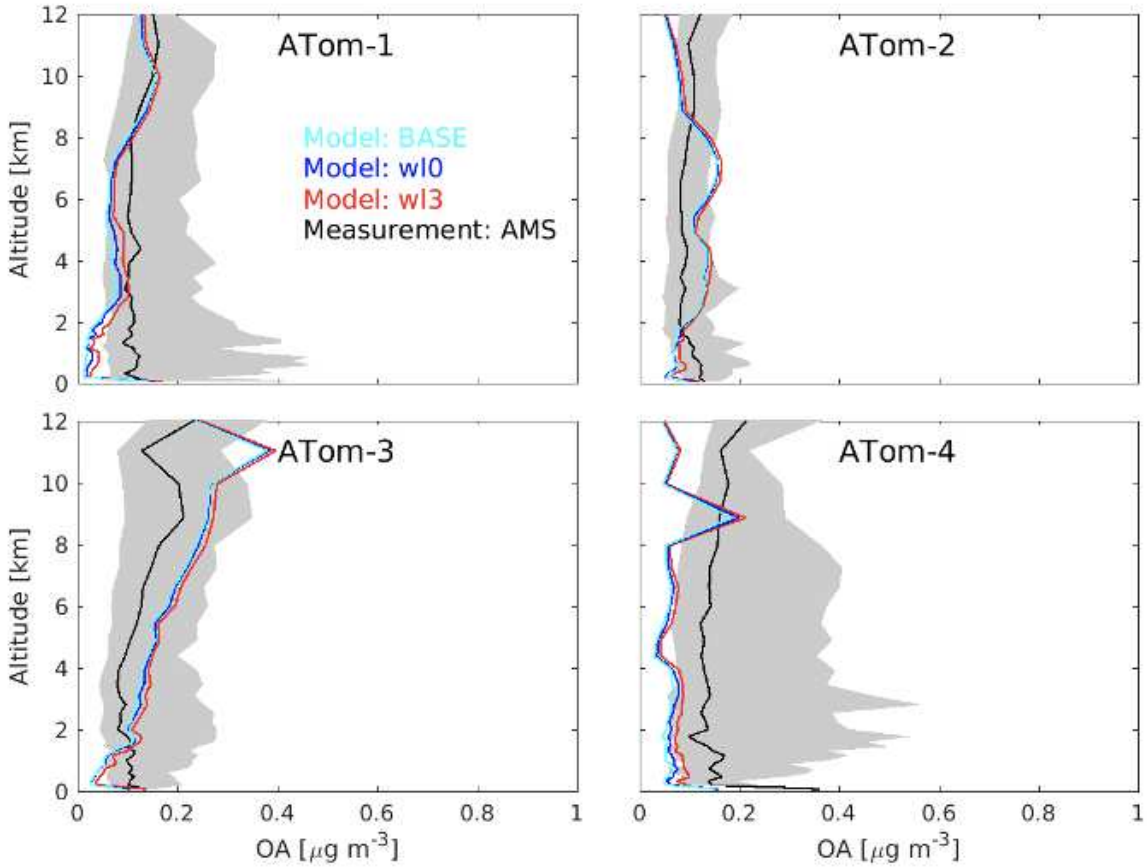

Figure D19: Global median OA along Atmospheric Tomography Mission (ATom) campaign tracks from the aerosol mass spectrometer (AMS) (in black) compared to the three GEOS-Chem simulations, BASE (in cyan), PWL (wl0; in blue) and PWL+V2PWL+VWL (wl3; in red). The 25th to 75th percentile of the OA measurements are shaded in grey. (The dates of the field campaigns are as follows: Atom-1: 29 July 2016 to 23; August 2016 Atom-2: 26 Jan 2017 to 21 Feb 2017; ATom-3: 14 Sept 2017 to 27 Oct 2017; Atom-4: 10 Apr 2018 to 21 May 2018.)

Table D1: Overview of chamber experiments used in this study. BDL = Below Detection Limit.

VOC	C#	$k_{OH}\times10^{12}$ ($cm^3\ s^{-1}$)	NO_x	NO_x (ppbv)	ΔVOC (ppbv)	SOA_{max} ($\mu g\ m^{-3}$)	SOA Yield	Reference
α-pinene	10	52.3	Low	BDL	45	50.6	0.20	Chhabra et al. (2011)
			High	847	45	49.7	0.20	
limonene	10	164.0	High	109	120	407.9	0.61	Ng et al. (2006)
β-caryophyllene	15	197.0	Low	BDL	88	325.6	0.44	
			High	28	37	201.2	0.65	
benzene	6	1.2	Low	BDL	98	48.0	0.15	Ng et al. (2007)
			High	169	84	25.8	0.10	
toluene	7	5.6	Low	BDL	40	21.6	0.14	
			High	946	64	25.0	0.10	
m-xylene	8	23.1	Low	BDL	19	20.8	0.25	
			High	945	81	17.0	0.05	
naphthalene	10	24.4	Low	BDL	63	187.3	0.57	Chan et al. (2009)
			High	377	40	68.9	0.33	

Table D2: VBS_{SOM} parameters for α-pinene for the PWL and PWL+V2PWL+VWL scenarios for high- and low-NOx experiments. The C^* column indicates the volatility bin.

NO_x	**C^* (μg m^{-3})**	**PWL**	**PWL+V2PWL+VWL**
High-NO_x	10^{-1}	0.027	0.073
	10^{0}	0.000	0.072
	10^{1}	0.072	0.119
	10^{2}	0.085	0.164
Low-NO_x	10^{-6}	0.073	0.073
	10^{-1}	0.067	0.131
	10^{0}	0.033	0.039
	10^{1}	0.026	0.083
	10^{2}	0.067	0.116

Table D3: The same as Table D2 but for limonene. Note high- and low-NO_x parameters are the same for limonene.

NO_x	**C^* (μg m^{-3})**	**PWL**	**PWL+V2PWL+VWL**
Low- and High-NO_x	10^{-1}	0.667	1.657
	10^{0}	0.341	0.000
	10^{1}	0.112	0.000
	10^{2}	0.178	0.000

Table D4: The same as Table D2 but for β-caryophyllene.

NO_x	**C^* (µg m^{-3})**	**PWL**	**PWL+V2PWL+VWL**
High-NO_x	10^{-1}	0.000	0.014
	10^{0}	0.000	0.000
	10^{1}	0.019	0.042
	10^{2}	0.039	0.010
Low-NO_x	10^{-6}	0.038	0.038
	10^{-1}	0.142	0.780
	10^{0}	0.202	0.204
	10^{1}	0.081	0.000
	10^{2}	0.262	0.210

Table D5: The same as Table D2 but for benzene.

NO_x	C^* (μg m^{-3})	PWL	PWL+V2PWL+VWL
High-NO_x	10^{-1}	0.780	0.000
	10^{0}	0.204	0.475
	10^{1}	0.000	0.392
	10^{2}	0.210	0.000
Low-NO_x	10^{-6}	0.005	0.005
	10^{-1}	0.022	0.036
	10^{0}	0.000	0.000
	10^{1}	0.083	0.138
	10^{2}	0.203	0.367

Table D6: The same as Table D2 but for toluene.

NO_x	C^* (μg m^{-3})	PWL	PWL+V2PWL+VWL
High-NO_x	10^{-1}	0.034	0.283
	10^{0}	0.249	0.212
	10^{1}	0.142	0.000
	10^{2}	0.112	0.000
Low-NO_x	10^{-6}	0.002	0.002
	10^{-1}	0.064	0.150
	10^{0}	0.020	0.000
	10^{1}	0.114	0.081
	10^{2}	0.526	1.537

Table D7: The same as Table D2 but for *m*-xylene.

NO_x	**C^* (μg m^{-3})**	**PWL**	**PWL+V2PWL+VWL**
High-NO_x	10^{-1}	0.034	0.481
	10^{0}	0.249	0.000
	10^{1}	0.145	0.000
	10^{2}	1.095	1.655
Low-NO_x	10^{-6}	0.031	0.031
	10^{-1}	0.064	0.150
	10^{0}	0.018	0.000
	10^{1}	0.134	0.081
	10^{2}	0.436	1.537

Table D8: The same as Table D2 but for naphthalene.

NO_x	C^* (μg m^{-3})	PWL	PWL+V2PWL+VWL
High-NO_x	10^{-1}	0.185	0.481
	10^{0}	0.000	0.000
	10^{1}	0.000	0.000
	10^{2}	1.278	1.655
Low-NO_x	10^{-6}	0.041	0.041
	10^{-1}	0.075	0.221
	10^{0}	0.000	0.000
	10^{1}	0.000	0.000
	10^{2}	0.800	1.207